Charles University in Prague

Faculty of Mathematics and Physics

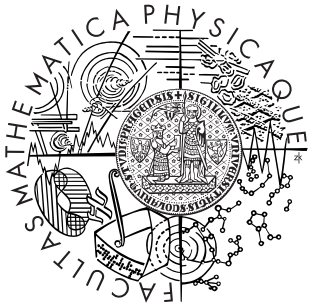

HABILITATION THESIS

Interfacial phase transitions and critical phenomena in non-planar confining geometries

Mgr. Alexandr Malijevský, Ph.D.

2014

Contents

1 Preamble

The presented habilitation thesis is based on ten selected papers I have published during the period of years 2010–2014. The timeliness of the works was not, however, the main criterion for the selection of the publications. Instead, I attempted to choose such studies which would well illustrate one particular topic of my recent research. These studies concern with a statistical-mechanical description of phase transitions and critical phenomena of continuous model systems that experience an influence of an external field, generated by confining walls. Although it is quite common in the theory of phase transitions to formulate the problems in terms of magnets, I will use the language of fluids throughout the thesis as I also do in my works. As the focus is on phase behaviour driven by the presence of a (solid) confinement, we study *interfacial phase transitions* that are not present and should be distinguished from bulk phase phenomena. I have studied the interfacial phenomena of the model systems in the framework of the statistical physics and in particular using the two following statistical-mechanical treatments. A microscopic approach, represented by the classical density functional theory (DFT) regarded nowadays as a standard tool in the statistical physics of liquids that provides a general framework for calculating density profiles, correlation functions and phase behaviour of model fluids defined by a given effective Hamiltonian. The only input to the theory is the interaction potential between fluid particles and the potential between fluid and wall particles. Although DFT can also be applied for modelling of complex systems, such as polymer solutions and polymer melts, colloidal dispersions and colloidal liquid crystals, the focus in the presented papers is on simple atomic systems. It is not only because it is for this class of models that DFT approximations are successfully developed but also because the main concern of the presented works is on general, fundamental aspects of a given model system, for which a selection of a particular fluid model is largely irrelevant. The second approach is a field-theoretical treatment based on a coarse-grained interfacial Hamiltonian model. In this case, rather than $\rho(\mathbf{r})$, the equilibrium density profile of the fluid, one attempts to find a solution for the local interface position $\ell(\mathbf{x})$ separating two coexisting fluid phases, stabilised by a presence of the wall. This mesoscopic approach considerable simplifies the problem and the great advantage of this approach is its mathematical tractability which often allows for analytic predictions. There exist well-developed mathematical methods that can be used to determine approximately or even exactly the partition function corresponding to a given model. This is, of course, at the cost of sacrificing a contribution of the microscopic degrees of freedom that may play a crucial role especially in the cases of strongly inhomogeneous systems. The combination of the two methods both of which have its pros and cons and which complement each other proved to be very fruitful in addressing the questions such as: What kind of phase transitions does the given system exhibit? What is the order of the transitions? What is the equilibrium structure of the fluid? What are the values of the pertinent critical exponents? Are

the fluctuation effects important (or even dominant) or is a description based on a mean-field theory sufficient? What is the effect of the system geometry and the microscopic features of the system constituents? What is the relation between phase behaviours in different geometries? What is the effect of the range of the intermolecular forces and what are the universality classes?

Although the phase behaviour of fluids adsorbed at a planar wall (wetting) or confined between two parallel walls (capillary condensation) is nowadays well understood, our understanding of the behaviour of fluids in systems of non-planar symmetries is still developing and a microscopic insight in this field is almost entirely lacking. One of the main motivations to pursuit such systems is the fact that the perfectly flat, structure-less walls, as commonly considered to be a model of solid substrates, are idealized. In fact, a fluid upon adsorption encounters geometrically and energetically heterogenous walls. It has been recognized that corrugation and roughness of the adsorbing surfaces can have a significant influence on their wettability and may induce entirely novel phenomena and fluctuation regimes.

Prior examining an influence of a geometrical heterogeneity of surfaces on their wettability it is necessary to understand the nature of the interfacial properties of fundamental non-planar objects, such as sphere, wedge-like cavity, edge-shaped structure, groove etc. It reveals that all of these geometries have some very specific features in terms of phase phenomena they induce. Furthermore, there exist hidden symmetries, or so called covariances, which relate local adsorption properties in different confining geometries. For more complex but still rather simple geometries, there may exist appealing interplay between these phenomena which eventually gives rise to very rich phase behaviour of the adsorbed fluid. The presented thesis describes my contribution to this intriguing field of the current research.

Attempting to make the text of the thesis self-contained, I start with a very brief overview of bulk critical phenomena (section 2) which is followed by a concise introduction to the theory of wetting transitions on planar surfaces (section 3). Regarding the latter, there has been no attempt to give a comprehensive review of this topic which has enormously grown over the last three decades. There are several classic textbooks or sections in monographs devoted to this subject[1]. In section 4, I give a brief description of the classical density functional theory. The main part of the thesis is section 5 which is devoted to interfacial phenomena in non-planar confining geometries that have been studied in the selected papers. The final part of the thesis form the enclosed publications.

[1]See, e.g., D. E. Sullivan and M. M. Telo da Gama, in *Fluid Interfacial Phenomena*, edited by C. A. Croxton (Wiley, New York, 1985); S. Dietrich, in *Phase Transitions and Critical Phenomena*, edited by C. Domb and J. L. Lebowitz (Academic, New York, 1988), Vol. 12.; M. Schick, in *Liquids and Interfaces*, edited by J. Chorvolin, J. F. Joanny, and J. Zinn-Justin (Elsevier, New York, 1990).

2 Bulk Critical Phenomena

Bulk phase transitions and critical phenomena occur in macroscopic systems where no confining walls and other external fields exist (or can be neglected). In figure 1 we sketch a P-T diagram where the lines represent the loci of points where two distinct phases coexist. When such lines are crossed during a thermodynamic process, the system undergoes first-order phase transition, characterised by a non-zero value of a latent heat which is adsorbed or released as the system transforms from one phase to another. The liquid-vapour line terminates at the *critical point* beyond which no distinction between the two phases can be made. This means that the coexistence line can be bypassed in a path connecting two distinct fluid phases. This contrasts with the solid-liquid and solid-vapour transitions since in these cases two phases of different symmetry are involved. The phenomena that occur near the critical point are called critical phenomena and can be characterised by strong fluctuation effects and by a power-law divergence of several physical quantities. The order parameter is a measure of the degree of order across the boundaries in a phase transition system. For the liquid-vapour system the order parameter is the density difference between the two phases, $\rho_L - \rho_V$, so that its value is zero above the critical temperature T_c and non-zero below. Instead of the critical temperature itself it is often more convenient to consider the reduced temperature $t = (T_c - T)/T_c$. The critical behaviour of a given system can be characterised by a set of *critical exponents* which quantify the singularities of the free-energy at the critical point as follows:

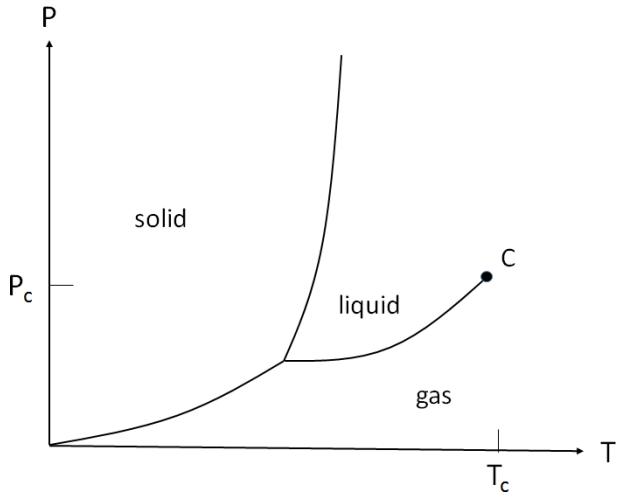

Figure 1: Temperature-pressure phase diagram of a simple substance. All the transitions are discontinuous except at the critical point (C).

- Specific heat: $C_v \propto |t|^{-\alpha}$ as $t \to 0$ at $\rho = \rho_c$;
- Density difference: $\rho_L - \rho_V \propto t^{\beta}$ as $t \to 0$;
- Isothermal compressibility: $\chi_T \propto |t|^{-\gamma}$ as $t \to 0$;
- Critical isotherm: $\rho_L - \rho_V \propto |P - P_c|^{1/\delta}$ as $P \to P_c$ at $t = 0$;
- Correlation length: $\xi \propto |t|^{-\nu}$ as $t \to 0$;
- Density-density correlation function: $G(r) \propto \frac{1}{r^{d-2+\eta}}$ at $t = 0$.

The concept of the critical point was introduced in 1869 when Andrews presented his experimental results on carbon dioxide. Soon after, van der Waals formulated first microscopic theory for fluid phase behaviour in which the critical point was included. Almost simultaneously, the critical point[2] was introduced in the theory of ferromagnets proposed by Weiss. These advances revealed a very interesting similarity between fluids and magnets; when the pressure is taken as the analogue of magnetic field H and the pressure difference as the analogue of magnetization M, the critical exponents for magnets can be defined in complete analogy to those for the liquid-vapour critical point. One of the most remarkable features of the van der Waals and Weiss theories is that they result in the same set of critical exponents. A more general view on the subject was later on provided by Landau's theory of critical phenomena, which also allowed an inclusion of small (Gaussian) fluctuations, an extension known as the Ornstein-Zernike theory. All these theories belong to the same class of mean-field (MF) theories and, as a result, predict identical, so called classical critical exponents that, however, do not match with the experiments. This is because the mean-field character of the theories underestimates (or neglects completely) critical fluctuations that turn out to play a dominating role near the critical point.

The behaviour of equilibrium systems with many degrees of freedom is generally governed by laws of statistical mechanics. It means that all physics of such systems can be obtained from suitable derivatives of the partition function

$$Z = \mathrm{Tr} e^{-\beta \mathcal{H}}\,, \tag{1}$$

where $\mathcal{H}$ is the Hamiltonian of a given system and $\beta = 1/k_B T$ is the inverse temperature with k_B being the Boltzmann constant. Generally, a computation of Z is a formidable task which becomes hopeless for any realistic Hamiltonian. Fortunately, an inherent feature of critical systems, so called *universality*, can be exploited. The universality principle tells us that the behaviour of a critical system is largely insensitive to the details of the model and is governed solely by the system dimensionality, the nature of the order parameter and the range of the interactions. Therefore, even

[2]For magnets, the critical point or critical temperature is often termed as Currie point and Currie temperature, respectively.

very simple models can be exploited to determine the values of the critical exponents for a wide range of fluids and magnets belonging to the same *universality class*. Especially fruitful turned out the studies of the famous Ising model, a model for a ferromagnet on a lattice, which nowadays serves as a metamodel in the theory of phase transitions and critical phenomena and which is usually defined by the Hamiltonian

$$\mathcal{H} = -J \sum_{\langle ij \rangle} S_i S_j - H \sum_i S_i \,, \tag{2}$$

where J is the interaction parameter and where it is assumed that the degrees of freedom $S_i = \pm 1$ interact only on neighbouring sites. Using the transfer matrix method, the model can be solved exactly for the dimension $d = 1$ to show that there is no phase transition at any finite temperature. In 1944 L. Onsager famously solved the Ising model in two dimensions for the quadratic lattice in a zero field and found non-classical critical exponents. Most importantly, the partition function was found non-analytic at T_c so that an expansion of the type used by Landau was invalidated and so the whole class of the mean-field theories.

In the next few decades, an enormous effort of the frontal theoretical physicists has been made to formulate a satisfactory theory for critical phenomena that would incorporate the influence of the fluctuations from the scratch, which turned out to be an extremely non-trivial task. In particular, it was found out that the critical exponents are not independent but they appear to satisfy several exponent equalities, such that they can be parameterized in terms of only two values. As first shown by Widom (1965), the existence of the exponent relations can be explained by *scaling* properties of the free energy near the critical point. This Widom's hypothesis also explains the phenomenon of data collapse when the plotted data are expressed in reduced units. The origin of the scaling has been heuristically explained by Kadanoff (1966) who introduced the block-spin idea that have been further elaborated and completed by Wilson (1971) who formulated the famous *renormalization-group* (RG) theory. The importance of RG theory is not only in its capability of estimating the critical exponents by proper treatment of the fluctuations but it also provides a natural framework in which the origin of scaling and universality can be understood. It also explains the onset of the *upper critical dimension*, d^*, above which the effect of the fluctuations is not essential and MF treatment is thus correct.

3 Interfacial Phase Transitions: Planar Geometry

Consider a planar wall[3] onto which some amount of liquid is poured. From a macroscopic viewpoint the wetting properties of the wall can be characterised by the contact angle θ at which the liquid drop meets the wall. If $\theta > 0$, the system is in a *partial wetting* regime and the liquid forms a hemispherical cap[4]. Balancing the net force per unit length acting along the boundary line between the three phases, the equilibrium contact angle is given by Young's equation

$$\gamma_{\rm wv} = \gamma_{\rm wl} + \gamma \cos\theta \,, \tag{3}$$

in terms of the tensions of the wall-vapor, wall-liquid and liquid-vapour interfaces. If adsorption properties of the wall are strong enough, the system can exhibit *wetting transition* at a wetting temperature T_w at which the wall surface becomes completely wet and $\theta = 0$. Eq. (3) then becomes Antonow's equation:

$$\gamma_{\rm wv} = \gamma_{\rm wl} + \gamma \,, \tag{4}$$

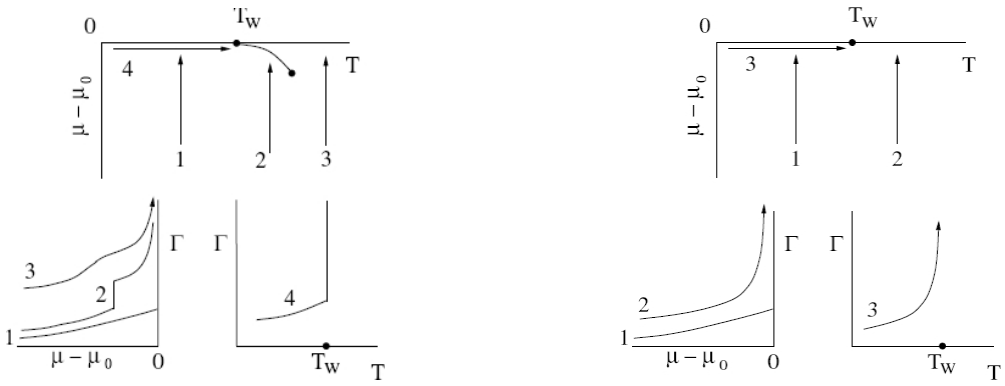

Figure 2: Phase diagrams of a first order (left) and a continuous (right) wetting transition. Also shown are representative thermodynamic paths on diagrams below.

Alternatively, the wetting transition can be viewed as an intrusion of the liquid layer into the wall-vapour interface. The partial wetting regime corresponds to a finite value of the liquid film thickness ℓ_π or, equivalently, the surface adsorption (or coverage) Γ. The film thickness (or adsorption) serves as the natural order parameter for the wetting transition, at which ℓ_π (or Γ) diverges (in the absence of gravity). There are two possible ways how this divergence can be realized:

[3]The wall is typically assumed to be of a solid material although this assumption is not necessary at this point.

[4]If not stated otherwise, we will implicitly consider only hydrophilic walls, such that $\theta < \pi/2$. In the opposite case, the wall is called to be dried (i.e., wetted by the vapour) which is just a reverse phenomenon to wetting.

- Firstly, as the wetting temperature is approached from below, i.e., as $T \to T_w^-$, along the bulk liquid-vapour coexistence line, such that the chemical potential $\mu = \mu_0(T)$, where $\mu_0(T)$ is the saturation chemical potential at a given temperature. This transition can be either discontinuous, i.e. *first-order wetting* (figure 2, left panel, path No. 4) or continuous – usually called *critical wetting* (figure 2, right panel, path No. 3). Clearly, the free energy is non-analytic at T_w in both cases and its singular part which is defined as

$$f_{\rm sing} = \gamma_{\rm wv} - (\gamma_{\rm wl} + \gamma) \tag{5}$$

vanishes at T_w according to

$$f_{\rm sing} \sim t^{2-\alpha_s}\,, t > 0\,, \tag{6}$$

where $t \equiv (T_w - T)/T_w$. For further purposes, it is useful to note that by combining (3) and (5) we obtain

$$f_{\rm sing} \approx -\frac{\gamma\theta^2}{2} \tag{7}$$

near T_w where the contact angle is small.

The value of the critical exponent α determines the order of the transition. From Eqs. (3) and (6) it follows that

$$1 - \cos\theta \sim t^{2-\alpha_s}\,, t > 0\,. \tag{8}$$

Now, the derivative of the contact angle with respect to the temperature,

$$\frac{{\rm d}\cos\theta}{{\rm d}T} \sim t^{1-\alpha_s}\,, \tag{9}$$

must be continuous at T_w for critical wetting (no latent heat) and therefore $\alpha_s < 1$. For first-order wetting, there is a latent heat at the transition, $\cos\theta$ is therefore discontinuous at T_w and $\alpha_s = 1$. For critical wetting we also define the critical exponent β_s which characterises the divergence of the film thickness (or adsorption) as T approaches T_w:

$$\ell_\pi \sim t^{-\beta_s}\,. \tag{10}$$

- Secondly, as the temperature $T_w < T < T_c$ is fixed and the coexistence line is approached from below (the lines Nos. 2 and 3 in the left panel and the line No. 2 in the right panel of figure 2). Within this process, the thickness of the liquid layer diverge as $\mu \to \mu_0^-$ according to the power-law

$$\ell_\pi(\delta\mu) = \delta\mu^{-\beta_s^{\rm co}}\,, \tag{11}$$

where $\delta\mu = \mu_0 - \mu$. This continuous divergence of the liquid film is called *complete wetting*. For the singular part of the free energy, we have by analogy with Eq. (6):

$$f_{\rm sing} \sim \delta\mu^{2-\alpha_s^{\rm co}}\,, \delta\mu > 0\,. \tag{12}$$

For the first-order wetting transitions, the singularity in the surface free energy at T_w extends above T_w and below μ_0 to a pre-wetting line which is the locus of coexistence between two distinct phases with thin and thicker wetting layers. This line terminates at its own critical temperature $T_{\rm sc}$ and approaches the coexistence line tangentially at T_w as $\delta\mu \sim (T - T_w)^{\frac{3}{2}}$.

In general, the surface critical exponents depend on the range of the fluid-fluid and wall-fluid interactions. Our main focus will be on models where the interaction between molecules is long-ranged (decaying as a power-law at infinity), with a particular emphasis on the most relevant case where the particles interact via van der Waals (dispersion) forces.

Wetting phenomena (in d dimensions) can be studied using the interfacial Hamiltonian model in terms of the height $\ell(x)$ of the liquid-gas interface (i.e., the local wetting film thickness)

$$\mathcal{H}_\pi[\ell] = \int \mathrm{d}\mathbf{x} \left[\frac{\gamma}{2}(\nabla\ell)^2 + W(\ell)\right] , \tag{13}$$

where $\mathbf{x}$ denotes the $(d-1)$ coordinates parallel to the wall. The first term in the integral is the energy cost of an undulation of the interface due to thermal fluctuations that are assumed to be small ($|\nabla\ell| \ll 1$). The second term, $W(\ell)$, represents effective interaction of the interface with the wall and is called *binding potential*. For the long range interactions, the binding potential has the asymptotic form:

$$W(\ell) = \frac{a(T)}{\ell^p} + \frac{b(T)}{\ell^q} + \cdots ; \ell > 0 \, , \tag{14}$$

where $p = 2$ and $q = 3$ for (non-retarded) van der Waals forces in three dimensions[5]. This binding potential is appropriate as far as two-phase coexistence is concerned, i.e, for $\mu = \mu_0$; this is the case of first-order or critical wetting. For complete wetting, we have $\mu < \mu_0$, and the energy cost for the presence of the metastable liquid must also be included:

$$W(\ell) = \delta\mu(\rho_l - \rho_g)\ell + \frac{a(T)}{\ell^p} + \cdots ; \ell > 0 \, . \tag{15}$$

If the interfacial fluctuations are neglected, $\ell(\mathbf{x}) = $ const, and the equilibrium wetting configuration is given simply by minimising the binding potential. The system is wet if the minimum corresponds to ℓ infinite which requires $a(T) > 0$. There are two mechanisms by which this global minimum can shift to a finite value of ℓ. The first mechanism can occur as $a(T)$ changes its sign with $b(T)$ positive. If $a(T) < 0$, the binding potential approaches zero asymptotically from below, which means that the minimum is at finite value of $\ell \sim a^{-1}$; the wall is not wet. However, as $a(T) \to 0$, the film thickness grows continuously and eventually diverges at T_w for which $a(T_w) = 0$ and $b(T_w) > 0$. Clearly, this mechanism corresponds to critical wetting. Note that

[5]The coefficient $a(T)$ is often termed the Hamaker constant.

as $a(T)$ changes its sign at the wetting temperature, $a \sim t$. From this it follows that $\beta_s = 1$ and upon substituting into (14) and (12) we get $\alpha_s = -1$ for van der Waals forces.[6] The second mechanism is realized if $b(T) < 0$ (or if the coefficient of a higher-order term in the expansion (14) is negative) and $a(T) > 0$, in which case the binding potential exhibits two minima at ℓ finite and ℓ infinite. In this case, T_w corresponds to the temperature below which finite ℓ minimum becomes the global minimum. This is the case of a first-order wetting. This mechanism is pertinent for systems in which the only forces that are long range are those between fluid and wall atoms; in this case $a(T)$ remains always positive. For complete wetting, the term linear in ℓ prevents from unbinding of the interface for any positive value of $\delta\mu = \mu_0 - \mu$. The wall thus becomes completely wet only in the $\mu \to \mu_0$ limit with the associated critical exponents $\alpha_s^{\rm co} = 4/3$ and $\beta_s^{\rm co} = 1/3$ for van der Waals forces.[7] Note that all terms beyond the ℓ^{-p} order are irrelevant for complete wetting.

The MF analysis can be complemented by the OZ approximation to obtain further critical exponents related with the structure of the interface. The OZ theory corresponds to the functional Taylor expansion of $\mathcal{H}_\pi[\ell]$ up to second order in fluctuations $\delta\ell(\mathbf{x}) = \ell(\mathbf{x}) - \ell_\pi$ around the mean value of the interface height $\langle\ell\rangle = \ell_\pi$. From this it follows that the transverse correlation length, defined by the OZ theory as

$$\gamma\xi_\parallel^{-2} \equiv \left.\frac{{\rm d}^2 W(\ell)}{{\rm d}\ell^2}\right|_{\ell=\ell_\pi} \tag{16}$$

behaves as

$$\xi_\parallel \sim t^{-\nu_\parallel}\,, \quad \text{(critical wetting)} \tag{17}$$

with $\nu_\parallel = 5/2$ for critical wetting and

$$\xi_\parallel \sim \delta\mu^{-\nu_\parallel^{\rm co}}\,, \quad \text{(complete wetting)} \tag{18}$$

with $\nu_\parallel^{\rm co} = 2/3$ for complete wetting.[8]

The MF theory is no longer correct when the fluctuation effects become important. The upper critical dimension where the MF theory ceases to hold, can be determined using the Ginzburg criterion. The contribution of the fluctuations to the surface free energy can be estimated as

$$f_s^f \approx k_B T/\xi_\parallel^{d-1} \sim t^{(d-1)\nu_\parallel}\,. \tag{19}$$

If compared with (6), we obtain the hyper-scaling relation

$$2 - \alpha_s = (d-1)\nu_\parallel \tag{20}$$

[6] More generally: $\alpha_s = (2-2p)/(q-p)$ and $\beta_s = 1/(q-p)$.
[7] More generally: $\alpha_s^{\rm co} = (p+2)/(p+1)$ and $\beta_s^{\rm co} = 1/(p+1)$.
[8] More generally: $\nu_\parallel = (q+2)/(2(q-p))$ and $\nu_\parallel^{\rm co} = (p+2)/(2p+2)$.

and, similarly, for complete wetting:

$$2 - \alpha_s^{\rm co} = (d-1)\nu_\parallel^{\rm co}\,. \tag{21}$$

The hyper-scaling relations are only valid for the MF critical exponents for $d = d^*$ and therefore

$$d^* = \frac{3q+2}{q+2} \quad \text{(critical wetting)} \tag{22}$$

and

$$d^* = \frac{3p+2}{p+2} \quad \text{(complete wetting)}\,. \tag{23}$$

For van der Waals forces, $d^* = 11/5$ for critical wetting and $d^* = 2$ for complete wetting. These results are important because they tell us that the MF theory of wetting is exact in $d = 3$ for long-range forces.

Although the MF theory of wetting is exact in the most relevant case of a three-dimensional system with long-range forces,[9] it is nevertheless desirable to account for the effect of fluctuations in systems of lower space dimensions. As we will see later on, this may occur to be very useful for a description of other interfacial phenomena that can be effectively mapped onto wetting phenomena at reduced dimensions. To properly include the fluctuations, exact transfer-matrix or approximate RG techniques have often been employed but much about their influence can be learnt from the simple arguments that I will demonstrate for dimension $d = 2$.

Fluctuations in ℓ decays in a distance of $\xi_\parallel$ and thus for the first term in Eq. (13) we have

$$\frac{\gamma}{2}(\nabla\ell)^2 \sim \frac{\ell^2}{\xi_\parallel^2}\,. \tag{24}$$

The fluctuations become important when $\ell \sim \xi_\perp$ where

$$\xi_\perp = \sqrt{\langle \ell(x)^2\rangle - \ell_\pi^2} \tag{25}$$

is the perpendicular correlation length or roughness. The transverse and correlation lengths are related through the wandering exponent as $\xi_\perp = \xi^\zeta$, so that

$$\frac{\gamma}{2}(\nabla\ell)^2 \sim \frac{\ell^2}{\xi_\parallel^2} \sim \ell^{-\tau}\,, \tag{26}$$

with $\tau = 2/\zeta - 2$. Adding this interaction term due to fluctuations to the binding potential with long-range forces (14), we obtain an effective potential:

$$W_{\rm eff}(\ell) = \frac{a(T)}{\ell^p} + \frac{b(T)}{\ell^q} + \frac{c(T)}{\ell^\tau}\,;\ell > 0\,. \tag{27}$$

[9] For systems with short-range forces $d^* = 3$ for both critical and complete wetting. In this case, the critical singularities are $\alpha_s = 0$, $\beta_s = 0(\ln)$ and $\nu_\parallel = 1$ and $f_s^{\rm co} = \delta\mu\ln\delta\mu$, $\beta_s^{\rm co} = 0(\ln)$ and $\nu_\parallel^{\rm co} = 1/2$.

Thus beside the two first energy terms that describe a direct interaction between the interface and the wall, we also have a competing term which includes an entropy loss due to the wall presence accounting for the restricted number of possible fluctuations of a bound state compared to an unbound state. The last term in (27)) is therefore repulsive, hence $c(T) > 0$ and it can be shown that $\tau = 2$ for $d = 2$. Depending on the values of p and q relative to τ, we obtain three scaling regimes for critical wetting:

1. $\tau > q$: *Mean-field regime.* Since the critical exponents for critical wetting are given by the first two terms in the binding potential, the fluctuation term has no effect and the MF theory is exact in this regime.

2. $p < \tau < q$: *Weak-fluctuation regime.* Now the fluctuation term is second largest and the critical exponents (that are now dimension-dependent) are not correctly predicted by the MF theory. However, the critical temperature which is given by the leading order term, is still given correctly by the MF theory and the critical exponents can be be obtained from the MF theory by replacing $q \to \tau$; in particular, $\beta_s = 1/(\tau - p)$.

3. $\tau < p < q$: *Strong-fluctuation regime.* In this regime, the fluctuation term is dominating and even the location of the wetting temperature is not correctly given by MF theory. For $d = 2$ when ℓ is a function of a single coordinate, the transfer-matrix method can be employed which transforms the statistical mechanical problem to the eigenvalue problem for the Schrödinger equation:

$$\left(\frac{1}{\gamma\beta^2}\frac{\mathrm{d}}{\mathrm{d}\ell^2} + W(\ell)\right)\psi_n(\ell) = E_n\psi_n(\ell)\,, \tag{28}$$

to determine $P(z) = |\psi_0(z)|^2$, the probability to find the interface at a height z.

For complete wetting, the situation is simpler, since only the leading order term in the binding potential is important for the critical exponents. This can be viewed from the fact that the binding potential (15) can be formally obtained from (14) by taking $a = \delta\mu$ and $p = -1$. As the leading order term is thus always lower than τ, there is no strong-fluctuation regime for complete wetting. For a fixed dimension $d < 3$, there is a marginal value $p^* = 2(d-2)/(3-d)$ of the exponent p, such that:

1. $p < p^*$: *Mean-field regime.* The MF theory is valid and the critical behaviour is determined by minimization of $W(\ell)$.

2. $p > p^*$: *Weak-fluctuation regime.* For systems with shorter-range forces than those corresponding to p^* fluctuation effects dominate. According to the RG theory, $\beta_s^{\mathrm{co}} = (3-d)/(d+2)$.

4 Density Functional Theory (DFT)

The interfacial model introduced in the previous section is a well established theoretical tool which provides us, often analytically, with a description of interfacial phenomena in terms of the interface height $\ell(\mathbf{x})$, a natural order parameter for unbinding processes such as the wetting and related transitions. For more intricate geometries and/or in cases when the inhomogeneous fluid structure due to a strong wall-fluid interaction or finite-size effects becomes important, the mesoscopic picture provided by the interfacial model may occur less satisfactory and the problem may call for more microscopic approaches based on many-body molecular Hamiltonians.

A very powerful approach to microscopic structure of inhomogeneous fluids is a (classical) density functional theory (DFT)[10] which is now regarded as a standard tool in statistical physics of liquids. The fluid is said to be inhomogeneous if one-body density (or density distribution) $\rho(\mathbf{r})$ is spatially varying. This is, of course, the case of all systems with confining walls and non-homogeneous external fields. The one-body density is defined as

$$\rho(\mathbf{r}) = \left\langle \sum_{i=1}^{N} \delta(\mathbf{r} - \mathbf{r}_i) \right\rangle \tag{29}$$

where N is the number of particles and $\langle \cdots \rangle$ denotes the ensemble average. Within DFT the effect of the walls is included via the external field $V(\mathbf{r})$ the walls exert. The DFT formalism establishes that for a given chemical potential μ and temperature T ($\beta = 1/k_B T$) and given inter-particle interaction $u(\mathbf{r}_i - \mathbf{r}_j)$ there is a unique intrinsic free energy functional $\mathcal{F}[\rho]$ of the density distribution $\rho(\mathbf{r})$ (and not of $V(\mathbf{r})$) and so is of the same form for any external potential. The equilibrium density distribution for the system in a given external field $V(\mathbf{r})$ is then obtained by minimizing the grand potential functional constructed from the Legendre transform of $\mathcal{F}[\rho]$:

$$\Omega[\rho] = \mathcal{F}[\rho] + \int \mathrm{d}\mathbf{r} \rho(\mathbf{r})(V(\mathbf{r}) - \mu)\,, \tag{30}$$

with respect to all possible functions $\rho(\mathbf{r})$. This leads to the Euler-Lagrange equation:

$$\left.\frac{\delta\Omega[\rho]}{\delta\rho(\mathbf{r})}\right|_{\rho(\mathbf{r})=\rho_{\mathrm{eq}}(\mathbf{r})} = 0 \Leftrightarrow \mu = \frac{\delta\mathcal{F}[\rho]}{\delta\rho(\mathbf{r})} + V(\mathbf{r}) \tag{31}$$

Moreover, for the equilibrium density profile $\rho(\mathbf{r}) = \rho_{\mathrm{eq}}(\mathbf{r})$ the grand potential functional reduces to the thermodynamic grand potential Ω.

An important feature of DFT is that it satisfies a number of the so called *sum rules*, i.e., the exact statistical mechanical relations between correlation functions and

[10] DFT has been originally developed as a quantum mechanical treatment for the ground state of inhomogeneous many-electron systems in 1960's. Its classical or statistical-mechanical version was formulated by Evans in 1979.

macroscopic thermodynamic quantities, which makes the direct link between microscopic correlations and physical properties of the macroscopic system. Particularly useful is the pressure sum rule relating the bulk pressure with the external field of the wall

$$\beta p = \int \mathrm{d}z \rho(z) \frac{\mathrm{d}}{\mathrm{d}z} \exp\left[-\beta V(z)\right] \tag{32}$$

and the Gibbs adsorption theorem which connects the excess adsorption with the surface tension:

$$\Gamma \equiv \int \mathrm{d}z (\rho(z) - \rho_b) = -\left(\frac{\mathrm{d}\gamma}{\mathrm{d}\mu}\right)_T , \tag{33}$$

where ρ_b is the bulk density. In both cases, a planar symmetry of the wall-fluid interface was assumed but a generalization of the theorems to other geometrises is straightforward. In DFT, these sum rules are also often used as a check of numerical consistency.

Thus far, the DFT formalism has been exact and thus the exact determination of $\Omega[\rho]$ is equivalent to the full evaluation of the grand partition function:

$$Z_{\mu VT} = \sum_N \frac{e^{\beta\mu N}}{N!\Lambda^{3N}} \int \Pi_{i=1}^N \mathrm{d}\mathbf{r}_i e^{-\beta U_N} , \tag{34}$$

where

$$U_N(\mathbf{r}_1, \mathbf{r}_2, \ldots, \mathbf{r}_N) = \Phi(\mathbf{r}_1, \mathbf{r}_2, \ldots, \mathbf{r}_N) + \sum_i V(\mathbf{r}_i) , \tag{35}$$

is the total potential of N particles including both the inter-particle interaction Φ and the external field V and Λ is the thermal de Broglie wavelength. This is, therefore, not surprising that there are no free energy functionals known exactly except for the toy one-dimensional models. However, the strength of DFT is that on searching a suitable approximation for $\mathcal{F}[\rho]$ the well established methods from statistical physics of homogeneous fluids can be used as a guide, which makes the task much easier compared to a direct treatment of the partition function. Also note that the density distribution can be much more easily obtained from Eq. (31) than from Eq. (29).

In modern approaches, it is common to develop DFT approximations for particular classes of fluid models (rather than constructing generic approximations). Typically, the total free energy functional is split into an ideal part

$$\mathcal{F}_{\mathrm{id}}[\rho] = \frac{1}{\beta} \int \mathrm{d}\mathbf{r} \rho(\mathbf{r}) \left[\ln(\rho(\mathbf{r})\Lambda^3) - 1\right] \tag{36}$$

which is known exactly, and an excess part $\mathcal{F}_{\mathrm{ex}}[\rho]$ which accounts for the interactions between the particles. For simple fluids the inter-particle potential Φ is pairwise additive and the interaction between the particles only depends on the distance between their centers. This is, e.g., the case of the well-known Lennard-Jones potential

$$u_{LJ} = 4\varepsilon \left[\left(\frac{\sigma}{r}\right)^{12} - \left(\frac{\sigma}{r}\right)^{6}\right] , \tag{37}$$

where the parameters ε and σ are then often used as the energy and length units.

In the spirit of van der Waals theory, the excess term of the free energy is treated in a perturbative manner, and is separated into a contribution modelling the repulsive hard-sphere (HS) core and a contribution from the attractive part $u_{\rm a}(r)$ of the fluid-fluid intermolecular potential. This is treated most commonly in mean-field fashion:

$$\mathcal{F}_{\rm ex}[\rho] = \mathcal{F}_{\rm HS}[\rho] + \frac{1}{2}\int\int {\rm d}\mathbf{r}{\rm d}\mathbf{r}'\rho(\mathbf{r})\rho(\mathbf{r}')u_{\rm a}(|\mathbf{r}-\mathbf{r}'|)\,, \tag{38}$$

where $\mathcal{F}_{\rm HS}[\rho]$ is the excess free energy functional of the hard-sphere fluid, with an appropriately chosen diameter.

Over the last three decades a number of approximative functionals for $\mathcal{F}_{\rm HS}[\rho]$ has been proposed. Arguably the most successful one, however, is the one produced by Rosenfeld within his *Fundamental Measure Theory* (FMT). The theory is based on the ansatz that the free energy functional for hard spheres (or a hard-sphere mixture) can be expressed in the form

$$\mathcal{F}_{\rm hs}[\rho] = \frac{1}{\beta}\int {\rm d}\mathbf{r}\,\Phi(\{n_\alpha\})\,. \tag{39}$$

in terms of a set of weighted densities

$$n_\alpha(\mathbf{r}) = \int {\rm d}\mathbf{r}'\rho(\mathbf{r}')\omega_\alpha(\mathbf{r}-\mathbf{r}')\,. \tag{40}$$

Here, the six weight functions are given by

$$\omega_3(\mathbf{r}) = \Theta(R-|\mathbf{r}|)\,, \tag{41}$$

$$\omega_2(\mathbf{r}) = \delta(R-|\mathbf{r}|)\,, \quad \boldsymbol{\omega}_2(\mathbf{r}) = \frac{\mathbf{r}}{r}\delta(R-|\mathbf{r}|)\,, \tag{42}$$

$$\omega_1(\mathbf{r}) = \delta(R-|\mathbf{r}|)\,, \quad \boldsymbol{\omega}_1(\mathbf{r}) = \frac{\mathbf{r}}{r}\delta(R-|\mathbf{r}|)\,, \tag{43}$$

$$\omega_0(\mathbf{r}) = \delta(R-|\mathbf{r}|)\,, \tag{44}$$

and the function $\Phi(\{n_\alpha\})$ can be determined from dimensional analysis and from requirements that the low- and high-density limits are obeyed exactly, which leads to

$$\Phi = -n_0\ln(1-n_3) + \frac{n_1n_2 - \mathbf{n_1}\cdot\mathbf{n_2}}{1-n_3} + \frac{n_2^3 - 3n_2\mathbf{n_1}\cdot\mathbf{n_2}}{24\pi(1-n_3)^2}\,. \tag{45}$$

In the limit of homogeneous fluid, this result is equivalent to the compressibility Percus-Yevick equation of state, although modified FMT versions of even more accurate underlying equation of state are now available. Importantly, the FMT functional satisfies the sum rules, Eqs. (32) and (33) (in contrast to some alternative approximative free energy functionals).

It is well known that the original Rosenfeld's functional provides an excellent description of the short-range correlations and satisfies the exact thermodynamic

conditions at planar walls and corners[11]. However, the entire class of functionals that are only based on the set (40) fails to describe the hard-sphere crystal and can produce spurious divergences for highly packed systems beyond the planar geometry. These problems have been fixed by Tarazona[12] who suggested to increase the set of weighted densities (40) by a tensor density with Cartesian components:

$$T_{ij}(\mathbf{r}) = \int \mathrm{d}\mathbf{r}' \rho(\mathbf{r}+\mathbf{r}') \frac{r_i' r_j'}{R^2} \delta(R - |\mathbf{r}'|)\,. \tag{46}$$

The free-energy density is then given by

$$\begin{aligned} \Phi &= -n_0 \ln(1-n_3) + \frac{n_1 n_2 - \mathbf{n}_{v1}\cdot\mathbf{n}_{v2}}{1-n_3} \\ &+ \frac{3}{16\pi} \frac{\mathbf{n}_{v2}\cdot\mathbf{T}\cdot\mathbf{n}_{v2} - n_2 n_{v2}^2 - \mathrm{Tr}[\mathbf{T}^3] + n_2 \mathrm{Tr}[\mathbf{T}^2]}{(1-n_3)^2}\,, \end{aligned} \tag{47}$$

where $\mathbf{T}$ is the matrix corresponding to (46).

Finally, it is important to see how DFT relates with the mesoscopic interfacial model described in the previous section. For concreteness, consider complete wetting at a planar wall-gas interface. If the undersaturation $\delta\mu$ is sufficiently small, a thick wetting layer forms at the wall. Adopting a coarse-graining of the microscopic Hamiltonian according to the *sharp-kink approximation* for the density profile, such that:

$$\rho(z) = \begin{cases} 0\,; & z<0\,, \\ \rho_l\,; & 0<z<\ell\,, \\ \rho_g\,; & z>\ell\,, \end{cases} \tag{48}$$

the complicated structure of the density distribution is reduced on a simple step-wise expression with a single free parameter ℓ determining the location of the liquid-vapour interface separating the (metastable) liquid of a density ρ_l and the bulk phase of a density ρ_g. Upon substituting Eq. (48) into Eqs. (30) and (38), the excess grand potential per unit area can be written in the form[13]

$$\frac{\Omega^{\mathrm{ex}}(\ell)}{A} \equiv \frac{\Omega(\ell)+pV}{A} = \delta\mu(\rho_l-\rho_g)\ell + \gamma_{wl} + \gamma + W(\ell)\,. \tag{49}$$

Here, the first term on the r.h.s. is the cost of the free energy for the presence of the metastable liquid,

$$\gamma_{wl} = -\frac{1}{2}{\rho_l}^2 \int_0^\infty \mathrm{d}z \Psi(z) + \rho_l \int_0^\infty \mathrm{d}z V(z)\,, \tag{50}$$

$$\gamma = -\frac{1}{2}(\Delta\rho)^2 \int_0^\infty \mathrm{d}z \Psi(z)\,, \tag{51}$$

[11] A. Malijevský and A. O. Parry, J. Phys.: Condens. Matter **25**, 305005 (2013).

[12] P. Tarazona, Phys. Rev. Lett. **84**, 694 (2000); Physica A **306**, 243 (2002).

[13] The grand potential of the bulk phase is $\Omega = -pV$, where V is the accessible volume and p is the bulk pressure.

are identified to be the surface tensions of the wall-liquid and liquid-gas interfaces, respectively, and the remaining term

$$W(\ell) = \rho_l^+ \Delta\rho \int_\ell^\infty \mathrm{d}z \Psi(z) - \Delta\rho \int_\ell^\infty \mathrm{d}z V(z) \tag{52}$$

yields the binding potential. The function $\Psi(z)$ is the potential of a fluid semi-infinite slab at a point a distance z away:

$$\Psi(z) = 2\pi \int_z^\infty \mathrm{d}z' \int_0^\infty \mathrm{d}\rho\, \rho\, u_a(\sqrt{\rho^2 + z'^2})\,, \tag{53}$$

where it is assumed that only the attractive part of the potential contributes. Further details on the sharp-kink approximation and the more elaborate soft-interface approximation can be found in appendices B and C of **Paper I**.

5 Interfacial Phase Transitions: Non-Planar Geometry

This section is devoted to interfacial phenomena that occur in systems exhibiting other than planar symmetry. There is, of course, no intention to provide a comprehensive review of studies dealing with this topic. Instead, this part, split into five paragraphs, is only based on the ten selected papers illustrating my contribution to this field.

5.1 Interfacial Phenomena at Spherical Surfaces

The effective potential (i.e., the coarse-grained excess grand potential per unit area) for complete wetting on a planar is given by formula (49), with

$$W(\ell) = \frac{a(T)}{\ell^2} + \cdots \tag{54}$$

for systems with long-range van der Waals (dispersion) forces in $d = 3$ (cf. Eq (14)). Since the upper critical dimension for complete wetting for such systems is $d^* = 2$, the influence of interfacial fluctuations is not essential and the MF theory holds exactly. The minimization of the interfacial potential with respect to ℓ leads to the well known asymptotic result[14]

$$\ell_\pi \sim \delta\mu^{-\frac{1}{3}}\,, \tag{55}$$

as $\delta\mu \to 0^+$.

Following **Paper I**, let us now consider complete wetting at a spherical wall of a radius R. Since the areas of the wall-liquid and liquid-gas interfaces are now different, the interfacial potential becomes

$$\frac{\Omega^{\rm ex}(\ell;R)}{4\pi R^2} = \delta\mu(\rho_l - \rho_g)\ell + \gamma_{wl}(R) + \gamma(R+\ell)\left(1 + \frac{2\ell}{R}\right) + W(\ell;R)\,, \tag{56}$$

where we have assumed that $\ell \ll R$ and expanded to first order in ℓ/R. The comparison between (49) and (56) reveals that in contrast with the planar symmetry, there is now an ℓ-dependence in the term associated with the liquid-gas surface tension. Therefore, while the contribution of the surface tension is irrelevant for complete wetting on a planar wall, it does play an important role for a spherical interface. In the limit of large R, the minimization of (56) leads to

$$\ell_{\rm eq} = \left(\frac{A}{\delta\mu(\rho_l - \rho_b) + 2\gamma(\infty)/R}\right)^{\frac{1}{3}}\,, \tag{57}$$

from which it can be seen that $\ell_{\rm eq}$ is finite even at bulk coexistence $\delta\mu = 0$. When the sharp-kink approximation (SKA) is employed (see Appendix B of **Paper I**),

[14] For systems with short-range forces the divergence is logarithmic.

the leading order curvature correction to the surface tension is predicted to be non-analytic:

$$\gamma^{\mathrm{SKA}}(R) = \gamma^{\mathrm{SKA}}(\infty)\left(1 - \frac{2}{9}\frac{\ln(R/\sigma)}{(R/\sigma)^2} + \cdots\right), \tag{58}$$

where we have adopted the Lennard-Jones potential for the fluid model.

In **Paper I** we have shown that the predictions of the SKA are fully satisfactory when compared with the direct numerical DFT solutions for complete wetting on a planar wall. However, for a spherical geometry, the prediction quality of SKA has been found to be limited. Namely, although SKA determines satisfactorily the functional form of the asymptotic behavior of the film thickness in the $R \to \infty$ limit, there is a significant quantitative disagreement in ℓ_{eq} with DFT results. The source of the deviation is the presence of the Laplace pressure that is not described accurately within SKA.

As shown in **Paper I**, the quality of the interfacial potential can be substantially improved if the assumption of the sharp liquid-gas interface is replaced by a less restrictive approximation in which the interface is treated as a continuous function of the density distribution. Using this so called soft-interface approximation (SIA) the leading curvature correction to the liquid-gas surface tension has been found to be linear:

$$\gamma^{\mathrm{SIA}}(R) = \gamma^{\mathrm{SIA}}(\infty)\left(1 - \frac{2\delta}{R} + \mathcal{O}\left(\frac{\ln(R/\sigma)}{(R/\sigma)^2}\right)\right), \tag{59}$$

where the amplitude of the first-order correction is known as the Tolman length. Using numerical DFT we have then shown that there is a correspondence between adsorption on a planar and a spherical wall, such that density profiles for a spherical wall at a two-phase coexistence $\delta\mu = 0$ are almost identical to those on a planar wall with $\delta\mu = 2\gamma(\infty)/R(\rho_l - \rho_g)$ for large R, according to Eq. (57), with the surface tension determined by SIA. Moreover, SIA revealed a significant improvement in the prediction of the film thickness as a function of the wall curvature over the results based on SKA. This is due to overestimation of the liquid-gas surface tension within SKA, which in turn underestimates the interface growth with R.

Some inherent limitations of SKA also exhibit themselves in the lack of broadening of the interface at high temperatures. As a consequence, as the bulk critical temperature is approached from below, the surface tension is predicted to vanish linearly according to SKA, i.e.,

$$\gamma^{\mathrm{SKA}} \sim t^{\mu}, \tag{60}$$

with $\mu = 1$ as $t = (T_c - T)/T_c \to 0$, in disagreement with mean-field (Landau-type) theory. In contrast, SIA, which relaxes the assumption of the interface rigidity, provides the expected mean-field behavior $\mu = 3/2$.

From a comparison of Eqs. (58) and (59) it follows that the value of the Tolman length is zero according to SKA. In contrast, SIA predicts a negative value of the Tolman length with the magnitude corresponding to a fraction of the Lennard-Jones

parameter σ.[15] This prediction is consistent with the value of Tolman's length determined in **Paper II** using a new simulation method to calculate the surface tension of small liquid drops applied for the Lennard-Jones fluid. After stabilizing a small drop of liquid in an NVT ensemble, the near spherical shape of the droplet was virtually perturbed by performing a coordinate transformation $x \to x\sqrt{1+\xi}$, $y \to y\sqrt{1+\xi}$ and $z \to z/(1+\xi)$ of the Cartesian system, with $\xi \ll 1$. Since the transformation conserves the volume of the system, the resulting change in the free energy corresponds to the change in the interfacial area and is thus directly associated with the surface tension:

$$\gamma = \left(\frac{\partial F}{\partial A}\right)_{NVT} . \tag{61}$$

The change in the free energy due to this isothermal, constant-volume deformation can be expressed in terms of the Boltzmann factor of the corresponding change in configuration energy ΔU:

$$\Delta F = -k_B T \ln \left\langle \exp\left(-\frac{\Delta U}{k_B T}\right)\right\rangle = \langle \Delta U\rangle - \frac{1}{2k_B T}\left(\langle \Delta U^2\rangle - \langle \Delta U\rangle^2\right) + \cdots \tag{62}$$

where the averages are taken over the reference (unperturbed) system. The surface tension is then obtained by extrapolating $\Delta F/\Delta A$ to $\Delta A \to 0$.

Now, to first-order in ΔU, the change in the free energy is $\Delta F \approx \langle \Delta U\rangle$. This leading order term is associated with the so-called virial expression for the tension, which is equivalent to the expression for the surface tension via the mechanical route from the pressure tensor components. The second-order term in (62) represents the Gaussian fluctuations; importantly, for the spherical interfaces it reveals that this term is comparable in magnitude to, but of opposite sign than, the first-order term. This strikingly contrasts with the case of planar interfaces, for which the second-order term is already negligible. These results thus demonstrate inadequacy of the mechanical route to the surface tension for spherical (curved, in general) interfaces (although frequently used in molecular dynamics simulation studies) neglecting the important influence of fluctuations. While the mechanical route predicts a monotonous decrease of the surface tension with curvature corresponding to $\delta > 0$, our results suggest non-monotonic behaviour of the surface tension with a corresponding weak maximum and the Tolman length $\delta \approx -0.2\sigma$.

The reason behind the failure of the mechanical route to the surface tension has been further analyzed in **Paper III**, where other alternative approaches have also been reviewed and examined. The paper highlights potential pitfalls and limitations of some of the approaches and in particular stresses out an inherent problem of the

[15] The value of δ has been found to be rather insensitive toward a (reasonable) choice of the test function approximating the density distribution of the liquid-gas interface. The most natural choice is hyperbolic tangent, which corresponds to the exact MF solution but cubic or linear approximations give similar results.

mechanical route which is related to an ambiguity in the definition of the local quantities that depend on particle interactions (such as the local pressure). The overview of the methods is complemented with the new results based on purely mechanical (newtonian), thermodynamic and statistical-mechanical treatments. In particular, it is argued that the new non-local mean-field DFT proposed for the Lennard-Jones fluid allows for a direct and unambiguous description of the interfacial properties of drops of an arbitrary size and provides the prediction for the Tolman length which is consistent with the simulation results presented in **Paper II**.

5.2 Wedge Filling

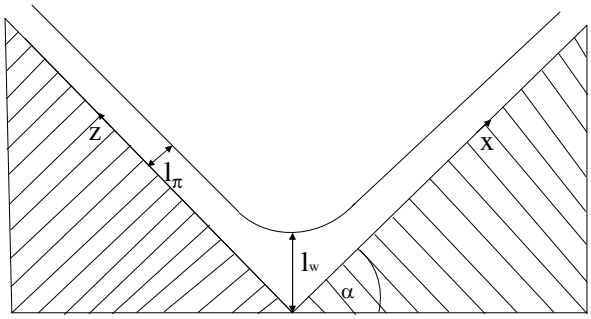

Figure 3: Schematic picture of the cross section of a right angle wedge with a tilt angle $\alpha = \pi/4$. Far from the apex, the wetting layer is of thickness ℓ_π. However, the height of the meniscus above the apex is ℓ_w. At a filling transition ℓ_w changes from microscopic to macroscopic.

Another example of a non-planar substrate geometry is a wedge structure formed by two identical infinite planar walls that meet at an opening angle $\pi - 2\alpha$ where α is the tilt angle with respect to the horizontal plane (see figure 3). Suppose the wedge is in contact with a bulk vapour phase at temperature $T < T_c$ and chemical potential μ. Macroscopic arguments[16] dictate that at bulk coexistence, $\mu = \mu_0$, the wedge is completely filled by liquid (ℓ_w becomes macroscopically large) for all temperatures $T > T_f$ where T_f is the *filling temperature* given implicitly by the simple condition

$$\theta(T_f) = \alpha \,, \tag{63}$$

where $\theta(T)$ is the contact angle of a sessile drop on a flat surface. Note that (63) is consistent with and generalizes the condition for wetting transition $\theta(T_w) = 0$ and implies that $T_f < T_w$, as the contact angle decreases with temperature. Thus, the

[16]E. H. Hauge, Phys. Rev. A **46**, 4994 (1992).

corresponding *filling transition* which occurs at T_f may be viewed as an interfacial geometry-induced unbinding transition in a system with broken translational invariance.

In **Paper IV**, the filling transitions in a right-angle wedge ($\alpha = \pi/4$) involving a long-range wall-fluid interaction were studied using a microscopic model within the density functional theory. Our DFT analysis showed that the filling transition is first order if it occurs far below the critical point but is continuous if T_f is close to T_c even though the walls still show first-order wetting behaviour. For this continuous transition the distance of the meniscus from the apex grows as

$$\ell_w \sim (T_f - T)^{-\beta_w}\,, \tag{64}$$

as $T \to T_f^-$, with the critical exponent estimated to be $\beta_w \approx 0.46$.

This value of the critical exponent can be compared with the mean-field value obtained from the Hamiltonian for a widely open wedge (assuming $\tan\alpha \approx \alpha$)

$$\mathcal{H}_w[\ell] = \int \mathrm{d}x \int \mathrm{d}y \left[\frac{\gamma}{2}(\nabla\ell)^2 + W(\ell - \alpha|x|)\right]\,, \tag{65}$$

where $\ell(x, y)$ is the local height of the liquid-vapour interface relative to the horizontal. Exploiting the translation invariance of the model along the wedge, the Euler-Lagrange equation for the equilibrium profile $\ell(x)$ is:

$$\gamma\frac{\mathrm{d}^2\ell}{\mathrm{d}x^2} = W'(\ell - \alpha|x|)\,, \tag{66}$$

where the prime denotes differentiation w.r.t. ℓ. This equation, subject to the boundary conditions $\dot{\ell}(0) = 0$ and $\ell(x) \to \ell_\pi + \alpha|x|$ for $|x| \to \infty$, has the first integral:

$$\frac{\gamma\alpha^2}{2} = W(\ell_w) - W(\ell_\pi)\,. \tag{67}$$

As $T \to T_f$, the meniscus unbinds from the wedge bottom, i.e. $\ell_w \to \infty$ and the first term on the r.h.s. becomes vanishingly small. Using Eq. (7) the result given by Eq. (63) is then immediately recovered. Furthermore, from Eq. (67) it follows that

$$W(\ell_w) = \frac{\gamma(\alpha^2 - \theta^2)}{2} \sim \alpha - \theta(T) \text{ as } T \to T_f\,. \tag{68}$$

Thus, at a critical filling transition the MF value of the order parameter critical exponent is simply determined by the leading-order decay of the binding potential $W(\ell) = A/\ell^p + \cdots$ by expanding the r.h.s. of Eq. (68) to first order at T_f, which yields $\beta_w = 1/p$. Recall that this result is completely different to the corresponding critical exponent for critical wetting $\beta_s = 1/(q - p)$ determined by both leading and next-to-leading order terms of the binding potential. For systems with van der Waals forces $p = 2$ and thus $\beta_w = 1/2$ ($\beta_s = 1$) which is in a good agreement with our DFT result.

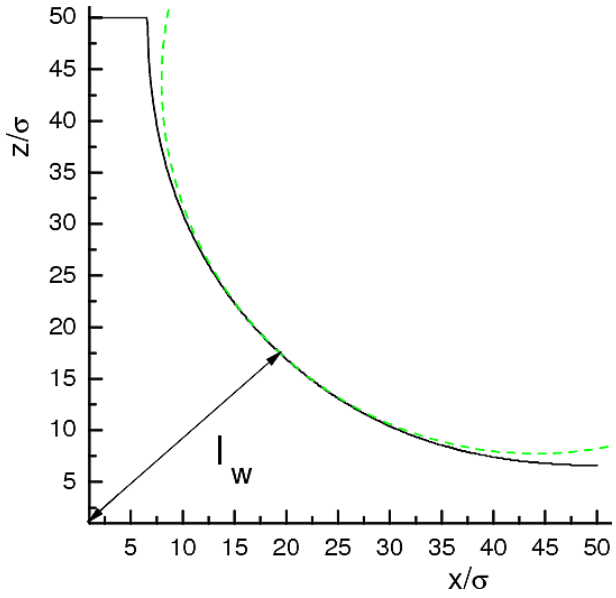

Figure 4: Contour of the meniscus as obtained from microscopic DFT. Also shown (dashed line) is a circular meniscus of Laplace radius $R = \gamma/(\delta\mu(\rho_l - \rho_g))$.

The main conclusion of this work is that it is possible to induce critical (continuous) interfacial transitions even at walls exhibiting themselves first-order wetting transitions by changing the wall geometry, which has been demonstrated for a realistic microscopic model involving dispersion interactions. It should be emphasised that for planar walls the critical wetting is a very rare phenomenon and in fact it has not been observed on solid substrates as yet. Moreover, the influence of interfacial fluctuations for wetting transitions in three dimensions is deemed to be hardly appreciable. Therefore, the wedge structure is found to be a promising candidate for a substrate for which an observation of interfacial critical phenomena is experimentally accessible.

Paper V complements these findings by investigating complete filling transition which refers to, in analogy to complete wetting, the continuous divergence of the adsorption (or ℓ_w) as $\mu \to \mu_0$ for $T > T_f$. If, furthermore, $\theta = 0$, the binding potential is of the form (15) and if substituted into Eq. (67) we obtain[17]

$$\ell_w \approx \frac{\gamma(\sec\alpha - 1)}{\delta\mu(\rho_l - \rho_g)} + \frac{\sec\alpha}{1 - \beta_s^{\rm co}}\ell_\pi + \cdots \tag{69}$$

The first term in (69) is universal, i.e., it does not depend on the nature of the interactions. This leading order term can be derived using purely macroscopic concept:

[17]C. Rascón and A. O. Parry, Phys. Rev. Lett. **94**, 096103 (2005).

a meniscus that grows at the wedge corner must have a circular cross-section with radius $R = \gamma/(\delta\mu(\rho_l - \rho_f))$, as determined by the Laplace pressure difference across the interface. Figure 4 shows that this macroscopic argument is fully consistent with the microscopic DFT results and thus remains valid even on a microscopic scale. Furthermore, the height ℓ_w then follows from the condition that the meniscus must meet each side of the wedge at the correct contact angle[18]. Figure 5 reveals, however, that this macroscopically predicted value of the interface height above the wedge corner as a function of $\delta\mu$ is systematically below the DFT results.

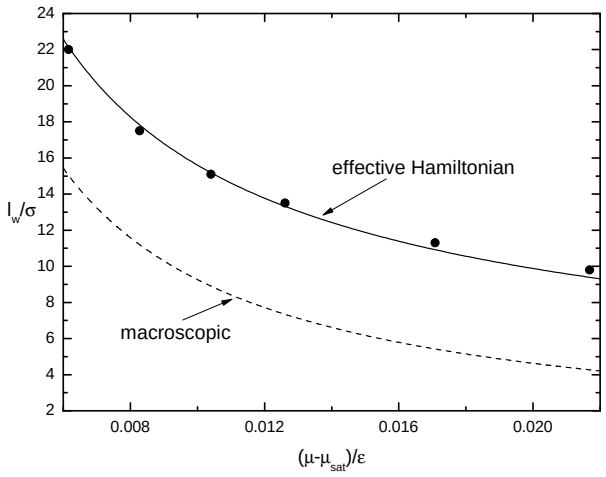

Figure 5: DFT results (symbols) for the divergence of the meniscus filling height ℓ_w, shown in comparison with the macroscopic expression given by the leading-order term in Eq. (69) (dashed curve) and the interfacial Hamiltonian prediction (solid curve) which includes the next-to-leading order correction.

From Eq. (69) it follows that the interfacial Hamiltonian theory extends these macroscopic results by predicting a presence of *non-universal* next-to-leading order singular term; this contribution depends on the nature of divergence of ℓ_π at a planar wall-gas interface, which in turn depends on the range of intermolecular forces (recall, $\beta_s^{\rm co} = 1/(p+1)$). When the non-universal correction is taken into account, one obtains a remarkably good agreement between the microscopic DFT results and Eq. (69), as shown in figure 5 for a right-angle wedge[19].

[18]For general value of the contact angle, the first term would be $\frac{\gamma(\sec\alpha\cos\theta - 1)}{\delta\mu(\rho_l - \rho_g)}$.

[19]The results in figure 5 correspond to the model of short-range interactions, for which $\beta_s^{\rm co} = 0$ and $\ell_\pi \sim -\ln(\delta\mu)$.

5.3 Complete Wetting on an Edge-Shaped Wall

In **Paper VI**, I studied complete wetting near an edge of a three-dimensional solid substrate (see figure 6) interacting with the fluid atoms via van der Waals forces. The curvature of the liquid-vapour interface dictates that the local height of the interface above the edge ℓ_E must remain finite at any subcritical temperature, even at bulk coexistence $\delta\mu = 0$, when a macroscopically thick film develops far from the edge. Thus, the influence of the edge is in some sense opposite to that of a wedge substrate, which promotes liquid adsorption. We now pose the question what is the equilibrium value of ℓ_E and what is the asymptotic form of $\ell_E(\delta\mu)$ as the chemical potential approaches the coexistence $\delta\mu \to 0^+$, such that complete wetting transition takes place far from the edge.

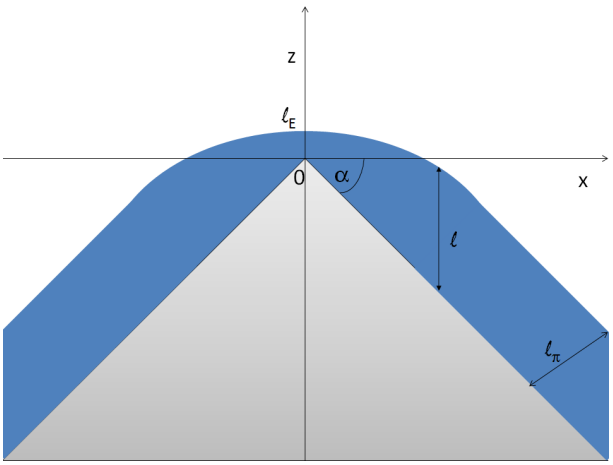

Figure 6: A sketch of the model of an edge-shaped substrate. The height of the liquid-gas interface is denoted as ℓ, the thickness of the layer far from the apex as ℓ_π and the height of the interface above the apex as ℓ_E. The sketch is projected to the x-z plane of the Cartesian coordinates.

The system has been studied using the following interfacial Hamiltonian model

$$\mathcal{H}_e[\ell] = \int \mathrm{d}x \left[\frac{\gamma}{2}(f'(x))^2 + W(\ell(x))\right] , \tag{70}$$

where $\ell(x)$ is thickness of the liquid-gas interface measured vertically and $f(x) = \ell(x) - \tan\alpha|a|$ denotes the local height of the liquid-gas interface relative to the horizontal (x axis). In Eq. (70), the translation symmetry along the y-axis is assumed so that $\mathcal{H}_e[\ell]$ is the effective Hamiltonian per unit length.[20]

[20]It should be noted that in contrast to $\mathcal{H}_w[\ell]$ considered in the previous subsection (Eq. (65)), the small-angle approximation was not adopted here.

The mean-field analysis of this model shows that the equilibrium height of the interface above the edge at coexistence is given by

$$\ell_E^0 = \ell(\delta\mu = 0) = \sqrt{\frac{2a}{\gamma \tan^2 \alpha}}\,, \tag{71}$$

where $a(T)$ is the Hamaker constant defined by the binding potential of the corresponding planar wall $W(\ell) = a/\ell^p + \cdots$. Furthermore, $\ell_E(\delta\mu)$ has been shown to approach the coexistence value according to

$$\delta\ell = \ell_E(0) - \ell_E(\delta\mu) \sim \delta\mu^{\beta_E^{\rm co}} \tag{72}$$

as $\delta\mu \to 0^+$. The new critical exponent for complete wetting on an edge $\beta_E^{\rm co}$ depends on the range of the molecular interaction, such that $\beta_E^{\rm co} = p/(p+1)$ and is related to the exponent $\alpha_s^{\rm co}$ (defined by Eq. (12)), according to $\beta_s^{\rm co} = 2 - \alpha_s^{\rm co}$. For systems with van der Waals forces, $\beta_E^{\rm co} = 2/3$. In contrast, the next-to-leading term in (72) has been found to be universal and scales linearly with $\delta\mu$, regardless of the nature of the molecular interactions.

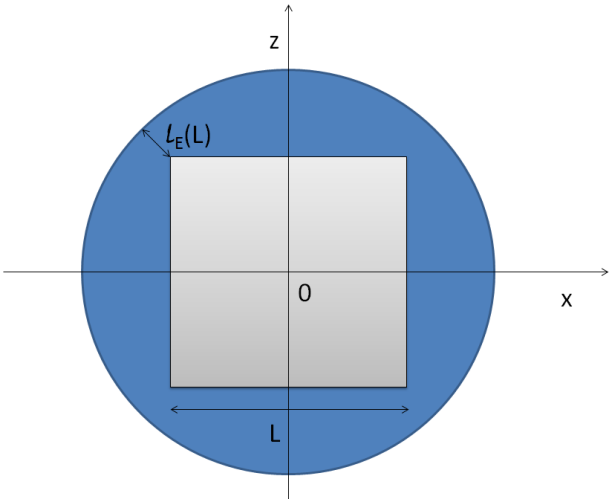

Figure 7: Schematic of the finite-wall model of a linear dimension L in the x-z projection. Translation invariance is assumed along the y-axis. The chemical potential is now fixed to its saturation value $\mu = \mu_0(T)$ and we wish to know how the result given by Eq. (71) for an unbounded wall is affected by the finite value of L.

I further considered a finite-wall model of a square cross-section of a linear dimension L (see figure 7) and ask what is the equilibrium value of the height of the liquid-vapour interface above the edge at bulk coexistence. The asymptotic ($L \to \infty$)

result is now subject to finite-size scaling of some scaling function F reflecting the competition between L and the correlation length $\xi_{||}$. For L finite, the leading-order-term in Eq. (72) modifies to $\delta\mu^{2-\alpha_s^{co}} F\left(\frac{L}{\xi_{||}}\right) \sim \delta\mu^{2-\alpha_s^{co}} F(L\delta\mu^{\nu_{||}^{co}})$ which is required to remain finite even when $\delta\mu \to 0$. This implies

$$\ell_E - \ell_E(L) \propto L^{\frac{\alpha_s^{co}-2}{\nu_{||}^{co}}} + L^{-\frac{1}{\nu_{||}^{co}}} + \cdots \tag{73}$$

where all the powers in the expansion depend on the details of the molecular interactions and can be expressed in terms of the critical exponents characterising wetting on a planar wall. In particular, for the van der Waals forces we obtain

$$\ell_E - \ell_E(L) \propto L^{-1} + \mathcal{O}(L^{-\frac{3}{2}})\,. \tag{74}$$

The analysis of both edge-shaped models have been further complemented with the microscopic DFT results (based on the fundamental measure theory) obtained numerically. The DFT results of the film height above the edge have been shown to be fully consistent with the predictions given by Eqs. (72) and (74).

5.4 Phase Transitions in a Capillary Groove and Grooved Surfaces

It is well known that in a slit pore formed by two parallel infinite walls a distance L apart, the fluid condensates at the chemical potential $\mu_{\rm cc} < \mu_0(T)$ which is well approximated by the macroscopic Kelvin equation

$$\mu_{\rm cc}(L) = \mu_0 - \frac{2\gamma\cos\theta}{(\rho_l - \rho_g)L} + \cdots \tag{75}$$

This *capillary condensation* is a first-order transition and corresponds to a shift of the ordinary bulk liquid-vapour transition due to finite size effects and the interaction of the fluid with the walls. Imagine now that we cap the slit pore at one end. How does the symmetry breaking in one dimension changes the condensation scenario?

The problem of the *groove condensation* was tackled in **Paper VII** using a microscopic DFT and the effective Hamiltonian based on the sharp-kink approximation. It has been shown that for temperatures greater than the wetting temperature a single meniscus separating capillary-liquid from capillary-gas forms near the groove bottom (as also dictated by macroscopic arguments) and continuously unbinds from the groove bottom as μ tends to $\mu_{\rm cc}$ from below where the groove becomes completely filled with liquid. The process in this regime has thus strong analogy to complete wetting on a planar wall. In contrast to the latter, however, the transition occurs at $\mu_{\rm cc}(L)$ (capillary coexistence) rather than at μ_0 (bulk coexistence). Furthermore, the

analysis based on the sharp-kink approximation (see figure 8)) reveals, that the rise of the meniscus has the asymptotic form

$$\ell_C \sim (\mu_{\rm cc}(L) - \mu)^{-1/4}\,, \tag{76}$$

where $\mu_{\rm cc}(L) = \mu_0 - \frac{2\gamma}{(\rho_l - \rho)(L - 3\ell_\pi)}$ satisfies the modified Kelvin equation with the microscopic correction due to wetting layers at the side walls. The meniscus unbinding can thus be characterised by the critical exponent $\beta_C = 1/4$ and the process is therefore somewhat slower than complete wetting for which $\beta_s^{\rm co} = 1/3$.

It has also been shown that in analogy to pre-wetting the rise of the meniscus can exhibit a finite jump. However, in contrast to pre-wetting, which is the genuine first-order transition, the transition associated with the meniscus jump must be necessarily rounded owing to its pseudo-one-dimensional nature.

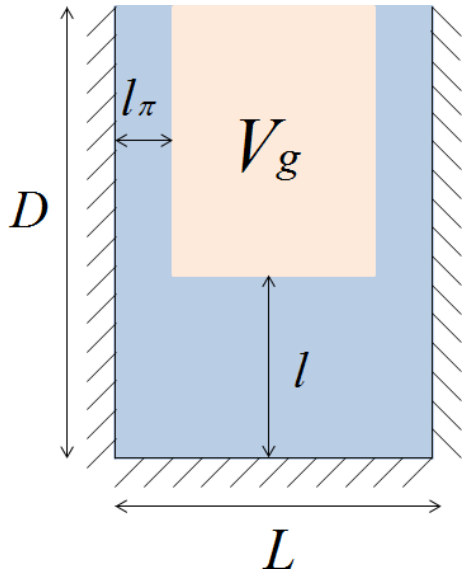

Figure 8: A schematic picture illustrating the sharp-kink approximation used for the capped capillary (groove) of width L and height D appropriate above the wetting temperature (such that the walls are wet). V_g denotes the volume filled by capillary gas. The side walls are coated with wetting layers of thickness ℓ_π which is assumed to be the same as for a single planar wall.

For temperatures below the wetting transition, however, the situation becomes different. The condensation process is now discontinuous in agreement with the macroscopic arguments according to which there exists a metastable extension of the condensation branch terminating at a spinodal point $\mu_{\rm sp}$. Within this macroscopic picture, two circular corner menisci develop for $\mu < \mu_{\rm cc}$ of Laplace radii that

grow continuously as the chemical potential increases. Note that the situation is pertinent to a previously discussed complete filling at two right-angle wedges. The spinodal $\mu_{\rm sp} > \mu_{\rm cc}$ corresponds to the chemical potential at which the two menisci merge; beyond this point, no continuous process is thermodynamically stable and the groove becomes completely filled.

This macroscopic scenario was compared with microscopic DFT in the subsequent **Paper VIII**. Interestingly, although the formation of two corner menisci (for $T < T_w$ and $\mu < \mu_{\rm sp}$) was not confirmed for microscopically narrow grooves, the location of the spinodal was still found in a surprisingly good agreement with the prediction based on the macroscopic arguments and leading to the so called complementary Kelvin equation.

In **Paper VIII** we also studied an inverse process to groove condensation, i.e., *groove evaporation* realized as $\mu_{\rm cc}$ is approached from above. In contrast to the groove condensation, the groove evaporation was found to be always continuous regardless of the temperature, such that the height of the meniscus from the top of the groove (a distance D from the groove bottom) decreases according to the power-law

$$D - \ell_z \sim (\mu_{\rm cc}(L) - \mu)^{-\beta_E} \,, \tag{77}$$

with a *different* critical exponent than that for groove condensation. The macroscopic arguments complemented by direct calculations based on the effective Hamiltonian (sharp-kink approximation), dimensional analysis and microscopic DFT calculations showed that $\beta_E = 1/3$ for dispersion forces, i.e., same as the one for complete wetting on a planar wall.

The analogy between groove evaporation and complete wetting was found to be even much stronger. The further analysis of the model revealed a relation between the distance of the meniscus from the open top $\ell_E = D - \ell$ and the film thickness on a planar wall:

$$\ell_E(\mu - \mu_{\rm cc}) = \ell_\pi(\mu_0 - \mu) \,, \tag{78}$$

which is an example of a *covariance law*, revealing hidden symmetry between interfacial phenomena at different geometries.

The final remark belongs to the effect of fluctuations. The mean-field analysis neglects the long wavelength, interfacial, fluctuations of the meniscus, the most dominant of which arise from those in the height of the meniscus along the groove. Owing to a reduced effective dimensionality of the groove, the fluctuation theory of meniscus unbinding is analogous to that of two dimensional complete wetting but with a line tension, resisting the undulations of the meniscus, which is $\tau \approx \gamma L$. Therefore, the relevant effective Hamiltonian that accounts for the fluctuations in the meniscus height along the groove is now of the form

$$\mathcal{H}_{\rm g}[\ell] = \int dy \left(\frac{\gamma L}{2} \left(\frac{d\ell(y)}{dy} \right)^2 + W(\ell) \right) . \tag{79}$$

Using Eq. (26), the relation[21] $\xi_\perp^2 = k_B T \xi/\tau$ and the fact that $\xi_\perp \approx \ell$ when fluctuations become important, we obtain the following estimation for the fluctuation term:

$$\gamma L \dot{\ell}^2 \approx \gamma L \frac{\xi_\perp^2}{\xi_\parallel^2} \approx \frac{(k_B T)^2}{\xi_\perp^2 \gamma L} \approx \frac{(k_B T)^2}{\ell^2 \gamma L} \,. \tag{80}$$

Since the binding potential for the groove evaporation reads

$$W_{\rm e} \approx (\mu - \mu_{\rm cc})(\rho_l - \rho_g) L (D - \ell) + \frac{a(T) L}{(D-\ell)^2} \,, \tag{81}$$

the repulsive term, which is of the order of $(D-\ell)^2$, is marginal because it is of the same order as the effective fluctuation term (80). This implies that the value of the exponent $\beta_E = 1/3$ is not altered by fluctuation effects. The only influence of the fluctuations is that the Hamaker constant becomes renormalized by a factor of $1 + \mathcal{O}((\beta\gamma L^2)^{-1})$, which is only important in the immediate vicinity of the capillary critical point.

For groove condensation, the appropriate binding potential is of the form

$$W_{\rm c} \approx (\mu - \mu_{\rm cc})(\rho_l - \rho_g) L \ell + \frac{a(T) L^2}{\ell^3} \tag{82}$$

and the repulsive term becomes irrelevant. Thus, for continuous condensation, the mean-field power-law divergence $\ell_C \approx ((\mu_{\rm cc} - \mu)/L)^{-\frac{1}{4}}$ will eventually cross-over to $\ell_C \approx (L^2 \mu_{\rm cc} - \mu)^{-\frac{1}{3}}$ as $\mu \to \mu_{\rm cc}$, changing the mean-field critical exponent $\beta_C^{\rm MF} = 1/4$ to the true value $\beta_C = 1/3$. However, a simple matching of these power laws shows that the size of the asymptotic regime is negligibly small since it scales as L^{-11}. Thus, the mean-field description of the continuous capillary condensation is exact except for extremely close vicinity of the capillary-coexistence curve $\mu = \mu_{\rm cc}$.

The model of a single capillary-groove has been extended in **Paper IX** to a model of a grooved substrate. Within this model, we consider a semi-infinite solid slab into which a one-dimensional array of infinitely long rectangular grooves is etched (see figure 9). By investigating the effect of the size and distribution of the grooves, as well as different paths leading to a completely wet surface, a rich variety of different wetting morphologies were found. The main findings can be summarised as follows:

1. It is possible to distinguish between four different wetting morphologies that can be characterised as: i) empty grooves, ii) filled grooves, iii) a formation of liquid

[21] R. Lipowsky and M.E. Fisher, Phys. Rev. B **36**, 2126 (1987).

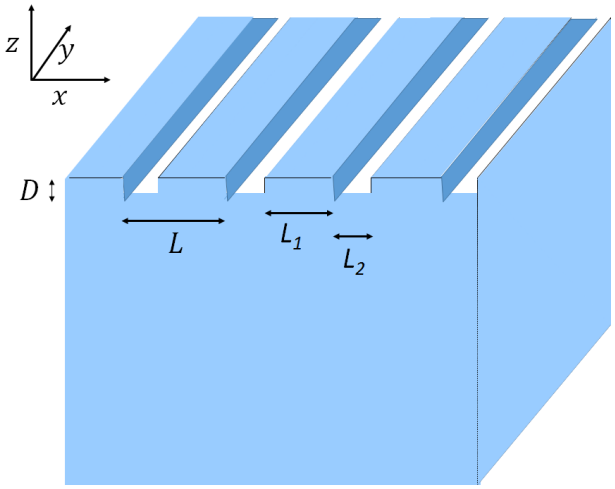

Figure 9: Sketch of the grooved substrate model.

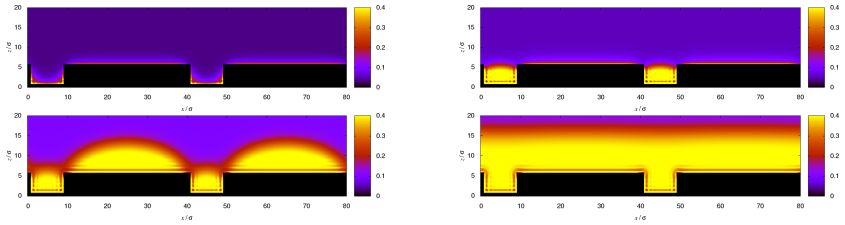

Figure 10: Four possible wetting regimes of a grooved substrate model.

bulges and iv) completely wet surface (see figure 10). These regimes are separated by first-order transitions, including the novel *bounded wetting* which separates the configurations ii) and iii). The nature of this transition is discussed and it is argued that the infinite periodicity of the system assures the transition to survive the capillary-wave fluctuations.

2. Owing to the first-order nature of these transitions, they all have off-coexistence extensions terminating at their own critical points. These transitions are analogues of pre-wetting on a planar wall. Here again, the infinite lateral periodicity of the system is crucial in that these transitions and not artifacts of the mean-field analysis. This is in contrast with a pre-filling transition in a single groove or in a single wedge, where the transition must be necessarily rounded when all the fluctuations are properly considered.

3. The wetting transition of the grooved substrate was found to occur in a considerably higher temperature than that for a flat wall. This result is important as it challenges the classical Wenzel law which states that surface roughness enhances wetting. To support this finding, an importance of considering an interplay of various interfacial phenomena occurring at planar walls, grooves, edges and wedges was highlighted as

well as the need to account for microscopic effects due to molecular interactions; all these aspects are ignored in the macroscopic arguments leading to Wenzel's and related phenomenological laws. Since for macroscopically corrugated surfaces the solid texture does indeed amplify wetting, it was concluded in a subsequent study[22] that there must exist a crossover between two length-scale regimes that are distinguished by opposite response on surface roughening.

5.5 Wetting Properties of a Heterogeneous Groove

Capillary condensation in a single groove (capped capillary) appears to be even more intriguing if the interaction of the fluid atoms with the bottom wall and the side walls is different. The model of this heterogeneous groove, studied in **Paper X**, reveals some unexpected behaviour in the case when both types of the wall are in a complete wetting regime (i.e., the considered temperature is greater than respective wetting temperatures of both walls). Within a sharp-kink approximation, the binding potential appropriate for a heterogeneous groove of a width L reads

$$W_{\mathrm{cap}}(\ell) = \delta\mu(\rho_l - \rho_g)\ell + \frac{a_2 - a_1}{\ell^2} + \frac{3a_1 L}{\ell^3} + \cdots , \tag{83}$$

where a_1 and a_2 are the Hamaker constants for the side and bottom walls, respectively. Note that the complete wetting regime requires that both a_1 and a_2 are positive. We can now identify three wetting scenarios determined by a relative strength between a_1 and a_2. i) For $a_1 = a_2$, i.e., in the case of a homogenous groove mentioned previously in the context of **Paper VIII**, the meniscus is repelled by a term decaying as $\sim \ell^{-3}$ which results to a continuous unbinding of the meniscus according to $\ell \sim \delta\mu^{-\frac{1}{4}}$ (cf. Eq. (76). ii) If $a_1 < a_2$, the meniscus repulsion is controlled by a term of $\mathcal{O}(\ell^{-2})$, which leads to a continuous meniscus growth according to $\ell \sim \delta\mu^{-\frac{1}{3}}$, as for complete wetting on a planar wall. iii) Finally, and most interestingly, if $a_1 > a_2$, i.e., if the fluid interaction with the side walls interaction is stronger than with the the bottom wall, the mismatch between the Hamaker constant leads to an interfacial attraction which bounds the meniscus to a finite distance even at the capillary phase boundary $\mu = \mu_{\mathrm{cc}}^-$. Since the groove must be completely filled for $\mu = \mu_{\mathrm{cc}}^+$, the transition is turned to be *first-order*, even though the transition would be continuous in a homogenous groove made up of either type of the wall.

It is important to note that the conclusion regarding the case iii) only applies if the bottom wall with the Hamaker constant a_2 spans the whole lower space. The simple dimensional analysis shows that if the wall spans only the space below tho groove (i.e., of a finite width L), the transition remains continuous, such that $\ell \sim \delta\mu^{-\frac{1}{4}}$.

The case iii) ($a_1 > a_2$) has remarkable repercussions: as the fluid state remains in the partial wetting state, it is possible – in analogy with Young's equation (3) – to

[22] A. Malijevský, *Does surface roughness amplify wetting?*, J. Chem. Phys. **141**, 184703 (2014).

define a *capillary contact angle*:

$$\gamma_{\rm wg}(L) = \gamma_{\rm wl}(L) + \gamma(L)\cos\theta^{\rm cap}\,, \tag{84}$$

valid for $\mu = \mu_{\rm cc}$. Here, the capillary surface tensions $\gamma_{\rm wg}(L)$, $\gamma_{\rm wl}(L)$ and $\gamma(L)$ are the surface free energies between groove bottom and capillary gas, groove bottom and capillary liquid and capillary gas and capillary liquid, respectively, per unit area of the groove bottom. For sufficiently wide grooves, the meniscus cross-section is near circular and thus $\gamma(L) \approx \pi/2\gamma$.

Therefore, somewhat counter-intuitively, if the attraction of the bottom wall is weaker than the attractive strength of the side walls, a liquid-vapour interface of a non-zero capillary contact angle forms in the groove even though $\theta^{\rm cap} = 0$ for the grooves of either material.

Apart from controlling the capillary contact angle by tuning the difference $a_2 - a_1$, we can also ask under what conditions the capillary wetting transition (i.e., vanishing of $\theta^{\rm cap}$) occurs for fixed parameters a_1 and a_2, as the groove width varies along the capillary coexistence line $\mu = \mu_{\rm cc}$. In order to account for the meniscus fluctuations along the groove, we adopted the interfacial Hamiltonian

$$\mathcal{H}_{\rm cap}[\ell] = L\int {\rm d}y \left[\frac{\gamma(L)}{2}\left(\frac{{\rm d}\ell(y)}{{\rm d}y}\right)^2 + W_{\rm cap}(\ell)\right] \tag{85}$$

where $\ell(y)$ is the local height of the fluctuating meniscus. The problem can be mapped onto a two-dimensional critical wetting and the corresponding partition function can be determined exactly using the transfer-matrix method from the Schrödinger equation (28) for a marginal value $p = 2$ of the asymptotic decay of the binding potential (cf. Eq. (27)), belonging to the so called intermediate fluctuation regime.[23] The analysis shows that the capillary contact angle can vanish in two ways:

- In the limit of macroscopically wide groove, in which case the interfacial fluctuations become negligible. In this *mean-field regime*, the capillary contact angle vanishes according to

$$\theta^{\rm cap}(L) \sim L^{-1}\,, \tag{86}$$

as $L \to \infty$.

- For a sufficiently narrow groove. As L decreases, the effective stiffness parameter $L\gamma(L)$ reduces and at some small value of the groove thickness $L = L_w$, the fluctuations become strong enough to allow the meniscus to tunnel out of the potential barrier represented by $W_{\rm cap}$. For the potential given by Eq. (83) with a positive next-to-leading interaction term, the situation of this *fluctuation dominated regime*

[23] R. Lipowsky and T. M. Nieuwenhuizen, J. Phys. A: Math. Gen. **21**, L89 (1988).

belongs to the third class of the intermediate fluctuation regime characterized by essential singularities and the capillary contact angle then vanishes as

$$\theta^{\rm cap}(L) \sim e^{-\frac{2\pi L_w}{\sqrt{L^2-L_w^2}}}\,; \quad L \to L_w\,, \tag{87}$$

where the critical value of the groove width is given by

$$L_w = \frac{k_B T}{2\sqrt{\pi\gamma(a_2-a_1)}}\,. \tag{88}$$

6 Selected Papers

Paper I

Wetting on a spherical wall: Influence of liquid-gas interfacial properties

Andreas Nold[*]
Center of Smart Interfaces, TU Darmstadt, Petersenstrasse 32, D-64287 Darmstadt, Germany and
Department of Chemical Engineering, Imperial College London, London SW7 2AZ, United Kingdom

Alexandr Malijevský[†]
E. Hála Laboratory of Thermodynamics, Institute of Chemical Process Fundamentals of ASCR, CZ-16502 Prague 6, Czech Republic and
Department of Physical Chemistry, Institute of Chemical Technology, Prague, CZ-166 28 Praha 6, Czech Republic

Serafim Kalliadasis[‡]
Department of Chemical Engineering, Imperial College London, London SW7 2AZ, United Kingdom
(Received 29 March 2011; published 22 August 2011)

We study the equilibrium of a liquid film on an attractive spherical substrate for an intermolecular interaction model exhibiting both fluid-fluid and fluid-wall long-range forces. We first reexamine the wetting properties of the model in the zero-curvature limit, i.e., for a planar wall, using an effective interfacial Hamiltonian approach in the framework of the well known sharp-kink approximation (SKA). We obtain very good agreement with a mean-field density functional theory (DFT), fully justifying the use of SKA in this limit. We then turn our attention to substrates of finite curvature and appropriately modify the so-called soft-interface approximation (SIA) originally formulated by Napiórkowski and Dietrich [Phys. Rev. B **34**, 6469 (1986)] for critical wetting on a planar wall. A detailed asymptotic analysis of SIA confirms the SKA functional form for the film growth. However, it turns out that the agreement between SKA and our DFT is only qualitative. We then show that the quantitative discrepancy between the two is due to the overestimation of the liquid-gas surface tension within SKA. On the other hand, by relaxing the assumption of a sharp interface, with, e.g., a simple "smoothing" of the density profile there, markedly improves the predictive capability of the theory, making it quantitative and showing that the liquid-gas surface tension plays a crucial role when describing wetting on a curved substrate. In addition, we show that in contrast to SKA, SIA predicts the expected mean-field critical exponent of the liquid-gas surface tension.

DOI: 10.1103/PhysRevE.84.021603 PACS number(s): 68.08.Bc, 05.20.Jj, 71.15.Mb, 05.70.Np

I. INTRODUCTION

The behavior of fluids in confined geometries, in particular, in the vicinity of solid substrates, and associated wetting phenomena are of paramount significance in numerous technological applications and natural phenomena. Wetting is also central in several fields, from engineering and materials science to chemistry and biology. As a consequence, it has received considerable attention, both experimentally and theoretically, for several decades. Detailed and comprehensive reviews are given in Refs. [1–4].

Once a substrate (e.g., a solid wall) is brought into contact with a gas, the substrate-fluid attractive forces cause adsorption of some of the fluid molecules on the substrate surface, such that at least a microscopically thin liquid film forms on the surface. The interplay between the fluid-fluid interaction (cohesion) and the fluid-wall interaction (adhesion) then determines a particular wetting state of the system. This state can be quantified by the contact angle at which the liquid-gas interface meets the substrate. If the contact angle is nonzero, i.e., a spherical cap of the liquid is formed on the substrate, the surface is called partially wet. In the regime of partial wetting, the cap is surrounded by a thin layer of adsorbed fluid which is of molecular dimension. Upon approaching the critical temperature, the contact angle continuously decreases and eventually vanishes. Beyond this wetting temperature one speaks of complete wetting and the film thickness becomes of macroscopic dimension. The transition between the two regimes can be qualitatively distinguished by the rate of disappearance of the contact angle, which is discontinuous in the case of a first-order transition or continuous for critical wetting.

From a theoretical point of view, it is much more convenient to take the adsorbed film thickness ℓ, rather than the contact angle, as an order parameter for wetting transitions and related phenomena. An interfacial Hamiltonian is then minimized with respect to ℓ as is typically the case with the (mesoscopic) Landau-type field theories and (microscopic) density functional theory (DFT)—where ℓ can be easily determined from the Gibbs adsorption, a direct output of DFT.

In this study, we examine the wetting properties of a simple fluid in contact with a spherical attractive wall by using an intermolecular interaction model with fluid-fluid and fluid-wall long-range forces. The curved geometry of the system prohibits a macroscopic growth of the adsorbed layer (and thus complete wetting), since the free-energy contribution due to the liquid-gas interface increases with the film thickness ℓ, and thus for a given radius of a spherical substrate there must be a maximum finite value of ℓ [1,5,6]. For the mesoscopic approaches, the radius of the wall R is a new field variable that

[*]andreas.nold09@imperial.ac.uk
[†]a.malijevsky@imperial.ac.uk
[‡]s.kalliadasis@imperial.ac.uk

introduces one additional ℓ-dependent term to the effective interface Hamiltonian of the system, compared to the planar geometry, where the only ℓ-dependent term is the binding potential between the wall-liquid and liquid-gas interfaces. Furthermore, for a fluid model exhibiting a gas-liquid phase transition, such as ours, it has been found that two regimes of the interfacial behavior should be distinguished: $R > R_c$, in which case the surface tension can be expanded in integer powers of R^{-1} and $R < R_c$, where the interfacial quantities exhibit a nonanalytic behavior [7]. Moreover, for an intermolecular interaction model with fluid-fluid long-range interactions, there is an additional $R^{-2} \ln R$ contribution to the surface tension in the $R > R_c$ regime [8]. These striking observations actually challenge all curvature expansion approaches. In addition, a certain equivalence between a system of a saturated fluid on a spherical wall and a system of an unsaturated fluid on a planar wall above the wetting temperature has been found [5,8]. Somewhat surprisingly, DFT computations confirmed this correspondence at the level of the density profiles down to unexpectedly small radii of the wall [8].

Most of these conjectures follow from the so-called sharp-kink approximation (SKA) [1], based on a simple piecewise constant approximation of a one-body density distribution of the fluid, i.e., a coarse-grained approach providing a link between mesoscopic Hamiltonian theories and microscopic DFT. The simple mathematical form of SKA has motivated many theoretical investigations of wetting phenomena, as it makes them analytically tractable. At the same time, SKA appears to capture much of the underlying fundamental physics for planar substrates (often in conjugation with exact statistical mechanical sum rules [9]).

However, as we show in this work, SKA is only qualitative for spherical substrates, even though the functional form of the film growth can still be successfully inferred from the theory [8]. We attribute this to the particular approximation of the liquid-gas interface adapted by SKA. In particular, since the ℓ-dependent contribution to the interface Hamiltonian due to the curvature is proportional to the liquid-gas surface tension, the latter plays an important role compared to the planar geometry.

More specifically, the curved geometry induces a Laplace pressure whose value depends on both film thickness and surface tension, and so the two quantities are now coupled, in contrast with the planar geometry where a parallel shift of the liquid-gas dividing surface does not influence the surface contribution to the free energy of the system. We further employ an alternative coarse-grained approach, a modification of the one originally proposed by Napiórkowski and Dietrich [10] for the planar geometry, which replaces the jump in the density profile at the liquid-gas interface of SKA by a continuous function restricted by several reasonable constraints. We show that in this "soft-interface approximation" (SIA) the leading curvature correction to the liquid-gas surface tension is $O(R^{-1})$, rather than $O(R^{-2} \ln R)$, in line with the Tolman theory. Once a particular approximation for the liquid-gas interface is taken, the corresponding Tolman length can be easily determined. Apart from this, we find that the finite width of the liquid-gas interface significantly improves the prediction of the corresponding surface tension when compared with the microscopic DFT computations, which consequently markedly improves the estimation of the film thickness in a spherical geometry.

In Sec. II we describe our microscopic model and the corresponding DFT formalism. In Sec. III we present results of wetting phenomena on a planar wall obtained from our DFT based on a continuation scheme that allows us to trace metastable and unstable solutions. The results are compared with the analytical prediction as given by a minimization of the interface Hamiltonian based on SKA. We also make a connection between the two approaches by introducing the microscopic model into the interfacial Hamiltonian. In Sec. IV we turn our attention to the main part of our study, a thin liquid film on a spherical wall. We show that SKA does not account for a quantitative description of the liquid-gas surface tension which plays a significant role when the substrate geometry is curved. We then introduce SIA and present an asymptotic analysis with our approach. Comparison with DFT computations reveals a substantial improvement of the resulting interface Hamiltonian, even for very simple approximations of the density distribution at the liquid-vapor interface, indicating the significance of a nonzero width of the interface. We conclude in Sec. V with a summary of our results and discussion. Appendix A describes the continuation method we developed for the numerical solution of DFT. In Appendix B we show derivations of the surface tension and the binding potential for both a planar and a spherical geometry within SKA. Finally, Appendix C shows derivations of the above quantities, including Tolman's length, using SIA.

II. DFT

A. General formalism

DFT is based on Mermin's proof [11] that the free energy of an inhomogeneous system at equilibrium can be expressed as a functional of an ensemble averaged one-body density, $\rho(\mathbf{r})$ (see, e.g., Ref. [12] for more details). Thus, the free-energy functional $\mathcal{F}[\rho]$ contains all the equilibrium physics of the system under consideration. Clearly, for a three-dimensional fluid model one has to resort to an approximative functional. Here we adopt a simple but rather well established local density approximation,

$$\mathcal{F}[\rho] = \int f_{\mathrm{HS}}[\rho(\mathbf{r})]\rho(\mathbf{r})\,d\mathbf{r} + \frac{1}{2}\iint \rho(\mathbf{r})\rho(\mathbf{r}')\phi(|\mathbf{r}-\mathbf{r}'|)\,d\mathbf{r}'\,d\mathbf{r}, \tag{1}$$

where $f_{\mathrm{HS}}[\rho(\mathbf{r})]$ is the free energy per particle of the hard-sphere fluid (accurately described by the Carnahan-Starling equation of state), including the ideal gas contribution. The contribution due to the long-range van der Waals forces is included in the mean-field manner. To be specific, we consider a full Lennard-Jones (LJ) 12-6 potential to model the fluid-fluid attraction according to the Barker-Henderson perturbative scheme

$$\phi(r) = \begin{cases} 0, & r < \sigma \\ 4\varepsilon\left[\left(\frac{\sigma}{r}\right)^{12} - \left(\frac{\sigma}{r}\right)^{6}\right], & r \geqslant \sigma, \end{cases} \tag{2}$$

where for the sake of simplicity the LJ parameter σ is taken equal to the hard-sphere diameter.

The free-energy functional $\mathcal{F}[\rho]$ describes the intrinsic properties of a given fluid. The total free energy, including also a contribution of the external field, is related to the grand potential functional through the Legendre transform

$$\Omega[\rho] = \mathcal{F}[\rho] + \int \rho(\mathbf{r})\,[V(\mathbf{r}) - \mu]\,d\mathbf{r}, \tag{3}$$

where μ is the chemical potential and $V(\mathbf{r})$ is the external field due to the presence of a wall $W \subset \mathbb{R}^3$,

$$V(\mathbf{r}) = \begin{cases} \infty, & \mathbf{r} \in W \\ \rho_w \int_W \phi_w(|\mathbf{r} - \mathbf{r}'|)\,d\mathbf{r}' & \text{elsewhere,} \end{cases} \tag{4}$$

consisting of the atoms interacting with the fluid particles via the LJ potential $\phi_w(r)$, with the parameters σ_w and ε_w, and uniformly distributed throughout the wall with a density ρ_w:

$$\phi_w(r) = 4\varepsilon_w\left[\left(\frac{\sigma_w}{r}\right)^{12} - \left(\frac{\sigma_w}{r}\right)^{6}\right]. \tag{5}$$

Applying the variational principle to the grand potential functional, Eq. (3), we attain the Euler-Lagrange equation:

$$\frac{\delta\mathcal{F}_{\mathrm{HS}}[\rho]}{\delta\rho(\mathbf{r})} + \int \rho(\mathbf{r}')\phi(|\mathbf{r} - \mathbf{r}'|)\,d\mathbf{r}' + V(\mathbf{r}) - \mu = 0, \tag{6}$$

where $\mathcal{F}_{\mathrm{HS}}[\rho]$ denotes the first term in the right-hand side of Eq. (1). In general, the solution to Eq. (6) comprises all extremes of the grand potential $\Omega[\rho]$ as given by Eq. (3) and not just the global minimum corresponding to the equilibrium state. Here we develop a pseudo arc-length continuation scheme for the numerical computation of Eq. (6) that enables us to capture both locally stable and unstable solutions and thus to construct the entire bifurcation diagrams for the isotherms (details of the scheme are given in Appendix A).

The excess part of the grand potential functional (3) over the bulk may be expressed in the form

$$\begin{aligned}\Omega_{\mathrm{ex}}[\rho(\mathbf{r})] = &-\int \{p[\rho(\mathbf{r})] - p(\rho_b)\}\,d\mathbf{r} \\ &+ \frac{1}{2}\iint \rho(\mathbf{r})[\rho(\mathbf{r}') - \rho(\mathbf{r})]\phi(|\mathbf{r}' - \mathbf{r}|)d\mathbf{r}'\,d\mathbf{r} \\ &+ \int \rho(\mathbf{r})V(\mathbf{r})\,d\mathbf{r},\end{aligned} \tag{7}$$

where ρ_b is the density of the bulk phase and

$$-p(\rho) = \rho f_{\mathrm{HS}}(\rho) + \alpha\rho^2 - \mu\rho \tag{8}$$

is the negative pressure, or grand potential per unit volume, of a system with uniform density ρ and $\alpha \equiv \frac{1}{2}\int \phi(|\mathbf{r}|)d\mathbf{r} = -\frac{16}{9}\pi\varepsilon\sigma^3$. In particular, the equilibrium value of the excess grand potential (7) per unit area of a two-phase system of liquid and vapor in the absence of an external field, yields the surface tension between the coexisting phases, γ_{lg}. The prediction of γ_{lg} as given by the minimization of Eq. (7) agrees fairly well with both computations and experimental data, as shown in Fig. 1.

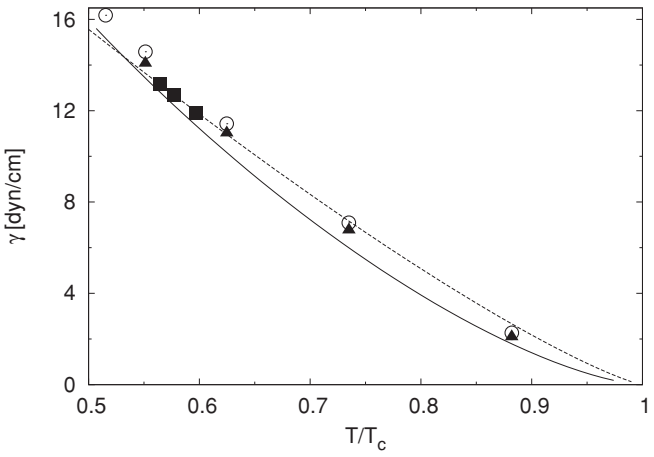

FIG. 1. Plots of surface tension as a function of dimensionless temperature, T/T_c. Solid line: numerical DFT results of our model scaled with $\varepsilon/k_B = 119.8$ K and $\sigma = 3.4$ Å; triangles: computational results by Toxvaerd for a 12-6 LJ fluid using the Barker-Henderson perturbation theory [13] with the Percus-Yevick solution [14] for the hard-sphere reference fluid and using the exact hard-sphere diameter [15]; circles: Monte Carlo simulations by Lee and Barker [16]; squares: experimental results for argon by Guggenheim [17]; dashed line: fit of experimental results to equation $\gamma(T) = \gamma_0(1 - T/T_c)^{1+r}$ by Guggenheim [17]. The resulting coefficients are $\gamma_0 = 36.31$ dyn/cm and $r = \frac{2}{9}$.

B. Translational symmetry: Planar wall

If the general formalism outlined above is applied on a particular external field attaining a certain symmetry, it will adopt a significantly simpler form. In the next section we will formulate the basic equations resulting from the equilibrium conditions obtained from the minimization of Eq. (7), for a spherical model of the external field, i.e., a system with rotational symmetry. But prior to that, it is instructive to discuss the zero-curvature limit of the above model, corresponding to an adsorbed LJ fluid on a planar wall, a system with translational symmetry.

For a planar substrate $W = \mathbb{R}^2 \times \mathbb{R}^-$ in Cartesian coordinates, the density profile is only a function of z, so that the Euler-Lagrange equation reads

$$\begin{aligned}&\mu_{\mathrm{HS}}[\rho(z)] + \int_0^\infty \rho(z')\Phi_{\mathrm{Pla}}(|z - z'|)\,dz' \\ &\quad + V_\infty(z) - \mu = 0 \quad (\forall z \in \mathbb{R}^+),\end{aligned} \tag{9}$$

where $\mu_{\mathrm{HS}}[\rho] = \frac{\partial[f_{\mathrm{HS}}(\rho)\rho]}{\partial\rho}$ is the chemical potential of the hard-sphere system. A fluid particle at a distance z from the wall experiences the wall potential:

$$\begin{aligned}V_\infty(z) &= \rho_w \int_W \phi_w\left(\sqrt{x'^2 + y'^2 + (z - z')^2}\right)dx'\,dy'\,dz' \\ &= \begin{cases} \infty, & z \leqslant 0 \\ 4\pi\rho_w\varepsilon_w\sigma_w^3\left[\frac{1}{45}\left(\frac{\sigma_w}{z}\right)^9 - \frac{1}{6}\left(\frac{\sigma_w}{z}\right)^3\right], & z > 0. \end{cases}\end{aligned} \tag{10}$$

$\Phi_{\mathrm{Pla}}(z)$ in Eq. (9) is the surface potential exerted by the fluid particles uniformly distributed (with a unit density) over the

x-y plane at distance z:

$$\Phi_{\rm Pla}(z) = \iint \phi(\sqrt{x^2+y^2+z^2})\,dy\,dx$$
$$= 2\pi \int_0^\infty \phi(\sqrt{z^2+r^2})\,r\,dr$$
$$= -\frac{6}{5}\pi\varepsilon\sigma^2 \times \begin{cases} 1, & z < \sigma \\ \frac{5}{3}\left(\frac{\sigma}{z}\right)^4 - \frac{2}{3}\left(\frac{\sigma}{z}\right)^{10}, & z \geqslant \sigma. \end{cases} \quad (11)$$

In the framework of DFT, the natural order parameter for wetting transitions is the Gibbs adsorption per unit area:

$$\Gamma_\infty[\rho(z)] = \int_0^\infty [\rho(z) - \rho_b]\,dz. \quad (12)$$

C. Rotational symmetry: Spherical wall

If the external field is induced by a spherical wall, $W = \{\mathbf{r} \in \mathbb{R}^3 : r \equiv |\mathbf{r}| < R\}$, the variational principle yields

$$\mu_{\rm HS}[\rho(r)] + \int_R^\infty \rho(r')\Phi_{\rm Sph}(r,r')dr' + V_R(r) - \mu = 0 \qquad (\forall r > R), \quad (13)$$

where $\Phi_{\rm Sph}(r,r')$ is the surface interaction potential per unit density generated by fluid particles uniformly distributed on the surface of the sphere $B_{r'}$ centered at the origin at distance r,

$$\Phi_{\rm Sph}(r,r') = \int_{\partial B_{r'}} \phi(|\mathbf{r}-\tilde{\mathbf{r}}|)\,d\tilde{\mathbf{r}}$$
$$= \frac{r'}{r}[\Phi_{\rm Pla}(|r-r'|) - \Phi_{\rm Pla}(|r+r'|)] \quad (14)$$

(see also Appendix B 1). The wall potential in Eq. (4) for the spherical wall, $W = \{\mathbf{r} \in \mathbb{R}^3 : r \equiv |\mathbf{r}| < R\}$, is

$$V_R(r) = \frac{\rho_w\varepsilon_w\sigma_w^4\pi}{3r}\left\{\frac{\sigma_w^8}{30}\left[\frac{r+9R}{(r+R)^9} - \frac{r-9R}{(r-R)^9}\right] + \sigma_w^2\left[\frac{r-3R}{(r-R)^3} - \frac{r+3R}{(r+R)^3}\right]\right\}. \quad (15)$$

Replacing the distance from the origin r by the radial distance from the wall $\tilde{r} = r - R$, one can easily see that the external potential (15) reduces to the planar wall potential (10), for $R \to \infty$. Analogously to the planar case, we define the adsorption Γ_R as the excess number of particles of the system with respect to the surface of the wall:

$$\Gamma_R[\rho(r)] = \int_R^\infty \left(\frac{r}{R}\right)^2 [\rho(r) - \rho_b]\,dr. \quad (16)$$

III. WETTING ON A PLANAR SUBSTRATE

In this section we make a comparison between the numerical solution of DFT and the prediction given by the effective interfacial Hamiltonian according to SKA for the first-order wetting transition on a planar substrate. More specifically, we consider a planar semi-infinite wall interacting with the fluid according to Eq. (10) with the typical parameters $\rho_w\varepsilon_w = 0.8\varepsilon/\sigma^3$ and $\sigma_w = 1.25\sigma$ that correspond to the class of intermediate-substrate systems [18] for which prewetting phase transitions can be observed. We note that wetting on planar and spherical walls is a multiparametric problem, and hence a full parametric study of the global phase diagram is a difficult task, beyond the scope of this paper.

A. Numerical DFT results of wetting on a planar wall

Figure 2 depicts the surface-phase diagram of the considered model in the $(\Delta\mu, T)$ plane, where $\Delta\mu = \mu - \mu_{\rm sat}$ is the departure of the chemical potential from its saturation value. The first-order wetting transition takes place at wetting temperature $k_BT_w = 0.621\varepsilon$, well below the critical temperature of the bulk fluid $k_BT_c = 1.006\varepsilon$ for our model. The prewetting line connects the saturation line at the wetting temperature T_w and terminates at the prewetting critical point, $k_BT_{\rm pwc} = 0.724\varepsilon$. The slope of the prewetting line is governed by a

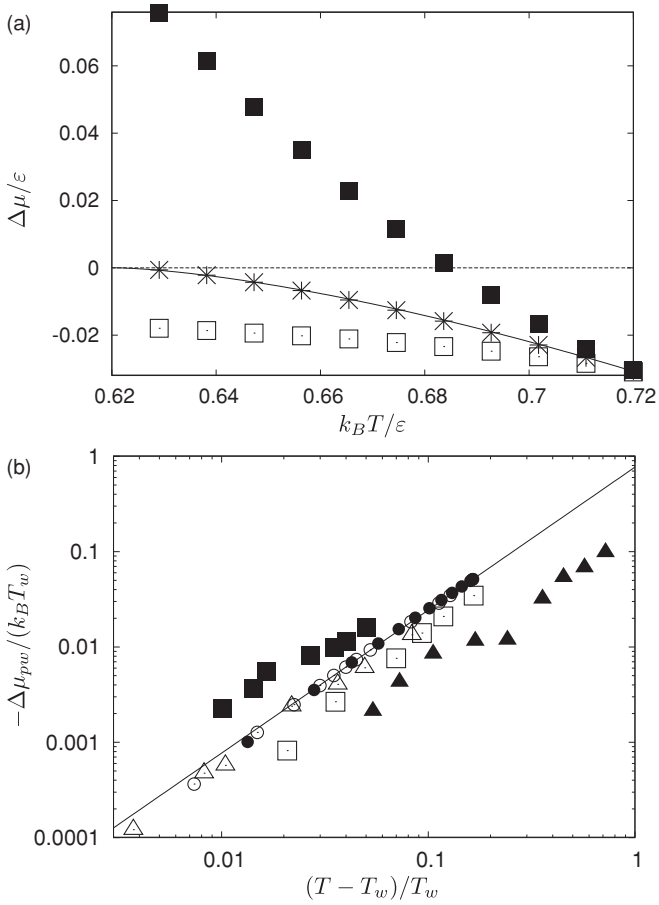

FIG. 2. (a) Deviation of the chemical potential from its saturation value at prewetting (crosses), and at the left (open squares) and right (filled squares) saddle nodes of bifurcation as a function of temperature. The dashed line marks the locus of the chemical potential at saturation for the given temperature, $\Delta\mu = 0$. The solid line is a fit to $-\Delta\mu_{\rm pw}(T)/(k_BT_w) = C[(T-T_w)/T_w]^{3/2}$, where the wetting temperature is $k_BT_w = 0.621\varepsilon$ and the prewetting critical temperature is $k_BT_{\rm pwc} = 0.724\varepsilon$. The resulting coefficient is $C = 0.77$. (b) Scaled prewetting phase diagrams for different systems. The circles are DFT calculations for an attractive wall with $\sigma_w = 1.25\sigma$ and $\rho_w\varepsilon_w = 0.8\varepsilon/\sigma^3$ (open circles) and $\rho_w\varepsilon_w = 0.75\varepsilon/\sigma^3$ (filled circles). Experimental data [21]: filled squares, methanol on cyclohexane [22]; open triangles, H_2 on rubidium [23]; filled triangles, He on caesium [24]; and open squares, H_2 on caesium [25].

Clapeyron-type equation [19], which, in particular, states that the prewetting line approaches the saturation line tangentially at T_w with

$$\left.\frac{d(\Delta\mu_{\rm pw})}{dT}\right|_{T=T_w} = 0, \tag{17}$$

in line with our numerical computations. Schick and Taborek [20] later showed that the prewetting line scales as $-\Delta\mu \sim (T - T_w)^{3/2}$. In Ref. [21], this power law was confirmed experimentally, such that

$$-\frac{\Delta\mu_{\rm pw}(T)}{k_B T_w} = C\left(\frac{T - T_w}{T_w}\right)^{3/2}, \tag{18}$$

with $C \approx \frac{1}{2}$. A fit of our DFT results with Eq. (18) leads to a coefficient $C = 0.77$, in reasonable agreement with the experimental data (see Fig. 2).

Figure 3 depicts the adsorption isotherm in terms of the thickness of the adsorbed liquid film ℓ as a function of $\Delta\mu$ for the temperature $k_B T = 0.7\varepsilon$ in the interval between the wetting temperature T_w and the prewetting critical temperature $T_{\rm pwc}$. ℓ can be associated with the Gibbs adsorption through

$$\ell = \frac{\Gamma_R[\rho]}{\Delta\rho}, \tag{19}$$

for both finite and infinite R, where $\Delta\rho = \rho_l^{\rm sat} - \rho_g^{\rm sat}$ is the difference between the liquid and gas densities at saturation.

The isotherm exhibits a van der Waals loop with two turning points depicted as B and C demarcating the unstable branch. Points A and D indicate the equilibrium between thin and thick layers, corresponding to a point on the prewetting line in Fig. 2. The location of the equilibrium points can be obtained from a Maxwell construction. Details of the numerical scheme we developed for tracing the adsorption isotherms are given in Appendix A.

B. SKA for a planar wall

For the sake of clarity and completeness we briefly review the main features of SKA for a planar geometry (details are given in Ref. [1]).

Let us consider a liquid film of thickness ℓ adsorbed on a planar wall. According to SKA the density distribution is approximated by a piecewise constant function

$$\rho_\ell^{\rm SKA}(z) = \begin{cases} 0, & z < \delta \\ \rho_l^+, & \delta < z < \ell \\ \rho_g, & z > \ell\,, \end{cases} \tag{20}$$

where ρ_g is the density of the gas reservoir and ρ_l^+ is the density of the metastable liquid at the same thermodynamic conditions stabilized by the presence of the planar wall, Eq. (10) and $\delta \approx \frac{1}{2}(\sigma + \sigma_w)$. The off coexistence of the two phases induces the pressure difference

$$p^+(\mu) - p(\mu) \approx \Delta\rho\Delta\mu, \tag{21}$$

where p^+ is the pressure of the metastable liquid and p is the pressure of the gas reservoir, and where we assume that $\Delta\mu = \mu - \mu_{\rm sat} < 0$ is small.

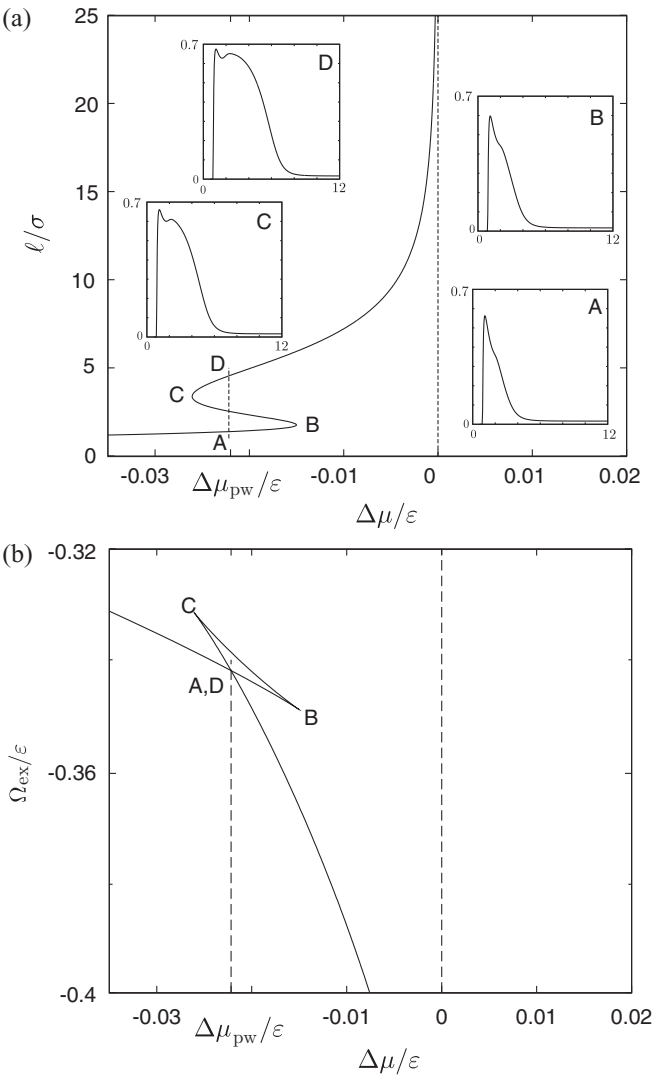

FIG. 3. (a) ℓ-$\Delta\mu$ bifurcation diagram for $k_B T = 0.7\varepsilon$ for a wall with $\rho_w\varepsilon_w = 0.8\varepsilon/\sigma^3$ and $\sigma_w = 1.25\sigma$. $\Delta\mu$ is the deviation of the chemical potential from its saturation value, $\mu_{\rm sat}$. The prewetting transition, marked by the dashed line, occurs at chemical potential $\Delta\mu_{\rm pw} = -0.022\varepsilon$. The inset subplots show the density $\rho\sigma^3$ as a function of the distance z/σ from the wall. (b) Excess grand potential $\Omega_{\rm ex}/\varepsilon$ as a function of $\Delta\mu/\varepsilon$ in the vicinity of the prewetting transition.

The excess grand potential per unit area $\mathcal{A}$ of the system then can be expressed in terms of macroscopic quantities as a function of ℓ

$$\frac{\Omega_{\rm ex}(\ell;\mu)}{\mathcal{A}} = -\Delta\mu\Delta\rho(\ell - \delta) + \gamma_{wl}^{\rm SKA}(\mu) + \gamma_{lg}^{\rm SKA} + w^{\rm SKA}(\ell;\mu), \tag{22}$$

where $\gamma_{wl}^{\rm SKA}$ and $\gamma_{lg}^{\rm SKA}$ are the SKAs to the wall-liquid and the liquid-gas surface tensions, respectively, and $w^{\rm SKA}(\ell)$ is the effective potential between the two interfaces (binding potential). In the following, we will suppress the explicit μ dependence of these quantities.

The link with the microscopic theory can be made if the contributions in the right-hand side of Eq. (22) are expressed in terms of our molecular model, which, when summed up,

give the excess grand potential (7), where we have substituted the ansatz (20):

$$\begin{aligned}\gamma_{wl}^{\mathrm{SKA}} &= -\frac{\rho_l^{+2}}{2}\int_{-\infty}^{0}\int_{0}^{\infty}\Phi_{\mathrm{Pla}}(|z-z'|)\,dz'\,dz \\ &\quad + \rho_l^{+}\int_{\delta}^{\infty}V_{\infty}(z)\,dz \\ &= \frac{3}{4}\pi\varepsilon\sigma^4\rho_l^{+2} + \frac{\pi}{90\delta^8}\left(\sigma_w^6 - 30\delta^6\right)\sigma_w^6\rho_w\varepsilon_w\rho_l^{+},\end{aligned} \tag{23}$$

$$\begin{aligned}\gamma_{lg}^{\mathrm{SKA}} &= -\frac{\Delta\rho^2}{2}\int_{-\infty}^{0}\int_{0}^{\infty}\Phi_{\mathrm{Pla}}(|z-z'|)\,dz'\,dz \\ &= \frac{3}{4}\pi\varepsilon\sigma^4\Delta\rho^2,\end{aligned} \tag{24}$$

$$\begin{aligned}w^{\mathrm{SKA}}(\ell) &= \Delta\rho\left(\rho_l^{+}\int_{\ell-\delta}^{\infty}\int_{z}^{\infty}\Phi_{\mathrm{Pla}}(z')\,dz'\,dz\right. \\ &\quad \left. - \int_{\ell}^{\infty}V_{\infty}(z)\,dz\right) \\ &= -\frac{A}{12\pi\ell^2}\left(1 + \frac{2+3\frac{\delta}{\ell}}{1-\frac{\rho_w\varepsilon_w\sigma_w^6}{\rho_l^{+}\varepsilon\sigma^6}}\frac{\delta}{\ell} + O\left((\delta/\ell)^3\right)\right),\end{aligned} \tag{25}$$

where we considered the distinguished limit $\delta \ll \ell$. A is the Hamaker constant given by:

$$A = 4\pi^2\Delta\rho\left(\rho_l^{+}\varepsilon\sigma^6 - \rho_w\varepsilon_w\sigma_w^6\right). \tag{26}$$

We note that the Hamaker constant is implicitly temperature dependent and that the attractive contribution of the potential of the wall enables the Hamaker constant to change its sign. Hence, in contrast with adsorption on a hard wall, where the Hamaker constant is always negative, there may be a temperature below which its sign is positive (large ρ_l) and negative above. Clearly, complete wetting is only possible for $A < 0$.

Making use of only the leading-order term in Eq. (25), the minimization of Eq. (22) with respect to ℓ gives

$$\Delta\rho\Delta\mu - \frac{A}{6\pi\ell^3} \approx 0. \tag{27}$$

Hence, at this level of approximation the equilibrium thickness of the liquid film is

$$\ell_{\mathrm{eq}} \approx \left(\frac{A}{6\pi\Delta\rho\Delta\mu}\right)^{1/3}. \tag{28}$$

When substituted into Eq. (22), the wall-gas surface tension to leading order reads

$$\gamma_{wg}^{\mathrm{SKA}} = \gamma_{wl}^{\mathrm{SKA}} + \gamma_{lg}^{\mathrm{SKA}} + \left(-\frac{9A}{16\pi}\right)^{1/3}|\Delta\rho\Delta\mu|^{2/3}. \tag{29}$$

Equation (28) can be confirmed by a comparison against numerical DFT (see Fig. 4). We observe that the prediction of SKA becomes reliable for $|\Delta\mu| < 0.01\varepsilon$, corresponding to a somewhat surprisingly small value of the liquid film, $\ell \approx 5\sigma$. Beyond this value, the coarse-grained approach loses its validity, and also, the prewetting transition is approached, both of which cause the curve in Fig. 4 to bend (see also Fig. 3).

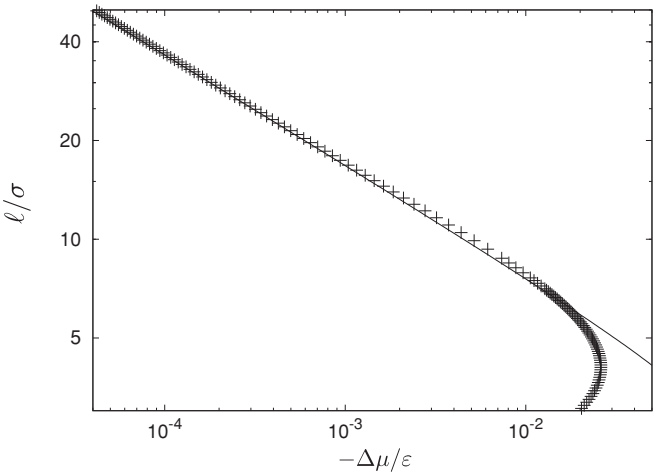

FIG. 4. Ln-ln plot of the film thickness as a function of deviation of the chemical potential from saturation, $\Delta\mu$, for $k_BT = 0.7\varepsilon$ and wall parameters $\rho_w\varepsilon_w = 0.8\varepsilon/\sigma^3$ and $\sigma_w = 1.25\sigma$. The crosses are results from DFT computations. The solid line is the analytical prediction in Eq. (27) obtained from SKA.

It is worth noting that the only term in Eq. (22) having an ℓ dependence and thus governing the wetting behavior, is the term related to the undersaturation pressure and the binding potential, $w^{\mathrm{SKA}}(\ell)$. Clearly, γ_{lg} does not come into play in the planar case since the translation of the liquid-gas interface along the z axis does not change the free energy of the system. The situation becomes qualitatively different if the substrate is curved. Nevertheless, at this stage we conclude in line with earlier studies, that SKA provides a fully satisfactory approach to the first-order wetting transition on a planar wall.

IV. WETTING ON A CURVED SUBSTRATE

A. SKA for the spherical wall

For the spherical geometry, SKA adopts the following form:

$$\rho_{R,\ell}^{\mathrm{SKA}}(r) = \begin{cases} 0, & r < R+\delta \\ \rho_l^{+}, & R+\delta < r < R+\ell \\ \rho_g, & R+\ell < r < \infty. \end{cases} \tag{30}$$

The corresponding excess grand potential now reads

$$\begin{aligned}\frac{\Omega_{\mathrm{ex}}(\mu,R,\ell)}{4\pi R^2} &= -\Delta\mu\Delta\rho\frac{(R+\ell)^3-\tilde{R}^3}{3R^2} + \gamma_{wl}^{\mathrm{SKA}}(R) \\ &\quad + \gamma_{lg}^{\mathrm{SKA}}(R+\ell)\left(1+\frac{\ell}{R}\right)^2 + w^{\mathrm{SKA}}(\ell;R),\end{aligned} \tag{31}$$

where $\tilde{R} = R + \delta$. Within this approximation, the liquid-vapor surface tension becomes (see also Appendix B)

$$\gamma_{lg}^{\mathrm{SKA}}(R) = \gamma_{lg}^{\mathrm{SKA}}(\infty)\left\{1 - \frac{2}{9}\frac{\ln(R/\sigma)}{(R/\sigma)^2} + O\left((\sigma/R)^2\right)\right\} \tag{32}$$

and an analogous expansion holds for $\gamma_{wl}^{\mathrm{SKA}}(R)$. The $\frac{\ln(R/\sigma)}{(R/\sigma)^2}$ correction to $\gamma_{lg}^{\mathrm{SKA}}(\infty)$ is due to the r^{-6} decay of our model. We note that short-range potentials lead to different curvature dependence of the surface tension, a point that has been

discussed in detail in Refs. [7,8,26]. Interestingly, the $O(\sigma/R)$ correction to the surface tension, as one would expect from the Tolman theory [27], is missing. It corresponds to a vanishing Tolman length within SKA, as we will explicitly show in the following section. Although the value of the Tolman length is still a subject of some controversy, it is most likely that its value is nonzero, unless the system is symmetric under interchange between the two coexisting phases [28]. This observation has been confirmed numerically in Ref. [8] from a fit of DFT results for the wall-gas surface tension in a nondrying regime for the hard-wall substrate. Thus, the linear term was included by hand into the expansion (32) [8].

Finally, the binding potential within SKA for the spherical wall yields

$$w^{\mathrm{SKA}}(\ell;R) = w^{\mathrm{SKA}}(\ell;\infty)\left(1+\frac{\ell}{R}\right), \tag{33}$$

where terms $O\left((\delta/\ell)^3, \delta/R, \frac{\ln(\ell/R)}{(R/\ell)^2}\right)$ have been neglected.

B. SIA for the spherical wall

As an alternative to SKA, Napiórkowski and Dietrich [10] proposed a modified version of the effective Hamiltonian, in which the liquid-gas interface was approximated in a less crude way by a continuous monotonic function, the SIA. Applied for the second-order wetting transition on a planar wall, SIA merely confirmed that SKA provides a reliable prediction for such a system. Formulated now for the spherical case, the density profile of the fluid takes the form

$$\rho^{\mathrm{SIA}}_{R,\ell}(r) = \begin{cases} 0, & r < R+\delta \\ \rho_l^+, & R+\delta < r < R+\ell-\frac{\chi}{2} \\ \rho_{lg}(r-R-\ell), & R+\ell-\frac{\chi}{2} < r < R+\ell+\frac{\chi}{2} \\ \rho_g & R+\ell+\frac{\chi}{2} < r < \infty. \end{cases} \tag{34}$$

Thus, a nonzero width of the liquid-vapor interface, χ, is introduced as an additional parameter. The density profile $\rho_{lg}(\cdot)$ in this region is not specified, but the following constraints are imposed:

$$\rho_{lg}\left(-\frac{\chi}{2}\right) = \rho_l^+ \quad \text{and} \quad \rho_{lg}\left(\frac{\chi}{2}\right) = \rho_g, \tag{35}$$

with an additional assumption of a monotonic behavior of the function $\rho_{lg}(r)$. An illustrative example of $\rho^{\mathrm{SIA}}_{R,\ell}(r)$ is given in Fig. 5. The corresponding excess grand potential takes the form

$$\frac{\Omega_{\mathrm{ex}}}{4\pi R^2} = -\Delta\mu\Delta\rho\frac{(R+\ell)^3-\tilde{R}^3}{3R^2} + \gamma_{wl}^{\mathrm{SIA}}(R) + \left(1+\frac{\ell}{R}\right)^2\gamma_{lg}^{\mathrm{SIA}}(R+\ell) + w^{\mathrm{SIA}}(R,\ell), \tag{36}$$

taking $R+\ell$ as the Gibbs dividing surface (so that ℓ is a measure of the number of particles adsorbed at the wall).

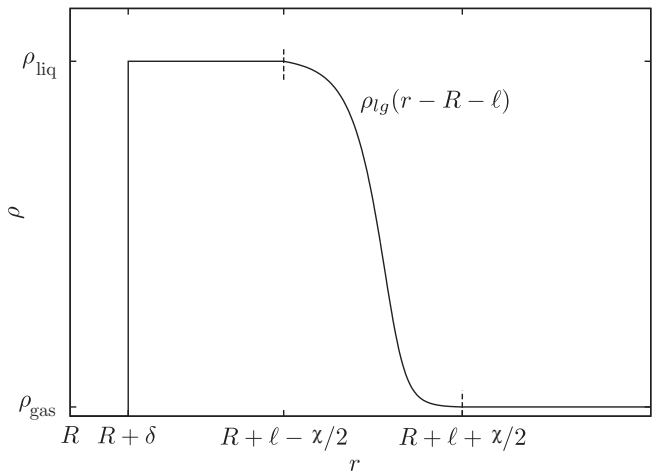

FIG. 5. Sketch of the density profile according to SIA for a certain film thickness ℓ. A piecewise function approximation is employed so that except for the interval $(R+\ell-\chi/2, R+\ell+\chi/2)$ the density is assumed to be piecewise constant.

The binding potential (see also Appendix C 3) is obtained from

$$w^{\mathrm{SIA}}(R,\ell) = \rho_l^+\int_{R+\ell-\chi/2}^{\infty}\left[\rho_l^+ - \rho^{\mathrm{SIA}}_{R,\ell}(r)\right]\Psi_{R+\delta}(r)\left(\frac{r}{R}\right)^2 dr - \int_{R+\ell-\chi/2}^{\infty}\left[\rho_l^+ - \rho^{\mathrm{SIA}}_{R,\ell}(r)\right]V_R(r)\left(\frac{r}{R}\right)^2 dr, \tag{37}$$

where $\Psi_R(r) = \int_0^R \Phi_{\mathrm{Sph}}(r,r')dr'$—see Appendix B 1 for the explicit form of the last expression.

The wall-liquid surface tension remains unchanged compared to that obtained from SKA, Eq. (24). However, the liquid-gas surface tension now reads (see Appendix C 1)

$$\gamma_{lg}^{\mathrm{SIA}}(R) = -\int_{R-\chi/2}^{R+\chi/2}\{p[\rho_{lg,R}(r)] - p_{\mathrm{ref}}\}\left(\frac{r}{R}\right)^2 dr + \frac{1}{2}\int_0^{\infty}\int_0^{\infty}\rho_{lg,R}(r)[\rho_{lg,R}(r') - \rho_{lg,R}(r)] \times \Phi_{\mathrm{Sph}}(r,r')\left(\frac{r}{R}\right)^2 dr'\,dr, \tag{38}$$

where p_{ref} is the pressure at saturation.

From now on, we neglect the curvature dependence of χ and $\rho_{lg,R}(\cdot)$, as they would introduce higher-order corrections not affecting the asymptotic results at our level of approximation. This is also in line with previous studies which show that the Tolman length only depends on the density profile in the planar limit [28]. Then Eq. (38) can be written as

$$\gamma_{lg}^{\mathrm{SIA}}(R) = \gamma_{lg}^{\mathrm{SIA}}(\infty)\left[1 - \frac{2\delta_\infty}{R} + O\left(\frac{\ln(R/\sigma)}{(R/\sigma)^2}\right)\right], \tag{39}$$

where δ_∞ is the Tolman length of the liquid-gas surface tension, as given by (Appendix C 2)

$$\delta_\infty = \frac{1}{\gamma_{lg}^{\mathrm{SIA}}(\infty)}\int_{-\chi/2}^{\chi/2}\{p[\rho_{lg}(z)] - p_{\mathrm{ref}}\}z\,dz. \tag{40}$$

The Tolman length is independent of the choice of the dividing surface. We also note that an immediate consequence of Eq. (40) is that within SKA the Tolman length vanishes.

The equilibrium film thickness then follows from setting the derivative of Eq. (36) with respect to ℓ equal to zero:

$$\begin{aligned}\frac{1}{4\pi R^2}\frac{d\Omega_{\rm ex}}{d\ell} &= -\Delta\mu\Delta\rho\left(1+\frac{\ell}{R}\right)^2+\frac{2}{R}\left(1+\frac{\ell}{R}\right)\\ &\times\gamma_{lg}^{\rm SIA}(R+\ell)+\left(1+\frac{\ell}{R}\right)^2\left.\frac{d\gamma_{lg}^{\rm SIA}}{d\ell}\right|_{R+\ell}\\ &+\rho_l^+\int_{R+\ell-\chi/2}^{R+\ell+\chi/2}\rho_{lg}'(r-R-\ell)\Psi_{R+\delta}(r)\\ &\times\left(\frac{r}{R}\right)^2 dr-\int_{R+\ell-\chi/2}^{R+\ell+\chi/2}\rho_{lg}'(r-R-\ell)\\ &\times V_R(r)\left(\frac{r}{R}\right)^2 dr. \end{aligned}\tag{41}$$

The last two terms of Eq. (41) are of the form

$$\int_{-\chi/2}^{\chi/2}\rho_{lg}'(r)f_{\rm I,II}(R+\ell+r)\,dr,\tag{42}$$

with $f_{\rm I}(r)=\rho_l^+\Psi_{R+\delta}(r)(\frac{r}{R})^2$ and $f_{\rm II}(r)=V_R(r)(\frac{r}{R})^2$. Since $\rho_{lg}(r)$ is monotonic, i.e., ρ_{lg}' does not change sign, the mean value theorem can be employed such that

$$\begin{aligned}&\int_{-\chi/2}^{\chi/2}\rho_{lg}'(r)f_{\rm I,II}(R+\ell+r)\,dr\\ &\quad=-\Delta\rho f_{\rm I,II}(R+\ell+\xi_{\rm I,II}),\end{aligned}\tag{43}$$

for some $\xi_{\rm I,II}\in(-\chi/2,\chi/2)$, where we made use of $\int\rho_{lg}'(r)dr=-\Delta\rho$. Substituting Eq. (43) into Eq. (41) and setting the resulting expression equal to zero, we obtain

$$\begin{aligned}\Delta\mu &= \frac{1}{\Delta\rho}\left(\frac{2\gamma_{lg}^{\rm SIA}(R+\ell)}{R+\ell}+\left.\frac{d\gamma_{lg}^{\rm SIA}}{d\ell}\right|_{R+\ell}\right)\\ &-\rho_l^+\Psi_{R+\delta}(R+\ell+\xi_{\rm I})\left(1+\frac{\xi_{\rm I}}{R+\ell}\right)^2\\ &+V_R(R+\ell+\xi_{\rm II})\left(1+\frac{\xi_{\rm II}}{R+\ell}\right)^2.\end{aligned}\tag{44}$$

So far, there is no approximation within SIA. Equation (44) can be simplified by appropriately estimating the values of the auxiliary parameters $\xi_{\rm I}$ and $\xi_{\rm II}$. To this end, we employ a simple linear approximation to the density profile at the liquid-gas interface, taking $-\rho_{lg}'(r)/\Delta\rho\approx 1/\chi$ in Eq. (43). Furthermore, we expand $f_{\rm I,II}$ in powers of $\ell/R,\sigma/\ell$,

$$\begin{aligned}f_{\rm I}(R+\ell+r) &= -\frac{2\pi\rho_l^+\varepsilon\sigma^6}{3(\ell+r-\delta)^3}\left[1+\frac{\ell+r+3\delta}{2R}\right.\\ &\left.+O\left(\left(\frac{\sigma}{\ell}\right)^6,\left(\frac{\ell}{R}\right)^2\right)\right],\end{aligned}\tag{45}$$

$$\begin{aligned}f_{\rm II}(R+\ell+r) &= -\frac{2\pi\rho_w\varepsilon_w\sigma_w^6}{3(\ell+r)^3}\left[1+\frac{\ell+r}{2R}\right.\\ &\left.+O\left(\left(\frac{\sigma}{\ell}\right)^6,\left(\frac{\ell}{R}\right)^2\right)\right],\end{aligned}\tag{46}$$

where we assumed the distinguished limits $r,\delta,\sigma\ll\ell\ll R$. Inserting Eqs. (45) and (46) into Eq. (43) yields for $\xi_{\rm I,II}$:

$$\xi_{\rm I,II}=-\frac{\chi^2}{6\ell}\left[1+O\left(\frac{\delta}{\ell},\frac{\ell}{R},\left(\frac{\chi}{\ell}\right)^2\right)\right].\tag{47}$$

From Eq. (44), we obtain to leading order,

$$\begin{aligned}&\rho_l^+\Psi_{R+\delta}(R+\ell+\xi_{\rm I})\left(1+\frac{\xi_{\rm I}}{R+\ell}\right)^2\\ &\quad=-\frac{2\pi}{3\ell^3}\rho_l^+\varepsilon\sigma^6\left[1+O\left(\frac{\delta}{\ell},\frac{\ell}{R},\left(\frac{\chi}{\ell}\right)^2\right)\right],\end{aligned}\tag{48}$$

$$\begin{aligned}&V_R(R+\ell+\xi_{\rm II})\left(1+\frac{\xi_{\rm II}}{R+\ell}\right)^2\\ &\quad=-\frac{2\pi}{3\ell^3}\rho_w\varepsilon_w\sigma_w^6\left[1+O\left(\frac{\ell}{R},\left(\frac{\chi}{\ell}\right)^2\right)\right].\end{aligned}\tag{49}$$

Finally, substituting Eqs. (48) and (49) into Eq. (44), we have to leading order

$$\Delta\rho\Delta\mu-\frac{2}{R}\gamma_{lg}^{\rm SIA}(\infty)\approx\frac{A}{6\pi\ell^3},\tag{50}$$

and hence, to leading order the equilibrium wetting film thickness is

$$\ell_{\rm eq}^{\rm SIA}\approx\left(\frac{A}{6\pi\left(\Delta\rho\Delta\mu-2\gamma_{lg,\infty}^{\rm SIA}/R\right)}\right)^{1/3}.\tag{51}$$

We note that this asymptotic analysis can be extended beyond Eq. (51), by including terms $O(\delta/\ell)$, $O(\ell/R)$, and $O((\chi/\ell)^2)$. The latter occurs due to the "soft" treatment of the liquid-vapor interface and is thus not present in SKA.

In Fig. 6 we compare two adsorption isotherms ($k_BT=0.7\varepsilon$) corresponding to wetting on a planar and a spherical wall ($R=100\sigma$). The two curves are mutually horizontally shifted by a practically constant value, in accordance with Eq. (50). This implies that the curve for the spherical wall crosses the saturation line $\Delta\mu=0$ at a finite value of ℓ, and eventually converges to the saturation line as $\Delta\mu^{-1}$ from the right, thus the finite curvature prevents complete wetting. The horizontal shift corresponds to the Laplace pressure contribution, $\Delta\mu=2\gamma_{lg}^{\rm SIA}(\infty)/(\Delta\rho R)$, as verified by comparison with the numerical DFT (Fig. 7). All these conclusions are in line with SKA. However, the difference between SKA and SIA consists in a different treatment of $\gamma_{lg}(\infty)$ [compare Eqs. (B4) and (C2)]. This is quite obvious, since the softness of the interface influences the free energy required to increase the film thickness. We will discuss this point in more detail in the following section.

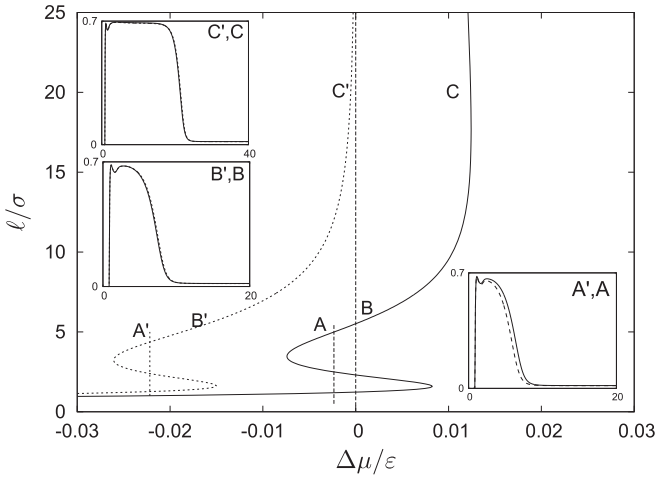

FIG. 6. Isotherms and density profiles for a planar wall (dashed lines) and a sphere with $R = 100\sigma$ (solid lines) at $k_BT = 0.7\varepsilon$ and with wall parameters $\rho_w\varepsilon_w = 0.8\varepsilon/\sigma^3$ and $\sigma_w = 1.25\sigma$. To directly compare the planar to the spherical case, the film thickness instead of adsorption is used as a measure. The subplots in the inset depict the density $\rho\sigma^3$ as a function of the distance from the wall z/σ and $(r - R)/\sigma$ for the planar and the spherical cases, respectively. The points A and A' are at the prewetting transitions. Points B,B' and C,C' correspond to the same film thickness. B is at saturation, whereas C is chosen such that the film thickness ℓ is 20σ.

C. Comparison of SKA and SIA

We now examine the repercussions of the way the liquid-gas interface is treated on the prediction of wetting behavior on a spherical surface. As already mentioned in Sec. IV B, the linear correction in the curvature to the planar liquid-gas surface tension, ignored within SKA, is properly captured by SIA. Furthermore, the presence of the Laplace pressure suggests that the liquid-gas surface tension plays a strong part in the determination of the equilibrium film thickness. This contrasts to the case of a planar geometry, where the term associated with the liquid-gas surface tension has no impact on the equilibrium configuration.

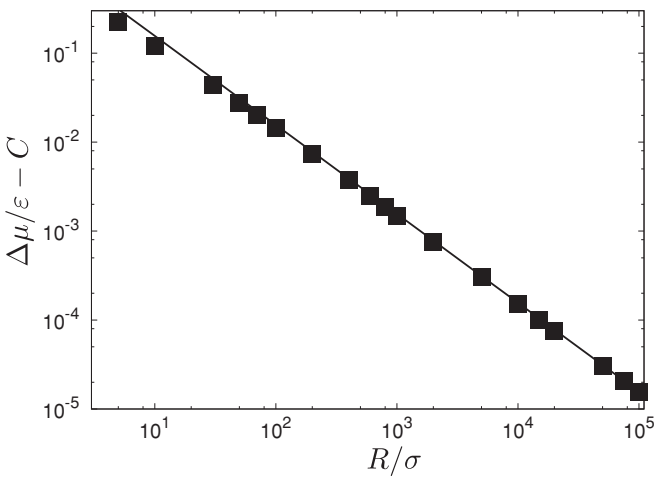

FIG. 7. Numerical verification of Eq. (50). The film thickness ℓ is fixed and corresponds to the adsorption $\Gamma_R = 3.905/\sigma^2$. The solid line corresponds to the analytical result, $\Delta\mu - 2\gamma_{lg}^{\mathrm{SIA}}(\infty)/(\Delta\rho R) = C\varepsilon$, where $\gamma_{lg}^{\mathrm{SIA}}(\infty) = 0.524\varepsilon/\sigma^2$ (see Table I). The symbols denote the numerical DFT results.

TABLE I. Planar surface tensions (Eq. (C2)), Tolman lengths (Eq. (40)), and the corresponding parameters for temperature $k_BT = 0.7\varepsilon$ according to a given auxiliary function approximating the density distribution of the vapor-liquid interface. The parameters are from auxiliary function minimization. The surface tension given by numerical DFT computations is $\gamma_{lg} = 0.517\varepsilon/\sigma^2$ and $\bar{\rho} = (\rho_l + \rho_g)/2$. Note that in the tanh case, the interface width is implicitly determined by the steepness parameter α.

Auxiliary function $\rho_{lg}(z)$	$\gamma_{lg}^{\mathrm{SIA}}(\infty)$	Argument	δ_∞
$\bar{\rho} - \Delta\rho\frac{z}{\chi}$	$0.544\varepsilon/\sigma^2$	$\chi = 4.0\sigma$	-0.07σ
$\bar{\rho} - \frac{3}{2}\Delta\rho\frac{z}{\chi} + 2\Delta\rho(\frac{z}{\chi})^3$	$0.532\varepsilon/\sigma^2$	$\chi = 5.4\sigma$	-0.09σ
$\bar{\rho} - \frac{\Delta\rho}{2}\tanh(\alpha z/\sigma)$	$0.524\varepsilon/\sigma^2$	$\alpha = 0.66$	-0.11σ

To investigate this point in detail, we will first compare the approximations of γ_{lg} as obtained by the two approaches. For this purpose, we start with SIA for a given parametrization of the liquid-gas interface. As shown in Table I, we employ linear, cubic, and hyperbolic tangent auxiliary functions, where the latter violates condition (35) negligibly. The particular parameters are determined by minimization of a given function with respect to the corresponding parameters. In Table I we display the planar liquid-gas surface tension associated with a particular parametrization and the Tolman length resulting from Eq. (40) for the temperature $k_BT = 0.7\varepsilon$. In all three cases the surface tension is close to the one obtained from the numerical solution of DFT and also, the predictions of the Tolman length are in reasonable agreement with the most recent simulation results [29–31], with thermodynamic results [32] as well as with results from the van der Waals square gradient theory [33].

It is reasonable to assume that from the set of considered auxiliary functions, the tanh approximation is the most realistic one, although the numerical results as given in Table I suggest that it is mainly the finite width of the liquid-gas interface, rather than the approximation of the density profile at this region, that matters. To illustrate this, we show in Fig. 8 the dependence of the surface tension on the steepness parameter α, determining the shape of the tanh function. Note that the limit $\alpha \to \infty$ corresponds to the surface tension as predicted by SKA, $\gamma_{lg,\infty}^{\mathrm{SKA}} = 1.060\varepsilon/\sigma^2$, for $k_BT = 0.7\varepsilon$. Such a value contrasts with the result of SIA, which corresponds to the minimum of the function, and yields $\gamma_{lg,\infty}^{\mathrm{SIA}} = 0.524\varepsilon/\sigma^2$, in much better agreement with the numerical solution of DFT, $\gamma_{lg,\infty}^{\mathrm{DFT}} = 0.517\varepsilon/\sigma^2$.

Asymptotic analysis of the film thickness in Eq. (50) reveals that the film thickness for large but finite R remains finite even at saturation with $\ell \sim R^{1/3}$ in line with earlier studies, e.g., Refs. [5,8]. From Eq. (50) one also recognizes a strong dependence of ℓ on the planar liquid-gas surface tension. In Fig. 9 we present the SIA and SKA predictions of the dependence on ℓ as a function of the wall radius. The comparison with the numerical DFT results reveals that for large R, SIA is clearly superior, reflecting a more realistic estimation of the liquid-gas surface tension. For small values of R (and ℓ) we observe a deviation between DFT and the

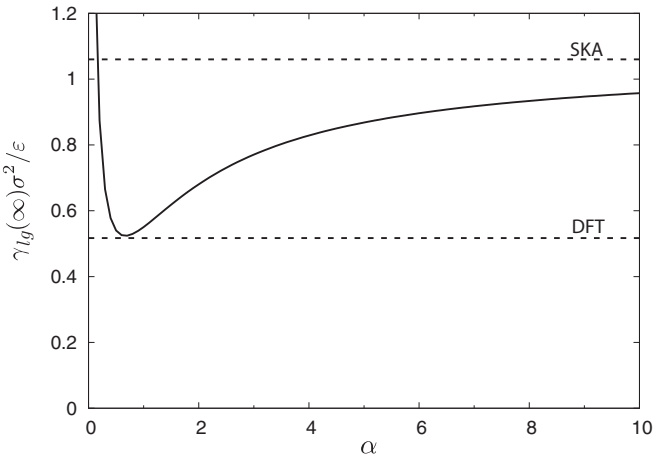

FIG. 8. Plot of a dimensionless planar liquid-gas surface tension for the liquid-gas interface approximation $\rho(z) = \frac{\rho_l+\rho_g}{2} - \frac{\Delta\rho}{2}\tanh(\alpha z/\sigma)$ for $k_BT = 0.7\varepsilon$ as a function of the steepness parameter α. The upper dashed line is the surface tension obtained from SKA, whereas the lower dashed line displays the surface tension obtained from numerical DFT.

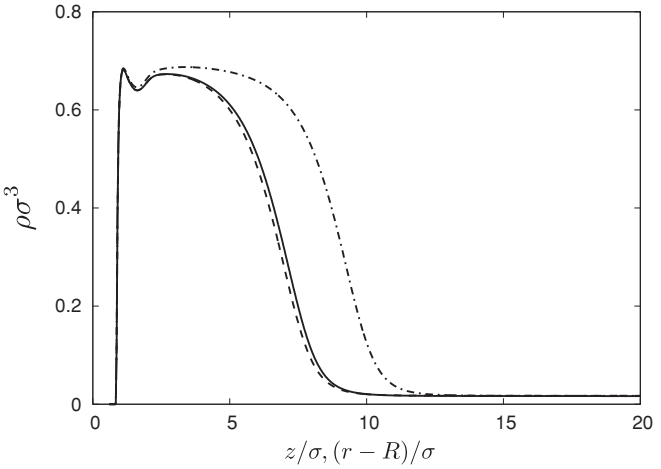

FIG. 10. Density profiles of the fluid adsorbed at the spherical walls of radii $R = 104.1\sigma$ (dashed) and $R = 210.6\sigma$ (dashed-dotted) in a saturated state and at the planar wall (solid line) in an undersaturated state, $\Delta\mu = -0.015\varepsilon$. The wall radii correspond to the equality $2\gamma^j_{lg,\infty}/R = \Delta\rho|\Delta\mu|$ for $j =$ SIA (dashed) and $j =$ SKA (dashed-dotted). $k_BT = 0.7\varepsilon$ and the wall parameters are $\rho_w\varepsilon_w = 0.8\varepsilon/\sigma^3$ and $\sigma_w = 1.25\sigma$.

SIA results. This indicates a limit of validity of our first-order analysis and the assumption of large film thicknesses.

The occurrence of the undersaturation pressure and the Laplace pressure on the left-hand side of Eq. (50) suggests a certain equivalence between the two systems of a planar and a spherical symmetry once the sum of the two pressures is fixed. In Fig. 10 we test this equivalence on the level of a density profile, where DFT results corresponding to the planar and the spherical case are compared, such that $\Delta\rho|\Delta\mu| = 2\gamma^j_{lg}(\infty)/R$, with $j = \{\text{SIA}, \text{SKA}\}$. A high value of $\gamma_{lg}(\infty)$ as given by SKA must now be compensated by a fairly large R. As we have seen in Fig. 6, the high value of R means that the saturation line

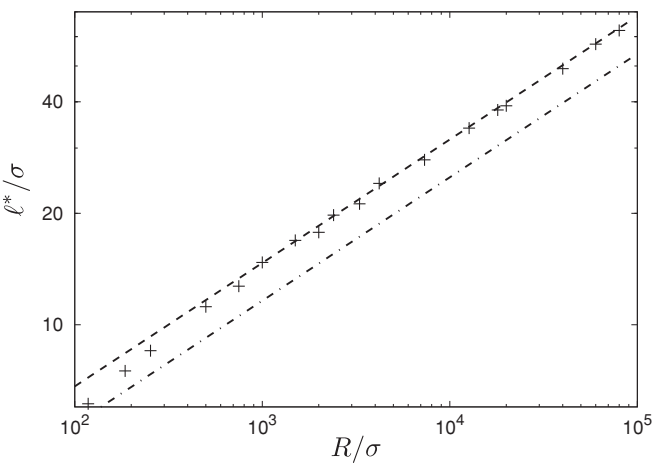

FIG. 9. Film thickness at saturation ($\Delta\mu = 0$) as a function of the wall radius. The symbols correspond to the numerical DFT results. The dashed line shows the prediction according to Eq. (51), where $\gamma^{\text{SIA}}_{lg}(\infty) = 0.524\varepsilon/\sigma^2$ (see Table I). The dashed-dotted line corresponds to Eq. (51) where $\gamma^{\text{SKA}}_{lg}(\infty) = 1.060\varepsilon/\sigma^2$ is used instead of $\gamma^{\text{SIA}}_{lg}(\infty)$. The wall parameters are $\rho_w\varepsilon_w = 0.8\varepsilon/\sigma^3$ and $\sigma_w = 1.25\sigma$ at $k_BT = 0.7\varepsilon$.

$\Delta\mu = 0$ is crossed by the adsorption isotherm at large ℓ, in agreement with the result depicted in Fig. 9. However, for a *given* R, ℓ as obtained by SKA is underestimated, which follows from Eq. (51) with $\gamma_{lg}(\infty) = \gamma^{\text{SKA}}_{lg}(\infty)$, which is also consistent with the physical observation that high surface tension inhibits growth of the liquid film.

Note that these results are not in conflict with the previous study in Ref. [8], where the SKA has been applied for drying on a spherical hard wall and very good agreement was obtained with DFT computations. This is because in Ref. [8] the "exact" (i.e., obtained from DFT computations) liquid-vapor surface tension was implemented into SKA with a view to verify the correctness of its functional form. Here, we show that the coarse-grained effective Hamiltonian approach is capable of a quantitatively reliable prediction of the adsorption phenomena on a spherical wall (for a sufficiently large R), if the restriction of the sharp liquid-gas interface is dropped. However, the price we have to pay is one more parameter (compared to SKA) that steps into the theory.

V. SUMMARY AND CONCLUSIONS

We have reexamined the properties of a well known coarse-grained interfacial Hamiltonian approach, originally proposed by Dietrich [1] for the study of wetting phenomena on a planar substrate and based on SKA. SKA relies on approximating the density profile by a piecewise constant function and has proved to provide significant insight into interfacial phenomena as it is mathematically tractable and gives reliable results for a wide spectrum of problems. This theory is phenomenological in its origin, but a link with a microscopic DFT can be made, which allows one to express all the necessary quantities in terms of fluid-fluid and fluid-substrate interaction parameters. Comparison with numerical DFT reveals that SKA provides a

fully satisfactory approach to the theory of complete wetting on a planar surface.

One of the aims of this study was to demonstrate that for a spherical geometry the prediction quality of SKA regarding interfacial properties and wetting characteristics is limited. More specifically, we demonstrated that SKA satisfactorily determines the functional form of the asymptotic behavior of the film thickness for large radii of the substrate but leads to a significant quantitative disagreement in the prediction of the adsorbed film thickness when compared against numerical DFT. The source of the deviation is the presence of the Laplace pressure that is not quantitatively captured within the framework of SKA. This contribution originates in the dependence of the free energy of the liquid-gas interface on a position of a dividing surface, a property that is absent in the planar case.

We then showed that the properties of the effective interfacial Hamiltonian approach can be substantially improved if SKA is replaced by SIA, where the assumption of the sharp liquid-gas interface is replaced by a less restrictive approximation in which the interface is treated as a continuous function of the density distribution. We demonstrated that SIA allows for mathematical scrutiny as it is still analytically tractable, e.g., it provides the curvature expansion of the surface tensions (nonanalytic in the wall curvature) with the leading-order term proportional to σ/R. Moreover, it allows one to express the corresponding coefficient, the Tolman length, in a fairly simple manner and the values it predicts for the Tolman length are in reasonable agreement with the latest simulation results.

This is in contrast with SKA, where the linear term in the surface tension expansion is missing, i.e., the Tolman length vanishes. This observation is in full agreement with the conclusion of Fisher and Wortis [28], since SKA treats the fluid in a "symmetric" way, and thus the Tolman length must disappear as for the Ising-like models. In other words, according to SKA, the surface tension of a large drop is equivalent to the one of a bubble, provided the density profiles of the two systems are perfectly antisymmetric in the planar limit. This is no more true for SIA, due to the asymmetry of the "local" contributions to the surface tension, i.e., the first term on the right-hand side of Eq. (38).

Furthermore, comparison with our numerical DFT revealed that the SIA results of the film thickness as a function of the wall radius offer a significant improvement to the ones obtained from SKA. This follows from the fact that the surface tension of the planar liquid-gas interface according to SKA is overestimated, which in turn underestimates the interface growth.

It should be emphasized that all the theoretical approaches we have considered in this work are of a mean-field character, i.e., they do not properly take into account the interfacial fluctuations (capillary waves) at the liquid-gas interface. However, for our fluid model of a power-law interaction, these fluctuations are not expected to play any significant role, since the upper critical dimension associated with the considered system is $d_c^* = 2$ [34]. Nevertheless, what one has to take into account in order to obtain the correct critical behavior, is the broadening of the interface at the critical region. Evidently, this feature is not provided by SKA. Consequently, within

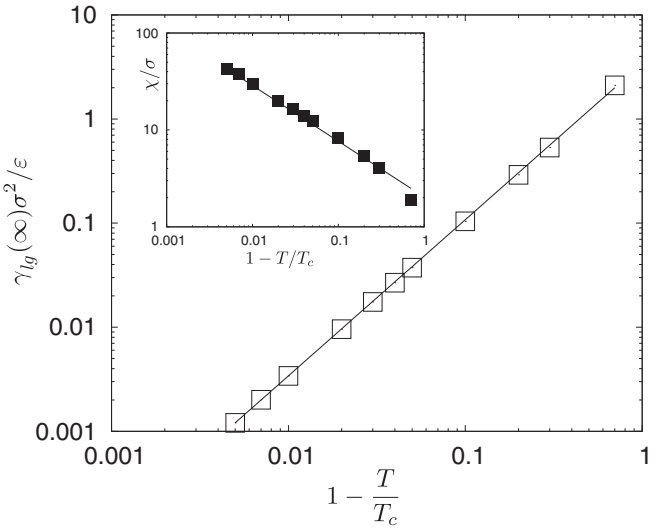

FIG. 11. Plot of liquid-gas surface tension vs $t = 1 - T/T_c$. The squares are the result of SIA, where a simple linear interpolant has been used to model the interface density profile. The surface tension has been obtained by minimizing the grand potential with respect to the interface width χ. The solid line is a fit to $\gamma_{lg}(\infty)\sigma^2/\varepsilon = Ct^{3/2}$, where the resulting coefficient is $C = 3.4$. The inset shows a plot of the interface width χ/σ over t. The solid line is a fit to $\chi = C_\chi t^{-\alpha}$, where $C_\chi = 2.0$ and $\alpha = 0.57$.

SKA the liquid-gas surface tension vanishes as $t = 1 - \frac{T}{T_c}$ [5]. In contrast, SIA provides the expected mean-field behavior $\gamma_{lg}(\infty) \sim t^{3/2}$, as it is able to capture the interface broadening near the critical point (see Fig. 11).

The SIA developed here can be naturally extended by "softening" the wall-liquid interface in an analogous way as done for the liquid-vapor interface. However, such a modification would have presumably only negligible impact on the prediction of the thickness of the adsorbed liquid film, since the contribution to the excess free energy from the wall-liquid surface tension has no ℓ dependence and the change of the binding potential is expected to be small. On the other hand, it may be interesting to find the influence of this refinement on quantities such as the density profile at contact with the wall. However, for this purpose a nonlocal DFT (e.g., Rosenfeld's fundamental measure theory) would be needed [8,35,36].

We also note that despite our restriction to a model of spherical symmetry, our conclusions should be relevant for general curved geometries and should capture some of the qualitative aspects of wetting on nonplanar substrates. Of particular interest would be the extension of this study to spatially heterogeneous, chemical, or topographical substrates. Such substrates have a significant effect on the wetting characteristics of the solid-liquid pair (e.g., Refs. [37–42]).

ACKNOWLEDGMENTS

We are grateful to Bob Evans for valuable comments and suggestions on an early version of the manuscript and for bringing to our attention Ref. [35]. We thank Antonio Pereira for helpful discussions regarding numerical aspects of our

study. This work is supported by the Rotary Clubs Darmstadt, Darmstadt-Bergstraße, and Darmstadt-Kranichstein, Engineering and Physical Sciences Research Council of England Platform Grant No. EP/E046029, European Union-FP7 ITN Grant No. 214919 (Multiflow) and European Research Council Advanced Grant No. 247031. A.M. is grateful for the financial support of the Ministry of Education, Youth and Sports of the Czech Republic under Project No. LC512 and the GAAS of the Czech Republic (Grant No. IAA400720710).

APPENDIX A: NUMERICAL METHODS

For our computations we employ dimensionless values. We use σ and ε as the characteristic length and energy scales, respectively.

1. Density profile

To obtain the equilibrium density profiles, the extremal conditions (9) and (13) for the planar and the spherical case, respectively, must be solved numerically. As both cases are of dimension one, the same numerical method can be applied and we restrict ourselves to presenting the numerical method for the planar wall, $W = \mathbb{R}^2 \times \mathbb{R}^-$.

The domain $\mathbb{R}$ normal to the wall is restricted to an interval of interest $[z_0, z_N]$ with boundary conditions $\rho(z) = 0$ for $z < z_0$ and $\rho(z) = \rho_g$ for $z > z_N$. $z_0 \in (0,1)$ is typically chosen to be 0.6. This can be done due to the repulsive character of the wall. The interval $[z_0, z_N]$ is then divided in a uniform mesh, $z_i = z_0 + i\Delta z$ with $i = 0, \ldots, N$, where $\Delta z = (z_N - z_0)/N$ is the grid size. Subsequently, the integral in Eq. (9) is discretized using a trapezoidal rule inside the domain $[z_0, z_N]$, whereas the analytical expression

$$\Psi_{\mathrm{Pla}}(z) = \int_z^\infty \Phi_{\mathrm{Pla}}(z')\,dz' = \begin{cases} \left(-\frac{16}{9}\pi + \frac{6}{5}\pi\frac{z}{\sigma}\right)\varepsilon\sigma^3, & \text{if } z < \sigma \\ 4\pi\varepsilon\sigma^3\left[\frac{1}{45}\left(\frac{\sigma}{z}\right)^9 - \frac{1}{6}\left(\frac{\sigma}{z}\right)^3\right], & \text{if } z \geqslant \sigma \end{cases}$$

is used for the integral outside that interval. Hence, we obtain a system of $N+1$ nonlinear equations with $\{\rho_i,\ i = 0, \ldots, N\}$ as unknowns, namely,

$$g_i(\rho_0, \ldots, \rho_N) := \mu_{\mathrm{HS}}(\rho_i) + V_\infty(z_i) - \mu + \rho_g \Psi_{\mathrm{Pla}}(z_N - z_i) + \frac{\Delta z}{2}\sum_{j=1}^{N-1}(2 - \delta_{j0} - \delta_{jN})\rho_j \Phi_{\mathrm{Pla}}(|z_j - z_i|) = 0, \qquad \text{(A1)}$$

where δ_{ij} denotes the Kroenecker delta, which we have used in order to take into account the grid size at the boundaries.

This system of equations is solved using a modified Newton method, where each step $\Delta\boldsymbol{\rho}$ is rescaled with a parameter λ such that $\boldsymbol{\rho}^{n+1} = \boldsymbol{\rho}^n + \lambda\Delta\boldsymbol{\rho}$ is bounded in $(0, 6/\pi)$ in order to avoid the singularity of Eq. (8). Note that we have made use of the vector notation $\boldsymbol{\rho} := (\rho_0, \ldots, \rho_n)^T$. In each Newton step n, the linear system of equations

$$\mathbf{J} \cdot \Delta\boldsymbol{\rho} = \mathbf{g}(\boldsymbol{\rho}^n) \qquad \text{(A2)}$$

has to be solved, where the elements of the Jacobian matrix $\mathbf{J}$ are given by

$$J_{ij} = \frac{\partial g_i}{\partial \rho_j} = \delta_{ij}\mu'_{\mathrm{HS}}(\rho_i) + \frac{\Delta z}{2}(2 - \delta_{j0} - \delta_{jN})\Phi_{\mathrm{Pla}}(|z_j - z_i|). \qquad \text{(A3)}$$

2. Adsorption isotherms

Solving Eq. (A1) will only give one density profile $\boldsymbol{\rho}$ for each chemical potential μ. However, in the case of a prewetting transition, there can be multiple solutions for the same chemical potential. From these solutions, only one is stable, whereas the other solutions are meta- or unstable (see also Sec. III A). In order to compute the full bifurcation diagram of the set of density profiles over the chemical potential, a pseudo arc-length continuation scheme is developed similar to the one employed by Salinger and Frink [43].

More specifically, we introduce an arc-length parametrization such that $(\mu(s), \boldsymbol{\rho}(s))$ with $s \in \mathbb{R}$ is a connected set of solutions of condition (A1), and where we have included the chemical potential μ as an additional variable:

$$\mathbf{g}(\mu, \boldsymbol{\rho}) \stackrel{!}{=} \mathbf{0}. \qquad \text{(A4)}$$

The main idea of the continuation scheme is to trace the set of solutions along the curve parametrized by s.

Assume that a point $(\mu^n, \boldsymbol{\rho}^n)$ at position s^n on the curve is given, where n is the step of the continuation scheme being solved for. First, the tangent vector $(\frac{d\mu}{ds}, \frac{d\boldsymbol{\rho}}{ds})$ at position s^n is computed. This is done by differentiating $\mathbf{g}(s) := \mathbf{g}(\mu(s), \boldsymbol{\rho}(s))$ with respect to s. From Eq. (A4), it is known that $\mathbf{g}$ is a constant equal to zero on the curve of solutions $[\mu(s), \boldsymbol{\rho}(s)]$. Hence, the differential $\frac{d\mathbf{g}}{ds}$ vanishes:

$$\frac{d\mathbf{g}}{ds} = \left(\frac{\partial \mathbf{g}}{\partial \mu} \quad \mathbf{J}\right) \cdot \begin{pmatrix} \frac{d\mu}{ds} \\ \frac{d\boldsymbol{\rho}}{ds} \end{pmatrix} = 0, \qquad \text{(A5)}$$

where $\mathbf{J}$ is the Jacobian as defined in Eq. (A3) and

$$\frac{\partial g_i}{\partial \mu} = -1 + \frac{d\rho_g}{d\mu}\Psi_{\mathrm{Pla}}(z_N - z_i). \qquad \text{(A6)}$$

The second term takes into account that ρ_g for the density at $z > z_N$ depends on the chemical potential. In our computations, we have approximated $\frac{\partial g_i}{\partial \mu}$ by -1. Equation (A5) is the defining equation for the tangent vector $(\mu_T^n, \boldsymbol{\rho}_T^n) = (\frac{d\mu}{ds}, \frac{d\boldsymbol{\rho}}{ds})$.

We remark that this homogeneous system of linear equations leaves one degree of freedom, as we only have $N+1$ equations, but $N+2$ variables, $(\mu_T, \boldsymbol{\rho}_T)$. An additional equation is then used to maintain the direction of the tangent vector on the curve of solutions:

$$\left(\mu_T^{n-1} \quad \left(\boldsymbol{\rho}_T^{n-1}\right)^T\right) \cdot \begin{pmatrix} \mu_T^n \\ \boldsymbol{\rho}_T^n \end{pmatrix} = 1,$$

where $(\mu_T^{n-1} \quad (\boldsymbol{\rho}_T^{n-1})^T)$ is the tangent vector of the previous iteration.

In a second step, an additional equation for a point at the step size θ away from $(\mu^n, \boldsymbol{\rho}^n)$ and in the direction of the tangent vector $(\mu_T^{n-1} \quad (\boldsymbol{\rho}_T^{n-1})^T)$ is set up. For this purpose we introduce a scalar product, which takes into account

the discretization of the density profile into N intervals of length Δz:

$$\langle(\mu_1,\boldsymbol{\rho}_1)|(\mu_2,\boldsymbol{\rho}_2)\rangle := \mu_1\mu_2 + \cdots + \frac{\Delta z}{2}\sum_{j=0}^{N}(2-\delta_{j0}-\delta_{jN})\rho_{1j}\rho_{2j}. \quad \text{(A7)}$$

The norm with respect to this scalar product is defined as

$$\|(\mu,\boldsymbol{\rho})\| := \langle(\mu,\boldsymbol{\rho})\,|\,(\mu,\boldsymbol{\rho})\rangle^{1/2}. \quad \text{(A8)}$$

The curve of solutions $(\mu(s),\boldsymbol{\rho}(s))$ is now parametrized by the arc length with respect to the norm given above, such that,

$$\int_{s^n}^{s^n+\theta}\left\|\left(\frac{d\mu}{ds},\frac{d\boldsymbol{\rho}}{ds}\right)\right\| ds = \theta. \quad \text{(A9)}$$

Linearizing the norm around s^n and making use of the approximate tangent vector $(\mu_T,\boldsymbol{\rho}_T)$ at s^n, one obtains

$$\left\langle\left(\mu_T^n,\boldsymbol{\rho}_T^n\right)\middle|\left(\mu(s^n+\theta)-\mu(s^n),\boldsymbol{\rho}(s^n+\theta)-\boldsymbol{\rho}(s^n)\right)\right\rangle = \theta, \quad \text{(A10)}$$

where we have made use of the normalized tangent vector such that

$$\|(\mu_T^n,\boldsymbol{\rho}_T^n)\| = 1. \quad \text{(A11)}$$

Inserting $(\mu^{n+1},\boldsymbol{\rho}^{n+1})$ for $(\mu(s^n+\theta),\boldsymbol{\rho}(s^n+\theta))$ into Eq. (A10) leads to the additional equation for the next point on the curve of solutions:

$$K_n(\mu^{n+1},\boldsymbol{\rho}^{n+1}) := \left\langle\left(\mu_T^n,\boldsymbol{\rho}_T^n\right)\middle|\left(\mu^{n+1}-\mu^n,\boldsymbol{\rho}^{n+1}-\boldsymbol{\rho}^n\right)\right\rangle - \theta \stackrel{!}{=} 0. \quad \text{(A12)}$$

For a geometric interpretation of Eq. (A12), see Fig. 12.

To obtain $(\mu^{n+1},\boldsymbol{\rho}^{n+1})$, Eq. (A12) is solved together with Eq. (A4). This is done using a Newton scheme. In each Newton step, the following system of linear equations is solved:

$$\begin{pmatrix}\mu_T^n & (\bar{\boldsymbol{\rho}}_T^n)^T\\ \frac{\partial\mathbf{g}}{\partial\mu} & \mathbf{J}\end{pmatrix}\cdot\begin{pmatrix}\Delta\mu^m\\ \Delta\boldsymbol{\rho}^m\end{pmatrix} = \begin{pmatrix}K_n(\mu^{n,m},\boldsymbol{\rho}^{n,m})\\ \mathbf{g}(\mu^{n,m},\boldsymbol{\rho}^{n,m})\end{pmatrix}, \quad \text{(A13)}$$

where we are considering the nth step of the continuation scheme and the mth step of the Newton method, such that

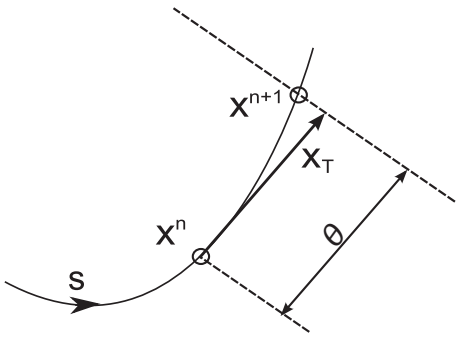

FIG. 12. Sketch of one iteration step of the continuation scheme. $\mathbf{x}^n$ and $\mathbf{x}^{n+1}$ are consecutive points of the iteration, where $\mathbf{x}=(\mu,\boldsymbol{\rho})$. $\mathbf{x}_T$ is the tangent vector at $\mathbf{x}^n$. By following the curve of solutions in the direction of the tangent vector, the pseudo arc-length continuation scheme is able to trace the curve of solutions through turning points with respect to the parameter μ.

$\Delta\mu^m := \mu^{n,m+1}-\mu^{n,m}$ and $\Delta\boldsymbol{\rho}^m := \boldsymbol{\rho}^{n,m+1}-\boldsymbol{\rho}^{n,m}$. Furthermore, we have made use of

$$\bar{\rho}_{T,j}^n := \frac{\Delta z}{2}(2-\delta_{j0}-\delta_{jN})\rho_{T,j}^n.$$

Finally, Eq. (A13) is solved using a conjugate gradient method, where the Jacobian (A3) of the system is approximated by introducing a cutoff of five molecular diameters for the intermolecular potential Φ_{Pla}.

APPENDIX B: SURFACE TENSION AND BINDING POTENTIAL IN SKA

1. Surface tension

According to Gibbsian thermodynamics, the surface tension is the free-energy cost to increase an interface by unit area, i.e., the excess free energy (excess grand potential for an open system) per unit area with respect to the corresponding uniform phases. Within SKA, the liquid-vapor surface tension can be obtained from Eq. (7), with

$$\rho(\mathbf{r}) = \begin{cases}\rho_A, & \mathbf{r}\in\mathbb{V}_A\\ \rho_B, & \mathbf{r}\in\mathbb{V}_B,\end{cases} \quad \text{(B1)}$$

where $\mathbb{V}_A\cap\mathbb{V}_B = 0$ and $\mathbb{V}_A\cup\mathbb{V}_B = \mathbb{R}^3$. The convenience of the expression for the excess grand potential as given by Eq. (7) becomes evident now, as for $\rho_A=\rho_l$, $\rho_B=\rho_g$, and no external field, only the second term in Eq. (7) matters. One then gets an immediate result for the liquid-gas surface tension,

$$\gamma_{lg}^{\text{SKA}} = \frac{\Omega_{\text{ex}}}{\mathcal{A}} = -\frac{(\rho_l-\rho_g)^2}{\mathcal{A}}I(\mathbb{V}_A,\mathbb{V}_B), \quad \text{(B2)}$$

where

$$I(\mathbb{V}_A,\mathbb{V}_B) \equiv \frac{1}{2}\int_{\mathbb{V}_A}\int_{\mathbb{V}_B}\phi(|\mathbf{r}_1-\mathbf{r}_2|)\,d\mathbf{r}_1\,d\mathbf{r}_2. \quad \text{(B3)}$$

For the surface tension of a planar interface we have $\mathbb{V}_A = \mathbb{V}_{z<0}$ and $\mathbb{V}_B = \mathbb{V}_{z\geqslant 0}$ such that

$$\frac{I(\mathbb{V}_{z<0},\mathbb{V}_{z\geqslant 0})}{\mathcal{A}} = \frac{1}{2}\int_{-\infty}^{0}\int_{0}^{\infty}\Phi_{\text{Pla}}(|z-z'|)\,dz'\,dz,$$

with Φ_{Pla} defined by Eq. (11). Thus, for the liquid-gas surface tension we obtain

$$\gamma_{lg}^{\text{SKA}}(\infty) = -\frac{\Delta\rho^2}{2}\int_{-\infty}^{0}\int_{0}^{\infty}\Phi_{\text{Pla}}(|z-z'|)\,dz'\,dz = \frac{3}{4}\pi\Delta\rho^2\varepsilon\sigma^4. \quad \text{(B4)}$$

In the case of a spherical symmetry, i.e., a drop of liquid of radius R, $\mathbb{V}_A = \{\mathbf{r}\in\mathbb{R}^3 : |\mathbf{r}| < R\}$ and $\mathbb{V}_B = \{\mathbf{r}\in\mathbb{R}^3 : |\mathbf{r}|\geqslant R\}$, the surface tension becomes

$$\begin{aligned}\gamma_{lg}^{\text{SKA}}(R) &= -\Delta\rho^2\frac{I(\mathbb{V}_{r<R},\mathbb{V}_{r\geqslant R})}{4\pi R^2}\\ &= -\frac{\Delta\rho^2}{2}\int_R^\infty\int_0^R\left(\frac{r}{R}\right)^2\Phi_{\text{Sph}}(r,r')\,dr'\,dr\\ &= -\frac{\Delta\rho^2}{2}\int_R^\infty\left(\frac{r}{R}\right)^2\Psi_R(r)\,dr\\ &= \gamma_{lg}(\infty)\left(1-\frac{2}{9}\frac{\ln(R/\sigma)}{(R/\sigma)^2}+O\left((\sigma/R)^2\right)\right), \quad \text{(B5)}\end{aligned}$$

where $\Delta\rho = \rho_l - \rho_g$ and $\Phi_{\rm Sph}(r,r') \equiv \int_{\partial B_{r'}} \phi(|\mathbf{r}-\mathbf{r}'|)d\mathbf{r}'$ can be advantageously expressed in terms of $\Phi_{\rm Pla}$:

$$\begin{aligned}
&\Phi_{\rm Sph}(r,r') \\
&= \int_0^{2\pi}\int_0^{\pi} \phi(|\mathbf{r}-\mathbf{r}'|)r'^2 \sin\vartheta'\, d\vartheta'\, d\varphi' \\
&= 2\pi r'^2 \int_0^{\pi} \phi(\sqrt{r^2 - 2rr'\cos\vartheta' + r'^2}) \sin\vartheta'\, d\vartheta' \\
&= \pi \frac{r'}{r} \int_{(r-r')^2}^{(r+r')^2} \phi(\sqrt{t})\, dt \\
&= \pi \frac{r'}{r} \left[\int_{(r-r')^2}^{\infty} \phi(\sqrt{t})\, dt - \int_{(r+r')^2}^{\infty} \phi(\sqrt{t})\, dt \right] \\
&= 2\pi \frac{r'}{r} \left[\int_0^{\infty} \phi(\sqrt{(r-r')^2 + u^2}) u\, du \right. \\
&\quad \left. - \int_0^{\infty} \phi(\sqrt{(r+r')^2 + u^2}) u\, du \right] \\
&= \frac{r'}{r} [\Phi_{\rm Pla}(|r-r'|) - \Phi_{\rm Pla}(|r+r'|)], \qquad \text{(B6)}
\end{aligned}$$

and for $r > R$,

$$\Psi_R(r) \equiv \int_0^R \Phi_{\rm Sph}(r,r')\, dr' = \frac{\pi\varepsilon\sigma^4}{3r} \begin{cases} \frac{\sigma^8}{30}\left[\frac{r+9R}{(r+R)^9} - \frac{r-9R}{(r-R)^9}\right] + \sigma^2\left[\frac{r-3R}{(r-R)^3} - \frac{r+3R}{(r+R)^3}\right], & R+\sigma < r \\ -\frac{26}{15}\frac{r}{\sigma} - \frac{9}{5\sigma^2}[R^2 - (r-\sigma)^2] + \frac{27}{10} + \frac{\sigma^8}{30}\frac{r+9R}{(r+R)^9} - \sigma^2\frac{r+3R}{(r+R)^3}, & r < R+\sigma. \end{cases} \qquad \text{(B7)}$$

Note that expression (B5) gives a vanishing Tolman's length.

2. Binding potential

The binding potential of a system possessing two interfaces is the surface free energy per unit area of the system minus the contribution due to the surface tensions of the two interfaces. It expresses an effective interaction between the interfaces induced by the attractive forces. If, analogously to the analysis above, we define three disjoint subspaces $\mathbb{V}_W$, $\mathbb{V}_A$, and $\mathbb{V}_B$, such that $\mathbb{V}_W \cup \mathbb{V}_A \cup \mathbb{V}_B = \mathbb{R}^3$, the density distribution of the wall-liquid-gas system within SKA is

$$\rho(\mathbf{r}) = \begin{cases} 0, & \mathbf{r} \in \mathbb{V}_W \\ \rho_l, & \mathbf{r} \in \mathbb{V}_A \\ \rho_g, & \mathbf{r} \in \mathbb{V}_B, \end{cases} \qquad \text{(B8)}$$

which when substituted into Eq. (7) gives for the excess grand potential:

$$\begin{aligned}
\Omega_{\rm ex} = &-\Delta\mu\Delta\rho V_A - {\rho_l}^2 I(\mathbb{V}_W,\mathbb{V}_A) - \rho_g^2 I(\mathbb{V}_W,\mathbb{V}_B) \\
&- (\Delta\rho)^2 I(\mathbb{V}_A,\mathbb{V}_B) + \int_{\mathbb{V}_A\cup\mathbb{V}_B} V(\mathbf{r})\rho(\mathbf{r})d\mathbf{r}. \qquad \text{(B9)}
\end{aligned}$$

We now rearrange the terms in Eq. (B9), such that

$$\frac{\Omega_{\rm ex}(\ell)}{\mathcal{A}} = -\Delta\mu\Delta\rho\frac{V_A}{\mathcal{A}} + \gamma_{wl}^{\rm SKA} + \frac{\mathcal{A}'}{\mathcal{A}}\gamma_{lg}^{\rm SKA} + w^{\rm SKA}(\ell), \qquad \text{(B10)}$$

where $\mathcal{A} = \int_{\partial\mathbb{V}_W} dS$ is the surface of the wall and $\mathcal{A}' = \int_{\partial(\mathbb{V}_W\cup\mathbb{V}_A)} dS$ is the surface of the liquid-gas interface. We obtain

$$\gamma_{wl}^{\rm SKA} = \frac{1}{\mathcal{A}}\left(-{\rho_l}^2 I(\mathbb{V}_W,\mathbb{V}_A\cup\mathbb{V}_B) + \rho_l\int_{\mathbb{V}_A\cup\mathbb{V}_B} V(\mathbf{r})\, d\mathbf{r}\right), \qquad \text{(B11)}$$

$$\gamma_{lg}^{\rm SKA} = -\frac{1}{\mathcal{A}'}(\Delta\rho)^2 I(\mathbb{V}_W\cup\mathbb{V}_A,\mathbb{V}_B), \qquad \text{(B12)}$$

and the binding potential $w^{\rm SKA}$ involving the remaining contribution

$$w^{\rm SKA}(\ell) = \frac{1}{\mathcal{A}}\left(2\rho_l\Delta\rho I(\mathbb{V}_W,\mathbb{V}_B) - \Delta\rho\int_{\mathbb{V}_B} V(\mathbf{r})\, d\mathbf{r}\right). \qquad \text{(B13)}$$

Having obtained the expressions of $I(X,Y)$ for systems possessing translational or spherical symmetry, we can evaluate the binding potential in the planar case by making use of $\mathbb{V}_w = \mathbb{R}^2\times(-\infty,\delta]$, $\mathbb{V}_A = \mathbb{R}^2\times(\delta,\ell)$ and $\mathbb{V}_B = \mathbb{R}^2\times[\ell,\infty)$:

$$\begin{aligned}
&w^{\rm SKA}(\ell) \\
&\overset{\rm plane}{=} \Delta\rho\left(\rho_l\int_{\ell-\delta}^{\infty}\int_z^{\infty}\Phi_{\rm Pla}(z')\, dz'\, dz - \int_{\ell}^{\infty} V_{\infty}(z)\, dz\right) \\
&= -\frac{A}{12\pi\ell^2}\left(1 + \frac{2+3\frac{\delta}{\ell}}{1-\frac{\rho_w\varepsilon_w\sigma_w^6}{\rho_l^2\varepsilon\sigma^6}}\frac{\delta}{\ell} + O\left((\delta/\ell)^3\right)\right). \qquad \text{(B14)}
\end{aligned}$$

In the spherical case we make use of $\mathbb{V}_w = \{\mathbf{r}\in\mathbb{R}^3 : |\mathbf{r}| \leqslant R+\delta\}$, $\mathbb{V}_A = \{\mathbf{r}\in\mathbb{R}^3 : R+\delta < |\mathbf{r}| < R+\ell\}$, and $\mathbb{V}_B = \{\mathbf{r}\in\mathbb{R}^3 : |\mathbf{r}| \geqslant R+\ell\}$ to obtain

$$w^{\rm SKA}(\ell;R) \overset{\rm sphere}{=} w^{\rm SKA}(\ell;\infty)\left(1 + \frac{\ell}{R}\right), \qquad \text{(B15)}$$

where we have neglected terms $O\left((\delta/\ell)^3, \delta/R, \frac{\ln(\ell/R)}{(R/\ell)^2}\right)$.

APPENDIX C: SURFACE TENSION, BINDING POTENTIAL, AND THE TOLMAN LENGTH IN SIA

1. Surface tension

The surface tension of a planar liquid-gas interface in SIA

$$\rho_{lg,\infty}(z) = \begin{cases} \rho_l, & z \leqslant -\chi/2 \\ \rho_{lg}(z), & |z| < \chi/2 \\ \rho_g, & z \geqslant \chi/2, \end{cases} \qquad \text{(C1)}$$

is obtained by substituting Eq. (C1) into Eq. (7) with $V(\mathbf{r}) = 0$,

$$\begin{aligned}\gamma_{lg}^{\mathrm{SIA}}(\infty) &= \frac{\Omega_{\mathrm{ex}}[\rho_{lg,\infty}]}{\mathcal{A}} \\ &= -\int_{-\chi/2}^{\chi/2}\{p[\rho_{lg,\infty}(z)] - p[\rho_{\mathrm{ref}}(z)]\}dz \\ &\quad + \frac{1}{2}\int_{-\infty}^{\infty}\int_{-\infty}^{\infty}\rho_{lg,\infty}(z)[\rho_{lg,\infty}(z') - \rho_{lg,\infty}(z)] \\ &\quad \times \Phi_{\mathrm{Pla}}(z,z')dz'\,dz, \end{aligned} \tag{C2}$$

where $\rho_{\mathrm{ref}}(z)$ denotes the density of a given bulk phase, i.e., $\rho_{\mathrm{ref}}(z) = \rho_l\Theta(-z) + \rho_g\Theta(z)$ such that at saturation $p[\rho_{\mathrm{ref}}(z)] \equiv p_{\mathrm{ref}} = \mathrm{const}$. We note that in the above approximation the contribution due to the excess local pressure is generally nonzero (in contrast to SKA).

In the spherical case, the density profile is

$$\rho_{lg,R}(r) = \begin{cases}\rho_{l,} & r \leqslant R - \chi/2 \\ \rho_{lg}(r-R), & |r-R| < \chi/2 \\ \rho_{g,} & r \geqslant R + \chi/2,\end{cases} \tag{C3}$$

and the surface tension of a liquid drop of radius R is

$$\begin{aligned}\gamma_{lg}^{\mathrm{SIA}}(R) &= \frac{\Omega_{\mathrm{ex}}[\rho_{lg,R}]}{4\pi R^2} \\ &= -\int_{R-\chi/2}^{R+\chi/2}\{p[\rho_{lg,R}(r)] - p_{\mathrm{ref}}\}\left(\frac{r}{R}\right)^2 dr \\ &\quad + \frac{1}{2}\int_0^{\infty}\int_0^{\infty}\rho_{lg,R}(r)[\rho_{lg,R}(r') - \rho_{lg,R}(r)] \\ &\quad \times \Phi_{\mathrm{Sph}}(r,r')\left(\frac{r}{R}\right)^2 dr'\,dr. \end{aligned} \tag{C4}$$

2. Tolman length

Here we calculate the Tolman length as given by SIA by a direct comparison of Eqs. (C2) and (C4). We first compare the second terms of Eqs. (C2) and (C4). For this purpose we define

$$\begin{aligned} h_R(r,r') &\equiv \rho_{lg,R}(r)[\rho_{lg,R}(r') - \rho_{lg,R}(r)] \\ \text{and} \quad h(r,r') &\equiv \rho_{lg,\infty}(r)[\rho_{lg,\infty}(r') - \rho_{lg,\infty}(r)], \end{aligned} \tag{C5}$$

and making use of Eq. (B6) we can express the double integral in Eq. (C4) as

$$\begin{aligned}&\frac{\sigma^2}{\varepsilon}\int_0^{\infty}\int_0^{\infty}h_R(r,r')\Phi_{\mathrm{Sph}}(r,r')\left(\frac{r}{R}\right)^2 dr'\,dr \\ &= \frac{\sigma^2}{\varepsilon}\int_{-R}^{\infty}\int_{-R}^{\infty}h(r,r')[\Phi_{\mathrm{Pla}}(|r-r'|) \\ &\quad -\Phi_{\mathrm{Pla}}(|2R + r - r'|)]\left(1+\frac{r'}{R}\right)\left(1+\frac{r}{R}\right)dr'\,dr \\ &= \frac{\sigma^2}{\varepsilon}\int_{-R}^{\infty}\int_{-R}^{\infty}h(r,r')\Phi_{\mathrm{Pla}}(|r-r'|) \\ &\quad \times\left(1+\frac{r'}{R}\right)\left(1+\frac{r}{R}\right)dr'\,dr + O\big((\sigma/R)^2\big) \\ &= \frac{\sigma^2}{\varepsilon}\int_{-R}^{\infty}\int_{-R}^{\infty}h(r,r')\Phi_{\mathrm{Pla}}(|r-r'|) \\ &\quad \times\left(1+\frac{r+r'}{R}\right)dr'\,dr + O\left(\frac{\ln(R/\sigma)}{(R/\sigma)^2}\right) \\ &= \frac{\sigma^2}{\varepsilon}\int_{-\infty}^{\infty}\int_{-\infty}^{\infty}h(r,r')\Phi_{\mathrm{Pla}}(|r-r'|) \\ &\quad \times\left(1+\frac{r+r'}{R}\right)dr'\,dr + O\left(\frac{\ln(R/\sigma)}{(R/\sigma)^2}\right). \end{aligned} \tag{C6}$$

Comparison with the double integral in Eq. (C2) then yields

$$\begin{aligned}&\frac{\sigma^2}{\varepsilon R}\iint_{-\infty}^{\infty}h(r,r')\Phi_{\mathrm{Pla}}(|r-r'|)(r+r')\,dr'\,dr \\ &\quad + O\left(\frac{\ln(R/\sigma)}{(R/\sigma)^2}\right) \\ &= \frac{\sigma^2}{\varepsilon R}\int_{-\infty}^{\infty}\int_{-\infty}^{\infty}r[h(r,r') + h(r',r)]\Phi_{\mathrm{Pla}}(|r-r'|)\,dr'\,dr \\ &\quad + O\left(\frac{\ln(R/\sigma)}{(R/\sigma)^2}\right) \\ &= -\frac{\sigma^2}{\varepsilon R}\int_{-\infty}^{\infty}\int_{-\infty}^{\infty}r[\rho_{lg,\infty}(r') - \rho_{lg,\infty}(r)]^2 \\ &\quad \times\Phi_{\mathrm{Pla}}(|r-r'|)dr'\,dr + O\left(\frac{\ln(R/\sigma)}{(R/\sigma)^2}\right). \end{aligned}$$

In the following, we focus on the asymmetry of the model due to the contribution of the pressure, but for simplicity we assume that the density profile is symmetric. In this case, the integrand in the above expression is antisymmetric with respect to the reflection transformation $r \to -r$ and $r' \to -r'$ and the term $O(\sigma/R)$ vanishes.

For the difference of the first terms of Eqs. (C4) and (C2) we obtain

$$\begin{aligned}&-\frac{\sigma^2}{\varepsilon}\int_0^{\infty}\{p[\rho_{lg,R}(r)] - p_{\mathrm{ref}}\}\left(\frac{r}{R}\right)^2 dr \\ &\quad + \frac{\sigma^2}{\varepsilon}\int_{-\infty}^{\infty}\{p[\rho_{lg,\infty}(z)] - p_{\mathrm{ref}}\}\,dz \\ &= -\frac{2\sigma^2}{\varepsilon R}\int_{-\chi/2}^{\chi/2}\{p[\rho_{lg,\infty}(z)] - p_{\mathrm{ref}}\}z\,dz \\ &\quad + O\big((\sigma/R)^2\big), \end{aligned} \tag{C7}$$

yielding a Tolman length

$$\delta_{\infty} = \frac{1}{\gamma_{lg}^{\mathrm{SIA}}(\infty)}\int_{-\chi/2}^{\chi/2}\{p[\rho_{lg}(z)] - p_{\mathrm{ref}}\}z\,dz. \tag{C8}$$

Note that in line with [28], the Tolman length does not depend on the choice of the dividing surface.

3. Binding potential

The extension of the expression for the binding potential, Eq. (B15), as given by SKA is rather straightforward. We consider the density distribution as follows:

$$\rho(\mathbf{r}) = \begin{cases}0, & \mathbf{r} \in \mathbb{V}_W \\ \rho_{l,} & \mathbf{r} \in \mathbb{V}_A \\ \rho_{lg}(\mathbf{r}), & \mathbf{r} \in \mathbb{V}_{AB} \\ \rho_{g,} & \mathbf{r} \in \mathbb{V}_B,\end{cases} \tag{C9}$$

for $\mathbb{V}_W$ a sphere of radius $R+\delta$, for $\mathbb{V}_W \cup \mathbb{V}_A$ a sphere of radius $R+\ell-\chi/2$, and for $\mathbb{V}_W \cup \mathbb{V}_A \cup \mathbb{V}_{AB}$ a sphere of radius $R+\ell+\chi/2$ and $\mathbb{V}_W \cup \mathbb{V}_A \cup \mathbb{V}_B \cup \mathbb{V}_{AB} = \mathbb{R}^3$. Such a model is relevant for the study of wetting on a spherical (R finite) and on a planar ($R \to \infty$) wall. It should be noted that in contrast to SKA, this density distribution is not piecewise constant, due to the position dependent part of $\rho(\mathbf{r})$ in the region $\mathbb{V}_{AB}$. Furthermore, we define the following operators:

$$[XY] \equiv -\frac{1}{2}\int_X\int_Y [\rho(\mathbf{r})-\rho(\mathbf{r}')]^2\phi(|\mathbf{r}-\mathbf{r}'|)\,d\mathbf{r}'\,d\mathbf{r},$$
$$[XY]_{wl} \equiv -\frac{1}{2}\int_X\int_Y [\rho_{wl}(\mathbf{r})-\rho_{wl}(\mathbf{r}')]^2\phi(|\mathbf{r}-\mathbf{r}'|)\,d\mathbf{r}'\,d\mathbf{r},$$
$$[XY]_{lg} \equiv -\frac{1}{2}\int_X\int_Y [\rho_{lg}(\mathbf{r})-\rho_{lg}(\mathbf{r}')]^2\phi(|\mathbf{r}-\mathbf{r}'|)\,d\mathbf{r}'\,d\mathbf{r},$$

with $\rho_{wl}(\mathbf{r}) \equiv \rho_l \chi_{\mathbb{R}^3\setminus\mathbb{V}_W}(\mathbf{r})$ and $\rho_{lg}(\mathbf{r}) \equiv \rho_l \chi_{\mathbb{V}_W\cup\mathbb{V}_{\mathbb{A}}}(\mathbf{r}) + \rho_{lg}(\mathbf{r})\chi_{\mathbb{V}_{AB}}(\mathbf{r}) + \rho_g\chi_{\mathbb{V}_B}(\mathbf{r})$, where $\chi_X(\mathbf{r})$ is the characteristic function of a subset X. Using this convention, the wall-liquid and liquid-gas surface tensions can be respectively expressed as

$$\gamma_{wl} = \frac{1}{\mathcal{A}}\left([\mathbb{V}_W\mathbb{V}_A] + [\mathbb{V}_W(\mathbb{V}_{AB}\cup\mathbb{V}_B)]_{wl} + \int \rho_{wl}(\mathbf{r})V(\mathbf{r})d\mathbf{r}\right)$$
$$\gamma_{lg} = \frac{1}{\mathcal{A}}\left([\mathbb{V}_{AB}\mathbb{V}_B] + \frac{1}{2}[\mathbb{V}_{AB}\mathbb{V}_{AB}] + [\mathbb{V}_A(\mathbb{V}_{AB}\cup\mathbb{V}_B)]\right.$$
$$\left. + [\mathbb{V}_W(\mathbb{V}_{AB}\cup\mathbb{V}_B)]_{lg} - \int_{\mathbb{V}_{AB}}\{p[\rho_{lg}(\mathbf{r})] - p_{\text{ref}}\}\,d\mathbf{r}\right),$$

where $\mathcal{A} = 4\pi R^2$. When this is subtracted from the surface grand potential (7), which can be written as

$$\frac{\Omega_{\text{ex}}}{\mathcal{A}} = \frac{1}{\mathcal{A}}\left([\mathbb{V}_W\mathbb{V}_A] + [\mathbb{V}_W(\mathbb{V}_{AB}\cup\mathbb{V}_B)]\right.$$
$$+ [\mathbb{V}_A(\mathbb{V}_{AB}\cup\mathbb{V}_B)] + \frac{1}{2}[\mathbb{V}_{AB}\mathbb{V}_{AB}] + [\mathbb{V}_{AB}\mathbb{V}_B]$$
$$\left. - \int_{\mathbb{V}_{AB}}\{p[\rho_{lg}(\mathbf{r})] - p[\rho_{\text{ref}}(\mathbf{r})]\}\,d\mathbf{r} + \int \rho(\mathbf{r})V(\mathbf{r})\,d\mathbf{r}\right), \tag{C10}$$

one obtains for the binding potential:

$$w^{\text{SIA}} = \frac{1}{\mathcal{A}}\left([\mathbb{V}_W(\mathbb{V}_{AB}\cup\mathbb{V}_B)] - [\mathbb{V}_W(\mathbb{V}_{AB}\cup\mathbb{V}_B)]_{wl}\right.$$
$$\left. - [\mathbb{V}_W(\mathbb{V}_{AB}\cup\mathbb{V}_B)]_{lg} + \int V(\mathbf{r})[\rho(\mathbf{r}) - \rho_{wl}(\mathbf{r})\,d\mathbf{r}]\right).$$

In spherical coordinates, the binding potential reads

$$w^{\text{SIA}} = \int_0^{R+\delta}\int_{R+\ell-\chi/2}^{\infty}\left(\frac{r}{R}\right)^2\rho_l[\rho_l - \rho(r')]$$
$$\times\Phi_{\text{Sph}}(r,r')dr'\,dr$$
$$+ \int_{R+\ell-\chi/2}^{\infty}[\rho(r)-\rho_l]\,V_R(r)\left(\frac{r}{R}\right)^2 dr. \tag{C11}$$

[1] S. Dietrich, in *Phase Transitions and Critical Phenomena*, edited by C. Domb and J. L. Lebowitz (Academic, New York, 1988), Chap. 1, p. 2.
[2] D. Bonn, J. Eggers, J. Indekeu, J. Meunier, and E. Rolley, Rev. Mod. Phys. **81**, 739 (2009).
[3] M. Schick, in *Liquids at Interfaces*, Les Houches Session XLVIII, edited by J. Charvolin, J.-F. Joanny, and J. Zinn-Justin (Elsevier, Amsterdam, 1990).
[4] D. E. Sullivan and M. M. T. da Gama, *Fluid Interfacial Phenomena*, edited by C. A. Croxton (Wiley, New York, 1986), p. 45.
[5] T. Bieker and S. Dietrich, Physica A **252**, 85 (1998).
[6] R. Hołyst and A. Poniewierski, Phys. Rev. B **36**, 5628 (1987).
[7] R. Evans, J. R. Henderson, and R. Roth, J. Chem. Phys. **121**, 12074 (2004).
[8] M. C. Stewart and R. Evans, Phys. Rev. E **71**, 011602 (2005).
[9] J. R. Henderson, *Fundamentals of Inhomogeneous Fluids*, edited by D. Henderson (Dekker, New York, 1992).
[10] M. Napiórkowski and S. Dietrich, Phys. Rev. B **34**, 6469 (1986).
[11] N. D. Mermin, Phys. Rev. **137**, A1441 (1965).
[12] R. Evans, Adv. Phys. **28**, 143 (1979).
[13] J. A. Barker and D. Henderson, J. Chem. Phys. **47**, 4714 (1967).
[14] G. J. Throop and R. J. Bearman, J. Chem. Phys. **42**, 2408 (1965).
[15] S. Toxvaerd, J. Chem. Phys. **55**, 3116 (1971).
[16] J. K. Lee and L. A. Barker, J. Chem. Phys. **60**, 1976 (1974).
[17] E. A. Guggenheim, J. Chem. Phys. **13**, 253 (1945).
[18] R. Pandit, M. Schick, and M. Wortis, Phys. Rev. B **26**, 5112 (1982).
[19] E. H. Hauge and M. Schick, Phys. Rev. B **27**, 4288 (1983).
[20] M. Schick and P. Taborek, Phys. Rev. B **46**, 7312 (1992).
[21] D. Bonn and D. Ross, Rep. Prog. Phys. **64**, 1085 (2001).
[22] H. Kellay, J. Meunier, and B. P. Binks, Phys. Rev. Lett. **69**, 1220 (1992).
[23] G. Mistura, H. Lee, and M. Chan, J. Low Temp. Phys. **96**, 221 (1994).
[24] J. E. Rutledge and P. Taborek, Phys. Rev. Lett. **69**, 937 (1992).
[25] D. Ross, J. A. Phillips, J. E. Rutledge, and P. Taborek, J. Low Temp. Phys. **106**, 81 (1997).
[26] A. O. Parry, C. Rascon, and L. Morgan, J. Chem. Phys. **124**, 151101 (2006).
[27] R. C. Tolman, J. Chem. Phys. **17**, 333 (1948).
[28] M. P. A. Fisher and M. Wortis, Phys. Rev. B **29**, 6252 (1984).
[29] J. G. Sampayo, A. Malijevský, E. A. Müller, E. de Miguel, and G. Jackson, J. Chem. Phys. **132**, 141101 (2010).
[30] B. J. Block, S. K. Das, M. Oettel, P. Virnau, and K. Binder, J. Chem. Phys. **133**, 154702 (2010).
[31] A. E. van Giessen and E. M. Blokhuis, J. Chem. Phys. **131**, 164705 (2009).
[32] L. S. Bartell, J. Chem. Phys. B **105**, 11615 (2001).
[33] E. M. Blokhuis and J. Kuipers, J. Chem. Phys. **124**, 074701 (2006).

[34] R. Lipowsky, Phys. Rev. Lett. **52**, 1429 (1984).
[35] M. C. Stewart and R. Evans, J. Phys.: Condens. Matter **17**, S3499 (2005).
[36] E. M. Blokhuis and J. Kuipers, J. Chem. Phys. **126**, 054702 (2007).
[37] L. W. Schwartz and R. R. Elley, J. Colloid Interface Sci. **202**, 173 (1998).
[38] C. M. Gramlich, A. Mazouchi, and G. M. Homsy, Phys. Fluids **16**, 1660 (2004).
[39] D. Quéré, in *Thin Films of Soft Matter*, edited by S. Kalliadasis and U. Thiele (Springer Wien, New York, 2007), p. 115.
[40] N. Savva and S. Kalliadasis, Phys. Fluids **21**, 092192 (2009).
[41] N. Savva, S. Kalliadasis, and G. A. Pavliotis, Phys. Rev. Lett. **104**, 084501 (2010).
[42] H. Bohlen, A. O. Parry, E. Díaz-Herrera, and M. Schoen, Eur. Phys. J. E **25**, 103 (2008).
[43] A. G. Salinger and L. J. D. Frink, J. Chem. Phys. **118**, 7457 (2003).

Paper II

Communications: Evidence for the role of fluctuations in the thermodynamics of nanoscale drops and the implications in computations of the surface tension

José G. Sampayo,[1] Alexandr Malijevský,[1,2] Erich A. Müller,[1] Enrique de Miguel,[3] and George Jackson[1,a)]

[1]*Department of Chemical Engineering, Imperial College London, South Kensington Campus, London SW7 2AZ, United Kingdom*

[2]*E. Hála Laboratory of Thermodynamics, Institute of Chemical Process Fundamentals of ASCR, 16502 Prague 6, Czech Republic*

[3]*Departamento de Física Aplicada, Facultad de Ciencias Experimentales, Universidad de Huelva, 21071 Huelva, Spain*

(Received 27 January 2010; accepted 10 March 2010; published online 9 April 2010)

Test-area deformations are used to analyze vapor-liquid interfaces of Lennard-Jones particles by molecular dynamics simulation. For planar vapor-liquid interfaces the change in free energy is captured by the average of the corresponding change in energy, the leading-order contribution. This is consistent with the commonly used mechanical (pressure-tensor) route for the surface tension. By contrast for liquid drops, one finds a large second-order contribution associated with fluctuations in energy. Both the first- and second-order terms make comparable contributions, invalidating the mechanical relation for the surface tension of small drops. The latter is seen to increase above the planar value for drop radii of ~8 particle diameters, followed by an apparent weak maximum and slow decay to the planar limit, consistent with a small negative Tolman length. © *2010 American Institute of Physics*. [doi:10.1063/1.3376612]

It is striking that though almost a century has passed since Gibbs formulated his thermodynamic theory of curved interfaces, there is still widespread controversy about the dependence of the surface tension on the curvature (size of a drop) and the validity of the mechanical route to the surface tension.[1–3] The formal approach of Gibbs is intimately connected with the relations of Laplace, $\Delta p = 2\gamma_s / R_s$, and Tolman, $\gamma(R)/\gamma_\infty = 1 - 2\delta_\infty / R + \ldots$, for drops of radius R. Here, $\Delta p = p_l - p_g$ is the pressure difference inside (l) and outside (g) the drop, $\gamma_s = \gamma(R_s)$ is the interfacial tension associated with the surface of tension R_s, γ_∞ is the value for the planar gas-liquid surface, and the Tolman[4] length δ_∞ is defined relative to the radius of the equimolar surface R_e as $\delta_\infty = \lim_{R_s \to \infty}(R_e - R_s)$.

There are three basic routes to the definition of the tension:[1] Thermodynamic (Gibbs and Tolman), mechanical (Laplace and Young), and statistical mechanical (density functional and related theories). The thermodynamic and mechanical routes are macroscopic theories, so there has been much debate about their applicability to small systems such as nanoscale liquid drops or bubbles. One key question is whether the mechanical relations based on the pressure virial (formulated in terms of the appropriate tensorial components) that make use of the concept of the bulk pressure of the coexisting states are appropriate at these length scales for curved surfaces.

While the Laplace equation essentially defines the ratio γ_s / R_s, the first-order form of Tolman's theory is appropriate only for sufficiently large drops. One can view δ_∞ as the leading-order correction to the tension of a planar surface. Despite its fundamental role in studies of interfacial properties of curved surfaces and theories of nucleation, there is still much controversy as to even the *sign* of δ_∞. Microscopic statistical mechanical approaches including square gradient theories (SGTs),[5,6] curvature expansions of the planar interface,[7,8] and density functional theories (DFTs), including local[9–11] and nonlocal[12–14] treatments, have led to conflicting views on the magnitude and sign of δ_∞, as well as the curvature dependence of the surface tension. The widely accepted view from this body of work is that $\delta_\infty \lesssim 0$ and that there is a small maximum in $\gamma_s(R)$ as the drop radius is decreased, then followed by a sharp decrease. This is supported by studies on the penetrable sphere model[15] (which can be solved exactly at the mean-field level at zero temperature) where one finds a negative Tolman length ($\delta_\infty = -\sigma/2$), with σ the molecular diameter.

By contrast, the vast majority of computer simulation studies suggests that $\delta_\infty > 0$. In most simulations of liquid drops, the mechanical route to the interfacial tension is employed, usually involving an integration of the gradient of the normal component of the pressure tensor from the center of the drop to the bulk vapor phase.[16–19] In this case one predicts a monotonous decrease in the surface tension with increasing curvature (decreasing drop radius) from the planar limit (infinite radius); this would correspond to $\delta_\infty > 0$ throughout. As was pointed out early on by Schofield and Henderson,[2] there are fundamental problems in employing local pressure tensors and the associated definition of the internal pressure for microscopic (high curvature) drops.

a)Author to whom correspondence should be addressed. Electronic mail: g.jackson@imperial.ac.uk.

This leads to a mismatch in the free energy of the formation of a drop determined via the mechanical and thermodynamic routes as observed in simulation.[20] Macroscopic thermodynamic routes based on a combination of the Laplace and Tolman relations have been employed[16] but also suffer from the ill-definition of the internal pressure and density of the liquid. One can estimate the interfacial tension from the free energy change accompanying a volume deformation of spherical surfaces using a virial-like expression;[21] these results for the surface tension are in disagreement with those obtained from the direct mechanical route. Recent grand canonical simulations[22] and a thermodynamic analysis of large drops based on the Laplace–Tolman relations[23] both now appear to suggest a small negative δ_∞, which is consistent with the findings of DFT.

The aim of this paper is to use a new method for the calculation of the surface tension of small liquid drops in molecular simulation, highlighting the role played by the fluctuations in the energy of deformation. The method relies on the thermodynamic definition of the surface tension and is thus free from the inconsistencies associated with the application of the mechanical route. A variant of the test-area (TA) method[24] is used where small virtual perturbations are made in the box dimensions of systems with interfaces to obtain the change in free energy associated with the corresponding change in surface area. For a fluid drop of radius R, the change in the Helmholtz free energy F is expressed thermodynamically as[1]

$$dF = -SdT - p_g dV_g + p_l dV_l + \mu dN + \gamma dA + CdR, \tag{1}$$

where S is the entropy, $V_{g,l}$ are the vapor and liquid volumes, T is the temperature, μ is the chemical potential, N is the number of particles, A is the interface area, and C is the conjugate variable for R. The surface tension of a drop is given by

$$\left(\frac{\partial F}{\partial A}\right)_{NVT} = \gamma_s, \tag{2}$$

where the minimal interfacial tension γ_s defines R_s and corresponds to taking $C=0$. The change in free energy ΔF due to a virtual change in area ΔA can be expressed as the average of the Boltzmann factor of the corresponding change in configurational energy ΔU,[24]

$$\Delta F = -kT \ln\left\langle \exp\left(-\frac{\Delta U}{kT}\right)\right\rangle \tag{3}$$

$$= \langle \Delta U\rangle - \frac{1}{2kT}\{\langle \Delta U^2\rangle - \langle \Delta U\rangle^2\} + \frac{1}{6(kT)^2}\{\langle \Delta U^3\rangle - 3\langle \Delta U^2\rangle\langle \Delta U\rangle + 2\langle \Delta U\rangle^3\}. \tag{4}$$

The averages are over configurations of the unperturbed reference system. In Eq. (4) ΔF is expressed as a perturbation series to $\mathcal{O}(\langle \Delta U^3\rangle)$, where the first-order average of the change in energy is $\Delta F_1 = \langle \Delta U\rangle$, the second-order energy fluctuation term is $\Delta F_2 = -\{\langle \Delta U^2\rangle - \langle \Delta U\rangle^2\}/(2kT)$, and the third-order contribution is denoted by ΔF_3. The full Boltzmann form, Eq. (3), is employed in, e.g., the test-particle approach for the chemical potential,[25] or the volume perturbation method for the pressure[26] and the pressure tensor.[27]

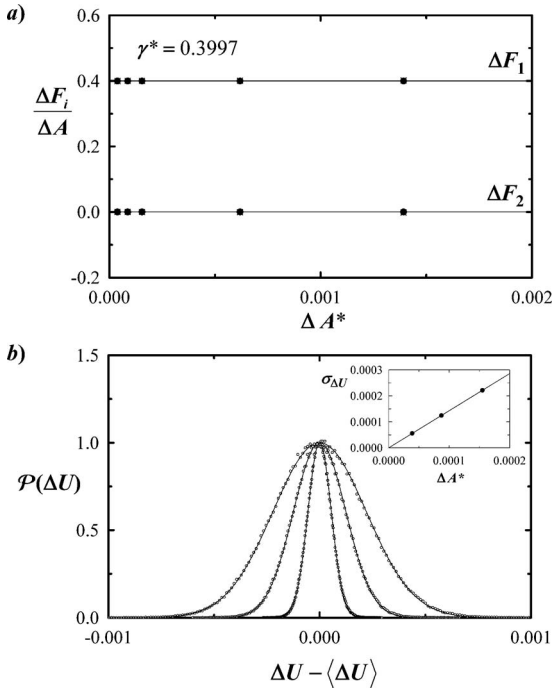

FIG. 1. TA deformations of a planar liquid-vapor interface of the LJ-TS fluid. MD simulations of $N=749$ particles in a periodic box of dimensions $L_x=L_y=7.885\sigma$ and $Lz=6L_x$ at $T^*=kT/\epsilon=0.8$ over 3×10^6 timesteps. The deformations correspond to changes in the box dimensions (particle coordinates) of $L'_x=L_x\sqrt{1+\xi}$, $L'_y=L_y\sqrt{1+\xi}$, and $L'_z=L_z/(1+\xi)$. (a) The contributions $\Delta F_1/\Delta A$ and $\Delta F_2/\Delta A$ to the change in free energy per unit area (in units of ϵ/σ^2) ($\Delta A^*<0$, +; $\Delta A^*>0$, ×; and average, ●). The interfacial tension $\gamma^*=\gamma\sigma^2/\epsilon$ is obtained by extrapolation to $\Delta A^*=\Delta A/\sigma^2=0$. (b) The distribution $\mathcal{P}(\Delta U)$ of the change in energy (relative to its average in units of ϵ) scaled at the maximum peak height for different relative deformations ΔA^*. The width (standard deviation, $\sigma_{\Delta U}$) is depicted in the inset.

The tension is obtained as the change in free energy per unit area for infinitesimal perturbations to $\mathcal{O}(\langle \Delta U^3\rangle)$,

$$\gamma = \lim_{\Delta A\to 0}\frac{\Delta F}{\Delta A} = \lim_{\Delta A\to 0}\left\{\frac{\Delta F_1}{\Delta A} + \frac{\Delta F_2}{\Delta A} + \frac{\Delta F_3}{\Delta A}\right\}. \tag{5}$$

The leading term, $\Delta F_1 = \langle \Delta U\rangle$, corresponds to the mechanical work involved in changing the area of the interface, which can be directly associated with the so-called virial expression for the tension[28] (expressed in terms of averages of the appropriate components α of the virial, $\langle x_\alpha(dU/dx_\alpha)\rangle$, at the Hookean linear-response level). The corresponding entropic contribution due to the deformation is[28] $T\Delta S = \{\langle U\rangle\langle \Delta U\rangle - \langle U\Delta U\rangle\}/(kT)$.

In the case of a planar interface, it is well known that the interfacial tension can be obtained formally from the virial expression,[1,28] i.e., entirely from the leading-order contribution of Eq. (5). This is exemplified for a planar vapor-liquid interface of Lennard-Jones (LJ) particles (of diameter σ and well depth ϵ, truncated and shifted TS at $r_c=2.5\sigma$) as shown in Fig. 1. A planar interface is first stabilized during an *NVT* molecular dynamics (MD) simulation of the inhomogeneous system with a liquid slab in the center of a box

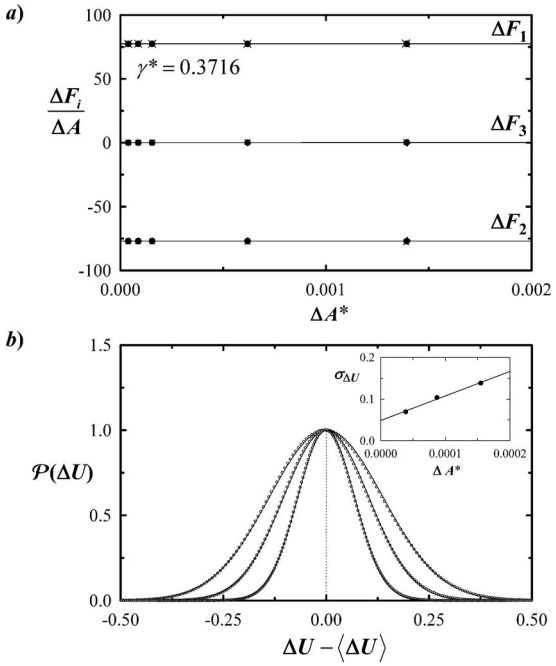

FIG. 2. TA ellipsoidal deformations of a spherical drop of LJ-TS liquid of radius $\langle R_e \rangle = 5.55\sigma$ in coexistence with its vapor. MD simulations of $N = 749$ particles in a periodic box of dimensions $L_x = L_y = L_z = 20\sigma$ at $T^* = 0.8$ over 1.5×10^9 timesteps. The deformations correspond to changes in the box dimensions (particle coordinates) of $L_i' = L_i\sqrt{1+\xi}$, $L_j' = L_j\sqrt{1+\xi}$, and $L_k' = L_k/(1+\xi)$ (where i, j, and k denote any of the Cartesian axes). (a) The contributions $\Delta F_1/\Delta A$, $\Delta F_2/\Delta A$, and $\Delta F_3/\Delta A$ to the change in free energy per unit area (in units of ϵ/σ^2) (prolate, +; oblate, ×; and average, ●). The tension $\gamma^* = \gamma\sigma^2/\epsilon$ is obtained by extrapolation to $\Delta A^* = \Delta A/\sigma^2 = 0$. (b) The distribution $\mathcal{P}(\Delta U)$ of the change in energy scaled at the maximum peak height for different relative deformations ΔA^*; the width $\sigma_{\Delta U}$ is depicted in the inset. The Gaussians for the planar interface are shown dotted (note the very small scale in comparison).

separated by two vapor regions. The change in configurational energy due to small test changes in the dimensions of the box such that the interfacial area is increased or decreased at fixed overall volume is then computed to estimate the various contributions in Eq. (5); the limit of infinitesimal deformations is obtained by extrapolation to $\Delta A \to 0$. From Fig. 1(a) it is clear that only the leading *mechanical* term $\Delta F_1/\Delta A$ contributes to the interfacial tension of a planar interface, confirming the validity of the pressure-tensor route in this case. The fluctuation term $\Delta F_2/\Delta A$ is very small by comparison and does not contribute to the tension in an appreciable way; this is also true for the third-order term. In Fig. 1(b) we plot the distribution $\mathcal{P}(\Delta U)$ of the change in configurational energy (relative to $\langle \Delta U \rangle$) for different area perturbations; the distribution is well represented by a Gaussian, the width of which ($\sigma_{\Delta U}$) decreases to zero with $\Delta A \to 0$, consistent with a very small $\Delta F_2/\Delta A \sim 1 \times 10^{-6}\epsilon/\sigma^2$.

The overall physical picture is fundamentally different for a nanosized spherical drop of liquid in contact with its vapor. Once the drop has been stabilized, its size can be characterized from the density profile $\rho(r)$ as a function of the distance r from its center by calculating the Gibbs dividing surface $R_e^3 = (\rho_v - \rho_l)^{-1} \int dr r^3 d\rho(r)/dr$, corresponding to an area of $A = 4\pi R_e^2$. Virtual perturbations from the equilibrium spherical drop geometry are made with test changes in the

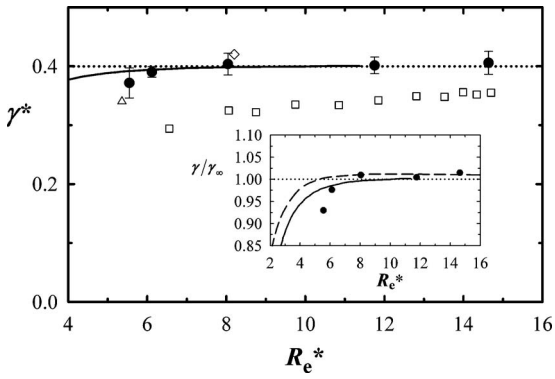

FIG. 3. The surface tension of spherical drops of LJ-TS fluids with average radii $\langle R_e/\sigma \rangle = 5.55$, 6.12, 8.04, 11.7, and 14.6 at $T^* = 0.8$ from TA ellipsoidal deformations (●), compared with the values from the mechanical route (Ref. 19) (□), and the data of Thomson *et al.* (Ref. 16) (△), El Bardouni *et al.* (Ref. 21) (◇), and Schrader *et al.* (Ref. 22) (continuous curve); the planar limit is shown dotted. The predictions of FMT (Ref. 14) are depicted in the inset (dashed curve).

dimensions of the simulation cube: Two of the Cartesian axes are decreased (or increased) in length, and the third is increased (or decreased) such that the overall volume remains constant. The perturbed states correspond to ellipsoidal drops of prolate (or oblate) shape, which always have larger surface areas than the original drop, $\Delta A > 0$. This essentially corresponds to the longest P_2 (Legendre polynomial) capillary-wave oscillations possible for the drop;[3] the capillary-wave surface tension is equivalent to the thermodynamic one at least to leading order in curvature $\mathcal{O}(1/R)$. Averages are then accumulated over very long runs of $\sim 1.5 \times 10^9$ timesteps, corresponding to microsecond runs for typical molecular parameters. The term $\Delta F_1/\Delta A$ is more than two orders of magnitude larger in the case of the drop than for the planar interface system of comparable size [cf. Figs 1(a) and 2(a)]. The most significant difference is the large contribution from the second-order energy "fluctuation" term $\Delta F_2/\Delta A$ for the drop, which was negligible for the planar interface; this term is now comparable in magnitude to, but of opposite sign than, the first-order term. The third-order terms remain essentially negligible. As a result, both the first- and second-order terms contribute to the surface tension of the drop. A thermodynamic characteristic of the drop is thus the nonvanishing (and large) fluctuation term, which is clearly an indication of an additional entropic contribution. This can be seen in the distribution of the change in configurational energy for different TA perturbations [Fig. 2(b)]. The data are again well described as Gaussians, but though the width now appears not to vanish in the limit $\Delta A \to 0$ its variance of course does, i.e., $\lim_{\Delta A \to 0} \sigma_{\Delta U}^2 = 0$ and where in this case $\lim_{\Delta A \to 0} \Delta F_2/\Delta A \neq 0$. The fact that $\lim_{\Delta A \to 0} \Delta F_3 \sim 0$ for both the planar and curved systems suggests symmetrical Gaussians.

The dependence of the surface tension computed from ellipsoidal deformations as a function of the drop size (for systems with $N = 749$ to 11 334) is depicted in Fig. 3. Here the tension is computed for R_e rather than R_s though $\gamma_e = \gamma_s$ to $\mathcal{O}(1/R^2)$. The behavior obtained with our thermodynamic TA approach does not support the findings obtained from a standard pressure-tensor route (e.g., the recent MD data of

Vrabec *et al.*[19]). This is in line with the concerns of Schofield and Henderson,[2] and others[8,20,29] about the inadequacy of the mechanical route for very small systems. For drops larger than $R_e \sim 8$ we observe values of the surface tension which appear to be slightly larger than the planar limit, $\gamma(R) > \gamma_\infty$; because the tension has to converge to γ_∞ when $R \to \infty$, this suggests a nonmonotonic behavior of the tension with increasing curvature and a corresponding weak maximum. Our values are consistent with the data point reported by El Bardouni *et al.*[21] estimated from the surface free energy change and with the small maximum observed by Schrader *et al.*[22] using a Landau free energy approach in the canonical ensemble (though the authors do not comment explicitly on this point). The calculations of the tension of curved interfaces from curvature corrections, SGT, and DFT (which have been brought into question because of their failure to reproduce existing simulation data) are now supported by our data. In the inset of Fig. 3 we compare the TA data for the surface tension of drops with those from a nonlocal DFT using fundamental measure theory (FMT) ;[14] a maximum is predicted with FMT at $R_e \sim 10$.

Three main conclusions can be gleaned from our study. First, there is clearly a large fluctuation contribution to the interfacial tension of nanoscale spherical drops (and most likely other curved surfaces) in addition to the underlying first-order (mechanical) contribution, which fully describes the planar interface. Such contributions from fluctuations in the energy are not found in the planar limit to any significant degree (at least for the conditions examined here away from the cricial region). Second, our results do not therefore support the validity of a mechanical (pressure-tensor) route to the interfacial tension for surfaces of high curvature such as small drops. This is in line with the warning of Blokhuis and Bedeaux[8] that the use of a mechanical approach in this context "is still a matter of concern" and that it is "advisable not to use the pressure-tensor whenever this can be avoided." Our data are not consistent with the monotonic dependence of the surface tension with curvature obtained from a mechanical treatment. As well as contributions in $\langle x_\alpha (dU/dx_\alpha)\rangle$, the correct "virial" expression for the surface tension would have to contain terms in averages of the type $\langle x_\alpha (dU/dx_\alpha)\rangle \times \langle x_\beta (dU/dx_\beta)\rangle$ and $\langle x_\alpha x_\beta (dU/dx_\alpha)(dU/dx_\beta)\rangle$, which would involve up to four-body correlations for pairwise additive potentials. This suggests that there are additional contributions to the change in the entropy due to the deformation of small drops involving quadratic terms in ΔU: $\langle \Delta U^2\rangle$, $\langle \Delta U\rangle^2$, $\langle U\Delta U^2\rangle$, $\langle \Delta U\rangle\langle U\Delta U\rangle$, $\langle U\rangle\langle \Delta U^2\rangle$, and $\langle U\rangle\langle \Delta U\rangle^2$. As a final point, the rise in the surface tension above that of the planar limit after a certain drop size would be consistent with a negative Tolman length. Our data for the larger drops suggest a value of $\delta_\infty/\sigma \sim -0.2 \pm 0.3$. Though the statistical uncertainty is large, our finding supports the exact mean-field predictions for the penetrable sphere model[15] and is consistent with the latest accurate value of -0.10 ± 0.02 determined from the Laplace relation for a large $N = 100\,000$ particle system.[23]

We are very appreciative to Jim Henderson for useful discussions. J.G.S. acknowledges financial support from the CONACYT of Mexico for a Ph.D studentship, A.M. from the GACR (Grant No. IAA200760905) and GAAS (Grant No. IAA400720710) of the Czech Republic, and E.d.M. from the DGI (Grant No. FIS2007–66079–C02–02) and the Junta de Andalucia (Grant No. P07–FQM02884) of Spain. We also acknowledge funding from the EPSRC of the United Kingdom (Grant No. EP/E016340).

[1] J. S. Rowlinson and B. Widom, *Molecular Theory of Capillarity* (Oxford University Press, Oxford, 1982).
[2] P. Schofield and J. R. Henderson, Proc. R. Soc. London **A379**, 231 (1982).
[3] J. R. Henderson, in *Fluid Interfacial Phenomena*, edited by C. A. Croxton (Wiley, New York, 1986).
[4] R. C. Tolman, J. Chem. Phys. **17**, 333 (1949).
[5] A. H. Falls, L. E. Scriven, and H. T. Davis, J. Chem. Phys. **75**, 3986 (1981).
[6] R. Guermeur, F. Biquard, and C. Jacolin, J. Chem. Phys. **82**, 2040 (1985).
[7] E. M. Blokhuis and D. Bedeaux, Physica A **184**, 42 (1992).
[8] E. M. Blokhuis and D. Bedeaux, J. Chem. Phys. **97**, 3576 (1992).
[9] D. J. Lee, M. M. Telo da Gama, and K. E. Gubbins, J. Chem. Phys. **85**, 490 (1986).
[10] D. W. Oxtoby and R. Evans, J. Chem. Phys. **89**, 7521 (1988).
[11] K. Koga, X. C. Zeng, and A. K. Shchekin, J. Chem. Phys. **109**, 4063 (1998).
[12] T. V. Bykov and X. C. Zeng, J. Chem. Phys. **117**, 1851 (2002).
[13] Z. Li and J. Wu, Ind. Eng. Chem. Res. **47**, 4988 (2008).
[14] A. Malijevský and G. Jackson (unpublished).
[15] S. J. Hemingway, J. R. Henderson, and J. S. Rowlinson, Faraday Symp. Chem. Soc. **16**, 33 (1981).
[16] S. M. Thompson, K. E. Gubbins, J. P. R. B. Walton, R. A. R. Chantry, and J. S. Rowlinson, J. Chem. Phys. **81**, 530 (1984).
[17] M. J. P. Nijmeijer, C. Bruin, A. B. van Woerkom, A. F. Bakker, and J. M. J. van Leeuwen, J. Chem. Phys. **96**, 565 (1992).
[18] Y. A. Lei, T. Bykov, S. Yoo, and X. C. Zeng, J. Am. Chem. Soc. **127**, 15346 (2005).
[19] J. Vrabec, G. K. Kedia, G. Fuchs, and H. Hasse, Mol. Phys. **104**, 1509 (2006).
[20] P. R. ten Wolde and D. Frenkel, J. Chem. Phys. **109**, 9901 (1998).
[21] H. El Bardouni, M. Mareschal, R. Lovett, and M. Baus, J. Chem. Phys. **113**, 9804 (2000).
[22] M. Schrader, P. Virnau, and K. Binder, Phys. Rev. E **79**, 061104 (2009).
[23] A. E. van Giessen and E. M. Blokhuis, J. Chem. Phys. **131**, 164705 (2009).
[24] G. J. Gloor, G. Jackson, F. J. Blas, and E. de Miguel, J. Chem. Phys. **123**, 134703 (2005).
[25] B. Widom, J. Chem. Phys. **39**, 2808 (1963).
[26] R. Eppenga and D. Frenkel, Mol. Phys. **52**, 1303 (1984).
[27] E. de Miguel and G. Jackson, J. Chem. Phys. **125**, 164109 (2006).
[28] J. Lekner and J. R. Henderson, Mol. Phys. **34**, 333 (1977).
[29] H. Reiss and D. Reguera, J. Phys. Chem. B **108**, 6555 (2004).

Paper III

IOP PUBLISHING JOURNAL OF PHYSICS: CONDENSED MATTER

J. Phys.: Condens. Matter **24** (2012) 464121 (28pp) doi:10.1088/0953-8984/24/46/464121

TOPICAL REVIEW

A perspective on the interfacial properties of nanoscopic liquid drops

Alexandr Malijevský[1,2] **and George Jackson**[3]

[1] E Hála Laboratory of Thermodynamics, Institute of Chemical Process Fundamentals of the ASCR, 16502 Prague 6, Czech Republic
[2] Department of Physical Chemistry, Institute of Chemical Technology, Prague, 166 28 Prague 6, Czech Republic
[3] Department of Chemical Engineering, Imperial College London, South Kensington Campus, London SW7 2AZ, UK

E-mail: a.malijevsky@imperial.ac.uk

Received 2 April 2012, in final form 2 July 2012
Published 31 October 2012
Online at stacks.iop.org/JPhysCM/24/464121

Abstract

The structural and interfacial properties of nanoscopic liquid drops are assessed by means of mechanical, thermodynamical, and statistical mechanical approaches that are discussed in detail, including original developments at both the macroscopic level and the microscopic level of density functional theory (DFT). With a novel analysis we show that a purely macroscopic (static) mechanical treatment can lead to a qualitatively reasonable description of the surface tension and the Tolman length of a liquid drop; the latter parameter, which characterizes the curvature dependence of the tension, is found to be negative and has a magnitude of about a half of the molecular dimension. A mechanical slant cannot, however, be considered satisfactory for small finite-size systems where fluctuation effects are significant. From the opposite perspective, a curvature expansion of the macroscopic thermodynamic properties (density and chemical potential) is then used to demonstrate that a purely thermodynamic approach of this type cannot in itself correctly account for the curvature correction of the surface tension of liquid drops. We emphasize that any approach, e.g., classical nucleation theory, which is based on a purely macroscopic viewpoint, does not lead to a reliable representation when the radius of the drop becomes microscopic. The description of the enhanced inhomogeneity exhibited by small drops (particularly in the dense interior) necessitates a treatment at the molecular level to account for finite-size and surface effects correctly. The so-called mechanical route, which corresponds to a molecular-level extension of the macroscopic theory of elasticity and is particularly popular in molecular dynamics simulation, also appears to be unreliable due to the inherent ambiguity in the definition of the microscopic pressure tensor, an observation which has been known for decades but is frequently ignored. The union of the theory of capillarity (developed in the nineteenth century by Gibbs and then promoted by Tolman) with a microscopic DFT treatment allows for a direct and unambiguous description of the interfacial properties of drops of arbitrary size; DFT provides all of the bulk and surface characteristics of the system that are required to uniquely define its thermodynamic properties. In this vein, we propose a non-local mean-field DFT for Lennard-Jones (LJ) fluids to examine drops of varying size. A comparison of the predictions of our DFT with recent simulation data based on a second-order fluctuation analysis (Sampayo *et al* 2010 *J. Chem. Phys.* **132** 141101) reveals the consistency of the two treatments. This observation highlights the significance of fluctuation effects in small drops, which give rise to additional entropic (thermal non-mechanical) contributions, in contrast to what one observes in the case of planar interfaces which are governed by the laws of mechanical equilibrium. A small negative Tolman length (which is found to be about a tenth of the molecular diameter) and a non-monotonic behaviour of the surface tension with the drop radius are predicted for the LJ fluid. Finally, the limits of the validity of the Tolman approach, the effect of the range of the intermolecular potential, and the behaviour of bubbles are briefly discussed.

(Some figures may appear in colour only in the online journal)

Contents

1. Introduction

The study of inhomogeneous systems presents a much more significant challenge than that of homogeneous fluids. By definition the non-uniformity of the number density throughout the sample adds a mathematical complexity to the theoretical description—the correlation functions become multivariable functions and, within a variational formalism, the thermophysical functions become functionals of the single-particle density, so that the partial derivatives relating the equilibrium properties with a particle density must be replaced with the corresponding variational expressions. At the level of a formal physical description, a more fundamental issue arises: the thermodynamic quantities that are familiar in studies of uniform fluids cannot always be defined uniquely in the inhomogeneous region. The interface between vapour and liquid phases or two liquid phases are ubiquitous examples of non-uniform systems. The study of two bulk phases separated by a planar interface (and stabilized by an arbitrary weak external field) does not present a particular problem, since the non-uniqueness in the definition of the local variables (such as the pressure tensor or the position of the interface) does not give rise to an ambiguity in the measurable quantities (such as the surface tension). The situation is not, however, as straightforward for systems exhibiting spherical symmetry, such as small liquid drops (liquid surrounded by vapour) or gas bubbles (vapour surrounded by liquid), and our goal in this paper is to provide a critical discussion of the most popular methodologies for treating the interfacial properties of such systems.

There are three general routes to the determination of interfacial properties of small fluid droplets or bubbles: these involve the choice of a mechanical, a thermodynamical, or a statistical mechanical description. The first successful mechanical description dates back to the beginning of nineteenth century, when Young [1] and Laplace [2] derived a relationship for the difference in pressure p between a phase α on one side of a curved interface and the surrounding phase β. For a macroscopic system their simple relation can be expressed as

$$p_\alpha - p_\beta = \frac{2\gamma}{R}, \tag{1}$$

where γ is the surface tension playing the role of the restoring force acting against changes in the area of the interface, and R is the radius of the drop or bubble; though Young's paper predates Laplace's more thorough derivation by a few months, the expression is more commonly referred to as the Laplace equation probably because Young only describes the dependence of curvature in words and not as an explicit formula [3]. Both derivations rely on macroscopic definitions of the quantities p_α, p_β, and R which are all considered to be uniquely defined. In particular, one assumes that both phases behave in the same way as the corresponding bulk phase. However, when one considers smaller and smaller drops, the surface contributions propagate progressively into the interior of the drop so that the density profile becomes highly structured (as we will show later in our paper), and the concepts of the 'bulk' density of the liquid, the scalar pressure, and the radius of the drop lose their unique characteristics; for an in-depth review of the problematic issues associated with spherical surfaces see the excellent account by Henderson [4].

A natural extension of the concept of the scalar pressure to non-uniform systems is the introduction of a second-rank tensor $\mathbf{P}(\mathbf{r})$, a local quantity related to the force between the interacting molecules at a point $\mathbf{r}$. In the absence of external fields, the sum of all forces $\mathbf{P}(\mathbf{r}) \cdot \hat{n}\, \mathrm{d}A$ acting on the infinitesimal area $\mathrm{d}A$, where $\hat{n}$ is the unit vector normal to the particular element of area, must balance:

$$\int_A \mathbf{P}(\mathbf{r}) \cdot \hat{n}\, \mathrm{d}A = 0. \tag{2}$$

As is customary, Gauss's divergence theorem can be employed to re-express the surface integral as one in the divergence of the pressure tensor over the entire volume V. The resulting equilibrium condition must apply to each infinitesimal element so that a microscopic mechanical treatment then relies on the simple condition of mechanical equilibrium at every point in the system [3]:

$$\nabla \cdot \mathbf{P}(\mathbf{r}) = 0. \tag{3}$$

It is clear, however, that equation (3) cannot be used to define the pressure tensor uniquely because any tensor $P'(\mathbf{r})$ which differs from $P(\mathbf{r})$ by a curl still satisfies the equilibrium condition (3). Even though the surface tension, which for a planar interface can be obtained from the pressure tensor as

$$\gamma = \int [P_\mathrm{n}(z) - P_\mathrm{t}(z)]\, \mathrm{d}z, \tag{4}$$

where $P_\mathrm{n}(z) = p_\mathrm{bulk}$ and $P_\mathrm{t}(z)$ are the normal and tangential components of $\mathbf{P}(\mathbf{r})$ relative to the interface, is invariant to the particular form chosen for the local pressure tensor, the first moment of the difference between the two components,

$$\gamma z_\mathrm{s} = \int z[P_\mathrm{n}(z) - P_\mathrm{t}(z)]\, \mathrm{d}z, \tag{5}$$

is not [3, 5, 6]. The latter defines the so-called surface of tension z_s, i.e., the surface at which the surface tension is deemed to act; the surface of tension plays a crucial role in the determination of the curvature dependence of the surface tension, as will be discussed in the subsequent discussion.

The first thermodynamic expression relating bulk thermodynamic properties to those associated with a liquid drop (at the same temperature T) is the familiar Kelvin equation [7]

$$\ln \frac{p_v(R)}{p_v^{sat}} = \frac{2\gamma_\infty}{\rho_l k_B T R}, \tag{6}$$

where $p_v(R)$ is the vapour pressure of a drop of radius R, p_v^{sat} is the saturation pressure, γ_∞ is the surface tension associated with the planar interface, ρ_l is the number density of the liquid, and k_B is the Boltzmann constant. The thermodynamic route to spherical interfaces was developed by Gibbs [8–10] and Tolman [11–13] (with further developments by Buff [6], Koenig [14], Hill [15], and Kondo [16] amongst others). According to Gibbs [8], the curvature corrections become essential only for very small droplets, with the conjecture that the surface tension decreases monotonically on decreasing the radius of the droplet. From another perspective the Thomsons (father and son) [17] suggested that one should allow for the possibility of a non-monotonic behaviour (actually a minimum in the surface tension with decreasing radius followed by one or more maxima), while Bakker [18] insisted on the invariance of the surface tension of the droplet with its radius. Tolman [13], who can be considered as one of the main proponents of the Gibbsian view, put forward a rigorous theory for the dependence of the surface tension on the radius of the drop based purely on thermodynamic arguments (essentially assuming that high-frequency, short-wavelength, capillary-wave terms and elastic deformations from spherical geometry are negligible, as one would expect at the level of leading order in curvature [4]):

$$\gamma(R) = \gamma_\infty \left(\frac{1}{1 + 2\delta/R} \right). \tag{7}$$

Here, $\gamma(R)$ is the surface tension of the droplet of arbitrary radius R, and $\delta = R_e - R_s$ is the difference in the distance between the surface of tension R_s (where the tension acquires its minimum) and the Gibbs equimolar dividing surface R_e (where the excess superficial density of particles effectively vanishes); the so-called Tolman length corresponds to the value of $\delta(R)$ in the limit of the planar interface $\delta = \lim_{R\to\infty}\delta(R) = z_e - z_s$, with the appropriate distances from the interfacial plane now represented by z_e and z_s. According to the Gibbs–Tolman view of a decrease in the surface tension with decreasing radius, the Tolman length would thus be a positive quantity, $\delta > 0$. It is important to realize that while for planar interfaces the choice of dividing surface is arbitrary, it is a 'necessity, not merely a convenience' for systems with curved interfaces [3]. Owing to the phenomenological origin of thermodynamic approaches of this type, the description is expected to become increasingly inappropriate when one attempts to represent smaller and smaller droplets, as was pointed out early on by Farkas [19], by Guggenheim [20], and by Tolman himself [13]. Though Tolman also incorporated higher-order terms in the radius dependence of the tension, it is questionable to what extent these are meaningful (or even physically relevant) for very small droplets; this is because, to higher order in curvature, the value of the surface tension becomes dependent on the choice of the dividing surface [3, 4]. Before proceeding we should, however, acknowledge that the description of curvature deformations for non-spherical geometries beyond a first-order correction are in common use, particularly in treating complex fluids with low tensions such as surfactant aggregates and membranes (e.g., see [21–24]); this introduces additional complications which are beyond the scope of our paper.

Apart from the aforementioned issues with a mechanical or thermodynamical treatment of curved interfaces, neither of the approaches provide us with a direct link between the microscopic (intermolecular interactions and local structure) and macroscopic (thermodynamic) properties of the fluid. This is possible with a full statistical mechanical description of the non-uniform fluid. Classical density functional theory (DFT) provides one with a very powerful tool for the description of inhomogeneous systems [25–27]. In a purely mechanical or thermodynamical approach one manipulates local many-body quantities such as the force, local energy, local pressure etc to describe the interfacial properties, but these can often be ill-defined as there is no unique way of assigning contributions from the intermolecular forces to a particular element of space [28]. By contrast, in a DFT treatment the full partition function (and therefore thermodynamic potential) of the system is formulated explicitly in a spatially dependent form in terms of the singlet density, which is a well-defined one-body function, allowing for a unique description of the thermodynamic properties. Such an approach is, however, still not entirely straightforward for inhomogeneous systems characterized by curved interfaces [4, 29], and care has to be taken with the precise route that one employs to compute the interfacial properties. In its original form, the DFT is formulated in the grand canonical ensemble in which an isolated finite-size drop of liquid is unstable with respect to its vapour. This leads one to an inevitable key question: How does one stabilize a drop of fluid of finite size? Assuming that a stabilized drop can then be examined to determine the equilibrium density profile by minimizing the appropriate functional, one then has to establish a unique and consistent methodology for the desired thermodynamic and interfacial quantities from a knowledge of structure of the fluid.

The system of an isolated drop of liquid surrounded by its vapour (or the inverse case of an isolated bubble of vapour in a liquid) is ubiquitous and has been studied extensively by experiment, theory and molecular simulation since the early description of Young and Laplace. Experimental evidence of the effect of the system's size and the curvature on the surface tension is scarce, as the variation from the macroscopic (planar) value is directly measurable for only very small dimensions. Early indications of curvature effects were obtained by Reinold and Rücher [30] from experiments on thin films of soap solutions, the thickness of which can

be estimated from the colour: the surface tension was found to be constant down to a thickness of ∼50 nm, followed first by a decrease with decreasing thickness and then by an inferred increase. Though this led to the Thomson view of the possibility of a non-monotonic behaviour for the tension [17], such an analysis should be made with particular care owing to the inherent difference between aqueous solutions of amphiphilic compounds (surfactants which will accumulate at the interface to differing degrees, and lead to a decrease in tension) and fluid drops of pure substances. At the turn of the twentieth century, Weber [31] also detected evidence of size effects on interfacial properties in his experiments of the contact angle in oil–water systems, though again the findings are difficult to interpret in such mixtures. In the more recent analyses of experimental data for the effect of curvature in fluid systems, the Tolman relation is often employed at leading order in curvature, together with the measured vapour and liquid densities and the surface adsorption, to estimate the surface tension: for example, in the case of a drop of water the surface tension is found to remain essentially constant (within a few per cent) for radii down to ∼10 nm, and to decrease rapidly thereafter [32]. However, as has already been emphasized, for small drops one is at the limit of the applicability of macroscopic thermodynamic approaches, and any tautological conclusions of this kind should be viewed with some scepticism. This having been said, a macroscopic treatment continues to be employed without reservation to this day, e.g., see the work of Xue *et al* [33]. The surface force apparatus was used early in its development by its pioneers to provide a direct measure of the interfacial forces of curved surfaces at the microscopic level: Fisher and Israelachvili [34–36] investigated the limit of validity of the Laplace and Tolman relations (using the corresponding Kelvin macroscopic thermodynamic description of the vapour pressure of curved interfaces) for a meniscus of hydrocarbon fluid between mica spheres/cylinders; notwithstanding some complications due to impurities, the Kelvin relation is found to be valid for menisci with radii down to ∼4 nm (corresponding to about 10 diameters of typical small molecules), with a marginal possible improvement in the description of the data for a Tolman-like leading-order dependence of the tension with curvature. We should note however that the analysis of Fisher and Israelachvili at very high curvature (small radii) was brought into question in a later study by Christenson [37], and the effect has now been found to be very sensitive to differences in the structure and polarity of the molecules [38]. A more recent lattice-gas Monte Carlo study of the atomic force microscope experiment has also indicated that there is a lower limit in the size of the system (corresponding to radii of about 2 nm) below which it is no longer possible to stabilize a meniscus of fluid [39]. Our overall understanding is not helped by the analysis of data for the deformation of fluid interfaces obtained from small angle x-ray and neutron scattering experiments, which for the vapour–liquid interface of water and organic molecules [40, 41] is consistent with a negative Tolman length, $\delta < 0$, while in the case of surfactant monolayers [42, 43] the data supports the original Gibbs–Tolman picture with $\delta > 0$; care should again be taken with the analysis for the more complex systems comprising amphiphilic compounds.

The body of work on molecular simulation of vapour–liquid drops and bubbles, though extensive, is understandably not as sizeable as that for its planar counterpart (see [44] for a recent review of the latter). In one of the first continuum studies of liquid drops carried out a few years before the better known work of Binder and co-workers [45, 46] with lattice-gas models, Rusanov and Brodskaya [47] examined drops of truncated Lennard-Jones (LJ) particles inside a spherical hard cavity by molecular dynamics (MD) simulation, calculating the pressure tensor of the system. Rusanov and Brodskaya showed that one cannot obtain a uniform value of the tensorial components of the pressure in the centre of small drops (bringing into question the validity of the macroscopic mechanical definition, though admittedly the uncertainty in the computed values is large), and instead calculated the tension from the Laplace relation with the pressure of the liquid interior obtained in a thermodynamically consistent way from a bulk system with an equivalent chemical potential. In agreement with the Gibbs–Tolman view, the tension was found to decrease with decreasing drop radius. Powles *et al* [48, 49] also simulated drops of LJ fluid (essentially for the full range of the pair interaction) in coexistence with its vapour using standard periodic boundary conditions and determined the tension and Tolman length from the Kelvin thermodynamic relation. In their well cited paper, Thompson *et al* [50] reported values of the surface tension of shifted and truncated LJ drops within soft-wall cavities and with dynamic walls (tied to the centre-of-mass of the drop) obtained by MD simulation from both mechanical (pressure-tensor) and thermodynamic (Tolman and Laplace) routes; Thompson *et al* recognized the problems associated with the use of such approaches to determine the surface tension for small drops, and highlighted the inadequacy of the Laplace and Kelvin relations for drop radii smaller than about 10 molecular diameters. These early simulation studies all appear to confirm the Gibbs–Tolman view of a decrease in the surface tension with decreasing drop size, corresponding to a positive value of the Tolman length, $\delta > 0$; one should stress, however, that only relatively small systems were examined, and the Tolman length is certainly expected to depend on the system size and on the range of the interactions (as we show later in our paper).

There have since been a number of computer simulation studies of liquid drops [51–79] and bubbles [80–89]; here we refer to some of the representative work where new findings relevant to our current study are reported, making no attempt to provide a full review of all the literature on curved interfaces of mixtures, nucleation, cavitation, and other non-equilibrium processes. In one of the first large-scale simulation studies, Nijmeijer *et al* [52] showed that due to statistical scatter there is a large uncertainty in the sign of the Tolman length; the main finding being that its value is close to zero, a conclusion supported by one of the latest simulation studies [79]. The small absolute value of the Tolman length is generally supported by the more recent simulation data (e.g., [53, 55, 62, 78]) for drops of up to $\sim 8 \times 10^5$ LJ

particles, corresponding to radii of almost 100 diameters [62]. It is also apparent that the fluid drops experience marked fluctuations in shape and size, particularly in the case of large systems, as has been shown by Arcidiacono *et al* [61] and Salonen *et al* [64]. With a thermodynamic approach based on a linear response of the free energy to small volume perturbations, El Bardouni *et al* [55] reported some values of the tension for spherical and cylindrical surfaces that are larger than the planar limit (corresponding to $\delta < 0$), though the uncertainty is such that they concluded that the tension is essentially curvature independent. This is not the case in the studies carried out by Vrabec *et al* [63], who used the conventional mechanical (pressure-tensor route) and found that the surface tension decreased sharply and monotonically with decreasing drop radius ($\delta > 0$). In related studies of nucleation in fluids, ten Wolde and Frenkel [54] and Neimark and Vishnyakov [67] have shown that erroneous nucleation barriers result from the use of pressure tensors (mechanical route), and that the Tolman equation is not valid for clusters with radii below four molecular diameters [67]. More recently, Binder and co-workers [68, 69, 73, 76, 78] have employed a thermodynamic analysis with a Landau free energy and grand canonical Monte Carlo approach to determine the surface free energy and interfacial tension for drops of varying size, finding that the curvature corrections cannot be described with the simple Tolman relation for small drops. These authors also find that the interfacial tension increases above that of the planar interface, albeit very marginally, for drops with radii larger than about 8 molecular diameters, which points to a small and negative Tolman length. Though this finding is in contradiction with the large body of work based on a purely mechanical analysis of the simulation data, it is consistent with the earlier study of El Bardouni *et al* [55], with a thorough analysis based on the Laplace relation for very large drops [71], and with the use of test-area deformations [72]. We shall return to this interesting feature later in our discussion.

In the case of bubbles within a fluid, Park *et al* [82] have used the mechanical expression for the normal and tangential components of the pressure tensor and the Laplace relation to estimate the tension and Tolman length of LJ particles; they find that though the tension of the bubble is now greater than that of the planar interface, the Tolman expression for the first-order curvature correction does not quantitatively reproduce the calculated surface tension of the bubble, possibly due to an inconsistency in the calculation of the Tolman length. By contrast, in their recent study of very small LJ bubbles, Matsumoto and Tanaka [85] determined the vapour pressure with an empirical equation of state (rather than via the pressure-tensor route), finding that the surface tension is independent of the radius of the bubble (which corresponds to $\delta = 0$), and confirming the validity of the Laplace relation for radii down to $\sim$1.7 nm (in terms of the LJ parameters for argon). However, the latest estimates of the Tolman length for bubbles by Block *et al* [73] now suggest a small negative Tolman length (corresponding to about a tenth of the molecular diameter) as in the case of liquid drops.

In view of the disparate findings reported in the various simulation studies of fluid drops and bubbles it would not be unfair to say that there is still no clear consensus regarding the curvature dependence of the surface tension and the sign of the Tolman length. Different (essentially macroscopic) routes are employed to analyse the data for the interfacial properties, the validity of which are in question for small systems. To add to the confusion, the treatment of the range of the intermolecular potential (long-ranged, versus truncated or truncated and shifted potentials) has been the bane of the calculation of the surface tension for planar interfaces (particularly in approaches employing a mechanical route because of the discontinuous nature of the forces), leading to general conclusions which are in apparent conflict; see the paper by Trokhymchuk and Alejandre [90] and references therein. The contradictory findings for curved interfaces are most certainly also compounded by the treatment of the range of the potential, as Lei *et al* [62] have demonstrated for large liquid drops, reiterating the fact that the surface tension and Tolman length are very sensitive to the value of the intermolecular potential cutoff that is employed.

The full armoury of phenomenological thermodynamic approaches and the more sophisticated statistical mechanical theories have been employed to describe the interfacial properties of systems with curved interfaces, including mean-field, square-gradient (generalized van der Waals), capillary-wave, density functional, and fundamental measure theories [91–160]. In the following discussion we will again not focus on studies of nucleation or criticality, which represent entire fields in themselves. The general conclusions that can be drawn from the theoretical studies are as inconclusive as those gleaned from direct molecular simulation. As we have already mentioned, using his macroscopic thermodynamic approach, Tolman [13] found a monotonically decreasing surface tension with decreasing drop radius, corresponding to $\delta > 0$, which was of the order of 0.1 nm; if one extends the concept of the Tolman length to a function $\delta(R) = R_e - R_s$ of the drop radius then a non-monotonic dependence of the surface tension with the radius can be obtained [150].

Hemingway *et al* [108] have compared thermodynamic, mechanical, and statistical mechanical routes for the vapour–liquid surface tension and Tolman length of the penetrable-sphere model. This provides evidence of the consistency between the thermodynamic and statistical mechanical routes (though it cannot be considered as a proof), while in the case of a mechanical treatment the value of the Tolman length depends on the choice of local pressure tensor (as demonstrated by Schofield and Henderson [5] and later by Blokhuis and Bedeaux [125]). One can formulate a form of the local pressure tensor that gives a unique expression for the surface of tension in the case of systems with spherical symmetry, as shown by Baus and Lovett [120, 124, 126], but the expressions are much more complicated and there are issues in their implementation to liquid drops [124, 128]. Sampayo *et al* [72] have also shown that a virial relation only corresponds to the leading-order term in the free-energy change due to the deformation of small drops, and that there are additional contributions from the second-order (fluctuation) term with a magnitude which is comparable to

the first-order contribution. Lekner and Henderson [104] have demonstrated that the first-order contribution to the change in free energy accompanying a change in the interfacial area captures the entire mechanical contribution that one would obtain for the difference in the appropriate components of the pressure tensor (cf the Irving–Kirkwood [94] expression in the case of a planar interface). It is therefore clear that first-order mechanical routes which rely on pressure tensors are to be avoided for small drops as they do not incorporate the large contributions due to thermal fluctuations. The main advantage of the penetrable-sphere model is that it can be solved exactly at the mean-field level at zero temperature where Hemingway *et al* [108] find a negative Tolman length, $\delta = -\sigma/2$, with σ the molecular diameter. It is not clear that the relation will still hold at higher temperatures; the main problem with such an approach is the lack of knowledge of a good approximation for the direct correlation function for generic fluid models [108].

The square-gradient theory (SGT), which belongs to a class of more general density functional theories [25], is rooted in van der Waals' [92] original treatment for fluid interfaces (and in the earlier work by Rayleigh [91]), which was rediscovered and popularized by Cahn and Hilliard [99]. Before we discuss the findings of microscopic SGT approaches, we should briefly mention the related phenomenological treatment referred to as capillary-wave theory. As Henderson [4] has pointed out, an analogy with hydrodynamics can be made to examine the surface tension of a fluid as the restoring force due to thermally excited surface waves; frequent use of a capillary-wave description has be made to describe planar interfaces [100, 102, 103] and to represent liquid drops [5, 108]. The bare capillary-wave surface tension corresponds to the equilibrium (infinite wavelength contribution) thermodynamic surface tension in the case of a planar interface and also to that of a spherical interface at the level of leading order in curvature [4, 121]. This means that the surface tension of the system is required as an input if one wants to employ capillary-wave approaches to describe interfacial systems. One of the first to use SGT to examine curved interfaces and liquid drops were Falls *et al* [107]: they approximated the so-called influence parameter by using the low-density limit of the direct correlation function (as the Mayer function of the pair potential) to get the density profile for the drop, and calculated the surface tension from the Irving–Kirkwood [94] pressure-tensor expression; a monotonic decrease of the surface tension with decreasing drop radius was predicted (corresponding to $\delta > 0$ throughout), as obtained by Tolman [13] thirty years earlier. The same was found by Hooper and Nordholm [113] with a similar generalized van der Waals approach. Guermeur *et al* [115] also employed SGT in a similar way to Falls *et al* [107], but using a density-dependent influence parameter, and computed the surface tension from an extended Laplace expression: by contrast, these authors found a non-monotonic dependence of the surface tension, which increases from below the value of the planar interface as the drop radius is increased, becomes larger than the planar value and exhibits a maximum at about 10 molecular diameters, then decaying slowly to the planar limit, corresponding to a small positive δ_∞. The same overall behaviour as that observed by Guermeur *et al* [115] has now been found in more recent studies with variants of the SGT approach (e.g., see Refs. [130, 132, 138, 141]).

Further controversy has surrounded attempts to include higher-order curvature corrections in the expansion of the surface tension, i.e., to add terms beyond the first-order Tolman correction. Strictly speaking, Tolman's original expression [13],

$$\log\left[\gamma(R)/\gamma_\infty\right] = \int_\infty^R \frac{2\delta/r^2\left[1+\delta/r+1/3(\delta/r)^2\right]}{1+2\delta/r\left[1+\delta/r+1/3(\delta/r)^2\right]}\,\mathrm{d}r, \tag{8}$$

does involve higher-order contributions, which after neglecting the terms $\mathcal{O}(\delta/r)$, and treating δ as a constant, leads to the compact relation (7). Tolman himself did not put a firm reliance on his expression when considering very small droplets. He questioned two assumptions leading to his final expression: firstly, that δ in equation (8) is a constant for any drop radius; and secondly, the anticipation of a bulk liquid behaviour in the centre of the drop. Interestingly, Tolman suggested that the thermodynamic concepts should be replaced by 'a more detailed molecular mechanics' treatment for very small droplets.

When generalizing the description to highly curved interfaces it is tempting to extend Tolman's theory to higher order with a formal expansion of the surface tension in powers of curvature. Helfrich [21] introduced such an expansion for the surface tension of general curved surfaces to second order in the curvature, which for a spherical interface can be expressed as

$$\gamma(R) = \gamma_\infty + 2\kappa C_0\frac{1}{R} + (2\kappa + 2\overline{\kappa})\frac{1}{R^2}, \tag{9}$$

where C_0 is the so-called spontaneous curvature, κ is the rigidity constant of bending, and $\overline{\kappa}$ is the rigidity constant associated with the Gaussian curvature (which is $1/R^2$ in the case of a sphere) characterizing the energy penalty for topological changes of the surface. The original expansion of Helfrich [21] is a general form of a second-order surface free energy and its derivation was motivated by the ultimate goal of describing the elasticity of lipid bilayers that make up cell membranes. It is wildly recognized as the basic formalism for the description of the mechanical behaviour of biomembranes and liquid crystalline phases. Clearly, by including the second-order term in the Helfrich expansion one takes the step from pure thermodynamics (Tolman's approach) to the theory of elasticity: while in the Gibbs–Tolman concept γ is viewed as an excess (over the respective bulk phases) interfacial free energy per unit area, it is the force acting against the distortion of the surface in the phenomenological Helfrich approach.

Fisher and Wortis [111] have used a curvature expansion of the density and chemical potential with a Landau free energy (of square-gradient form) to examine the Tolman length. Using an Ising-like model they showed that $\delta = 0$ is a general result for models characterized by a symmetrical order parameter (density) profile, a conclusion also arrived at by Rowlinson [128]. In the more general case of an asymmetric

fluid treated at the van der Waals level $\delta \sim -0.02\sigma$, which complements the exact results for the penetrable-sphere model (for which Hemingway *et al* [108] found the exact result $\delta = -\sigma/2$ in the zero-temperature limit) as the Landau approach is a mean-field theory applicable in the vicinity of the critical point. For another typical application of the Helfrich curvature expansion within a density functional theory the reader is directed to work of Romero-Rochin *et al* [122].

Blokhuis and co-workers [127, 137, 149] have examined the thermodynamic properties of curved interfaces with curvature expansions of the free energy in a series of enlightening papers. Making use of the Helfrich curvature expansion, van Giessen *et al* [137] found negative Tolman lengths for liquid drops at all temperatures, and demonstrated that the sign of the Tolman length is very sensitive to the details of the free energy. A negative value of the Tolman length has also been predicted on the basis of purely thermodynamic expansions by Bartell [142] and by Blokhuis and Kuipers [149], proposing a simple relation between the Tolman length and the isothermal compressibility κ_1 of the liquid at two-phase coexistence, $\delta \approx -\kappa_1\gamma$.

Controversies associated with the use of curvature expansions, and in particular the relevance of the second-order correction to the surface tension, follow from the fact that the second-order term is proportional to the area of the interface and does not therefore contribute to the overall free energy, i.e., it just leads to a shift of the thermodynamic potential and cannot thus play any role in the restoring force acting against the surface distortion. There is also evidence of a non-analyticity in the curvature expansion of the free energy [4, 101, 128, 135, 144, 145, 155, 156], which suggests that the expansion of the surface tension in R^{-1} is generally inappropriate beyond the leading-order term. Studies of fluids in contact with hard spherical substrates lead to the conclusion that there is a non-analytical contribution of the $\ln R$ form [135, 144, 145, 156]; though such a system is clearly not the same as a free liquid drop one may expect a curvature dependence of this type for particles with long-ranged interactions, particularly in the vicinity of the critical point, but this would be very difficult to identify in practice.

It was recognized early on that the most promising route to understanding the intricacies of curved surfaces, and liquid drops in particular, would involve a rigorous microscopic statistical mechanical treatment. Classical density functional theory has amply proved to be a powerful tool for the description of the interfacial properties of fluids [25], and is therefore a particularly appropriate approach. One of the first applications of DFT for liquid drops was by Lee *et al* [116] who employed a mean-field perturbation theory in the canonical ensemble with a local density approximation (LDA) for the hard-core reference term (MF-DFT). As will be reinforced later in our paper, the advantage of the canonical ensemble is that one can study 'stable' equilibrium droplets to provide the thermodynamic and structural properties of the system [110, 112]. Lee *et al* [116] evaluated the interfacial tension of the drop using a combination of the Laplace and Tolman relations, with the pressure tensor at the centre of the drop as the corresponding value of the internal liquid pressure (obtained locally by identifying the tangential component of the pressure as the negative of the grand potential). This approach leads to a monotonically decreasing dependence of the surface tension from the planar limit with increasing curvature, and correspondingly a positive Tolman length; though the extrapolated value for the planar limit of the function $\delta(R)$ appears to tend to zero, the corresponding error bar is large. In the subsequent work of Talanquer and Oxtoby [131] with a similar MF-DFT approach, a small negative value of the Tolman length was obtained by extrapolation, but again a near monotonic decrease of the surface tension with curvature was found. Both the Lee *et al* [116] and Talanquer and Oxtoby [131] studies were carried out in the canonical ensemble, where it is straightforward to stabilize the drop in a finite-sized system. By contrast, Oxtoby and Evans [118] studied the nucleation of liquid drops with MF-DFT in an open system (grand canonical ensemble), and determined the barrier of nucleation from the maximum in the grand potential as a function of the supersaturation (drop radius). The predictions of the MF-DFT for the barrier in the grand potential were compared with those obtained with classical nucleation theory (CNT) (which requires the planar vapour–liquid tension as input): the barrier height obtained from MF-DFT was lower than the value obtained from CNT in the case of small drops, and was seen to increase above it as the drop size was increased. As there is a direct link between the barrier in the grand potential (work of drop formation) and the surface tension, this finding of Oxtoby and Evans [118] implies that the tension of the drop rises above that of the planar limit (which would thus be consistent with a maximum in the surface tension and a negative Tolman length). In a subsequent paper Zeng and Oxtoby [123] extended the treatment for the more realistic Lennard-Jones potential, and good agreement is found for the condensation nucleation rates of nonane.

For the sake of a mathematical convenience, Oxtoby and Evans [118] applied the Sullivan hard-core Yukawa model [105]. The advantage of using such a model is that the Euler–Lagrange equation corresponding to the minimization of the grand potential functional can be written down in the form of a differential equation that is easier to solve than the integral equation obtained from the standard variational approach. In contrast to the original Sullivan study of a planar interface, however, the boundary conditions for the spherical geometry are much less obvious for the liquid phase. The Sullivan MF-DFT model was also adopted by Hadjiagapiou [129] and, following a mechanical (pressure-tensor) route, a non-monotonic dependence of the surface tension as a function of the drop radius was found. This is consistent with the findings of Oxtoby and Evans [118], but in contradiction with those of Lee *et al* [116]. However, the surface tension reported by Hadjiagapiou [129] is higher than that of the planar surface over the whole range of radii considered, and $\delta(R) = R_e - R_s < 0$ is found to decay almost linearly with increasing drop radius, which is rather surprising particularly in view of its magnitude ($\delta \sim 10$ for $R = 50\sigma$).

Instead of using a mechanical approach that suffers from the ambiguity of the definition of the pressure tensor, Koga *et al* [136] have undertaken a very clear and thorough DFT study of both the Lennard-Jones and Yukawa models within the LDA, analysing the surface properties of the liquid drop on the basis of the Gibbsian thermodynamic theory of capillarity. In qualitative agreement with the work of Hadjiagapiou [129], Koga *et al* obtained a non-monotonic behaviour for the surface tension and a negative Tolman length, but the functional dependence found for $\delta(R)$ is very different: there is a rapid increase in δ on decreasing R for $R \lesssim 10\sigma$, with a change in sign from negative to positive, suggesting a rapid decrease of the surface tension below its limiting planar value for drops corresponding to a few molecular diameters. For $R \gtrsim 10\sigma$ the length $\delta(R)$ decays very slowly to its asymptotic value (Tolman length) reaching a magnitude of about one tenth of the molecular diameter. However, the authors still consider the sign of the Tolman length to be elusive and suggest that this merits further investigation.

All of the DFT studies mentioned thus far follow a local treatment of the reference free energy, neglecting the short-range correlations in density and subsequent inhomogeneities which may be important in the case of small drops. A weighted density approximation (WDA) can be used to incorporate these correlations in the free-energy functional. The first to employ this type of non-local DFT were Bykov and Zeng [140, 143, 148], using the WDA-DFT of Tarazona [161] combined with the generalized formula for the surface tension and Tolman length of Blokhuis and Bedeaux [127]. A non-monotonic curvature dependence and negative Tolman length were found by Bykov and Zeng, though rather surprisingly the difference between the WDA and the LDA treatment was rather small. In more recent work Li and Wu [154] have used a non-local DFT, the fundamental measure theory (FMT) of Rosenfeld [162], to treat the hard-core reference perturbation term, together with a quadratic expansion of the attractive contribution to the free energy where the direct correlation function is described with the mean-spherical approximation (MSA). In contrast to the findings of a number of the other DFT studies (cf [129, 136, 140, 143]), Li and Wu [154] reported a monotonic decrease in the surface tension with increasing curvature, a feature that is consistent with the early LDA-DFT work of Lee *et al* [116]. However, unlike Lee *et al*, the Tolman length calculated by Li and Wu is negative, which appears to be inconsistent with the behaviour observed for the curvature dependence of the surface tension. In more recent calculations with a similar FMT–DFT [72, 73, 78] a non-monotonic dependence of the surface tension with curvature was found, and the Tolman length was calculated to be small but negative.

It is useful at this stage to summarize the rather muddled state of play of the work involving DFT calculations: the non-monotonic behaviour and weak maximum in the surface tension observed with varying drop radius in the latest FMT–DFT studies [72, 73, 78] are in line with the findings of much of the other work employing the extension of the Sullivan model to a spherical geometry within LDA-DFT [118, 129, 136] and non-local WDA-DFT [140, 143, 148] approaches, and with the latest simulation data [68, 72, 73], but are in contradiction with the results of the DFT studies by Lee *et al* [116], Li and Wu [154], Zhou *et al* [159], and Corti *et al* [157]. In the case of bubbles, the FMT–DFT calculations of Binder and co-workers [73, 78] lead to the expected monotonic decay of the surface tension from the planar limit as the radius of the bubble is decreased; this corresponds to a negative Tolman length as obtained for drops. We should note that Binder and co-workers perform their variational analysis in the grand canonical ensemble, which involves locating a saddle point in the free-energy surface. As Oxtoby and Evans [118] have pointed out, such an approach requires a specific numerical procedure. An analysis in the canonical ensemble is simpler as this involves the minimization of the free-energy functional [116]. We will discuss full details of our analysis of the curvature dependence of the interfacial properties of both drops and bubbles with a FMT–DFT treatment in the canonical ensemble in later sections of our current paper.

It is apparent that the collective conclusions of the large body of theoretical work on the curvature dependence of the surface tension and the sign and magnitude of the Tolman length is still a matter of controversy. This is also true of the conclusions drawn from the corresponding simulation studies. In our paper we return to the main question of the curvature dependence (monotonic or non-monotonic) of the surface tension, the sign of the Tolman length, and the applicability of the Tolman equation. We will show that it is not just a matter of choosing the appropriate simulation methodology (pressure-tensor route, free-energy calculation etc) or theoretical approach (SGT, LDA-DFT, FMT–DFT etc), but that the specific analysis of the interfacial properties, including the density profile and excess free energy, is of key importance. We start by making some general observations regarding purely mechanical approaches (section 2), where we show how the surface tension and Tolman length can be represented with a classical Newtonian picture. In section 3 we revisit the main developments of the Gibbsian theory for the thermodynamics of spherical interfaces, and discuss the key features of the Tolman approach. A novel generic expansion of the thermodynamic relations in terms of the curvature of the drop is also developed in this section. The more detailed molecular-level statistical mechanical approaches are discussed in section 4, including the pressure-tensor (mechanical) routes to the surface properties and density functional theories. The specific details of a non-local (FMT) approach in the canonical ensemble are then described. The numerical calculations with our FMT–DFT for drops and bubbles are presented in section 5, and a detailed analysis of the theoretical results is made from the macroscopic mechanical and thermodynamic perspectives in order to assess the applicability of the various routes to the interfacial properties of systems with curved surfaces.

2. Mechanical approach

A mechanical treatment of interfacial properties dates back to the beginning of the nineteenth century, when an

understanding of the behaviour of matter relied entirely on Newtonian classical mechanics. It was therefore natural to explain phenomena such as a capillary rise from a mechanical perspective, based on the assumption of a uniform distribution of molecules interacting via strong and short-ranged (compared to gravity) attractive forces. This followed from the observation that the height and the curvature of the meniscus of a liquid in a small capillary is independent of a thickness of the material making up its walls. A crude mechanical treatment of matter, though unsuitable for a description of interfacial properties of very small droplets, can still provide some insight on the link between intermolecular forces and the macroscopic properties of liquids based on the exclusive application of Newtonian physics.

The existence of a surface tension at a liquid interface was recognized in the earliest studies of interfacial phenomena. In the following development of a entirely mechanical expression for the surface tension, we generalize the formal approach of Laplace [2], Dupré [164], Maxwell [165], Rayleigh [91] and others (as exposed so beautifully by Rowlinson and Widom, see [3] and references therein) for the work associated with the separation of two planar liquid surfaces to form a spherical cavity. This allows us to obtain purely mechanical expressions for the surface tension and the Tolman length of liquid drops. A molecular concept of the surface tension can be established on the basis of a mechanical equilibrium condition assuming the existence of pairwise additive attractive interactions $u(r)$ between molecules, where the integral

$$\Phi = \tfrac{1}{2}\rho \int \mathrm{d}\mathbf{r}\, u(\mathbf{r}) = 2\pi\rho \int_0^d \mathrm{d}r\, r^2 u(r), \tag{10}$$

is taken to express the mean-field cohesive energy per particle. Here, we further assume that $u(r)$ is only a function of the radial distance and negligible beyond a certain cutoff distance d (so that $u(r) = 0$ for $r \geq d$) which is small compared to the size of the system. Furthermore one assumes that the number density ρ is constant, i.e., that correlations between particles are neglected (mean-field approximation). The latter requires, in particular, that the integral in equation (10) is taken in the isotropic part of the liquid, at least within the range of $u(r)$. A superficial particle (one at the interface between the liquid and its vapour, the density of which is neglected in our current development) lacks some portion of the cohesive energy compared to a particle in the interior due to a lower number of neighbours and is therefore in a state of higher potential energy. This, in turn, means that in the absence of an external field the liquid will strive to minimize its surface area. The surface tension γ can then be defined as the work that has to be done to increase the area of a liquid surface by unit area,

$$\delta W = \gamma \delta A, \tag{11}$$

or, alternatively, as the restoring force per unit length acting against an increase in surface area.

The radius of a mechanically stable liquid drop can be determined directly from the principle of virtual work. Let p_l and p_v be the (scalar) pressures of the (interior) liquid and the (exterior) vapour phases, respectively. The work necessary to bring about the change in volume due to an infinitesimal isotropic expansion is

$$\delta W_V = (p_\mathrm{v} - p_\mathrm{l}) A \delta R, \tag{12}$$

where $A = 4\pi R^2$ is the area of the unperturbed surface and δR represents the displacement of the surface towards the vapour phase. Such an expansion of the drop leads also to an increase in the surface area by an amount $\delta A = 8\pi R \delta R$, producing a corresponding surface contribution to the work δW_A. The total work due to the virtual volume expansion in the drop radius is therefore given by

$$\delta W = \delta W_V + \delta W_A = 4\pi R^2 (p_\mathrm{v} - p_\mathrm{l}) \delta R + 8\pi R \gamma \delta R. \tag{13}$$

In (mechanical) equilibrium the work has to be zero from which one immediately obtains the Laplace relation (1).

By employing a simple static molecular model a link between the surface tension and the intermolecular forces can be made. To this end, we calculate the work required to separate a drop of liquid of radius R from a bulk liquid (i.e., the formation of a vacuum cavity of radius $R + d$ in a uniform liquid with a liquid drop of radius R at its centre) by calculating

$$\delta W = \int_0^d F(\ell)\, \mathrm{d}\ell, \tag{14}$$

where $F(\ell)$ is the force between two concentric spherical surfaces a distance ℓ apart (see figure 1). In the following development we assume $d \ll R$. This type of approach has also been used by Fowler [163] to represent the surface tension of a perfectly sharp vapour–liquid interface. Now we set out to calculate the work needed to unbind the molecules in the outer layer from the drop. The radial (and the only non-zero) component of the force between the drop and the

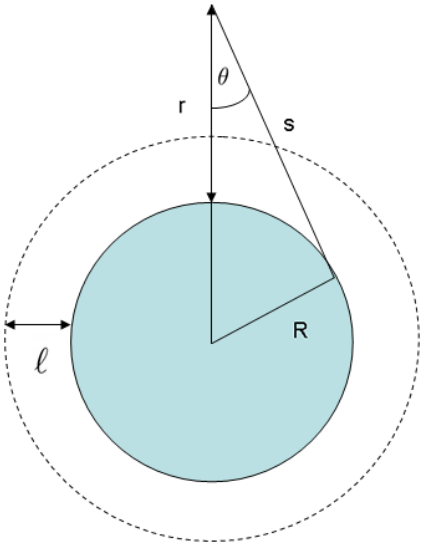

Figure 1. Sketch illustrating the variables for the calculation of the surface tension $\gamma(R)$ of a drop with a static mechanical approach.

molecules that are at a distance ℓ from the drop surface (see figure 1) can be obtained from

$$F_{\rm r}(\ell) = -4\pi\rho^2 \int_\ell^d {\rm d}r\,(r+R)^2 \int_r^{r+2R} {\rm d}s f(s) s^2 \times \int_0^{\cos^{-1}\left[\frac{r^2+2rR+s^2}{2s(r+R)}\right]} {\rm d}\theta\ \sin\theta\cos\theta \int_0^{2\pi} {\rm d}\varphi, \quad (15)$$

where $f(s) = -\frac{{\rm d}u(s)}{{\rm d}s}$ is the force between two molecules a distance s apart, $\cos\theta f(s)$ is the projection of the force in the radial direction, and ϕ is the azimuthal angle in the usual spherical coordinate system.

After integration over the angular variables one obtains the following expression:

$$\frac{F_{\rm r}(\ell)}{4\pi^2\rho^2} = -\int_\ell^d {\rm d}r(r+R)^2 \int_r^{r+2R} {\rm d}s f(s) \times \left[s^2 - \frac{(r^2+2rR+s^2)^2}{4(r+R)^2}\right] = -\int_\ell^d {\rm d}r \int_r^d {\rm d}s f(s)[r^2 s + 2rsR + 2sR^2 - s^3]. \quad (16)$$

We proceed by expressing the force as an expansion to leading order in the curvature $(1/R)$ about the planar limit:

$$F_{\rm r}(\ell) \equiv 4\pi^2 R^2 \rho^2 \left(F_0 + \frac{1}{R}F_1 + \mathcal{O}\left(\frac{1}{R^2}\right)\right), \quad (17)$$

where the reference planar term is

$$F_0 = -2\int_\ell^d {\rm d}r \int_r^d {\rm d}s\, su(s) = 2\ell \int_\ell^d {\rm d}s\, su(s) + 2\int_\ell^d {\rm d}r\, r\frac{\rm d}{{\rm d}r}\int_r^d {\rm d}s\, su(s) = 2\ell\int_\ell^d {\rm d}r\, ru(r) - 2\int_\ell^d {\rm d}r\, r^2 u(r), \quad (18)$$

and the leading-order curvature correction is

$$F_1 = -2\int_\ell^d {\rm d}r\, r\int_r^d {\rm d}s\, su(s) = \ell^2\int_\ell^d {\rm d}r\, ru(r) - \int_\ell^d {\rm d}r\, r^3 u(r). \quad (19)$$

After substituting equations (17)–(19) into equation (14) and integrating by parts, one can express the work done in creating a cavity around the drop of liquid as

$$W = \int_0^d F_{\rm r}(\ell)\,{\rm d}\ell = 4\pi^2 R^2\rho^2 \int_0^d \left[F_0(\ell) + \frac{1}{R}F_1(\ell)\right]{\rm d}\ell = 4\pi^2 R^2\rho^2\left(W_0 + \frac{1}{R}W_1\right), \quad (20)$$

where

$$W_0 = 2\int_0^d {\rm d}\ell\,\ell\int_\ell^d {\rm d}r\, ru(r) - 2\int_0^d {\rm d}\ell \int_\ell^d {\rm d}r\, r^2 u(r) = -\int_0^d {\rm d}\ell\,\ell^2\frac{\rm d}{{\rm d}\ell}\int_\ell^d {\rm d}r\, ru(r) + 2\int_0^d {\rm d}\ell\,\ell\int_\ell^d {\rm d}r^2\, ru(r) = -\int_0^d {\rm d}\ell\,\ell^3 u(\ell), \quad (21)$$

and

$$W_1 = \int_0^d {\rm d}\ell\,\ell^2\int_\ell^d {\rm d}r\, ru(r) - \int_0^d {\rm d}\ell\int_\ell^d {\rm d}r^3\, ru(r) = -\tfrac{2}{3}\int_0^d {\rm d}\ell\,\ell^4 u(\ell). \quad (22)$$

The expression W_0 for the planar limit was already know to Laplace [2] and Dupré [164], but to our knowledge the first-order curvature correction W_1 has not been developed in this manner before. The surface tension corresponds to the work per unit area, $\gamma(R) = \frac{W}{8\pi R^2}$, since two surfaces with areas $4\pi R^2$ and $4\pi(R+d)^2 \approx 4\pi R^2$ have been created:

$$\gamma(R) = -\pi\rho^2\left[\frac{1}{2}\int_0^d {\rm d}\ell\,\ell^3 u(\ell) + \frac{1}{3R}\int_0^d {\rm d}\ell\,\ell^4 u(\ell)\right] + \mathcal{O}\left(\frac{1}{R^2}\right) \equiv \gamma_\infty\left(1 - \frac{2\delta}{R}\right) + \mathcal{O}\left(\frac{1}{R^2}\right), \quad (23)$$

where

$$\gamma_\infty = -\tfrac{1}{2}\pi\rho^2\int_0^d {\rm d}\ell\,\ell^3 u(\ell) \quad (24)$$

is the surface tension of a planar interface, and the coefficient proportional to the first-order curvature correction,

$$\delta = -\frac{\int_0^d {\rm d}\ell\,\ell^4 u(\ell)}{3\int_0^d {\rm d}\ell\,\ell^3 u(\ell)}, \quad (25)$$

is effectively a mechanical representation of the Tolman length, which will be defined on thermodynamic grounds and discussed in detail in section 3. The expression for the planar contribution is of course identical to the one obtained when two planar liquid surfaces are separated from each other (e.g., see the derivation by Rowlinson and Widom [3]). Our expression for the Tolman length is different from that obtained by Kirkwood and Buff [93] or by Schofield and Henderson [109]. The Tolman length in our equation (25) is expressed as the ratio of the fourth and third moments of the pair potential energy. Following a pressure-tensor route for the surface tension and the surface of tension, Kirkwood and Buff [93] obtained a relation for the Tolman length which is proportional to the ratio of the fifth and fourth moments of the corresponding pair virial (force). Our expression (25) yields a Tolman length which is always negative, while that obtained by Kirkwood and Buff is of roughly the same magnitude but is always positive. For a square-well potential of range 1.5σ we find $\delta \sim -0.4\sigma$, where σ is the hard-core diameter, and in the case of the (full) Lennard-Jones potential $\delta = -\frac{2}{3}\sigma$ (where the integration is carried out from σ up to infinity in both cases).

We shall return to the issue of the sign of the Tolman length later in the discussion.

3. Thermodynamic approach

It is evident that the properties of liquids are highly dependent on temperature. This feature is ignored within a purely mechanical perspective, such as the one described in section 2, where the molecules are presumed to be at rest in positions of minimum potential energy. By the last quarter of the nineteenth century, Boltzmann [166] had developed his kinetic theory of gases, a molecular theory based on Newtonian mechanics, revealing that the temperature of the system is related to the mean-square velocity of the chaotic motion of the particles. As a result, a dynamic, rather than a static view of molecular systems began to be accepted. Boltzmann's theory provided a dramatically new insight into the behaviour of fluids, but remained essentially inapplicable until the advent of computers and the development of numerical molecular dynamics techniques. It is now fully accepted that mechanics itself describes only a part of the physics of fluids, that directing a system towards its energetic minimum, but not its counterpart which demands a maximization of its entropy. Within a strict thermodynamic treatment of the interfacial properties of liquids one abandons the molecular picture, describing matter as structureless, providing instead general relations between its macroscopic properties. The thermodynamic description of finite systems, such as a drop of liquid nucleating in a fluid, is far less obvious and cannot be properly handled when the dimension becomes truly microscopic. However, the concept of the surface tension and the related characteristics of the surface can be rigorously formulated within the Gibbsian thermodynamic approach without any restrictions, as will be briefly summarized in section 3.1.

3.1. Theory of Gibbs

We consider a one-component system containing a liquid drop surrounded by its vapour. In section 2 we implicitly assumed that such a system could be characterized by a parameter R, representing the radius of the drop. However, such a division of the system into two physical subsystems, one corresponding to the liquid and one to the vapour phase, is not evident unless the interface is perfectly sharp, which is never the case. In order to avoid this problem, Gibbs [8–10] introduced a mathematically rigorous theory where one relies on a formal definition of a dividing surface separating the system into two hypothetical uniform subsystems. Thus, the volume V of the entire system is expressed as a sum of volumes of the two subsystems

$$V = V_\mathrm{l} + V_\mathrm{v}, \tag{26}$$

with the liquid volume expressed as $V_\mathrm{l} = \frac{4}{3}\pi R^3$. Any surface variable is now defined as the excess of the variable X of the entire system over the sum of the corresponding variables in the two bulk subsystems:

$$X_\mathrm{s} \equiv X - X_\mathrm{l} - X_\mathrm{v}, \tag{27}$$

where X_l and X_v are the properties of the liquid and vapour systems, respectively, at the same thermodynamic conditions as the system of interest. The latter condition is the key to the thermodynamic treatment of interfacial systems. With this division of space in hand, one can define the surface adsorption per unit area as

$$\Gamma(R) = \frac{1}{A(R)}(N - N_\mathrm{l} - N_\mathrm{v}) = \frac{N_\mathrm{s}(R)}{A(R)}, \tag{28}$$

where one refers to a given choice of radius R which also defines the dividing surface.

In terms of thermodynamics, the mechanical model adopted in section 2 corresponds to an adiabatic process with the internal energy playing the role of the thermodynamic potential being minimized by an appropriate compromise between the volume and the surface corresponding to a force balance (cf equation (13)). If the processes are carried out at fixed temperature, which is both experimentally relevant and computationally more convenient, the relevant thermodynamic potential is a free energy. For a one-component liquid drop, the choice of R defines the liquid and the vapour volumes, V_l and V_v, and the total differential of the Helmholtz free energy can be expressed as

$$\mathrm{d}F = -p_\mathrm{l}\,\mathrm{d}V_\mathrm{l} - p_\mathrm{v}\,\mathrm{d}V_\mathrm{v} + S\,\mathrm{d}T + \mu\,\mathrm{d}N + \gamma\,\mathrm{d}A + C\,\mathrm{d}R, \tag{29}$$

where p_l and p_v are the scalar pressures of the uniform liquid and vapour systems corresponding to a given equilibrium chemical potential μ, and C is the conjugate variable to R. In equation (29) the use of the general equilibrium conditions $T = T_\mathrm{l} = T_\mathrm{v}$ and $\mu = \mu_\mathrm{l} = \mu_\mathrm{v}$ has been made implicitly. Equation (29) can be integrated over the whole spherical surface at fixed R and T [3]

$$F = -p_\mathrm{l}V_\mathrm{l} - p_\mathrm{v}V_\mathrm{v} + \gamma A + \mu N \tag{30}$$

and, from equation (27), the surface free energy can be identified as

$$F_\mathrm{s} = \gamma A + \mu N_\mathrm{s}, \tag{31}$$

so that, when referred to a given dividing surface R, the surface tension can be expressed as

$$\gamma(R) = \frac{F_\mathrm{s}}{A} - \Gamma. \tag{32}$$

In other words the surface tension is the surface free energy per unit area, providing there is no net adsorption $\Gamma = 0$. In a one-component system the choice corresponding to vanishing adsorption is the equimolar or Gibbs dividing surface: $R = R_\mathrm{e}$.

In an open or inhomogeneous system it is more convenient to use the grand potential defined as the Legendre transform $\Omega = F - \mu N$. In terms of the grand potential the surface tension is given by

$$\gamma(R) = \frac{\Omega_\mathrm{s}}{A}, \tag{33}$$

regardless of the choice of the dividing surface.

As the dividing surface is fixed by convention, the free energy for fixed N, V, and T or the grand potential for fixed μ, V, and T cannot depend on this formal choice (nor can any

other thermodynamic quantity, such as p_l, p_v, μ or T). If, for a given drop, we take the formal derivative of equation (30) with respect to R and compare it with equation (29), one obtains a generalized Laplace relation,

$$p_l - p_v = \frac{2\gamma(R)}{R} + \frac{C}{A}, \tag{34}$$

(cf equation (1)), with an explicit form for the conjugate variable:

$$C = \frac{\partial\gamma(R)}{\partial R}A. \tag{35}$$

The dividing surface R_s for which $C = 0$, i.e., the one for which the macroscopic Laplace relation (cf equation (1)) is satisfied, is commonly referred to as the surface of tension at which the tension acts [3]. This requires that the formal derivative of the surface tension with the position of the surface be at an extremum:

$$\left.\frac{\partial\gamma(R)}{\partial R}\right|_{R=R_s} = 0. \tag{36}$$

The generalized Laplace equation can be re-written as $\frac{d}{dR}[R^2\gamma(R)] = R^2\Delta p$, and on integrating from the surface of tension R_s to another dividing surface R, one obtains [3, 108]:

$$\frac{\gamma(R)}{\gamma(R_s)} = 1 + \left(\frac{R - R_s}{R}\right)^2 \frac{R_s + 2R}{3R_s}. \tag{37}$$

From equation (37) it follows that $\gamma(R)$ is at a minimum at the surface of tension, and that, for $R \approx R_s$, $\gamma(R_s)$ differs from $\gamma(R)$ by terms of order $1/R_s^2$.

3.2. Theory of Tolman

Gibbs' theory for the surface tension is based on a definition of the dividing surface which is taken to separate the two coexisting phases and to which the surface tension and the other superficial quantities are referred. There are two useful definitions of the dividing surface: the equimolar (or Gibbs) dividing surface R_e, defined by $\Gamma(R_e) = 0$, and the surface of tension R_s, defined by equation (36). Tolman [13] extended the general thermodynamic theory of Gibbs, exploiting the Gibbs–Duhem relation to obtain a thermodynamic expression for the curvature dependence of the surface tension. More specifically, Tolman expressed the adsorption in terms of the difference in the two dividing surfaces $\delta = R_e - R_s$. The adsorption relative to the surface of tension can be written in terms of the appropriate integrals over the number density profile $\rho(r)$ as

$$\begin{aligned}\Gamma(R_s) &= \frac{1}{4\pi R_s^2}\left[\int_0^{R_s}(\rho(r) - \rho_l)r^2\,dr \right.\\ &\quad \left. + \int_{R_s}^{\infty}(\rho(r) - \rho_v)r^2\,dr\right]\\ &= \int_{-R_s}^{0}[\rho(r + R_s) - \rho_l]\left(1 + \frac{r}{R_s}\right)dr\\ &\quad + \int_0^{\infty}[\rho(r + R_s) - \rho_v]\left(1 + \frac{r}{R_s}\right)dr. \end{aligned}\tag{38}$$

Now, if the equimolar dividing surface is a distance δ from the surface of tension, $R_e = R_s + \delta$, the adsorption $\Gamma(R_e)$ at R_e can be expressed as

$$\begin{aligned}\Gamma(R_s + \delta) &= \int_{-R_s}^{\delta}[\rho(r + R_s) - \rho_l]\left(1 + \frac{r}{R_s}\right)dr\\ &\quad + \int_{\delta}^{\infty}[\rho(r + R_s) - \rho_v]\left(1 + \frac{r}{R_s}\right)dr = 0.\end{aligned}\tag{39}$$

After combining equations (38) and (39), one obtains [13]

$$\frac{\Gamma(R_s)}{\rho_l - \rho_v} = \delta\left[1 + \frac{\delta}{R_s} + \frac{1}{3}\frac{\delta^2}{R_s^2}\right], \tag{40}$$

which relates a microscopic property of a drop characterized by the Tolman length δ, to thermodynamic quantities that can be obtained directly from Gibbsian thermodynamics. Indeed, if the Gibbs adsorption equation at constant temperature (which follows from equations (29) and (30)),

$$d\gamma = -\Gamma\,d\mu, \tag{41}$$

is combined with the Gibbs–Duhem relations ($dp_i = \rho_i d\mu$ for $i = l, v$, at constant T), one obtains

$$d\gamma = -\frac{\Gamma}{\rho_l - \rho_v}\,d(p_l - p_v). \tag{42}$$

By describing the pressure difference $\Delta p = p_l - p_v$ with the Laplace equation one can write

$$d\gamma(R) = -\frac{\Gamma}{\rho_l - \rho_v}\,d(2\gamma(R)/R). \tag{43}$$

This leads to a differential equation for $\gamma(r)$ in terms of the radial integration variable r:

$$\frac{d\gamma(r)}{\gamma(r)} = \frac{\frac{2}{r^2}\frac{\Gamma}{\rho_l - \rho_v}}{\left[1 + \frac{2}{r}\left(\frac{\Gamma}{\rho_l - \rho_v}\right)\right]}\,dr. \tag{44}$$

Using equation (40) and integrating the last expression from the plane surface ($r = \infty$) to R one finds

$$\ln\frac{\gamma(R)}{\gamma_\infty} = \int_\infty^R \frac{\frac{2}{r^2}\frac{\Gamma}{\rho_l - \rho_v}}{\left[1 + \frac{2}{r}\left(\frac{\Gamma}{\rho_l - \rho_v}\right)\right]}dr, \tag{45}$$

which with the help equation (40) at lowest order, i.e., $\Gamma = \delta\Delta\rho$ leads to the Tolman equation:

$$\gamma(R) = \gamma_\infty\left(1 - \frac{2\delta}{R}\right) + \text{H.O.T.} \tag{46}$$

In the considerations leading to equation (46) one assumes that δ is a constant, so that the Tolman length can be expressed in the planar limit, such as

$$\delta = \lim_{R_s\to\infty}(R_e - R_s) \equiv z_e - z_s, \tag{47}$$

where the z_e and z now define the corresponding perpendicular distances from the interfacial plane.

The extension of equation (46) beyond the first-order correction in curvature is still a matter of controversy. In

his derivation, Tolman [13] obtained terms of order $1/R^2$ and $1/R^3$, cf equation (8), but neglected them and expressed doubts about their physical relevance taking into account the macroscopic origin of his approach. On the other hand, in his phenomenological theory, cf equation (9), Helfrich [21] included a $1/R^2$ 'elastic' contribution, which he related to the surface rigidity. The relevance of the $1/R^2$ contribution has been questioned [111, 128] owing to the fact that it corresponds only to a constant term in the free energy (in three dimensions) and as a consequence cannot contribute to the restoring force acting against surface deformations. Instead, there is some evidence [101, 135, 144, 145, 155, 156] for the existence of non-analytic terms, such as $\sim \ln R$, which are still a matter of some debate.

3.3. Curvature expansion

We have already showed in section 2 that the Tolman length can be represented within a primitive purely mechanical standpoint. In the following sections we will show how a statistical mechanical treatment can be used to provide a reliable and physically consistent estimate of δ. Prior to this, a procedure is proposed for the determination of the Tolman length from a purely macroscopic thermodynamic basis by assuming the analyticity of thermodynamic quantities in the curvature $c \equiv R^{-1}$ of the drop. We start by considering a thermodynamic state in a metastable region on the vapour side of the phase diagram, i.e., a supersaturated vapour with a chemical potential which is slightly higher than the saturation value. The chemical potential, density and other thermodynamic functions of such a system can be characterized in terms of the radius of the critical nucleus, $R = 1/c$, and we can thus develop a Taylor expansion about the planar limit as

$$\mu(c) = \mu(0) + \mu'(0)c + \tfrac{1}{2}\mu''(0)c^2 + \cdots \tag{48}$$

$$\rho_{\mathrm{i}}(c) = \rho_{\mathrm{i}}(0) + \rho'(0)c + \tfrac{1}{2}\rho''(0)c^2 + \cdots, \qquad \mathrm{i} = \mathrm{l}, \mathrm{v}, \tag{49}$$

where $'$ denotes the derivative with respect to the curvature, $\frac{\mathrm{d}}{\mathrm{d}c}$, and (0) the reference saturation value. As the state is supersaturated with $\mu(c) - \mu(0) > 0$ and $\rho_{\mathrm{i}}(c) - \rho_{\mathrm{i}}(0) > 0$, it follows that the sum of the first-order terms on the right-hand sides of equations (48) and (49) must be positive.

The free-energy density $f \equiv F/V$ of both phases is then expanded up to second order in density, making use of equations (48) and (49), and the thermodynamic relation $\partial f/\partial\rho = \mu$:

$$\begin{aligned} f(\rho_{\mathrm{i}}(c)) &= f(\rho_{\mathrm{i}}(0)) + \left.\frac{\partial f}{\partial \rho_{\mathrm{i}}}\right|_0 [\rho_{\mathrm{i}}(c) - \rho_{\mathrm{i}}(0)] \\ &\quad + \frac{1}{2}\left.\frac{\partial^2 f}{\partial \rho_i^2}\right|_0 [\rho_{\mathrm{i}}(c) - \rho_{\mathrm{i}}(0)]^2 + \mathcal{O}((\rho_{\mathrm{i}}(c) - \rho_{\mathrm{i}}(0))^3) \\ &= f(\rho_{\mathrm{i}}(0)) + \mu(0)[\rho_{\mathrm{i}}(c) - \rho_{\mathrm{i}}(0)] \\ &\quad + \frac{1}{2}\left.\frac{\partial \mu}{\partial \rho_{\mathrm{i}}}\right|_0 [\rho_{\mathrm{i}}(c) - \rho_{\mathrm{i}}(0)]^2 + \mathcal{O}((\rho_{\mathrm{i}}(c) - \rho_{\mathrm{i}}(0))^3) \\ &= f(\rho_{\mathrm{i}}(0)) + \mu(0)[\rho_{\mathrm{i}}'(0)c + \tfrac{1}{2}\rho_{\mathrm{i}}''(0)c^2] \\ &\quad + \frac{1}{2}\left.\frac{\partial \mu}{\partial \rho_{\mathrm{i}}}\right|_0 \left[\rho_{\mathrm{i}}'(0)c + \frac{1}{2}\rho_{\mathrm{i}}''(0)c^2\right]^2 + \mathcal{O}(c^3) \\ &= f(\rho_{\mathrm{i}}(0)) + c\mu(0)\rho_{\mathrm{i}}'(0) \\ &\quad + c^2\frac{1}{2}\left[\left.\frac{\partial \mu}{\partial \rho_{\mathrm{i}}}\right|_0 (\rho_{\mathrm{i}}'(0))^2 + \rho_{\mathrm{i}}''(0)\mu(0)\right] + \mathcal{O}(c^3). \end{aligned} \tag{50}$$

Likewise, using the formal thermodynamic identity relating the pressure and chemical potential to the free energy, both the liquid and vapour pressure can be expressed as the corresponding expansions about their saturation values up to second order:

$$\begin{aligned} p_{\mathrm{i}}(c) &= \mu(c)\rho_{\mathrm{i}}(c) - f(\rho_{\mathrm{i}}(c)) \\ &= [\mu(0) + \mu'(0)c + \tfrac{1}{2}\mu''(0)c^2] \\ &\quad \times [\rho_{\mathrm{i}}(0) + \rho_{\mathrm{i}}'(0)c + \tfrac{1}{2}\rho_{\mathrm{i}}''(0)c^2] \\ &\quad - f(\rho_{\mathrm{i}}(0)) - c\mu(0)\rho_{\mathrm{i}}'(0) \\ &\quad - c^2\frac{1}{2}\left[\left.\frac{\partial \mu}{\partial \rho_{\mathrm{i}}}\right|_0 (\rho_{\mathrm{i}}'(0))^2 + \rho_{\mathrm{i}}''(0)\mu(0)\right] + \mathcal{O}(c^3) \\ &= \mu(0)\rho_{\mathrm{i}}(0) - f(\rho_{\mathrm{i}}(0)) \\ &\quad + c\left[\mu(0)\rho_i'(0) + \mu'(0)\rho_{\mathrm{i}}(0) - \mu(0)\rho_i'(0)\right] \\ &\quad + c^2\left[\mu'(0)\rho_{\mathrm{i}}'(0) + \tfrac{1}{2}\mu''(0)\rho_{\mathrm{i}}(0) + \tfrac{1}{2}\mu(0)\rho_{\mathrm{i}}''(0)\right. \\ &\quad \left. - \frac{1}{2}\left.\frac{\partial \mu}{\partial \rho_{\mathrm{i}}}\right|_0 (\rho_{\mathrm{i}}'(0))^2 - \frac{1}{2}\rho_{\mathrm{i}}''(0)\mu(0)\right] + \mathcal{O}(c^3) \\ &= p(0) + c\mu'(0)\rho_{\mathrm{i}}(0) \\ &\quad + c^2\left[\mu'(0)\rho_{\mathrm{i}}'(0) + \frac{1}{2}\mu''(0)\rho_{\mathrm{i}}(0) - \frac{1}{2}\left.\frac{\partial \mu}{\partial \rho_{\mathrm{i}}}\right|_0 (\rho_{\mathrm{i}}'(0))^2\right] \\ &\quad + \mathcal{O}(c^3). \end{aligned} \tag{51}$$

The pressure difference $\Delta p = p_{\mathrm{l}} - p_{\mathrm{v}}$ can thus be obtained in compact form as

$$\begin{aligned} \Delta p = c\mu'\Delta\rho + c^2\left[\mu'\Delta\rho' + \frac{1}{2}\mu''\Delta\rho - \frac{1}{2}\frac{\partial \mu}{\partial \rho_{\mathrm{l}}}\rho_{\mathrm{l}}'^2\right. \\ \left. + \frac{1}{2}\frac{\partial \mu}{\partial \rho_{\mathrm{v}}}\rho_{\mathrm{v}}'^2\right] + \mathcal{O}(c^3), \end{aligned} \tag{52}$$

where the explicit dependence on the curvature has been dropped bearing in mind that all of the terms that are retained correspond to saturation and $\Delta\rho = \rho_{\mathrm{l}} - \rho_{\mathrm{v}}$. Expression (52) can be compared to the combination of the Laplace and the Tolman relations, cf equations (1) and (46), $\Delta p = 2\gamma C - 2\gamma\delta C^2$. On equating the first-order terms we obtain

$$\mu'\Delta\rho = 2\gamma, \tag{53}$$

implying that $\mu'' = -2\gamma/(\Delta\rho)^2\Delta\rho'$. One should note that equation (53) is consistent with the Laplace relation to first order (i.e., for $\gamma(c) = \gamma(0)$), as can be seen by combining equation (53) with the Gibbs–Duhem equation and integrating the resulting differential equation from the planar limit to some finite curvature.

An examination of the second-order terms leads to

$$\frac{2\gamma}{\Delta\rho}\Delta\rho' - \frac{\gamma}{\Delta\rho}\Delta\rho' - \frac{1}{2}\frac{\partial \mu}{\partial \rho_{\mathrm{l}}}\rho'^2 + \frac{1}{2}\frac{\partial \mu}{\partial \rho_{\mathrm{v}}}\rho'^2 = -2\gamma\delta, \tag{54}$$

and using equation (53) we find that

$$\frac{\partial \mu}{\partial \rho_{\rm i}} = \frac{\mu'}{\rho_{\rm i}'} = \frac{2\gamma}{\Delta\rho\rho_{\rm i}'},$$

finally arriving at

$$\frac{2\gamma}{\Delta\rho}\Delta\rho' - \frac{\gamma}{\Delta\rho}\Delta\rho' - \frac{\gamma}{\Delta\rho}\Delta\rho' = -2\gamma\delta,$$

where the terms on the right-hand side are seen to cancel, implying that $\delta = 0$.

One therefore reaches the interesting conclusion that despite the fact that Tolman's theory is constructed purely on thermodynamical grounds, a purely macroscopic thermodynamic treatment yields a trivial solution with a vanishing Tolman length: this implies that in the thermodynamic limit, the Gibbs dividing surface corresponds to the surface of tension. One can regard this apparent paradox as a consequence of Tolman's theory only providing relations between thermodynamically observable quantities, which although well defined at the macroscopic scale, their differences are of microscopic dimensions, and so beyond the scope of a thermodynamical treatment. It is interesting to note that Wortis and Fisher [111] also find that $\delta = 0$ in their analysis of symmetrical interfaces with a Landau free energy of the square-gradient form; the interfaces are symmetrical by construction in our purely thermodynamic curvature expansion. It is rather ironic, however, that a non-zero and physically reasonable representation of the Tolman length is obtained with the purely mechanical treatment developed in section 2, despite the fact that the interface is assumed be a sharp symmetrical step (see also the discussion in [156]). In order to obtain any useful information from the Gibbs–Tolman theory one therefore has to adopt a molecular (microscopic) approach.

4. Statistical mechanical approach

Statistical mechanical approaches of inhomogeneous systems are generally based on determining the response to changes in the external conditions. In contrast with the approaches discussed in sections 2 and 3, statistical mechanics allows for a microscopic treatment where molecular-level detail can be taken into account in a formal manner.

In this section we outline the common statistical mechanical routes for inhomogeneous systems. These routes are not independent and it is important to highlight the important interrelationships. One approach (usually referred to as the 'mechanical' route) relies on the mechanical definition of the surface tension as the stress transmitted across a strip of unit width normal to an interface. This leads to an expression for the surface tension in terms of components of the microscopic stress tensor (negative of the pressure tensor), and can thus be viewed as a microscopic-level description of the theory of elasticity. A second approach, the so-called 'virial' route, leads to an expression for the surface tension which is based on the isochoric–isothermal change in free energy due to an increase in the interfacial surface by unit area. A third, the 'compressibility' route, relies on a calculation of the change in free energy arising from an increase in surface area caused by density fluctuations. Finally, we present a 'thermodynamic' route which allows for the determination of the surface tension directly from Gibbsian thermodynamics as presented in section 3.1. With this disparate variety of methodologies that are at our disposal for a statistical mechanical description of interfacial systems it is therefore not altogether surprising that there is little convergence in the findings for even the most basic of properties.

4.1. Mechanical (pressure-tensor) route

Let us consider a spherical drop in a fixed volume V for a system of particles interacting via a pairwise potential $u(r_{ij})$ (although this assumption is not restrictive) and calculate the instantaneous force on the drop. The force is related to the flux of linear momentum density through the volume, $F_V^\alpha(t) = \int_V \mathrm{d}\mathbf{r}\, J^\alpha(\mathbf{r}, t)$, where $J^\alpha(\mathbf{r}, t)$ can be expressed as

$$J^\alpha(\mathbf{r}, t) = \nabla^\beta \sigma^{\alpha\beta}(\mathbf{r}, t) \tag{55}$$

when no fields are considered. The common implicit summation notation of Einstein is used, if not otherwise stated. The stress tensor $\sigma^{\alpha\beta}(\mathbf{r}, t)$ incorporates the change in momentum due to particles crossing the boundary of V,

$$\sigma_k^{\alpha\beta}(\mathbf{r}, t) = -\sum_i \frac{p_{\rm i}^\alpha p_{\rm i}^\beta}{m_i}\delta(\mathbf{r} - \mathbf{r}_i), \tag{56}$$

where $\delta(\mathbf{r} - \mathbf{r}_i)$ is the Dirac delta function, and the configurational part of the stress induced by the intermolecular forces is

$$\nabla^\beta \sigma_{\rm c}^{\alpha\beta}(\mathbf{r}, t) = -\tfrac{1}{2}\sum_i \sum_{j\neq i} \nabla_i^\alpha(r_{ij})[\delta(\mathbf{r} - \mathbf{r}_i) - \delta(\mathbf{r} - \mathbf{r}_j)]. \tag{57}$$

$\sigma_{\rm c}^{\alpha\beta}$ itself is not given uniquely, but in general can be expressed as [109]

$$\sigma_{\rm c}^{\alpha\beta}(\mathbf{r}, t) = \frac{1}{2}\sum_i \sum_{j\neq i} r_{ij}^\alpha \frac{u'(r_{ij})}{r_{ij}} \int_{C_{ij}} \mathrm{d}l^\beta\, \delta(\mathbf{r} - \hat{\mathbf{l}}), \tag{58}$$

where $u'(r_{ij}) = \mathrm{d}u(r_{ij})/\mathrm{d}r_{ij}$, for an arbitrary contour C_{ij} joining $\mathbf{r}_i$ and $\mathbf{r}_j$.

Defining the pressure tensor as the negative of the time average of the stress tensor

$$p^{\alpha\beta}(\mathbf{r}) = -\langle \sigma^{\alpha\beta}(\mathbf{r}, t)\rangle, \tag{59}$$

and noting that the average of the left-hand side of equation (55) is zero at equilibrium, one obtains the differential conservation law

$$\nabla^\beta p^{\alpha\beta}(\mathbf{r}) = 0, \tag{60}$$

in the absence of external fields. It should also be pointed out that the substitution of equations (56) and (57) into equation (60) and the use of the equipartition theorem leads to the first equation of the BBGKY hierarchy [3].

From equation (57) it follows that the components of the pressure tensor depend on the choice of the contour joining the two interacting particles; hence there is an infinite

number of 'acceptable' definitions for the pressure tensor. This ambiguity can thus be attributed to specifying the portion of the intermolecular forces that act across an elementary area [94]. As has been discussed at length by Rowlinson [28], the problem with the uniqueness of the definition of the pressure tensor is just a particular case of the more general problem with the local definition of any many-body thermodynamic quantity; the only exception is the chemical potential as neatly captured by the potential distribution theorem [167]. Difficulties associated with the local definition of thermodynamic quantities do not reveal themselves for uniform systems, where any possible ambiguities average to zero, but they become relevant for systems with broken symmetry.

Before discussing the repercussions of the arbitrary nature of the definition of the pressure tensor, it is worth noting that the ambiguity may also be understood from a different viewpoint. According to Noether's theorem [168], conservation laws are reflections of the continuous symmetry of a given system. In our system we assume translational and rotational symmetry of the intermolecular potential: the former has been used in the derivation of equation (57) [109]. Thus, equation (60) may be viewed as a consequence of the symmetry of the Hamiltonian of the system defining the conserving current (through Stoke's theorem). If there are no further constraints set on $p^{\alpha\beta}$, then a class of third-rank tensor, the 'superpotentials' $q^{\alpha\beta\delta}$, which are antisymmetric in the last two indices, generate an infinite number of pressure tensors differing by $\nabla^{\delta} q^{\alpha\delta\beta}$, all satisfying the condition embodied in equation (60). One can take advantage of the non-uniqueness in the definition of $p^{\alpha\beta}$ to cast the tensor in a symmetric form which allows for a definition of the angular momentum. The non-uniqueness of the closely related quantity, the energy–momentum tensor, is a well known issue in field theory and, in particular, in general relativity, where the search for the local components of the energy–momentum tensor is sometimes referred to as 'looking for the right answer to the wrong question' [169][4].

In spherical symmetry, the pressure tensor possesses two independent components:

$$\mathbf{P}(\mathbf{r}) = P_{\mathrm{n}}(r)\mathbf{e}_r\mathbf{e}_r + P_{\mathrm{t}}(r)(\mathbf{e}_\theta\mathbf{e}_\theta + \mathbf{e}_\phi\mathbf{e}_\phi), \tag{61}$$

where $\mathbf{e}_r$, $\mathbf{e}_\theta$, and $\mathbf{e}_\phi$ are the unit basis vectors, and P_{n} and P_{t} are the normal and transverse components, respectively. Upon substitution of equation (61) into the condition of a mechanical stability, equation (60), one obtains [3]

$$\frac{\mathrm{d}}{\mathrm{d}r}(r^i P_{\mathrm{n}}(r)] = r^{i-1}[(i-2)P_{\mathrm{n}}(r) + 2P_{\mathrm{t}}(r)], \tag{62}$$

for all values of i. In particular, for $i = 0$

$$\Delta p = \int_0^\infty \mathrm{d}r\, \frac{2}{R}\,[P_{\mathrm{n}}(r) - P_{\mathrm{t}}(r)]\,. \tag{63}$$

The integration of equation (62) over the interface gives rise to expressions for Δp and, using the Laplace relation, it allows one to determine the ratio $\gamma_{\mathrm{s}}/R_{\mathrm{s}}$, though it would be preferable to determine γ_{s} and R_{s} independently of each other; the latter would provide information on the curvature dependence of surface tension through the Tolman relation (47). To this end, based on a consideration of the force acting on a flat radial strip and the moment about the centre of the drop, the following expressions can be obtained [3]:

$$\gamma(R_{\mathrm{s}})R_{\mathrm{s}} = \int_0^\infty [p_{\mathrm{lv}}(r) - P_{\mathrm{t}}(r)]\, r\, \mathrm{d}r \tag{64}$$

and

$$\gamma(R_{\mathrm{s}})R_{\mathrm{s}}^2 = \int_0^\infty [p_{\mathrm{lv}}(r) - P_{\mathrm{t}}(r)]\, r^2\, \mathrm{d}r, \tag{65}$$

where $p_{\mathrm{lv}}(r) = p_{\mathrm{l}}\Theta(R_{\mathrm{s}} - r) + p_{\mathrm{v}}\Theta(r - R_{\mathrm{s}})$, with Θ representing the Heaviside step function. In the planar limit these expressions simplify to [93]

$$\gamma_\infty = \int_{-\infty}^\infty [P_{\mathrm{n}}(z) - P_{\mathrm{t}}(z)]\, \mathrm{d}z \tag{66}$$

and

$$z_{\mathrm{s}} = \frac{1}{\gamma_\infty}\int_{-\infty}^\infty [P_{\mathrm{n}}(z) - P_{\mathrm{t}}(z)]z\, \mathrm{d}z, \tag{67}$$

which are equations (4) and (5) repeated here for convenience. The first explicit form of the local pressure tensor for a planar liquid–vapour interface was proposed by Irving and Kirkwood [94], who also pointed out its inherent non-uniqueness. As an appropriate contour joining the two interacting particles they chose a straight line, and obtained the normal and tangential components of the pressure tensor as

$$P_{\mathrm{n}}^{\mathrm{IK}}(z) = k_{\mathrm{B}}T\rho(z) - \frac{1}{2}\int \mathrm{d}\mathbf{r}_{12}\, \frac{z_{12}^2}{r_{12}^2}u'(r_{12}) \times \int_0^1 \mathrm{d}\alpha\, \rho^{(2)}(r_{12}, z - \alpha z_{12}, z + (1-\alpha)z_{12}) \tag{68}$$

and

$$P_{\mathrm{t}}^{\mathrm{IK}}(z) = k_{\mathrm{B}}T\rho(z) - \frac{1}{4}\int \mathrm{d}\mathbf{r}_{12}\, \frac{x_{12}^2 + y_{12}^2}{r_{12}^2}u'(r_{12}) \times \int_0^1 \mathrm{d}\alpha\, \rho^{(2)}(r_{12}, z - \alpha z_{12}, z + (1-\alpha)z_{12}). \tag{69}$$

From equation (60) it immediately follows that the normal component is constant for the planar interface $P_{\mathrm{n}}(z) = p$. Evidently, this condition has to be satisfied by any pressure tensor regardless of the choice of contour. Harasima [98] subsequently suggested a different, asymmetric path, dividing the vector $\mathbf{r}_{ij}$ into parallel and normal components with respect to the interface:

$$P_{\mathrm{t}}^{\mathrm{H}}(z) = k_{\mathrm{B}}T\rho(z) - \frac{1}{4}\int \mathrm{d}\mathbf{r}_{12}\, \frac{x_{12}^2 + y_{12}^2}{r_{12}^2}u'(r_{12})\rho^{(2)}(r_{12}, z, z + z_{12}). \tag{70}$$

[4] See the analogy between consequences of the equivalence principle (leading to the difficulty of a local definition of the gravitational energy) and the non-uniqueness of the distribution of the potential energy of two interacting particles in an inhomogeneous system.

Furthermore, Harasima [98] showed that the integral

$$\int z^n P_t(z)\,dz \tag{71}$$

is invariant to the choice of pressure tensor for $n = 0$, but not for the higher moments.

If we return back to equation (62), it follows that for $i = 2$,

$$\Delta p = \frac{2}{R_s^2}\int_0^\infty dr r\,[p_{lv} - P_t(r)]\,, \tag{72}$$

i.e., the first moment of $p_{lv} - P_t$ is invariant to the choice of contour in the definition of P_t, but not the higher moments [109]. Therefore, with a mechanical route based on a microscopic definition of the pressure tensor one is unable to determine z_s or R_s uniquely and cannot therefore provide a consistent way of obtaining the curvature dependence of the surface tension. In general, $\gamma(R_s)$ and δ determined from equations (64) and (65) or equations (66) and (67) differ from those obtained from the Gibbs–Tolman theory.

Equation (65) was originally derived by Buff [97], who calculated the work accompanying a differential increase in the area of a spherical segment, keeping the dividing surface constant. In an open system, the associated work can be identified with the change in the grand potential, so that equation (65) may be re-written as

$$\Delta\Omega = -\int P_t(r)\,d\mathbf{r}, \tag{73}$$

according to which the transverse component of the pressure tensor plays the role of the grand potential density. This expression has been used frequently (e.g., in the LDA-DFT studies of Lee *et al* [116]) since the calculation of P_t allows for a determination of all of the thermodynamic and interfacial properties, including the surface tension of the drop. However, expression (73) involves the second moment of P_t, and thus depends on the choice of pressure tensor. A thermodynamically consistence grand potential requires relation (73) to be invariant with respect to the choice of pressure tensor, in essence corresponding to a tautological definition of the pressure tensor such that its transverse component corresponds to the negative of the grand potential functional. Thus, the problem can be recast as the need of finding the grand potential of a given molecular model. In section 4.3 we show that it can be obtained more directly using the compressibility route.

4.2. Virial route

A virial route within a statistical mechanical framework is based on a generalization of the mechanical formulae for the work needed to deform a system. This route provides a definition of surface tension as the isochoric–isothermal change in the free energy (or the grand potential in an open system) during a formation of a unit area of surface. Note that such a treatment is often denoted as a thermodynamic definition of surface tension, since it stems from the thermodynamic expression

$$\gamma = \left(\frac{\partial F}{\partial A}\right)_{NVT}. \tag{74}$$

However, here we associate 'thermodynamic' with the route based on a determination of the free energy of the entire system, such as provided by DFT (cf section section 4.4). On the other hand one should not confuse virial approaches with those stemming from mechanical expressions based on the forces acting between the particles (cf section 4.1).

The canonical partition function in the limit of zero external field can be expressed as

$$Z(N,V,T) = \frac{\Lambda^{3N}}{N!}\int \Pi_i\,d\mathbf{r}_i\,\exp\left[-\frac{U(\{\mathbf{r}_i\})}{k_B T}\right]. \tag{75}$$

If the system is perturbed by a transformation $\mathbf{r}' = \mathbf{r}+\boldsymbol{\xi}(\mathbf{r})$, the partition function of the deformed system acquires the form:

$$Z'(N,V,T) = \frac{\Lambda^{3N}}{N!}\int \Pi_i\,d\mathbf{r}_i\,\det\left(\frac{\partial r'^{\alpha_i}}{\partial r_i^\beta}\right)\exp\left[-\frac{U(\{\mathbf{r}_i'\})}{k_B T}\right]. \tag{76}$$

The associated change of free energy to first order in $\boldsymbol{\xi}$ is

$$(\Delta F)_{NVT} = \left\langle -k_B T\sum_i^N \nabla\cdot\boldsymbol{\xi}(\mathbf{r}_i) + \sum_i^N \boldsymbol{\xi}(\mathbf{r}_i)\nabla_i U\right\rangle. \tag{77}$$

A link between the mechanical and virial route can be made at first order, if we introduce the configurational pressure tensor $p_c^{\alpha\beta}(\mathbf{r}) = -\langle\sigma_c^{\alpha\beta}(\mathbf{r},t)\rangle$ from equation (57) and substitute it into (77). After some algebra one obtains

$$\Delta F = -\int d\mathbf{r}\,p^{\alpha\beta}(\mathbf{r})\nabla^\beta u^\alpha(\mathbf{r}), \tag{78}$$

corresponding to the well known 'stress–strain' expression from the theory of elasticity. Considering now a class of deformations with zero divergence, so that the change of the free energy at first order is associated solely with the change of area [109], then (78) leads to equation (63).

MacLellan [95] used the virial route to derive the following expression for the surface tension of the planar vapour–liquid interface:

$$\gamma = \frac{1}{2}\int_{-\infty}^{\infty} dz_1 \int d\mathbf{r}_{12}\left(x_{12}^2\frac{\partial^2 u_{12}}{\partial z_{12}^2} - z_{12}^2\frac{\partial^2 u_{12}}{\partial x_{12}^2}\right) \times \rho^{(2)}(\mathbf{r}_1,\mathbf{r}_2), \tag{79}$$

first derived by Kirkwood and Buff [93] from the mechanical route, cf equation (66). Later, Lekner and Henderson [104] reduced equation (79) to a simpler three-fold integral. Notwithstanding the growing complexity of the corresponding algebra, one can go beyond first order in $\boldsymbol{\xi}$ (cf [44], where the so-called test-area method for the planar interface was developed; within this treatment one can in principle determine terms of arbitrary order in the interfacial free energy). Recently, a free-energy expansion due to a perturbative deformation has been applied to spherical liquid drops including the higher-order terms [72], where the change in the free energy can be expressed as

$$\Delta F = \langle \Delta U \rangle - \frac{1}{2k_{\mathrm{B}}T}[\langle \Delta U^2 \rangle - \langle \Delta U \rangle^2] + \frac{1}{6(k_{\mathrm{B}}T)^2}[\langle \Delta U^3 \rangle - 3\langle \Delta U^2 \rangle \langle \Delta U + 2\langle \Delta U^3 \rangle \rangle] + \mathcal{O}(\Delta U^4). \quad (80)$$

The first term in the average of the deformation energy has been shown [72, 104] to be equivalent to that obtained from the mechanical route (cf the Kirkwood–Buff expression [93]). The perturbation contributions determined numerically by molecular dynamics simulation of Lennard-Jones fluids revealed that the second-order terms of the free-energy expansion do not contribute in any appreciable way in the case of the planar vapour–liquid interface. This supports the consistency between the mechanical and virial routes to surface tension for a planar geometry. It turns out, however, that the second-order term in equation (80) becomes comparable in magnitude (but of opposite sign) to the leading-order term for small drops [72]. This is a clear consequence of the enhanced effect of fluctuations in nanoscale drops when compared to the planar vapour–liquid interface. Attempts to describe the interfacial behaviour of a microscopic drop by means of the mechanical route or first-order virial expressions are therefore clearly invalidated. A thorough analysis of the specific role of the energetic fluctuations on the thermodynamic properties of small drops and bubbles will be the subject of future work.

4.3. Compressibility route

The virial route to surface tension leads to a statistical mechanical expression involving the gradient of the intermolecular potential and the pair correlation function. As shown in section 4.2, the standard stress–strain formulae follow from the first-order change in free energy due to a deformation of the area and lead to the mechanical expression of Kirkwood and Buff [93]. Triezenberg and Zwanzig [102] obtained an alternative result in terms of the one-body density and the direct correlation function. This expression can be derived formally as a functional Taylor expansion in the intrinsic free energy up to second order in the density distortion due to an external field [102]:

$$\Delta\mathcal{F} = \int \mathrm{d}\mathbf{r}\, \delta\rho(\mathbf{r}) \frac{\delta\mathcal{F}}{\delta\rho(\mathbf{r})} + \frac{1}{2}\int \mathrm{d}\mathbf{r} \int \mathrm{d}\mathbf{r}'\, \delta\rho(\mathbf{r})\delta\rho(\mathbf{r}') \frac{\delta^2\mathcal{F}}{\delta\rho(\mathbf{r})\delta\rho(\mathbf{r}')} + \cdots = \int \mathrm{d}\mathbf{r}\, \delta\rho(\mathbf{r})[\mu - \varphi(\mathbf{r})] + \frac{kT}{2}\int \mathrm{d}\mathbf{r} \times \int \mathrm{d}\mathbf{r}' \delta\rho(\mathbf{r})\delta\rho(\mathbf{r}') \left[\frac{\delta(\mathbf{r}-\mathbf{r}')}{\rho(\mathbf{r})} - c(\mathbf{r},\mathbf{r}')\right] + \cdots, \quad (81)$$

where $\mathcal{F}$ represents the intrinsic free-energy functional. From equation (81) the 'compressibility' form of the surface tension for a planar vapour–liquid interface can be obtained as [102]

$$\gamma = \tfrac{1}{4}kT \int \mathrm{d}z_1\, \rho'(z_1) \int \mathrm{d}\mathbf{r}_2\, \rho'(z_2)(r_{12}^2 - z_{12}^2)c(r_{12}, z_1, z_2), \quad (82)$$

where $\rho'(z) = \mathrm{d}\rho/\mathrm{d}z$ denotes the gradient of the density profile (which characterizes the compressibility of the system). Schofield [106] has shown that this expression is equivalent to the one of Kirkwood and Buff [93], cf equation (66).

Hemingway *et al* [108] extended the result to spherical interfaces, where one finds

$$\gamma = \frac{\pi kT}{2}\int_0^\infty \mathrm{d}r_1 \int_0^\infty \mathrm{d}r_2 \rho'(r_1)\rho'(r_2) \times \int_{|r_1-r_2|}^\infty \mathrm{d}r_{12} r_{12}[r_{12}^2 - (r_1 - r_2)^2]c(r_{12}, r_1, r_2). \quad (83)$$

Expression (83) has been assessed for the penetrable-sphere model [3, 108], where an approximation for $c(\mathbf{r}_1, \mathbf{r}_2)$ is available at the mean-field level, and a consistency between the compressibility route and the thermodynamic expressions for γ and δ (cf equations (1), (46), and (47)) was found. In the zero-temperature limit the model is solvable exactly and in this case the value of the Tolman length is $\delta = -\sigma/2$.

A connection with the mechanical route can again be made by expressing $\Delta\rho(\mathbf{r})$ in terms of the strain field and by introducing the pressure tensor. Schofield and Henderson [5] showed that equation (81) reduces to

$$\Delta\mathcal{F} = -\int \mathrm{d}\mathbf{r}\, p^{\alpha\beta}[\nabla^\beta \xi(\mathbf{r})^\alpha - \tfrac{1}{2}\nabla^\beta(\xi^\gamma(\mathbf{r})\nabla^\gamma\xi^\alpha(\mathbf{r}))] - \tfrac{1}{2}\int \mathrm{d}\mathbf{r}\, \Delta p^{\alpha\beta}\nabla^\beta\xi^\alpha(\mathbf{r}) + \mathcal{O}(\xi^3). \quad (84)$$

From this expression one can see that the compressibility route captures terms up to second order in $\boldsymbol{\xi}$, which can be interpreted as capillary wave fluctuations, whereas in the first-order virial expression, cf equation (78), these fluctuations are absent.

4.4. Thermodynamic route—DFT

As we have seen in section 4.3, an expansion of the intrinsic free-energy functional up to second order gives rise to an expression for the interfacial tension in terms of the direct correlation function. Unfortunately, good approximations for $c^{(2)}(\mathbf{r}_1, \mathbf{r}_2)$ are generally not forthcoming, and this puts limits on the applicability of the method. On the other hand, accurate and well tested approximations for the full free-energy functional are now available that enable one to determine the thermodynamic properties of the entire (inhomogeneous) system. Following Gibbsian thermodynamics as described in section 3.1, the surface tension can be obtained from equation (33), but now expressed specifically in terms of the surface of tension R_{s}:

$$\gamma(R_{\mathrm{s}}) = \frac{\Omega + p_{\mathrm{l}}V_{\mathrm{l}} + p_{\mathrm{v}}V_{\mathrm{v}}}{4\pi R_{\mathrm{s}}^2}. \quad (85)$$

Here, p_{l} and p_{v} are the scalar pressures of two hypothetical bulk phases corresponding to a bulk liquid and a metastable

supersaturated vapour, characterized by the temperature T and chemical potential μ; the departure of the chemical potential from its saturation value is denoted by $\delta\mu \equiv \mu - \mu^{s} > 0$. Expression (85) only provides a formal relation between $\gamma(R_s)$ and R_s, and in order to obtain a complete solution of the curvature dependence of the surface tension an independent route to either is required; a knowledge of R_s would enable the determination of the Tolman length. Separate expressions follow directly from equation (85) when expressed in terms of a general dividing surface radius R, such that $\frac{d\gamma(R)}{dR}|_{R=R_s} = 0$, which implies

$$R_s = \left(\frac{3\Delta\Omega}{2\pi\,\Delta p}\right)^{1/3} \tag{86}$$

and

$$\gamma(R_s) = \left(\frac{3\Delta\Omega(\Delta p)^2}{16\pi}\right)^{1/3}, \tag{87}$$

where again $\Delta p = p_l - p_v$, and $\Delta\Omega = \Omega + p_v V$ is the work associated with the creation of the liquid drop.

A DFT approach is based on the construction of a functional of the one-body density, which exhibits a minimum at equilibrium that can be associated with the thermodynamic grand potential [25]. In the absence of an external field, the grand potential functional is of the form

$$\Omega[\rho(\mathbf{r});\mu] = \mathcal{F}[\rho(\mathbf{r})] - \mu\int d\mathbf{r}\,\rho(\mathbf{r}). \tag{88}$$

The intrinsic free-energy functional $\mathcal{F}[\rho(\mathbf{r})]$ can be written as a sum of the ideal and excess $\mathcal{F}^{ex}$ contributions as

$$\mathcal{F}[\rho(\mathbf{r})] = k_B T\int d\mathbf{r}\,\rho(\mathbf{r})[\log\Lambda^3\rho(\mathbf{r}) - 1] + \mathcal{F}^{ex}[\rho(\mathbf{r})], \tag{89}$$

where Λ is the de Broglie wavelength. Variations of $\mathcal{F}^{ex}$ with respect to density distribution provide correlation functions of arbitrary order.

For a thermodynamically stable state the second variation $\frac{\delta\Omega}{\delta\rho(\mathbf{r})\delta\rho(\mathbf{r}')}$ must be positive, so that the solution of equation (88) is stable with respect to small perturbations. For a macroscopic two-phase system this scenario is realized only for a planar ($\delta\mu = 0$) interface; here, however, we are concerned with a drop in a thermodynamically metastable state ($\delta\mu > 0$), which is unstable with respect to a uniform liquid and thus $\frac{\delta\Omega}{\delta\rho(\mathbf{r})\delta\rho(\mathbf{r}')} < 0$. As a consequence, a drop placed in an open system with a radius which is smaller than the so-called critical radius will evaporate, while larger drops will grow in an unbounded manner, resulting in the complete condensation of the system. In order to stabilize the drop, we consider a closed system, characterized by a finite number N of particles, with the free energy as the thermodynamic potential. As an alternative one could consider a weak spherically symmetric external field $\phi_{ext}(r)$, eventually taking the limit $\phi_{ext}(r) \to 0$. The constraint of fixing the total number of particles prevents the unlimited growth of the drop as this would lead to a depletion in the vapour phase and thus to a decrease in the undersaturation. In our current work, the attractive part of the intrinsic free-energy functional is approximated as a perturbation from a hard-sphere reference fluid at the mean-field level:

$$F[\rho(\mathbf{r})] = k_B T\int d\mathbf{r}\,\rho(\mathbf{r})[\log\Lambda^3\rho(\mathbf{r}) - 1] + F_{hs}[\rho(\mathbf{r})] + \tfrac{1}{2}\int d\mathbf{r}\int d\mathbf{r}'\,\rho(\mathbf{r})\rho(\mathbf{r}')u_{att}(|\mathbf{r}-\mathbf{r}'|). \tag{90}$$

Our model thus consists of a hard-sphere repulsive core giving rise to $\mathcal{F}_{hs}$ in equation (90) and an attractive term represented with a truncated Lennard-Jones potential according to Weeks–Chandler–Andersen [170] perturbation theory:

$$u_{att}(r) = \begin{cases} -\varepsilon & r \le r_{min}, \\ 4\epsilon\left[\left(\frac{\sigma}{r}\right)^{12} - \left(\frac{\sigma}{r}\right)^{6}\right] & r_{min} < r < r_c \\ 0 & r > r_c, \end{cases} \tag{91}$$

with $r_{min} = 2^{1/6}\sigma$, and $r_c = 2.5\sigma$ is taken as the cutoff distance in our calculations.

For the hard-sphere contribution to the free-energy functional we employ the approximation proposed by Rosenfeld [162] in his fundamental measure theory:

$$\mathcal{F}_{hs}[\rho(\mathbf{r})] = k_B T\int\Phi(\{n_\alpha\}), \tag{92}$$

where the free-energy density $\Phi(\{n_\alpha\})$ can be expressed in terms of weighted densities defined as

$$n_\alpha(\mathbf{r}) = \int d\mathbf{r}'\rho(\mathbf{r})'w_\alpha(\mathbf{r}-\mathbf{r}') \qquad \alpha = \{0, 1, 2, 3, v1, v2\}. \tag{93}$$

Here, $w_3(\mathbf{r}) = \Theta(\tilde{r}-r)$, $w_2(\mathbf{r}) = \delta(\tilde{r}-r)$, $w_1(\mathbf{r}) = w_2(\mathbf{r})/4\pi\tilde{r}$, $w_0(\mathbf{r}) = w_2(\mathbf{r})/4\pi\tilde{r}^2$, $w_{v2}(\mathbf{r}) = \frac{\mathbf{r}}{r}\delta(\tilde{r}-r)$, and $w_{v1}(\mathbf{r}) = w_{v2}(\mathbf{r})/4\pi\tilde{r}$; the hard-sphere radius is set to $\tilde{r} = \sigma/2$. An FMT treatment is deemed necessary for small drops because of the large density oscillations, which can be present particularly in the central liquid region at the lower temperatures, corresponding to higher density states.

The general expressions given by equation (93) can be simplified significantly for some particular geometries. In the case of a perfectly spherical drop, the density varies only in the radial dimension r, so that the calculation of the integrals in equation (93) reduces to a problem of one-dimensional quadrature:

$$\begin{aligned} n_3(r) &= \frac{\pi}{r}\int_{|r-\tilde{r}|}^{r+\tilde{r}} dr'\,r'[\tilde{r}^2 - (r-r')^2]\rho(r'), \\ n_2(r) &= \frac{2\pi\tilde{r}}{r}\int_{r-\tilde{r}}^{r+\tilde{r}} dr'\,r'\rho(r'), \\ n_{v2}^z(r) &= \frac{\pi}{r^2}\int_{|r-\tilde{r}|}^{r+\tilde{r}} dr'\,r'(\tilde{r}^2 + r^2 - r'^2)\rho(r') \\ n_{v2}^x(r) &= n_{v2}^y(r) = 0. \end{aligned} \tag{94}$$

The equilibrium density profile is found by minimizing the free-energy functional, equation (89), which leads to the

following Euler–Lagrange equation:

$$k_{\mathrm{B}}T\log\Lambda^3\rho(\mathbf{r})+\frac{\delta F_{\mathrm{hs}}[\rho(\mathbf{r})]}{\delta\rho(\mathbf{r})}+\int \mathrm{d}\mathbf{r}'\rho\mathbf{r}'u_{\mathrm{att}}(|\mathbf{r}-\mathbf{r}'|)=0, \tag{95}$$

subject to the constraint

$$\int \mathrm{d}\mathbf{r}\,\rho(\mathbf{r})=N. \tag{96}$$

Equations (95) and (96) can be solved self-consistently from

$$\rho(r)=\frac{N\exp[c^{(1)}(r)]}{4\pi\int_0^{r_d}\mathrm{d}r\,r^2\exp[c^{(1)}(r)]}, \tag{97}$$

where is $c^{(1)}(\mathbf{r})=-\frac{\delta F_{\mathrm{ex}}[\rho(\mathbf{r})]/k_{\mathrm{B}}T}{\delta\rho(\mathbf{r})}$ is the single-particle direct correlation function. The latter can be separated into repulsive and attractive contributions as

$$c^{(1)}(r)=\sum_\alpha c_\alpha^{(1)}(r)+c_{\mathrm{att}}^{(1)}(r), \tag{98}$$

where $c_\alpha^{(1)}(r)=\frac{\partial\Phi}{\partial n_\alpha}\otimes w_\alpha(r)$ has the same form as $n_\alpha(r)$ with $\rho(r)$ replaced by $\frac{\partial\Phi}{\partial n_\alpha}$, and

$$c_{\mathrm{att}}^{(1)}(r>r_{\mathrm{c}})=-\frac{2\pi}{r}\int_{r-r_{\mathrm{c}}}^{r+r_{\mathrm{c}}}\mathrm{d}r'\,r'\rho(r')\xi(r,r'), \tag{99}$$

$$c_{\mathrm{att}}^{(1)}(r<r_{\mathrm{c}})=-\frac{2\pi}{r}\int_0^{r_{\mathrm{c}}-r}\mathrm{d}r'\,\rho(r')r'\tilde{\xi}(r,r') -\frac{2\pi}{r}\int_{r_{\mathrm{c}}-r}^{r_{\mathrm{c}}+r}\mathrm{d}r'\,r'\rho(r')\xi(r,r'), \tag{100}$$

with $\xi(r,r')=\int_{|r-r'|}^{r_{\mathrm{c}}}\mathrm{d}r''\,r''u_{\mathrm{att}}(r'')/k_{\mathrm{B}}T$ and $\tilde{\xi}(r,r')=\int_{|r-r'|}^{r+r'}\mathrm{d}r''\,r''u_{\mathrm{att}}(r'')$.

In section 5 we present the findings of calculations with our non-local FMT–DFT for liquid drops of varying size. A detailed analysis of the density profiles, the coexistence densities of the vapour and liquid regions, the curvature dependence of the vapour–liquid tension, and the Tolman length is undertaken, making appropriate comparisons with existing work wherever possible.

5. Numerical results

In this section we present an analysis of the interfacial properties of small liquid drops surrounded by vapour for a one-component system. If not stated otherwise, the description is obtained with the FMT–DFT described in section 4.4 in the canonical ensemble for a Lennard-Jones 12-6 WCA potential truncated at $r_{\mathrm{c}}=2.5\sigma$ (cf equation (91)) by solving equation (97) using a standard Picard iteration method. In order to represent the non-local functional for the hard-sphere reference potential, a modified version of Rosenfeld's FMT based on the highly accurate equation of state for hard-sphere fluid mixtures proposed by Boublík [172] is used (see [173] for details).

All the quantities are expressed in reduced units: $r^*=r/\sigma$, $R^*=R/\sigma$, $\rho^*=\rho\sigma^3$, $T^*=k_{\mathrm{B}}T/\epsilon$, and $\gamma^*=\gamma\sigma^2/\epsilon$, where σ and ϵ are the size and energy parameters of the Lennard-Jones potential.

5.1. Structure of a microscopic drop

In figure 2 we present density profiles obtained from our non-local mean-field DFT for three temperatures $T^*=0.7$, $T^*=1$, and $T^*=1.2$ (corresponding to reduced temperatures: $T_{\mathrm{r}}=T^*/T_{\mathrm{c}}^*=0.526, 0.752$, and 0.902, respectively). The latter temperature is already rather close to the critical point of the bulk vapour–liquid coexistence, $T_{\mathrm{c}}^*=1.33$. One can highlight several general characteristic features of the structure of a liquid drop from these profiles. At a temperature close to the triple point, which in this case occurs at $T_{\mathrm{t}}^*\sim 0.6$, the structure inside the drops exhibits strong undamped oscillations which extend from the surface to the centre of the dense liquid. This type of highly correlated structure in the dense interior of the drop cannot be accurately described with a traditional square-gradient treatment (e.g., the work of Falls *et al* [107], Guermeur *et al* [115], and the more recent papers [130, 132, 138, 141]) or local DFTs (e.g., the studies by Lee *et al* [116], Oxtoby and co-workers [118, 123, 131], Hadjiagapiou [129], and Koga *et al* [136]). Note that it is the non-local character of our density functional, (cf equation (92)), which enables one to capture this type of fine structure. These oscillations can also be observed to a lesser degree on the liquid side of a planar vapour–liquid interface [175], but in the case of a spherical interface both the amplitude and range of the oscillation is significantly enhanced. It is clear that there is a strong inhomogeneity in the density of small drops at low temperatures, and any assumption of a uniform liquid region would evidently be unrealistic. In particular, one should note that the density at the centre of the drop depends on the amplitude and wavenumber of the almost periodic density profile at $r=0$, and on the size of the drop. At the intermediate temperature of $T^*=1$, the oscillations almost vanish and the density profiles become monotonically decaying functions. This means that in the temperature interval $T_{\mathrm{FW}}^*\in(0.7;1)$ there is a crossover between an oscillatory and monotonically decaying density profile corresponding to a Fisher–Widom line [174, 175]; the construction of the Fisher–Widom (FW) diagram is beyond the scope of the present paper. Another salient feature is that the density $\rho(0)$ in the centre of the drop remains somewhat higher than that of the saturated liquid density and is nearly independent of the size of the drop up to some value of the drop radius where a sudden decrease in $\rho(0)$ occurs. For the highest value of the temperature considered here, we observe a very diffuse interface between the drop and the vapour; as a consequence any approximation based on the assumption of a sharp interface would presumably lead to quantitatively unreliable results as one approaches the critical point. Nonetheless, we stress that a Gibbsian thermodynamic treatment involving the mapping of the system into two uniform regions separated by a well-defined dividing surface is free of any ambiguity and thus fully applicable regardless of the drop size. The density in the centre of the drop is clearly rather sensitive to the size of the drop; for a drop of intermediate size corresponding to the system with $N=800$ at $T^*=1.2$ the density at the centre of the drop is essentially the same as that of bulk system, so that the vapour–liquid coexistence crosses the bulk binodal curve at this point.

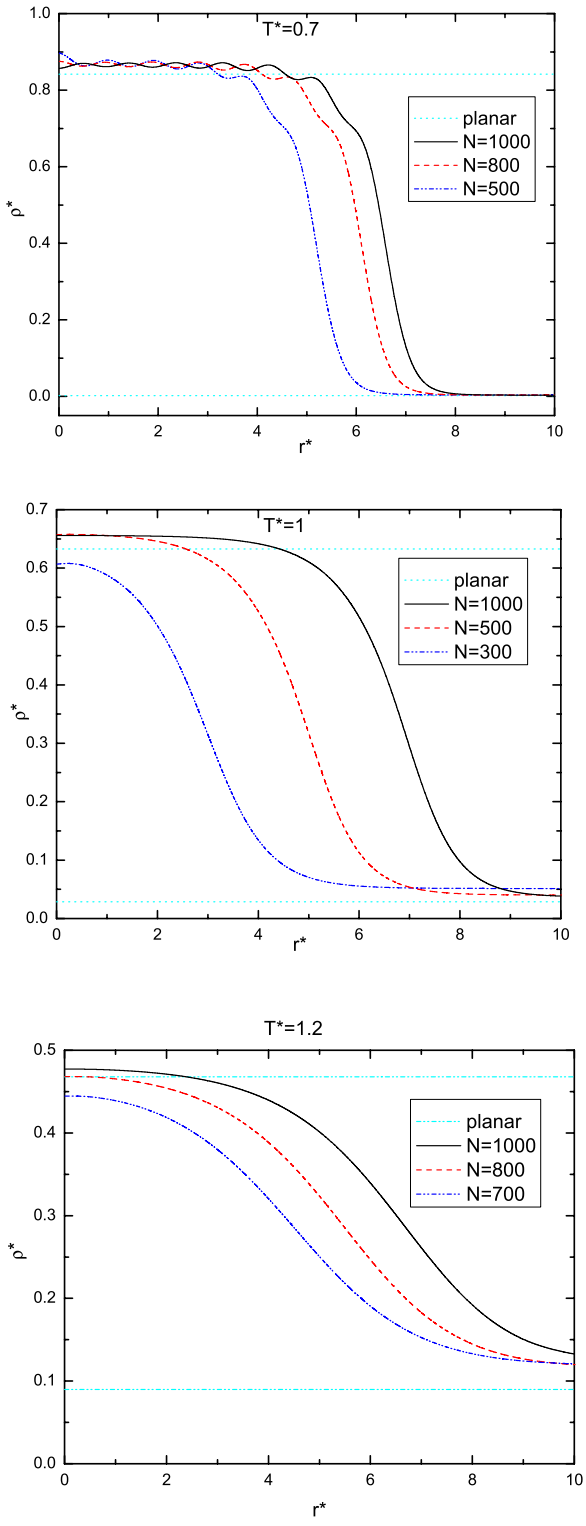

Figure 2. Density profiles of liquid drops of Lennard-Jones fluid as predicted with our non-local canonical mean-field FMT–DFT (cf section 4.4) for three temperatures and system sizes. The system size is controlled by fixing the number of particles inside a spherical container of fixed radius $d = 10\sigma$. The horizontal lines denote saturation densities of the bulk vapour and liquid phases for the corresponding temperature.

In order to shed further insight into the structure of the liquid drop, we depict in figure 3 the dependence of the liquid density on the drop radius, taken as that corresponding

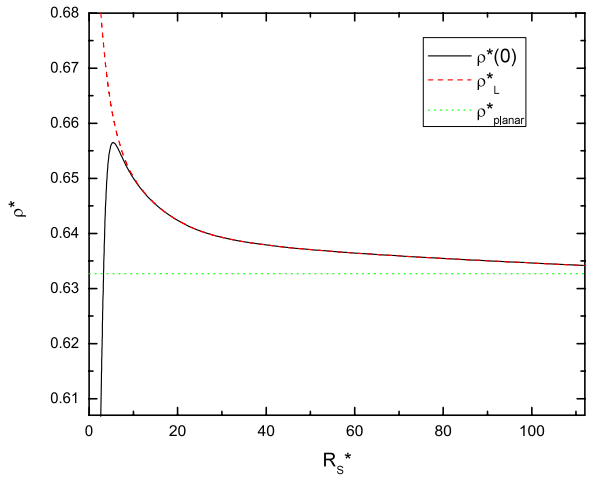

Figure 3. The density in the centre of the liquid Lennard-Jones drop $\rho(0)$ and the liquid density of the corresponding hypothetical bulk phase $\rho_\mathrm{l}(T, \mu)$ as a function of the drop radius obtained with our canonical mean-field FMT–DFT (cf section 4.4). The LJ system is at a temperature of $T^* = 1$.

to the Gibbs dividing surface R_e. Two definitions are commonly considered to represent the liquid density of a microscopic drop. In one, the density at the centre of the drop $\rho(0)$ is frequently interpreted as the liquid density in computer simulation studies. In the other common choice, a thermodynamic definition of the liquid density $\rho_\mathrm{l}(T, \mu)$ is taken, i.e., one corresponding to that of a hypothetical bulk phase with the same chemical potential and temperature as the system containing a drop. For relatively large radii, the two definitions of the liquid density practically coincide and exhibit a monotonic curvature dependence in line with that predicted from the Laplace equation (see figure 3). However, below a drop radius of $R_\mathrm{e}^* \sim 10\sigma$ a striking difference between the curvature dependence exhibited by these two densities becomes apparent. While $\rho_\mathrm{l}(T, \mu)$ remains monotonic, $\rho(0)$ exhibits a maximum and its value eventually drops below the bulk saturation density. The presence of the maximum reflects the non-monotonic curvature dependence of the surface tension, as will be shown in the subsequent discussion. Two opposing effects thus determine $\rho(0)$ at small R: the linear increase of the capillary pressure with curvature due to the factor $1/R$ in the Laplace equation; and the decrease of the surface tension for small R (the latter is a surface contribution $\sim R^2$ that becomes dominant for sufficiently small R). On the other hand, the thermodynamic definition of the liquid density is merely controlled by the value of the chemical potential, i.e., by the measure of the extent of supersaturation. Following an isotherm from the binodal to the spinodal (the limit of thermodynamic stability), the critical radius of the metastable drop decreases while the corresponding liquid density must increase.

The difference between the thermodynamic definition ρ_l and $\rho(0)$ is also apparent from an inspection of figure 4, where we compare the vapour–liquid phase coexistence behaviour for systems of different size, with stabilized drop radii ranging from 3σ to 26σ. The vapour branches of the finite systems

are shifted towards higher densities in all cases, in a manner commensurate with the corresponding curvature of the drop (cf the upper panel of figure 4). Evidently, the vapour pressure and thus the density of a drop must be larger than the saturation pressure, and the difference is described by the Kelvin relation (6). If the density of the drop is defined thermodynamically as in the lower panel of the figure 4, there is a similar shift of the whole of the coexistence envelope to the right. In all cases the vapour is supersaturated so that $\delta\mu > 0$ and as a consequence the density of the liquid phase must also be higher than the saturation value. When the density of a liquid drop is associated with the value $\rho(0)$ of the density profile at the centre of the drop, the scenario is quite different. For a sufficiently small drop, $\rho(0)$ may decrease below the saturated liquid density, as has already been observed in figure 2. For the smallest system ($N = 300$) shown in the upper panel of figure 4, the liquid branch crosses the binodal at $T^* \sim 0.95$, since at these conditions the drop is sufficiently small. We should note that the 'critical point' of the drop (if one is able to define the instability of the drop in this way) is always lower than that of the bulk fluid.

5.2. Surface tension and Tolman length

5.2.1. Surface tension. One of the most advantageous features of DFT is that once the solution of the Euler–Lagrange equation, equation (97), for the density profile which minimizes the grand potential Ω (or free energy F) is known, the surface tension of the drop can be obtained directly from equation (33) (or (32)), since Ω (or F) is a direct output of the theory. In this way, a direct thermodynamic route to the determination of the curvature dependence of the surface tension and Tolman length can be followed, without the necessity to determine ill-defined local thermodynamic functions. We should note however that the use of a local thermodynamic route within a DFT treatment has been commonplace (e.g., see [116, 154]). Alternatively, a knowledge of the equilibrium density profile allows one to calculate the Tolman length by making use of the ratio $\gamma(R)/\gamma_\infty$ according to the Tolman relation, equation (46).

In figure 5 we compare the description with our canonical mean-field FMT–DFT (cf section 4.4) for the curvature dependence of surface tension with the recent simulation data obtained from canonical [72] and grand canonical [68] simulation. The most important observation that can be gleaned from figure 5 is that, according to both our DFT and the simulation data, the surface tension of the LJ drop is characterized by a maximum between $R \sim 5\sigma$ and 10σ. This finding is clearly inconsistent with studies reporting a monotonic curvature dependence of the surface tension. In particular, one should single out any mechanical treatment based on the computation of the pressure-tensor components (e.g., equation (64)), including the majority of the simulation studies which follow the mechanical approach originally presented by Thompson *et al* [50]. As can be seen in figure 5, the surface tension obtained by Vrabec *et al* [63] from a very thorough molecular dynamics study following the mechanical route is in contradiction with the latest

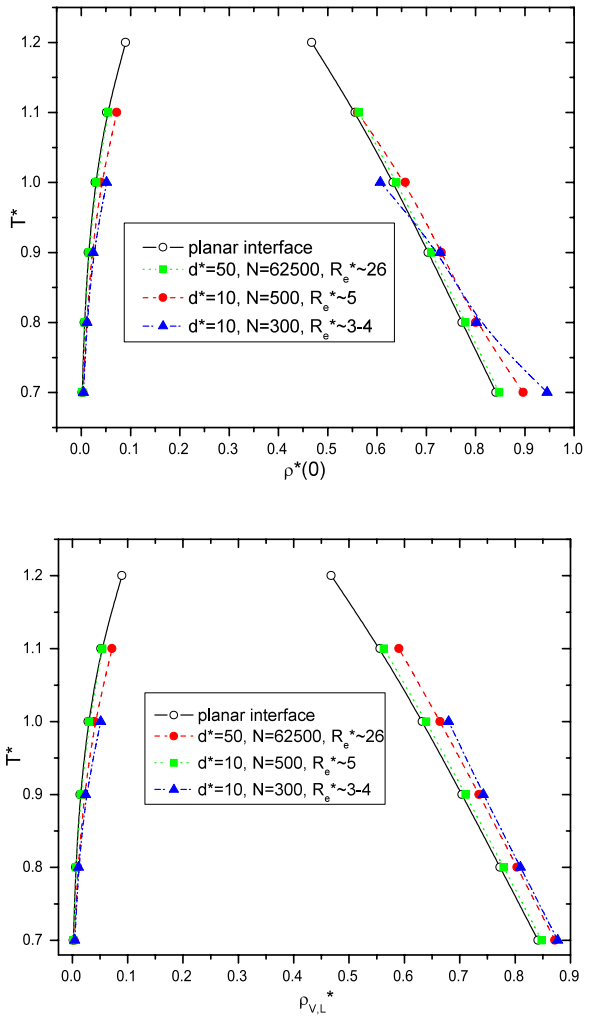

Figure 4. The vapour–liquid coexistence phase diagrams in the density–temperature plane obtained for Lennard-Jones drops with our canonical mean-field FMT–DFT (cf section 4.4). In the upper panel, the liquid density is defined as the density $\rho(0)$ in the centre of the drop, while in the lower panel, the liquid density $\rho(T, \mu)$ is determined according to the theory Gibbs for a corresponding hypothetical bulk phase. The phase behaviour of three finite systems is complemented with that for the essentially infinite planar vapour–liquid interface. The reduced radius of the container is denoted as $d^\star$.

simulation data (and our DFT prediction): not only is the curvature dependence of the tension seen to be monotonic throughout, but the numerical values are up to 25% lower than the more recent calculations following a thermodynamic route [68, 72, 73]. As was mentioned in section 1, predictions with square-gradient and density functional theories have suggested both monotonic (e.g., [107, 116, 154]) and non-monotonic (e.g., [115, 136, 149]) curvature dependences for the surface tension. It is however surprising to note that the most sophisticated study to date [154] (FMT–DFT that goes beyond a mean-field approximation for the attractive contribution) suggests a monotonic dependence of the surface tension with curvature; this is inconsistent with our DFT results and the latest simulation studies (most likely due to the use of classical nucleation theory as a connection

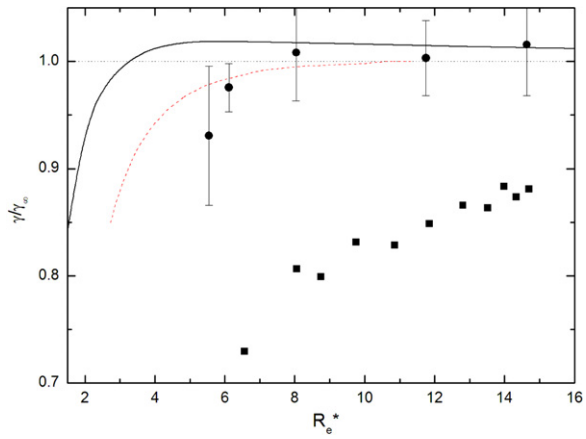

Figure 5. The deviation of surface tension $\gamma(R)$ from the planar limit γ_∞ for Lennard-Jones drops as a function of the drop radius corresponding to the Gibbs dividing surface. The prediction of our canonical mean-field FMT–DFT following the thermodynamic route (continuous curve) are compared with the simulation results: test-area deformations in the canonical ensemble, Sampayo *et al* [72] (circles); grand canonical ensemble, Schrader *et al* [68] (dashed); molecular dynamics simulation following the mechanical route, Vrabec *et al* [63] (squares). The LJ system is at a temperature of $T^* = 0.8$.

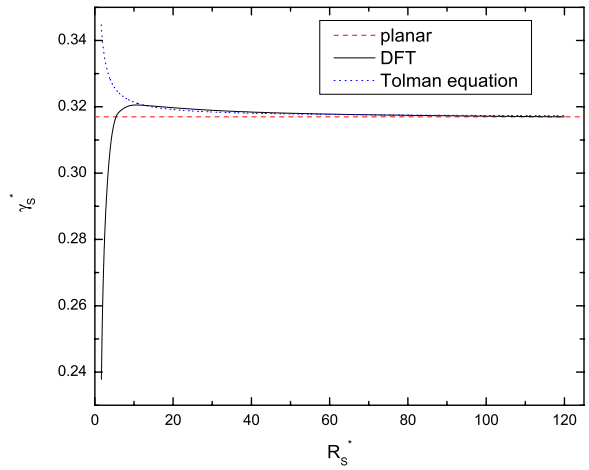

Figure 6. The surface tension of Lennard-Jones drops as a function of drop radius corresponding to the surface of tension. The continuous curve denotes the results from a direct determination of the surface tension with our canonical mean-field FMT–DFT (see section 4.4), while the dotted curve is obtained from the Tolman equation (cf equation (46)). The planar value of the surface tension for planar vapour–liquid interface is indicated by the dashed line. The LJ system is at a temperature of $T^* = 1.0$.

to the surface tension which is known to break down for small drops [118]). The fact that $\gamma(R) > \gamma_\infty$ over the whole region of R beyond the maximum suggests a negative Tolman length, an observation which is again in conflict with the predictions from a mechanical treatment. On the other hand, for drop radii below the maximum in the surface tension, the surface tension steeply decreases below its planar limit. It can thus be supposed that the radius corresponding to the maximum of $\gamma(R)$ sets a limit to the validity of the Tolman relation, which, in view of the definition of δ_∞, leads to a monotonic behaviour for the curvature dependence of $\gamma(R)$. This can be assessed with a direct calculation of the Tolman length using equation (47) with the equimolar surface (obtained directly from the density profile) and the surface of tension (cf equation (86)). A comparison of the curvature dependence of the surface tension as obtained directly from the Gibbs–Tolman theory (cf equation (46)) is made in figure 6 for Lennard-Jones drops at a temperature of $T^* = 1$. It is seen that the difference between the two approaches is nearly indistinguishable beyond $R > 10\sigma$, i.e., almost over the whole range of radii where $\gamma(R)$ is monotonic. For smaller drops with radii below the maximum, the descriptions with the full DFT and Gibbs–Tolman approach start to deviate dramatically, with an increase in the respective absolute slopes but in opposite directions. On the one hand, this supports the consistency of a thermodynamic treatment for large drops; on the other, such an analysis highlights the limit of validity of the Gibbs–Tolman treatment, which is a macroscopic thermodynamic approach. It is important to reiterate that our DFT predictions are in a qualitative disagreement with the results based on a mechanical approach (i.e., one relying on the pressure tensor), where a monotonically decreasing dependence of the surface tension with drop size is obtained (the latter corresponding to a positive Tolman length).

A consequence of the non-monotonic behaviour obtained for the surface tension is that the assumptions leading to the derivation of the Tolman equation must fail when the radius of the drop is of order of the range of the intermolecular potential. One possible route beyond the Tolman equation is to extend the curvature correction to the planar surface tension by including higher-order terms. Alternatively, one can relax the assumption of a constant value of δ in the Tolman equation [136, 138, 150] and determine the curvature dependent $\delta(R)$ from equation (40). The curvature dependence of $\delta(R)$ obtained from our FMT–DFT (equations (46) and (86)) is displayed in figure 7 for truncated Lennard-Jones drops of various size at $T^* = 0.8$, for which the Tolman length is determined to be $\delta = \lim_{R\to\infty}\delta(R) = -0.0708\sigma$; this value is completely in line with the FMT–DFT estimates of Block *et al* [72]. We observe a steep increase of $\delta(R)$ at small values of R, and an analysis of the data suggests a dependence of the form $\delta(R) = \delta_\infty + a/R^2$, which indicates that $\delta(R) \simeq \delta_\infty$ for $R > 10\sigma$. The lack of a term in $1/R$ for $\delta(R)$ supports the view of Rowlinson [128] that terms in $1/R^2$ should not contribute to the surface tension of a fluid as they do not give rise to a restoring force on deforming the interface; the term in $1/R^3$ (corresponding to terms in $1/R^2$ for δ) would of course contribute to the surface tension. One should note that terms in $\ln R/R^2$ for the surface tension have been attributed to the long-ranged potentials in the studies of wetting on spherical substrates [135, 145, 155]; such a logarithmic dependence in $\gamma(R)$ has not been identified from our FMT–DFT calculations for the free drops of particles interacting via the truncated LJ potential. When our simple quadratic curvature dependence for $\delta(R)$ is introduced in equation (8) and integrated, the resulting surface tension is in remarkably good agreement with the values obtained from our FMT–DFT with the direct thermodynamic route over the

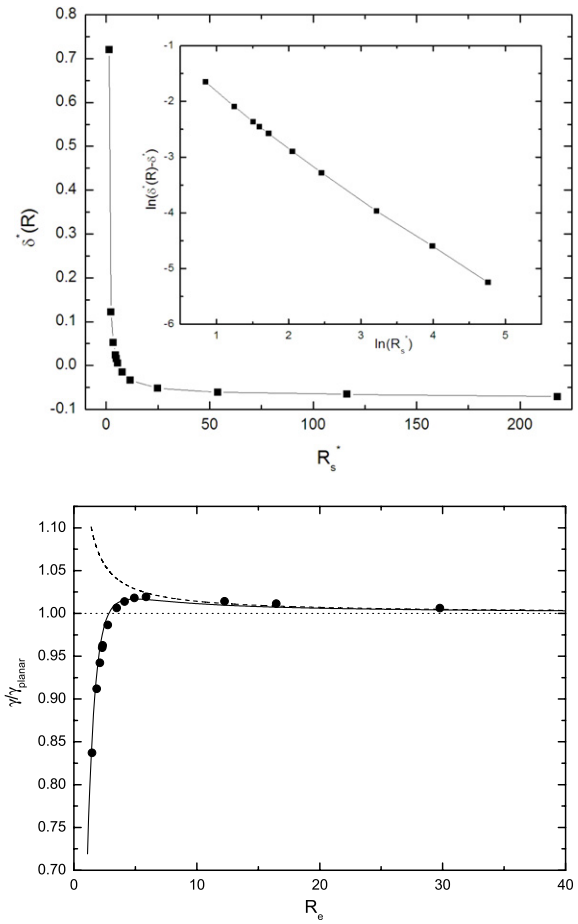

Figure 7. Upper panel: the curvature dependence of $\delta(R) = R_e - R_s$ of Lennard-Jones drops obtained from our canonical mean-field FMT–DFT with equation (40). Lower panel: surface tension as a function of radius R_e corresponding to the Gibbs dividing surface. The symbols represent calculations with the Gibbs theory (cf equation (85)), the dashed line to the Tolman equation (46) and the full curve to the modified Tolman equation with $\delta^*(R^*) = \delta^* + a/R^{*2}$ and $a = 1.527\,33$. The value of the planar limit of the surface tension is denoted by the dotted line. The LJ system is at a temperature of $T^* = 0.8$.

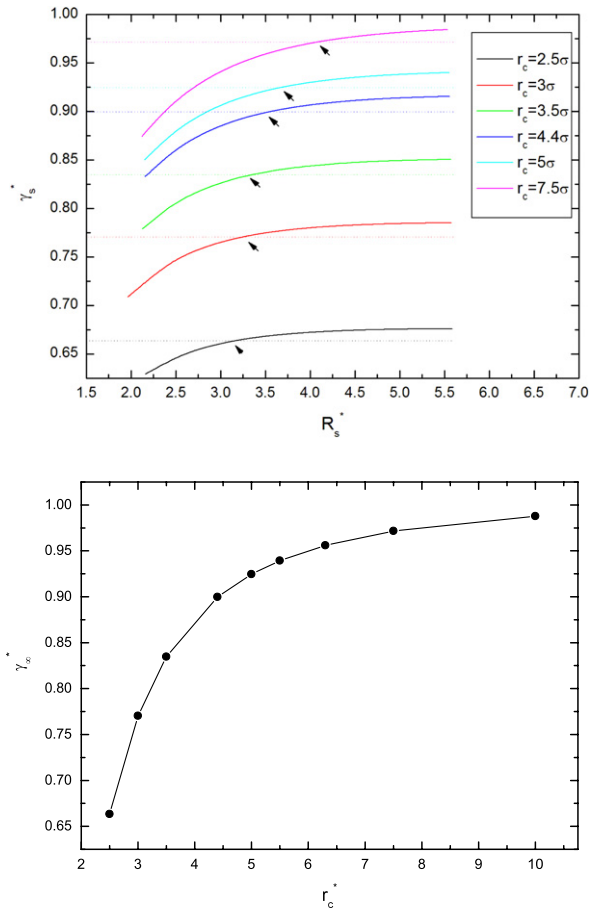

Figure 8. Upper panel: the curvature dependence of the surface tension of liquid drops obtained with our canonical mean-field FMT–DFT for Lennard-Jones particles with different values of the cutoff of the potential. The arrows indicate where $\gamma(R) = \gamma_\infty$. The values for the planar limit of the surface tension are denoted by the dotted lines. Lower panel: the values of the planar vapour–liquid surface tension γ_∞ corresponding to LJ systems with different cutoffs. The state corresponds to a temperature of $T^* = 0.8$ in all cases.

whole range of radii. This numerical analysis should not, however, be taken as an extension of the original theory of Tolman, as one cannot establish the physical relevance of the correction term and, in particular, one is unable to predict the value of the constant a. Nevertheless, empirical approaches of this type could be useful in, e.g., representing the curvature dependent surface tension for use in extended nucleation theories.

Throughout our computations we have considered a molecular model with Lennard-Jones attractive interactions truncated at a distance $r_c^* = 2.5$ from the centre of the particle. One may ask how the range of the attractive forces affects the interfacial properties of small drops of liquid. In figure 8 we plot the curvature dependence of the surface tension for drops of LJ particles with different cutoff distances that are frequently used in simulation studies. The corresponding planar values of the bulk vapour–liquid surface tension increase with r_c: a larger cutoff implies stronger cohesion and thus a higher value of the surface tension, as is also apparent from figure 8. Qualitatively, however, the non-monotonic behaviour of the surface tension with curvature remains unchanged. It is perhaps just worth noting, however, that the radius below which $\gamma(R) < \gamma_\infty$ (indicated by the arrows in figure 8) increases with increasing r_c. We recall that such a crossover occurs when the surface effects begin to dominate the forces in the interior volume, i.e., when no 'bulk' fluid region can be assigned inside the drop. In this case even particles in the centre of the drop 'feel' the interface, a scenario that becomes increasingly true for longer ranged interactions.

For completeness, we now undertake a brief final analysis of a bubble of gas enclosed by a liquid reservoir, where $\delta\mu < 0$, which is the antipodal system to a drop of liquid. The mean-field FMT–DFT approach described in section 4.4 is again employed to determine the density profiles of the bubble and the interfacial properties such as the curvature dependence of the surface tension and the Tolman length. This is equivalent to the recent DFT study reported by Block

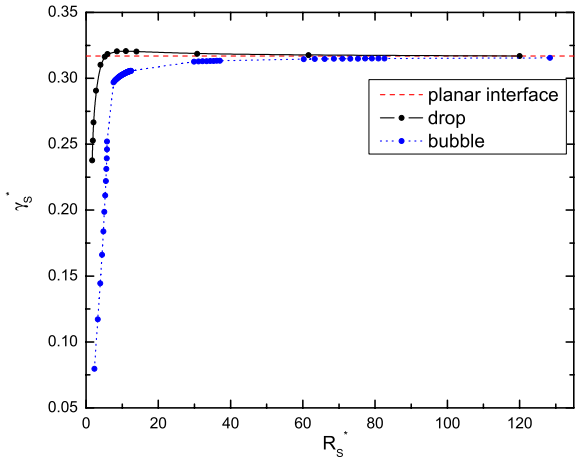

Figure 9. Comparison of the curvature dependence of the surface tension of a drop and a bubble obtained with our canonical mean-field FMT–DFT. The value of the planar limit of the surface tension is denoted by the dashed line. The LJ system is at a temperature of $T^* = 1.0$ in both cases.

et al [73]. As shown in figure 9, the curvature dependence of the surface tension for a bubble is of a qualitatively different form to that of a liquid drop, since in this case the dependence is monotonic, such that $\gamma(R) < \gamma_\infty$ for all R. Taking into account that the curvature is now negative $R < 0$ for a bubble, this is consistent with a negative value of the Tolman length as for the liquid drop; however, in the case of bubbles $\delta(R)$ remains negative throughout. This general result is supported by the findings of the recent simulation by Block *et al* [73]. Nevertheless, in other quite recent simulation studies employing a mechanical route to analyse the data it has been reported that the surface tension increases slightly as the radius decreases [89], or that no curvature effects for bubbles can be detected [85]. We believe that this qualitative discrepancy is again due to the inadequacy of a mechanical route to the surface tension.

6. Summary and conclusion

The purpose of our paper has been to give a comprehensive and up-to-date review of the different approaches to the description of structure and interfacial properties of microscopic liquid drops and gas bubbles, complemented with novel mechanical and thermodynamic developments, a thorough analysis, and detailed calculations. This includes a state-of-the-art description with a non-local density functional theory, which, in our opinion, is the most direct and rigorous way to understanding and describing the properties of nanoscale drops and bubbles of arbitrary size as the approach enables one to represent the marked inhomogeneities of the system. Following a historical introduction, we started our analysis with a purely mechanical approach, treating the fluid as a static ensemble of interacting particles distributed uniformly within the liquid phase (of the drop), while the density of the surrounding gas is neglected; the interface is thus perfectly sharp in this case (often referred to as the Fowler approximation [163]). Such an approach is clearly rather crude, but, as we show, a simple representation can be developed for the vapour–liquid surface tension as the work per unit area needed to separate the liquid drop from the rest of the fluid. In this type of macroscopic mechanical description the surface tension of the spherical interface turns out to be proportional to the third moment of the pair potential energy; the expression is consistent with that obtained for the planar limit by Laplace and Rayleigh in the nineteenth century (cf [3]). In addition we develop a novel analytical expression for the Tolman length, as the ratio of the fourth and third moments of the pair potential; the latter measure which characterizes the curvature dependence of the interfacial free energy is found to be negative from this static mechanical perspective, with a magnitude for typical intermolecular models of simple fluids of about a half of the molecular size. We then turned our attention to a purely (macroscopic) thermodynamic approach that sacrifices the molecular view but now incorporates the concept of entropy. Macroscopic thermodynamic approaches, as originally introduced by Gibbs and then elaborated by Tolman and others, lead to a mathematically rigorous description of a liquid drop but, as shown in the last part of section 3, cannot in themselves be used to determine the curvature dependence of the surface tension, either directly (which would require a knowledge of the free-energy density of the entire inhomogeneous system), or from the determination of the surface of tension. The latter is found to coincide with the Gibbs dividing surface so that the surface tension takes on its value in the planar limit $\gamma(R) = \gamma_\infty$ for any R, which would correspond to a Tolman length of zero ($\delta = 0$), rendering the Tolman theory inapplicable. In order to make progress, the microscopic methods of the statistical mechanics are clearly required.

There are essentially two ways of defining the surface tension within a statistical mechanical treatment. One approach relies on a mechanical definition of the surface tension as the stress transmitted across a strip of unit length normal to the interface. In this way, a connection between the macroscopic theory of elasticity and the components of a microscopic pressure tensor is made to determine the surface tension. Beyond the planar limit, however, one encounters conceptual difficulties with this approach, due to arbitrary nature of the definition of the pressure tensor. This lack of uniqueness was already appreciated by Irving and Kirkwood [94] and by Harasima [98], and later analysed in a detail for curved interfaces by Schofield and Henderson [5], who attributed this arbitrariness to the fundamental problem of the local definition of thermodynamic functions depending on two- or higher-body interactions (with the exception of the chemical potential). Surprisingly, these warnings are still often ignored and a mechanical treatment relying on a calculation of the surface tension via the pressure tensor is frequently adopted. There are two main reasons for the ill-advised popularity of a mechanical treatment: first of all, any problems related to the non-unique definition of the microscopic pressure tensor are apparent only beyond the planar limit, and secondly, the use of this route is tempting in simulation studies as one requires a knowledge of the forces

between two interacting particles in molecular dynamics simulation, and thus the components of the pressure tensor can be obtained easily.

The alternative route is based on the thermodynamic definition of the surface tension as the isochoric–isothermal change in the free energy per unit area due to the deformation of the interface. Within this approach one only deals with transformations of the partition function, so that any problems related with the pressure tensor inherent in the mechanical route can be avoided. Nevertheless, a consideration of first-order changes in surface area leads to an expression involving the gradient of the potential energy and the correlation function, which for a pairwise interaction gives an identical 'stress–strain' relation to that obtained with the mechanical route. By incorporating an auxiliary external field (the magnitude of which is eventually taken to zero) the second-order changes in surface area can be analysed in two ways: as a calculation of the magnitude of the external field needed to bend the surface; and as the change in the free energy accompanying an increase in surface area caused by capillary-wave density fluctuations. Both methods lead to identical formulae involving the one-body density distribution function and the direct correlation function. These expressions are not exact, but sound arguments provide support for their adequacy up to first order in curvature and, in particular, its consistency with the thermodynamic expression for the Tolman length.

From a more general point of view, the statistical mechanical expressions relating the macroscopic properties of fluids to a given microscopic model can be divided into the so-called virial and compressibility approaches. Expressions involving the direct correlation function clearly correspond to the latter, as commonly implemented in a standard statistical mechanical treatment of fluid systems. The use of the term 'virial' can however lead to some confusion. It is important to realize that what is often referred to as the virial route is actually only its first-order formulation, stemming from the virial theorem of Clausius [176]. This is the case with the common microscopic representations of the mechanical approach, which amount to a first-order change in free energy per unit area implicit in the thermodynamic approach, and which have been shown to be valid for homogeneous bulk systems. On the other hand the virial route is not in principle restricted to a first-order representation, even though the resulting extension to higher order in the deformation leads to expressions involving three- and higher-body correlation functions. Nevertheless, these higher-order terms can be extracted from simulation data for the distribution of the change in free energy associated with the deformation of the interface [72]: the second-order (fluctuation) term in the expression for the free-energy change turns out to be of the same order of magnitude as the first-order term for nanoscale drops. This clearly emphasizes the fact that the use of a first-order virial expression, such as that resulting from a standard mechanical treatment, neglects important contributions due to fluctuations. This will be the subject of a separate detailed study [171].

All the painful scrutiny and inconsistency of a mechanical (or virial) treatment can be avoided with the help of density functional theory (DFT), a thermodynamic path closely related to that of the compressibility route. Instead of determining the direct correlation function, however, one simply minimizes the grand potential functional to find the equilibrium density profile, and then all of the thermodynamic properties of the inhomogeneous system that are required for a Gibbs–Tolman thermodynamic description are available. In our current paper we have demonstrated the capability and tractability of DFT in providing an unambiguous description of the density profile and interfacial properties of liquid drops and gas bubbles. Using a non-local mean-field DFT in the canonical ensemble together with a consistent Gibbs–Tolman thermodynamic analysis we come to the following conclusions for liquid drops: the curvature dependence of the vapour–liquid interfacial tension of nanoscopic drops is non-monotonic, rising over the value for the planar limit, and then decaying slowly to this limit as the radius of the drop is further increased; this is consistent with a negative Tolman length, which we estimate to be about a tenth of the molecular diameter; the non-monotonic behaviour of the surface tension is reflected in the behaviour of the density at the centre of the drop, which is seen to cross the saturation values of the bulk system at higher temperatures; our analysis supports the validity of a first-order curvature dependence of the surface tension as predicted by the Tolman theory for drops with microscopic radii down to about 10 diameters (below which such a macroscopic approach is not expected to be valid); for smaller drops it appears that an additional curvature dependence of the $1/R^3$ form is required in the Tolman treatment of the surface tension in order to reproduce the full DFT results. The findings for nanoscale bubbles of vapour in a bulk liquid are more widely accepted: the curvature dependence of the surface tension is monotonic, remaining below the planar limit for all bubble radii; this again corresponds to a negative Tolman length, which indicates that as expected the tension acts on the liquid side of the interface.

Regarding the particular choice of density functional (local or non-local, mean-field etc), it is not fully clear what impact a given approximation has on the interfacial properties of microscopic drops. It is apparent, however, that to first order in the curvature of the drop the qualitative conclusions are rather insensitive to the particular form of free-energy functional. There now appears to be some consensus in the most recent DFT studies that the magnitude of the Tolman length is of the order of a tenth of a molecular diameter and of a negative sign. It is likely, however, that in attempts to go beyond a first-order curvature correction, the non-local nature of the density functional will play a significant role. In studies of more complex fluids, such as charged particles, polymer or surfactant solutions that may exhibit self-assembly, one would also expect that a non-local DFT which goes further than a mean-field treatment of the attractive perturbation term will provide a more appropriate description.

Acknowledgments

We are very grateful to Jim Henderson for his valuable comments and for stimulating discussions throughout the

course of this work, and thank Kurt Binder, Siegfried Dietrich, Bob Evans, Alejandro Gil-Villegas and Martin Horsch for their very helpful input. AM thanks the Engineering and Physical Sciences Research Council (EPSRC) of the UK for the award of a postdoctoral fellowship. Additional funding to the Molecular Systems Engineering Group from the EPSRC (grants GR/T17595, GR/N35991, and EP/E016340), the Joint Research Equipment Initiative (JREI) (GR/M94426), and the Royal Society-Wolfson Foundation refurbishment scheme is also gratefully acknowledged.

References

[1] Young T 1805 *Phil. Trans. R. Soc.* **95** 65
[2] Laplace P S 1806 *Traité de Mécanique Céleste; Supplément au Dixième Livre, Sur l'Action Capillaire* (Paris: Courcier)
[3] Rowlinson J S and Widom B 1982 *Molecular Theory of Capillarity* (Oxford: Clarendon)
[4] Henderson J R 1986 Statistical mechanics of spherical interfaces *Fluid Interfacial Phenomena* ed C A Croxton (New York: Wiley)
[5] Schofield P and Henderson J R 1982 *Proc. R. Soc. Lond.* A **379** 231
[6] Buff F P 1951 *J. Chem. Phys.* **19** 1591
[7] Thomson W (Lord Kelvin) 1871 *Phil. Mag.* **42** 448
[8] Gibbs J W 1875–1878 *Trans. Conn. Acad. Arts Sci.* **3** 108 343
[9] Gibbs J W 1878 *Am. J. Sci.* **16** 441
[10] Gibbs J W 1928 *The Collected Works of J Willard Gibbs* (New York: Longmans, Green and Co.)
[11] Tolman R C 1948 *J. Chem. Phys.* **16** 758
[12] Tolman R C 1949 *J. Chem. Phys.* **17** 118
[13] Tolman R C 1949 *J. Chem. Phys.* **17** 333
[14] Koening F O 1950 *J. Chem. Phys.* **18** 449
[15] Hill T L 1952 *J. Phys. Chem.* **56** 526
[16] Kondo S 1956 *J. Chem. Phys.* **25** 662
[17] Thomson J J and Thomson G P 1928 *Conduction of Electricity through Gases* 3rd edn (Cambridge: Cambridge University Press)
[18] Bakker G 1928 Kappillaritat und Oberflachenspannung *Handbuch der Experimentalphysik* vol 6 (Leipzig: Akademische Verlags gesselschaft)
[19] Farkas L 1927 *Z. Phys. Chem.* **125** 236
[20] Guggenheim E A 1940 *Trans. Faraday Soc.* **36** 397
[21] Helfrich W 1973 *Z. Naturf.* c **28** 693
[22] Gaydos J, Boruvka L, Rotenberg Y, Chen P and Neumann A W 1996 Generalized theory of capillarity *Applied Surface Thermodynamics* ed A W Neummann and J K Spelt (New York: Dekker)
[23] Oversteegen S M, Barneveld P A, van Male J, Leermakers F A M and Lyklema J 1999 *Phys. Chem. Chem. Phys.* **1** 4987
[24] Boruvka L and Neumann A W 1977 *J. Chem. Phys.* **66** 5464
[25] Evans R 1979 *Adv. Phys.* **28** 144
[26] Henderson D 1992 *Fundamentals of Inhomogeneous Fluids* (New York: Dekker)
[27] Davis H T 1996 *Statistical Mechanics of Phases and Interfaces and Thin Films* (Weinheim: Wiley)
[28] Rowlinson J S 1993 *Pure Appl. Chem.* **65** 873
[29] Blokhuis E M and Bedeaux D 1994 *Heterog. Chem. Rev.* **1** 55
[30] Reinold A W and Rücher A W 1886 *Phil. Trans. R. Soc.* **177** 627
[31] Weber R H 1901 *Ann. Phys.* **309** 706
[32] Defay R, Prigogine I and Bellemans A 1996 *Surface Tension and Adsorption* ed D H Everett (London: Longman) (translated from the French)
[33] Xue Y-Q, Yang X-C, Cui Z-X and Lai W-P 2011 *J. Phys. Chem.* B **115** 109
[34] Fisher L R and Israelachvili J N 1979 *Nature* **277** 548
[35] Fisher L R and Israelachvili J N 1980 *Chem. Phys. Lett.* **76** 325
[36] Fisher L R and Israelachvili J N 1981 *J. Colloid Interface Sci.* **80** 528
[37] Christenson H K 1988 *J. Colloid Interface Sci.* **121** 170
[38] Matsuoka H, Fukui S and Kato T 2002 *Langmuir* **18** 6796
[39] Jang J, Schatz G C and Ratner M A 2004 *Phys. Rev. Lett.* **92** 085504
[40] Fradin C, Braslau A, Luzet D, Smilgies D, Alba M, Boudet N, Mecke K and Daillant J 2000 *Nature* **403** 871
[41] Daillant J and Alba M 2000 *Rep. Prog. Phys.* **63** 1725
[42] Kellay H, Meunier J and Binks B P 1993 *Phys. Rev. Lett.* **70** 1485
[43] Kellay H, Binks B P, Hendrikx Y, Lee L T and Meunier J 1994 *Adv. Int. Colloid Sci.* **49** 85
[44] Gloor G J, Jackson G, Blas F J and de Miguel E 2005 *J. Chem. Phys.* **123** 134703
[45] Binder K and Kalos M H 1980 *J. Stat. Phys.* **22** 363
[46] Furukawa H and Binder K 1982 *Phys. Rev.* A **26** 556
[47] Rusanov A I and Brodskaya E N 1977 *J. Colloid Interface Sci.* **62** 542
[48] Powles J G, Fowler R F and Evans W A B 1983 *Chem. Phys. Lett.* **96** 289
[49] Powles J G, Fowler R F and Evans W A B 1983 *Phys. Lett.* A **98** 421
[50] Thompson S M, Gubbins K E, Walton J P R B, Chantry R A R and Rowlinson J S 1984 *J. Chem. Phys.* **81** 530
[51] Brodskaya E N and Rusanov A I 1987 *Mol. Phys.* **62** 251
[52] Nijmeijer M J P, Bruin C, van Woerkom A B, Bakker A F and van Leeuwen J M J 1992 *J. Chem. Phys.* **96** 565
[53] Haye M J and Bruin C 1994 *J. Chem. Phys.* **100** 556
[54] ten Wolde P R and Frenkel D 1998 *J. Chem. Phys.* **109** 9901
[55] El Bardouni H, Mareschal M, Lovett R and Baus M 2000 *J. Chem. Phys.* **113** 9804
[56] Moody M P and Attard P 2001 *J. Chem. Phys.* **115** 8967
[57] van Giessen A E and Blokhuis E M 2002 *J. Chem. Phys.* **116** 302
[58] Moody M P and Attard P 2003 *Phys. Rev. Lett.* **91** 056104
[59] Virnau P, Müller M, MacDowell L G and Binder K 2004 *New J. Phys.* **6** 7
[60] MacDowell L G, Virnau P, Müller M and Binder K 2004 *J. Chem. Phys.* **120** 5293
[61] Arcidiacono S, Poulikakos D and Ventiko Y 2004 *Phys. Rev.* E **70** 011505
[62] Lei Y A, Bykov T, Yoo S and Zeng X C 2005 *J. Am. Chem. Soc.* **127** 15346
[63] Vrabec J, Kedia G K, Fuchs G and Hasse H 2006 *Mol. Phys.* **104** 1509
[64] Salonen M, Napari I and Vehkamäki H 2007 *Mol. Sim.* **33** 245
[65] Hołyst R and Litniewski M 2008 *Phys. Rev. Lett.* **100** 055701
[66] Horsch M, Vrabec J and Hasse H 2008 *Phys. Rev.* E **78** 011603
[67] Neimark A V and Vishnyakov A 2005 *J. Chem. Phys.* **122** 174508
[68] Schrader M, Virnau P and Binder K 2009 *Phys. Rev.* E **79** 061104
[69] Schrader M, Virnau P, Winter D, Zykova-Timan T and Binder K 2009 *Eur. Phys. J. Spec. Top.* **177** 103

[70] Baidakov V G, Protsenko S P and Gorbatovskaya G G 2009 *Colloid J.* **71** 437
[71] van Giessen A E and Blokhuis E M 2009 *J. Chem. Phys.* **131** 164705
[72] Sampayo J G, Malijevský A, Müller E A, de Miguel E and Jackson G 2010 *J. Chem. Phys.* **132** 141101
[73] Block B J, Das S K, Oettel M, Virnau P and Binder K 2010 *J. Chem. Phys.* **133** 154702
[74] Julin J, Napari I, Merikanto J and Vehkamäki H 2010 *J. Chem. Phys.* **133** 044704
[75] Zhu R-Z and Yan H 2011 *Chin. Phys.* B **20** 016801
[76] Das S K and Binder K 2011 *Phys. Rev.* E **84** 061607
[77] Nakamura T, Shinoda W and Ikeshoji T 2011 *J. Chem. Phys.* **135** 094106
[78] Tröster A, Oettel M, Block B, Virnau P and Binder K 2012 *J. Chem. Phys.* **136** 064709
[79] Horsch M, Hasse H, Shchekin A K, Agarwal A, Eckelsbach S, Vrabec J, Müller E A and Jackson G 2012 *Phys. Rev.* E **85** 031605
[80] Kinjo Y and Matsumoto M 1998 *Fluid Phase Equilib.* **144** 343
[81] Kinjo Y, Ohguchi K, Yasuoka K and Matsumoto M 1999 *Comput. Mater. Sci.* **14** 138
[82] Park S H, Wang J G and Tien C L 2001 *Int. J. Heat Mass Transfer* **44** 1849
[83] Xiao C, Heyes D M and Powles J G 2002 *Mol. Phys.* **100** 3451
[84] Okumura H and Ito N 2003 *Phys. Rev.* E **67** 045301
[85] Matsumoto M and Tanaka K 2008 *Fluid Dyn. Res.* **40** 546
[86] Tsuda S, Takagi S and Matsumoo Y 2008 *Fluid Dyn. Res.* **40** 606
[87] Yamamoto T and Ohnishi S 2010 *Phys. Chem. Chem. Phys.* **12** 1033
[88] Torabi K and Corti D S 2010 *J. Chem. Phys.* **133** 134505
[89] Rezaei Nejad H, Ghassemi M, Mirnouri Langroudi S M and Shahabi A 2011 *Mol. Simul.* **37** 23
[90] Trokhymchuk A and Alejandre J 1999 *J. Chem. Phys.* **111** 8510
[91] Strutt J W (Lord Rayleigh) 1890 *Phil. Mag.* **30** 285
Strutt J W (Lord Rayleigh) 1890 *Phil. Mag.* **30** 456
[92] van der Waals J D 1893 *Z. Phys. Chem.* **13** 657
[93] Kirkwood J G and Buff F P 1949 *J. Chem. Phys.* **17** 338
[94] Irving J H and Kirkwood J G 1950 *J. Chem. Phys.* **18** 817
[95] MacLellan A G 1952 *Proc. R. Soc.* A **213** 274
[96] Harasima A 1953 *J. Phys. Soc. Japan* **8** 343
[97] Buff F P 1955 *J. Chem. Phys.* **23** 419
[98] Harasima A 1958 *Adv. Chem. Phys.* **1** 203
[99] Cahn J W and Hilliard J E 1958 *J. Chem. Phys.* **28** 258
[100] Buff F P, Lovett R A and Stillinger F H 1965 *Phys. Rev. Lett.* **15** 612
[101] Fisher M E 1967 *Physics* **3** 255
[102] Triezenberg D G and Zwanzig R 1972 *Phys. Rev. Lett.* **28** 1183
[103] Lovett R, DeHaven P W, Vieceli J J and Buff F P 1973 *J. Chem. Phys.* **58** 1880
[104] Lekner J and Henderson J R 1977 *Mol. Phys.* **34** 333
[105] Sullivan D E 1979 *Phys. Rev.* B **20** 3991
[106] Schofield P 1979 *Chem. Phys. Lett.* **62** 413
[107] Falls A H, Scriven L E and Davis H T 1981 *J. Chem. Phys.* **75** 3986
[108] Hemingway S J, Henderson J R and Rowlinson J S 1981 *Faraday Symp. Chem. Soc.* **16** 33
[109] Schofield P and Henderson J R 1982 *Proc. R. Soc.* A **379** 231
[110] Yang A J 1983 *J. Phys. Chem.* **79** 6289
[111] Fisher M P A and Wortis M 1984 *Phys. Rev.* B **29** 6252
[112] Yang A J 1985 *J. Phys. Chem.* **82** 2082
[113] Hooper M A and Nordholm S 1984 *J. Chem. Phys.* **81** 2431
[114] Powles J G 1985 *J. Phys. A: Math. Gen.* **18** 1551
[115] Guermeur R, Biquard F and Jacolin C 1985 *J. Phys. Chem.* **82** 2040
[116] Lee D J, Telo da Gama M M and Gubbins K E 1986 *J. Chem. Phys.* **85** 490
[117] Rowlinson J S 1987 *Pure Appl. Chem.* **59** 15
[118] Oxtoby D W and Evans R 1988 *J. Chem. Phys.* **89** 7521
[119] Melrose J C 1989 *Langmuir* **5** 290
[120] Baus M and Lovett R 1990 *Phys. Rev. Lett.* **65** 1781
[121] Gelfand M P and Fisher M E 1990 *Physica* A **166** 1
[122] Romero-Rochin V, Varea C and Robledo A 1991 *Phys. Rev.* A **44** 8417
[123] Zeng X C and Oxtoby D W 1991 *J. Chem. Phys.* **94** 4472
[124] Baus M and Lovett R 1991 *Phys. Rev.* A **44** 12411
[125] Blokhuis E M and Bedeaux D 1992 *J. Chem. Phys.* **97** 3576
[126] Lovett R and Baus M 1992 *Physica* A **181** 309
[127] Blokhuis E M and Bedeaux D 1992 *Physica* A **184** 42
[128] Rowlinson J S 1994 *J. Phys.: Condens. Matter* **6** A1
[129] Hadjiagapiou I 1994 *J. Phys.: Condens. Matter* **6** 5303
[130] Iwamatsu M 1994 *J. Phys.: Condens. Matter* **6** L173
[131] Talanquer V and Oxtoby D W 1995 *J. Phys. Chem.* **99** 2865
[132] Baidakov V G and Boltachev G Sh 1995 *Russ. J. Phys. Chem.* **69** 468
[133] Wallqvist A and Berne B J 1995 *J. Phys. Chem.* **99** 2885
[134] Somoza A M, Chacón E, Mederos L and Tarazona P 1995 *J. Phys.: Condens. Matter* **7** 5753
[135] Bieker T and Dietrich S 1998 *Physica* A **252** 85
[136] Koga K, Zeng X C and Shchekin A K 1998 *J. Chem. Phys.* **109** 4063
[137] van Giessen A E, Blokhuis E M and Bukman D J 1998 *J. Chem. Phys.* **108** 1148
[138] Granasy L 1998 *J. Phys. Chem.* **109** 9660
[139] Stuart S J and Berne B J 1999 *J. Phys. Chem.* A **103** 10300
[140] Bykov T V and Zeng X C 2001 *J. Phys. Chem.* B **105** 11586
[141] Schmelzer J W P and Baidakov V G 2001 *J. Phys. Chem.* B **105** 11595
[142] Bartell L S 2001 *J. Phys. Chem.* B **105** 11615
[143] Bykov T V and Zeng X C 2002 *J. Phys. Chem.* **117** 1851
[144] Evans R, Henderson J R and Roth R 2004 *J. Chem. Phys.* **121** 12074
[145] Stewart M C and Evans R 2005 *Phys. Rev.* E **71** 011602
[146] Xiao C, Heyes D M and Powles J G 2005 *Phys. Status Solidi* **242** 749
[147] Ruckenstein E and Djikaev Y S 2005 *Adv. Colloid Interface Sci.* **118** 51
[148] Bykov T V and Zeng X C 2006 *J. Chem. Phys.* **125** 144515
[149] Blokhuis E M and Kuipers J 2006 *J. Chem. Phys.* **124** 074701
[150] Santiso E and Firoozabadi A 2006 *AIChE J.* **52** 1
[151] Hennequin Y, Aarts D G A L, van der Wiel J H, Wegdam G, Eggers J, Lekkerkerker H N W and Bonn D 2006 *Phys. Rev. Lett.* **97** 244502
[152] Chakraborty P and Zachariah M R 2007 *J. Phys. Chem.* A **111** 5459
[153] Brus D, Ždímal V and Smolík J 2008 *J. Chem. Phys.* **129** 174501
[154] Li Z and Wu J 2008 *Ind. Eng. Chem. Res.* **47** 4988
[155] Nold A, Malijevský A and Kalliadasis S 2011 *Eur. Phys. J. Spec. Top.* **197** 185
[156] Nold A, Malijevský A and Kalliadasis S 2011 *Phys. Rev.* E **84** 021603
[157] Corti D S, Kerr K J and Torabi K 2011 *J. Chem. Phys.* **135** 024701
[158] Ghosh S and Ghosh S K 2011 *J. Chem. Phys.* **135** 124710
[159] Zhou D, Zeng M, Mi J and Zhong C 2011 *J. Phys. Chem.* B **115** 57
[160] Lutsko J F 2011 *J. Chem. Phys.* **134** 164501
[161] Tarazona P 1984 *Mol. Phys.* **52** 81

[162] Rosenfeld Y 1989 *Phys. Rev. Lett.* **63** 980
[163] Fowler R H 1937 *Proc. R. Soc. Lond.* **159A** 229
[164] Dupré A 1869 *Théorie Mécanique de la Chaleur* (Paris: Gauthier-Villars)
[165] Maxwell J C 1876 *Capillary Action, Encyclopaedia Britannica* 9th edn (London: A&C Black)
[166] Boltzmann L 1872 *Sitz. Akad. Wiss. Wien* **66** 275
[167] Widom B 1963 *J. Chem. Phys.* **39** 2808
[168] Noether E 1918 Invariante variationsprobleme *Nachr. D. König. Gesellsch. D. Wiss. Zu Göttingen Math-phys. Klasse* 235
[169] Misner C W, Thorne K S and Wheeler J A 1973 *Gravitation* (San Francisco: Freeman)
[170] Weeks J D, Chandler D and Andersen H C 1971 *J. Chem. Phys.* **54** 5237
[171] Sampayo J G, Malijevský A, Müller E A, de Miguel E and Jackson G 2012 in preparation
[172] Boublík T 1986 *Mol. Phys.* **59** 371
[173] Malijevský A 2006 *J. Chem. Phys.* **125** 194519
[174] Fisher M E and Widom B 1969 *J. Chem. Phys.* **50** 3756
[175] Henderson J R, Evans R, Hoyle D C, Parry A O and Sabeur Z A 1993 *Mol. Phys.* **80** 755
[176] Clausius R J E 1870 *Phil. Mag.* **40** 122

Paper IV

Critical Point Wedge Filling

Alexandr Malijevský
Department of Physical Chemistry, Institute of Chemical Technology, Prague, 166 28 Praha 6, Czech Republic

Andrew O. Parry
Department of Mathematics, Imperial College London, London SW7 2B7, United Kingdom

(Received 9 January 2013; published 17 April 2013)

We present results of a microscopic density functional theory study of wedge filling transitions, at a right-angle wedge, in the presence of dispersionlike wall-fluid forces. Far from the corner the walls of the wedge show a first-order wetting transition at a temperature T_w which is progressively closer to the bulk critical temperature T_c as the strength of the wall forces is reduced. In addition, the meniscus formed near the corner undergoes a filling transition at a temperature $T_f < T_w$, the value of which is found to be in excellent agreement with macroscopic predictions. We show that the filling transition is first order if it occurs far from the critical point but is continuous if T_f is close to T_c even though the walls still show first-order wetting behavior. For this continuous transition the distance of the meniscus from the apex grows as $\ell_w \approx (T_f - T)^{-\beta_w}$ with the critical exponent $\beta_w \approx 0.46 \pm 0.05$ in good agreement with the phenomenological effective Hamiltonian prediction. Our results suggest that critical filling transitions, with accompanying large scale universal interfacial fluctuation effects, are more generic than thought previously, and are experimentally accessible.

DOI: 10.1103/PhysRevLett.110.166101 PACS numbers: 68.08.Bc, 64.60.F−, 68.03.Cd

There is now direct experimental evidence for the thermal excitation of the gravity stabilized capillary-wave-like fluctuations at the interface between coexisting fluid phases [1]. Over the last few decades theory has predicted that such fluctuation effects are particularly important at certain types of interfacial phase transitions such as critical wetting [2–6]. Wetting refers to the unbinding of a fluid interface from a solid substrate (or another fluid interface) on approaching a temperature T_w, at which the contact angle θ vanishes. The order of these transitions is determined by the subtle interplay between wall-fluid and fluid-fluid intermolecular forces and also interfacial fluctuations. The original macroscopic argument for wetting transitions had predicted that the transition would be first order, and should necessarily occur on approaching the bulk critical temperature T_c [7]. Model calculations soon revealed that the location and order of the transition are more general than this. In particular, Nakanishi and Fisher showed that, for systems with short-ranged forces, the transition should change from first order to continuous, if the surface forces are weakened and T_w approaches T_c [8]. While this has been fully tested in Ising model studies [9], this scenario is altered by the presence of long-ranged, dispersionlike intermolecular forces. In order to see continuous (now referred to as "critical") wetting transitions one requires a fine tuning of the range and strengths of the solid-fluid and fluid-fluid forces [2,10]. Consequently while there are many examples of first-order wetting, there are no unambiguous experimental examples of critical wetting for solid-fluid interfaces, although the transition has been seen in a few binary mixtures [5].

One way around this, which would allow one to see the strong influence of interfacial fluctuations on a continuous phase transition, is to consider fluid adsorption in a linear wedge for which there is an analogous transition referred to as filling [11–15]. This transition is far more common in nature than the wetting transition and was first studied experimentally almost 40 years ago [16] although the order of the transition was not considered. Recent phenomenological effective Hamiltonian models have predicted that fluctuation effects are enhanced compared to wetting and also that the requirements that the transition can be continuous are more relaxed [17–19]. While this has been studied extensively in the Ising model [20–24], the more realistic case of long-ranged forces has not been studied in detail. In this Letter we present the results of a study of filling in the presence of dispersion forces, based on a microscopic classical density functional theory (DFT). The latter has been instrumental in developing our understanding of inhomogeneous fluids but is most usually applied to systems in which the equilibrium density depends on only one coordinate [25–28]. Here we use a two-dimensional DFT to study filling transitions and compare with the predictions of thermodynamic arguments and effective Hamiltonian theory. We find that close to T_c the filling transition is continuous even though the walls of the wedge themselves still exhibit first-order wetting. This result allows us to check interfacial Hamiltonian predictions for the critical behavior and offers strong encouragement that continuous filling transitions may be found in the laboratory similar to experiments on complete wedge filling [29].

Consider a wedge geometry formed by two identical infinite planar walls that meet at an opening angle 2ψ in contact with a bulk vapor at the chemical potential μ, tuned to saturation $\mu = \mu_{\rm sat}^-$ at a temperature $T < T_c$. The wedge may be thought of as being a missing link between a planar wall ($\psi = \pi/2$) and a capillary slit ($\psi = 0$) and shows a phase transition (filling) which is distinct from wetting and capillary condensation. Far from the apex the thickness of the liquid wetting layer ℓ_π is the same as for a planar wall. However near the apex, the thickness of the meniscus can be much greater. Macroscopic arguments dictate that the wedge is completely filled above a filling transition temperature T_f which occurs when the contact angle of a liquid drop satisfies [11–14]

$$\theta(T_f) = \frac{\pi}{2} - \psi. \tag{1}$$

The wedge filling transition corresponds to the change from microscopic to macroscopic adsorption, as $T \to T_f$, and may be first order or continuous (critical filling) corresponding to the discontinuous or continuous divergence of the adsorption. Because Eq. (1) is an exact requirement, the filling transition is ubiquitous in nature for all fluids that form drops with a finite contact angle.

Within classical DFT the equilibrium density profile is found by minimizing the grand potential functional $\Omega[\rho] = F[\rho] + \int d\mathbf{r}\rho(\mathbf{r})[V(\mathbf{r}) - \mu]$, where $V(\mathbf{r})$ is the external potential [30]. We consider a right angle wedge ($\psi = \pi/4$) so that the potential $V(\mathbf{r}) = V(x, z)$ is a function of Cartesian coordinates x, $z > 0$ and is translationally invariant along the wedge. Here $F[\rho]$ is the intrinsic free energy functional of the fluid one-body density $\rho(\mathbf{r})$, which can be split into ideal and excess parts. Modern DFT often divides the latter into a hard-sphere part $F_{\rm hs}[\rho]$ and an attractive contribution $F_a[\rho] = \frac{1}{2}\int\int d\mathbf{r}_1 d\mathbf{r}_2 \rho(\mathbf{r}_1)\rho(\mathbf{r}_2)u_a(r_{12})$ where $u_a(r)$ is the attractive part of the fluid-fluid potential. We take this to be a Lennard-Jones (LJ) potential $u_a(r) = -4\varepsilon(\sigma/r)^6 H(r-\sigma)$ which is truncated at $r_c = 2.5\sigma$, where σ is the hard-sphere diameter and $H(x)$ is the Heaviside function. For $F_{\rm hs}[\rho]$ we use Rosenfeld's fundamental theory which accurately models packing effects if the density is high close to the walls [31,32]. The external potential arises from a uniform distribution of wall atoms, with density ρ_w, which for $r > \sigma$ interact with the fluid atoms via the LJ potential $\phi_w(r) = -4\varepsilon_w(\frac{\sigma}{r})^6$, leading to

$$V(x, z) = \alpha_w\left[\frac{1}{z^3} + \frac{2z^4 + x^2z^2 + 2x^4}{2x^3z^3\sqrt{x^2 + z^2}} + \frac{1}{x^3}\right], \tag{2}$$

where $\alpha_w = -(1/3)\pi\varepsilon_w\rho_w\sigma^6$. There is a hard-wall repulsion if x, $z < \sigma$. Infinitely far from the wedge apex, the potential close to either surface recovers that of a planar wall, e.g., $V(\infty, z) = 2\alpha_w/z^3$. The functional $\Omega[\rho]$ is minimized numerically on an $L \times L$ grid where the lateral dimension of our box is $L = 50\sigma$ and the grid has a discretization size 0.05σ. To mimic the bulk boundary conditions we impose $\rho(L, z) = \rho_\pi(z)$ and $\rho(x, L) = \rho_\pi(x)$ where $\rho_\pi(z)$ is the equilibrium profile for a planar wall-fluid interface with $\rho_\pi(L)$ fixed to the bulk gas density ρ_g. In our model DFT $k_BT_c/\varepsilon = 1.414$ and temperature is expressed either in fractions of T_c or in dimensionless units $T^* = k_BT/\varepsilon$.

We have considered a variety of wall strengths and present results for $\varepsilon_w = 1.2\varepsilon$, $\varepsilon_w = \varepsilon$, and $\varepsilon_w = 0.8\varepsilon$. For each, we first considered the planar wall with the potential $V_\pi(z) = 2\alpha_w/z^3$ and determined the density profile $\rho_\pi(z)$ and surface tensions $\gamma_{\rm wg}$, $\gamma_{\rm wl}$, and γ of the wall-gas, wall-liquid and liquid-gas interfaces, respectively. From Young's equation $\cos\theta = (\gamma_{\rm wg} - \gamma_{\rm wl})/\gamma$ we determined $\theta(T)$ for each of these systems (see Fig. 1). Each system exhibits a wetting transition, with T_w determined from the crossing of $\gamma_{\rm wg}$ and $\gamma_{\rm wl} + \gamma$. These occur at $T_w = 0.83T_c$, $T_w = 0.93T_c$ and $T_w = 0.99T_c$ as ε_w is reduced. The wetting transitions are all first order; that is, the thickness of the liquid layer ℓ_π jumps from a microscopic to macroscopic value at T_w. This is to be expected since the wall-fluid potential is long ranged but the truncated LJ fluid-fluid interaction is effectively short ranged [2]. This prohibits critical wetting, which is important for our study. Also, as expected, the strength of the first-order transition decreases as T_w approaches T_c. This is apparent when one determines the interfacial binding potential $W(\ell)$ corresponding to the excess grand potential of a wetting film constrained to be of thickness ℓ. The global minimum of this determines the equilibrium film thickness ℓ_π. This is shown in Fig. 2 for the case $\varepsilon_w = 0.8\varepsilon$ close to the wetting temperature and shows an activation barrier, characteristic of first-order wetting, at $\ell_B \approx 10\sigma$. For comparison the barrier for the binding potential for $\varepsilon_w = \varepsilon$ is an order of magnitude larger and located at $\ell_B \approx 4\sigma$.

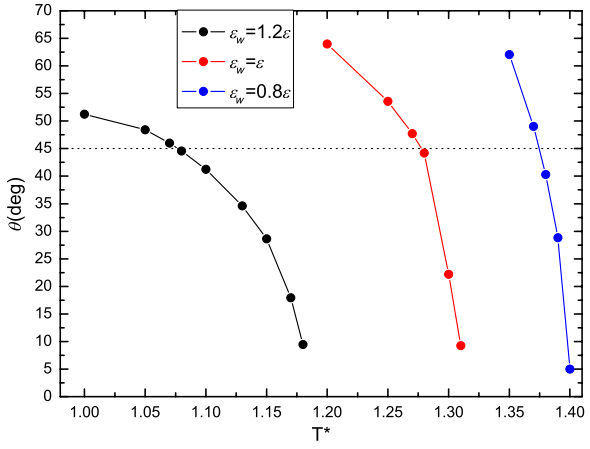

FIG. 1 (color online). Variation of the contact angle with T for different wall strengths. The intersection with the dashed line at $\theta = 45°$ is the thermodynamic prediction for T_f.

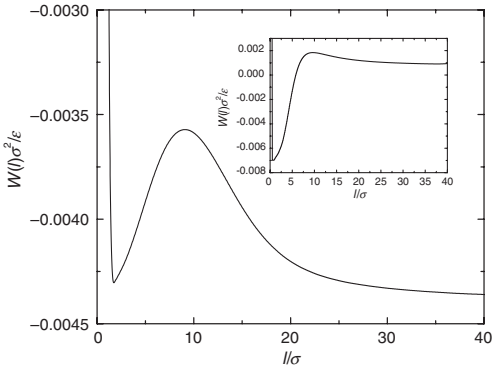

FIG. 2. Binding potential function $W(\ell)$ for $\varepsilon_w = 0.8\varepsilon$ close to a first-order wetting transition at $T_w^* = 1.4$ showing an activation barrier at $\ell_B \approx 10\sigma$. In the inset we show the binding potential at a lower temperature close to $T_f^* \approx 1.38$ for which the activation barrier is still present. In both cases the results correspond to a bulk coexistence.

According to the thermodynamic prediction Eq. (1), the location of the filling transitions can be determined from the intersection of the contact angle curves with $\psi = \pi/4$ and gives $T_f = 0.76T_c$, $T_f = 0.90T_c$, and $T_f = 0.97T_c$ as ε_w decreases in strength. To check this we set $\mu = \mu_{\rm sat}^-$ and minimize $\Omega[\rho]$ to a global or local minimum Ω, starting from different high density and low density configurations. For first-order filling these will converge to different equilibrium profiles, corresponding to microscopic and macroscopic adsorptions, which coexist at T_f. This is what is found for the two strongest walls as illustrated in Fig. 3 where we plot the excess grand potential $\Omega^{\rm ex} = \Omega + pV$ per unit volume as a function of T. The values for T_f obtained are in near exact agreement with the thermodynamic predictions and differ from them only due to the limitations of numerical discretization and finite size. In Fig. 4 we show the coexisting density profiles $\rho(x, z)$, corresponding to macroscopic (left) and

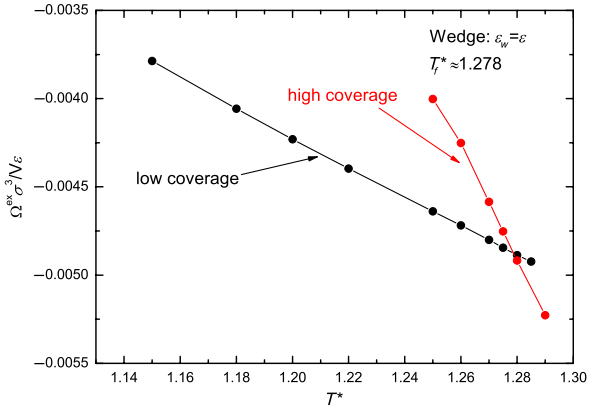

FIG. 3 (color online). Location of a first-order filling transition for $\varepsilon_w = \varepsilon$. Here V is the available volume which is the length of the wedge multiplied by $(L - \sigma)^2$.

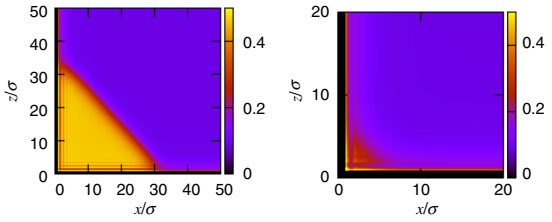

FIG. 4 (color online). Coexisting macroscopic (left) and microscopic (right) density profiles at a first-order filling transition for $\varepsilon_w = \varepsilon$.

microscopic (right) states, for $\varepsilon_w = \varepsilon$. From these we can determine the thickness ℓ_w of the meniscus above the wedge apex defined as the distance from the origin to a point on a diagonal where $\rho(x, x) = (\rho_l + \rho_g)/2$. The macroscopic meniscus is nearly flat (as it should be since we are at bulk coexistence) and meets each wall at the correct contact angle $\theta \approx \pi/4$. Of course the size of this macroscopic state is limited by our numerical grid and scales with the system size L. For the microscopic configuration the meniscus thickness ℓ_w is larger than the wetting layer thickness ℓ_π but of the same order as the distance of the activation barrier $\ell_B \approx 4\sigma$ for the corresponding binding potential for the wetting transition. This is precisely the expectation for first-order filling from effective Hamiltonian theory [18]. Both microscopic and macroscopic profiles show layering behavior close to the apex.

For the weakest wall strength $\varepsilon_w = 0.8\varepsilon$, however, both initial coverages converge to a unique phase indicating that the transition, which is of course rounded by the finite size of our system, is continuous. A plot of the adsorption $\Gamma = \iint dxdz(\rho(x, z) - \rho_g)$ vs T is shown in Fig. 5 and shows a dramatic but continuous increase in the adsorption near the anticipated $T_f^* \approx 1.38$. A cross section of the density

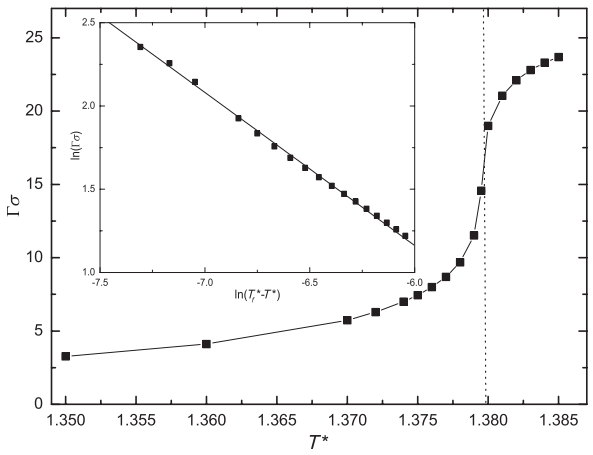

FIG. 5. Temperature dependence of the adsorption in the wedge with the weakest wall interaction $\varepsilon_w = 0.8\varepsilon$. The inset shows the log-log plot of the adsorption vs the scaling field $T_f - T$. The slope of the straight line is -0.92.

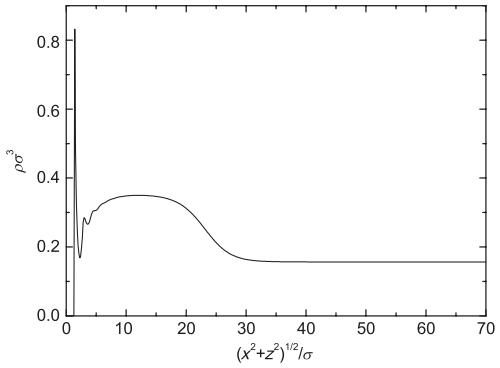

FIG. 6. Density profile along the diagonal from (0, 0) to (L, L) at the filling temperature T_f for $\varepsilon_w = 0.8\varepsilon$.

profile along the diagonal $\rho(x, x)$ for $T \approx T_f$ is also shown (see Fig. 6). This indicates that the order of the filling transition is changed near the vicinity of T_c. Support for this comes from the two sources. First, near T_f the meniscus height $\ell_w \approx 22\sigma$ is considerably larger than the location of the activation barrier $\ell_B \approx 10\sigma$ associated with the wetting binding potential (see the inset in Fig. 2). This is not at all expected for first-order filling [18]. Second, we can compare quantitatively with predictions for critical filling. If the transition is critical then in an infinite wedge we expect that $\ell_w \sim (T_f - T)^{-\beta_w}$ with $\Gamma \propto \ell_w^2$ owing to the triangular shape of the meniscus. Effective Hamiltonian theory predicts that the critical singularities depend on the power law describing the dominant wall-fluid or fluid-fluid interaction which we may write more generally as $V(z) \approx 1/z^{p+1}$. The critical behavior falls into two regimes with $\beta_w = 1/p$ for $p < 4$ and $\beta_w = 1/4$ for $p > 4$ [18]. Thus we anticipate $\beta_w = 1/2$ in our model since $p = 2$. The inset in Fig. 5 shows a log plot of the adsorption for $T < T_f$, in which we use an unfitted estimate of the filling temperature $T_f^* = 1.38$ obtained from Eq. (1). This gives $\beta_w = 0.46 \pm 0.05$ in good agreement with the predicted value.

The presence of a critical (or at least effectively critical) filling transition when T_f is close to T_c, when the walls still exhibit first-order wetting, and in the presence of realistic long-ranged interactions is the main new result of our Letter, and is we believe encouraging for experimental studies. To date there have only been detailed laboratory studies of complete filling in linear wedges corresponding to the approach to coexistence when the walls are completely wet ($\theta = 0$) [29]. However the observation of critical filling would be more interesting because fluctuation effects are much stronger. For example, we expect that beyond mean-field level, capillary-wave fluctuations do not alter the divergence of $\ell_w \approx (T_f - T)^{-1/2}$ but do lead to a universal interfacial roughness (width) $\xi_\perp \approx (T_f - T)^{-1/4}$ which is much bigger than for complete filling and also critical wetting [18]. These fluctuations are not captured by the present DFT and consequently the density profiles will be broader than predicted here. However our DFT should be otherwise extremely accurate regarding the location of the transition, its order, and the adsorption. The observed change in order from first order to continuous filling has only been partially anticipated by the previous effective Hamiltonian theory. This had been predicted on the basis of a simple interfacial model, valid only for shallow wedges, but the proposed mechanism required that both the wall-fluid and fluid-fluid forces be of the same range. Then it was noted that even for first-order wetting, the filling transition would be continuous if it occurs at a temperature below which the activation barrier forms in the binding potential $W(\ell)$ [18]. However in the present DFT study a small activation barrier is still present at T_f (see the inset in Fig. 2), indicating that the prediction of the simple, shallow wedge, effective Hamiltonian theory is not completely correct. Nevertheless we believe that the substantial reduction in the size of the barrier as T approaches T_c plays a prominent role in the change of order of the filling transition. Finally it would be interesting to know if the change in order occurs via a tricritical or critical end point and also what happens for more acute wedges with stronger wall potentials.

In this Letter we have presented our results of numerical studies of first-order and critical filling transitions in a rectangular wedge using a nonlocal density functional theory. This is the first time that filling transitions have been studied using modern microscopic DFT in the presence of long-ranged wall-fluid interactions, and the results show that close to the bulk critical temperature the wedge filling transition may be continuous even though the walls themselves exhibit first-order wetting.

A. M. acknowledges a support from the Czech Science Foundation, Project No. 13-09914S.

[1] D. G. A. L. Aarts, M. Schmidt, and H. N. W. Lekkerkerker, Science **304**, 847 (2004).
[2] S. Dietrich, in *Phase Transitions and Critical Phenomena*, edited by C. Domb and J. L. Lebowitz (Academic, New York, 1988), Vol. 12.
[3] D. E. Sullivan and M. M. Telo da Gama, in *Fluid Interfacial Phenomena*, edited by C. A. Croxton (Wiley, New York, 1985).
[4] M. Schick, in *Liquids and Interfaces*, edited by J. Chorvolin, J. F. Joanny, and J. Zinn-Justin (Elsevier, New York, 1990).
[5] D. Bonn, J. Eggers, J. Indekeu, J. Meunier, and E. Rolley, Rev. Mod. Phys. **81**, 739 (2009).
[6] W. F. Saam, J. Low Temp. Phys. **157**, 77 (2009).
[7] J. W. Cahn, J. Chem. Phys. **66**, 3667 (1977).
[8] H. Nakanishi and M. E. Fisher, Phys. Rev. Lett. **49**, 1565 (1982).
[9] K. Binder and D. P. Landau, Phys. Rev. B **37**, 1745 (1988).

[10] R. Lipowsky and D. M. Kroll, Phys. Rev. Lett. **52**, 2303 (1984).
[11] R. Shuttleworth and G. L. J. Bailey, Discuss. Faraday Soc. **3**, 16 (1948).
[12] P. Concus and R. Finn, Proc. Natl. Acad. Sci. U.S.A. **63**, 292 (1969).
[13] Y. Pomeau, J. Colloid Interface Sci. **113**, 5 (1986).
[14] E. H. Hauge, Phys. Rev. A **46**, 4994 (1992).
[15] K. Rejmer, S. Dietrich, and M. Napiorkówski, Phys. Rev. E **60**, 4027 (1999).
[16] P. Concus and R. Finn, Proc. Natl. Acad. Sci. U.S.A. **63**, 292 (1969).
[17] A. O. Parry, C. Rascón, and A. J. Wood, Phys. Rev. Lett. **83**, 5535 (1999).
[18] A. O. Parry, C. Rascón, and A. J. Wood, Phys. Rev. Lett. **85**, 345 (2000).
[19] N. R. Bernardino, A. O. Parry, and J. M. Romero-Enrique, J. Phys. Condens. Matter **24**, 182202 (2012).
[20] A. Milchev, M. Müller, K. Binder, and D. P. Landau, Phys. Rev. Lett. **90**, 136101 (2003); Phys. Rev. E **68**, 031601 (2003).
[21] M. Müller and K. Binder, J. Phys. Condens. Matter **17**, S333 (2005).
[22] A. O. Parry, A. J. Wood, E. Carlon, and A. Drzewinski, Phys. Rev. Lett. **87**, 196103 (2001).
[23] D. B. Abraham and A. Maciołek, Phys. Rev. Lett. **89**, 286101 (2002).
[24] D. B. Abraham, V. Mustonen, and A. J. Wood, Europhys. Lett. **63**, 408 (2003).
[25] R. Evans, U. Marini Bettolo Marconi, and P. Tarazona, J. Chem. Phys. **84**, 2376 (1986).
[26] R. Evans, J. Phys. Condens. Matter **2**, 8989 (1990).
[27] M. C. Stewart and R. Evans, Phys. Rev. E **71**, 011602 (2005).
[28] A. Nold, A. Malijevský, and S. Kalliadasis, Phys. Rev. E **84**, 021603 (2011).
[29] L. Bruschi, A. Carlin, and G. Mistura, Phys. Rev. Lett. **89**, 166101 (2002).
[30] R. Evans, Adv. Phys. **28**, 143 (1979).
[31] Y. Rosenfeld, Phys. Rev. Lett. **63**, 980 (1989).
[32] R. Roth, J. Phys. Condens. Matter **22**, 063102 (2010).

Paper V

J. Phys.: Condens. Matter **25** (2013) 305005 (11pp) doi:10.1088/0953-8984/25/30/305005

Density functional study of complete, first-order and critical wedge filling transitions

Alexandr Malijevský[1,2] **and Andrew O Parry**[3,4]

[1] E. Hála Laboratory of Thermodynamics, Institute of Chemical Process Fundamentals, Academy of Sciences, 16502 Prague 6, Czech Republic
[2] Department of Physical Chemistry, Institute of Chemical Technology, Prague, 16628 Praha 6, Czech Republic
[3] Department of Mathematics, Imperial College London, London SW7 2B7, UK
[4] Departmento de Matematicas, Universidad Carlos III Madrid, Leganés, Madrid, Spain

Received 9 April 2013, in final form 12 June 2013
Published 9 July 2013
Online at stacks.iop.org/JPhysCM/25/305005

Abstract
We present numerical studies of complete, first-order and critical wedge filling transitions, at a right angle corner, using a microscopic fundamental measure density functional theory. We consider systems with short-ranged, cut-off Lennard-Jones, fluid–fluid forces and two types of wall–fluid potential: a purely repulsive hard wall and also a long-ranged potential with three different strengths. For each of these systems we first determine the wetting properties occurring at a planar wall, including any wetting transition and the dependence of the contact angle on temperature. The hard wall corner is completely filled by vapour on approaching bulk coexistence and the numerical results for the growth of the meniscus thickness are in excellent agreement with effective Hamiltonian predictions for the critical exponents and amplitudes, at leading and next-to-leading order. In the presence of the attractive wall–fluid interaction, the corresponding planar wall–fluid interface exhibits a first-order wetting transition for each of the interaction strengths considered. In the right angle wedge geometry the two strongest interactions produce first-order filling transitions while for the weakest interaction strength, for which wetting and filling occur closest to the bulk critical point, the filling transition is second-order. For this continuous transition the critical exponent describing the divergence of the meniscus thickness is found to be in good agreement with effective Hamiltonian predictions.

(Some figures may appear in colour only in the online journal)

1. Introduction

Wetting transitions and related fluid interfacial phenomena have been extensively studied over the past few decades (see, for example, the excellent review articles [1–5]). The vast majority of early theoretical studies focused on fluid adsorption on idealized planar substrates, or between parallel plates [6, 7] or around spheres and cylinders [8–11], in which the equilibrium density profile is one-dimensional and depends only on the coordinate normal to the substrate. More recently, however, there has been considerable interest in adsorption and wetting at micro-patterned surfaces in which the substrate is non-planar [12] or is chemically heterogeneous [13]. This work has been motivated mainly by improvements in surface lithography and related techniques, which now allow the controlled fabrication of the tailored substrates which are central to the development of microfluidics. At a more fundamental level, however, such studies have revealed new examples of interfacial phase transitions and fluctuation effects, as well as surprising connections between adsorption in different geometries [14–21].

A particularly simple and important example of a non-planar substrate is a wedge geometry formed by two identical infinite planar walls that meet at an opening angle $2\psi = \pi - 2\alpha$, where α is the tilt angle with respect to the

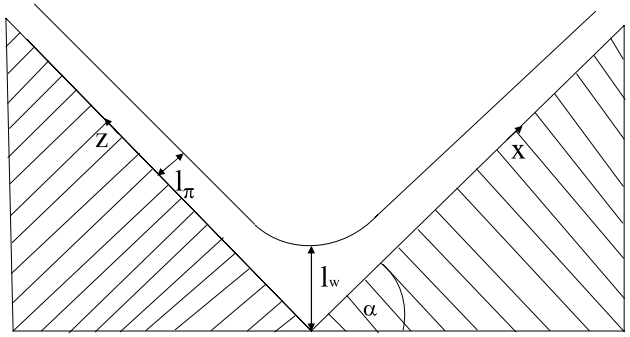

Figure 1. Schematic picture of the cross-section of a right angle wedge for which $\alpha = \pi/4$. Far from the apex, the wetting layer is of thickness ℓ_π. However, the height of the meniscus above the apex is ℓ_w. At a filling transition ℓ_w changes from microscopic to macroscopic. The Cartesian coordinates x and z used in our analysis are shown.

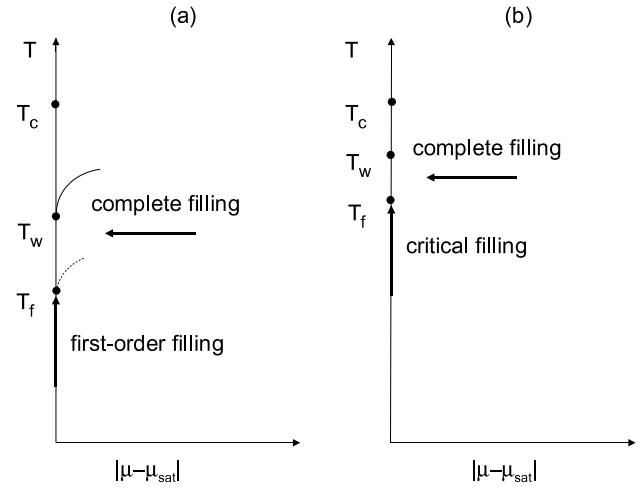

Figure 2. Schematic phase diagrams for wetting and filling at a wedge–vapour interface; (a) first-order wetting and filling transitions, (b) continuous wetting and filling transitions. If the wetting transition is weakly first-order the filling transition may be continuous (critical), in which case the pre-filling line (dotted) is absent.

horizontal plane (say). In figure 1 we schematically show a section of a three-dimensional wedge where the walls meet at a right angle corresponding to $\alpha = \pi/4$. The wedge geometry may be thought as being a missing link between the very well studied examples of a planar wall ($\alpha = 0$) and a capillary-slit ($\alpha = \pi/2$) and shows a phase transition which is distinct from wetting and capillary condensation. Let us suppose that the substrate is in contact with a bulk vapour at chemical potential μ, tuned to saturation $\mu = \mu_{\rm sat}^-$, and at a temperature T less than the bulk critical temperature T_c. Gravity is ignored. Macroscopic arguments, which have been discovered independently by several authors [22–25], dictate that the wedge is completely filled with liquid when $\theta < \alpha$, where $\theta(T)$ is the contact angle defined for a macroscopic sessile drop on a flat surface. However, for $\theta > \alpha$ the adsorption of liquid at the wedge is microscopic. The *wedge filling transition* corresponds to the transition from microscopic to macroscopic preferential adsorption of liquid, at a filling temperature T_f, which satisfies the exact condition

$$\theta(T_f) = \alpha. \tag{1}$$

Since the contact angle usually decreases with temperature it follows that $T_f < T_w$, where T_w is the wetting temperature at which the contact angle vanishes. In other words, wedge filling precedes wetting, i.e. the wedge can be completely filled with liquid even though the walls are only partially wet. In figure 2 we show two possible phase diagrams illustrating first-order and continuous wedge filling transitions. In each case the filling transition refers to the change from microscopic to macroscopic adsorption as $T \to T_f$ along the coexistence line $\mu = \mu_{\rm sat}^-$. In figure 2(a) we suppose this transition is first-order, while in figure 2(b) we suppose it is continuous (critical filling). In the latter case the equilibrium height ℓ_w of the meniscus above the wedge bottom diverges continuously in this limit. For the case of first-order filling, a pre-filling line (shown as dotted), corresponding a thin–thick transition extends above T_f and off coexistence, analogous to the pre-wetting line which is also shown. However, unlike pre-wetting, the pre-filling transition is necessarily rounded since it is pseudo-one-dimensional and thus the pre-filling line does not end in a genuine critical point. Both phase diagrams also show the *complete filling* transition, which corresponds to the continuous divergence of the meniscus height as $\mu \to \mu_{\rm sat}^-$ for $T > T_f$.

Over the past decade, effective interfacial Hamiltonian models have been used extensively to study the order of wedge filling transitions and have shown how these are sensitive to the range of the intermolecular forces and also interfacial fluctuation effects [26–37]. These turn out to be rather subtle issues. For example, while in open wedges (small α) the order of the transition is qualitatively the same as that of the underlying wetting transition, the critical exponents which characterize three-dimensional critical filling are quite different from those of critical wetting, and fluctuation effects are much larger. For acute wedges, on the other hand, effective Hamiltonians predict that the order of the filling transition may be different from that of the wetting transition [28, 36]. While some of these predictions have been verified in computer simulations [38, 39], exact Ising model calculations [31, 32] and simple square-gradient mean-field theory [36], to the best of our knowledge the filling transition has not been studied using modern microscopic classical density functional theory (DFT) [40] or for systems with realistic long-ranged intermolecular forces. DFT has proved an invaluable tool in the study of inhomogeneous fluids, including interfacial properties, wetting, layering and capillary condensation transitions. As mentioned above, studies of such transitions are simplified because the density profile is one-dimensional. The purpose of this paper is to apply modern DFT to the study of the wedge filling transition, for which of course the density profile is two-dimensional. In this way our work complements recent studies of condensation in capped capillaries [41, 42]. A preliminary account of some of our results has appeared earlier [45].

In our work we use Rosenfeld's fundamental measure theory (FMT) [43, 44] combined with a simple mean-field treatment of the attractive part of the intermolecular interaction, which is taken to be a cut-off Lennard-Jones potential. We consider a right angle wedge and two different types of wall–fluid interaction, which allow us to address the following points and compare with effective Hamiltonian theory. (1) For a purely hard wall, for which the contact angle $\theta = \pi$, we study predictions for universal critical singularities for the complete wedge filling (of gas). In this case the complete filling occurs at the wedge–liquid interface as $\mu \to \mu_{\rm sat}^{+}$. (2) We consider walls with long-ranged wall–fluid interactions, which leads to a finite contact angle and a wetting transition at which the contact angle vanishes. The wetting transition is always first-order but the strength of it is weakened the closer the transition occurs to the bulk critical temperature. In this way we can see if the order of the filling transition can change and be different from the order of the underlying wetting transition. If this is the case we wish to extract the critical exponents and compare with effective Hamiltonian predictions.

Our paper is organized as follows. We start with a description of our model DFT, the intermolecular forces, the wedge geometry and boundary conditions used. We first consider the case of complete wedge filling occurring at the interface between a hard wall wedge and a bulk liquid. We check that our numerical results satisfy exact sum-rules for a planar hard wall, using the full 2D code, and then extract the equilibrium meniscus shape and excess adsorption for the right angle wedge geometry and compare with effective Hamiltonian predictions for critical exponents and critical amplitudes. We then add an attractive long-ranged wall–fluid potential and first determine the contact angle and wetting transition temperature for a planar wall–gas interface. For the corresponding wedge geometry we determine numerically the location and order of the filling transition and compare with the thermodynamic and effective Hamiltonian predictions. We finish with a summary of our results and discuss some open questions.

2. Density functional theory and model interactions

In this section we describe our model and outline the main features of the microscopic DFT that have been used in this work.

Within classical density functional theory [40], the equilibrium density profile is found by minimizing the grand potential functional

$$\Omega[\rho] = \mathcal{F}[\rho] + \int \mathrm{d}\mathbf{r}\rho(\mathbf{r})[V(\mathbf{r}) - \mu], \tag{2}$$

where μ is the chemical potential and $V(\mathbf{r})$ is the external potential. Here $\mathcal{F}[\rho]$ is the intrinsic free energy functional of the fluid one-body density, $\rho(\mathbf{r})$, which can be split into ideal and excess parts. Following the spirit of van der Waals, modern DFT often further divides the latter into a hard-sphere and an attractive contribution

$$\mathcal{F}_{\rm ex}[\rho] = \mathcal{F}_{\rm hs}[\rho] + \tfrac{1}{2}\iint \mathrm{d}\mathbf{r}\mathrm{d}\mathbf{r}'\rho(\mathbf{r})\rho(\mathbf{r}')u_{\rm a}(|\mathbf{r}-\mathbf{r}'|), \tag{3}$$

where $u_{\rm a}(r)$ is the attractive part of the fluid–fluid interaction potential. In our analysis we take this to be a truncated Lennard-Jones-like potential

$$u_{\rm a}(r) = \begin{cases} 0; & r < \sigma, \\ -4\varepsilon\left(\dfrac{\sigma}{r}\right)^6; & \sigma < r < r_{\rm c}, \\ 0; & r > r_{\rm c}, \end{cases} \tag{4}$$

which is cut-off at $r_{\rm c} = 2.5\sigma$, where σ is the hard-sphere diameter. The hard-sphere part of the excess free energy is approximated by the FMT functional [43],

$$\mathcal{F}_{\rm hs}[\rho] = \frac{1}{\beta}\int \mathrm{d}\mathbf{r}\,\Phi(\{n_\alpha\}), \tag{5}$$

where Φ is a function of six weighted densities $n_\alpha(\mathbf{r})$, and $\beta = 1/k_{\rm B}T$ is the inverse temperature. Rosenfeld's FMT accurately captures short-range correlations and thus the functional (3) should describe strong packing effects for liquid adsorption at the surface of the wall and near the apex.

The confining wedge is treated as an external field, $V(\mathbf{r})$, exerted on the fluid atoms. The potential is assumed to be translationally invariant along the wedge which is formed from two semi-infinite planar slabs (walls) that meet at a right angle, so that $\alpha = \pi/4$. We will consider two types of wedge–fluid interaction. One is a purely hard wall wedge, whose potential is simply

$$V^{\rm hw}(x,z) = \begin{cases} \infty; & x < \sigma \text{ or } z < \sigma, \\ 0; & \text{elsewhere}, \end{cases} \tag{6}$$

where the x and z Cartesian coordinates run parallel to the left and right hand side walls respectively (see figure 1).

The second wall potential is long-ranged and is assumed to arise from a uniform distribution of wall atoms, with a one-body density $\rho_{\rm w}$. These interact with the fluid atoms via the Lennard-Jones potential

$$\phi_{\rm w}(r) = -4\varepsilon_{\rm w}\left(\frac{\sigma}{r}\right)^6; \qquad r > \sigma. \tag{7}$$

After integrating $\phi_{\rm w}(\mathbf{r})$ over the whole depth of the wall, the potential of the wedge can be expressed as

$$V^{\rm LJ}(x,z) = \begin{cases} \infty; & x < \sigma \text{ or } z < \sigma, \\ \tilde{V}(x,z); & \text{elsewhere}, \end{cases} \tag{8}$$

with

$$\tilde{V}(x,z) = \alpha_{\rm w}\left[\frac{1}{z^3} + \frac{2z^4 + x^2z^2 + 2x^4}{2x^3z^3\sqrt{x^2+z^2}} + \frac{1}{x^3}\right] \tag{9}$$

and

$$\alpha_{\rm w} = -\tfrac{1}{3}\pi\varepsilon_{\rm w}\rho_{\rm w}\sigma^6. \tag{10}$$

Notice that infinitely far from the wedge apex, the potential close to either surface recovers that of a planar wall $V(x,\infty) = 2\alpha_{\rm w}/x^3$ or $V(\infty,z) = 2\alpha_{\rm w}/z^3$. Minimization of (2) leads to an Euler–Lagrange equation, which is solved numerically. This is done on an $L \times L$ Cartesian grid, where the lateral dimension of our box size is $L = 50\sigma$ and the grid

has discretization size $0.05\,\sigma$. To mimic the bulk boundary conditions we impose that $\rho(L, z) = \rho_\pi(z; L)$ and $\rho(x, L) = \rho_\pi(x; L)$, where $\rho_\pi(z; L)$ is the equilibrium profile for a planar wall–fluid interface with $\rho_\pi(L; L)$ fixed to the bulk density. The latter is, for the sake of numerical consistency, determined from the full 2D DFT. Once the equilibrium density profile is found, the corresponding grand potential is calculated from (2). From this, all the thermodynamical properties of the system can be determined. For the most part we express our temperature scale in fractions of the bulk critical temperature $k_B T_c/\varepsilon = 1.414$ or in dimensionless units $T^* = k_B T/\varepsilon$ where more convenient. Similarly, densities are written in dimensionless units $\rho^* = \rho\sigma^3$, as are wetting film thicknesses $\ell^* = \ell/\sigma$ and distances $z^* = z/\sigma$, etc.

3. Numerical results

3.1. Complete filling at a hard wall wedge

As described in the introduction, the complete filling transition refers to the continuous divergence of the meniscus height ℓ_w on approaching two-phase coexistence when the contact angle $\theta < \alpha$. Effective Hamiltonian studies predict that this transition is dominated by the geometry of the wedge and displays universal critical properties [12]. For example, at leading order the meniscus height is predicted to diverge as

$$\ell_w \approx \frac{\gamma(\sec\alpha\cos\theta - 1)}{\delta\mu\,\Delta\rho} \tag{11}$$

where γ is the surface tension of the liquid–gas interface and $\Delta\rho = \rho_l - \rho_g$ is the difference between the bulk densities. The power-law dependence on $\delta\mu = |\mu - \mu_{sat}|$ is universal and is independent of the range of the intermolecular forces and fluctuation effects. This universal behaviour can be understood very simply using macroscopic concepts [12]. As coexistence is approached, the meniscus that grows at the wedge corner must have a circular cross-section with radius $R = \gamma/\delta\mu\Delta\rho$, as determined by the Laplace pressure difference across it. The height ℓ_w then follows from the condition that the meniscus must meet each side of the wedge at the correct contact angle. Notice that the amplitude of the divergence vanishes at the filling phase boundary $\theta = \alpha$, consistent with the requirement that the adsorption becomes microscopic for $T < T_f$.

A particular case of complete wedge filling occurs when the walls are completely wet, $\theta = 0$, or completely dry, $\theta = \pi$ (if one studies the wedge–liquid interface). In this case there are also singular next-to-leading order contributions to the divergence, such that [16]

$$\ell_w \approx \frac{\gamma(\sec\alpha - 1)}{\delta\mu\,\Delta\rho} + \frac{\sec\alpha}{1 - \beta_s^{co}}\ell_\pi + \cdots \tag{12}$$

where $\ell_\pi \approx \delta\mu^{-\beta_s^{co}}$ is the thickness of the complete wetting layer at a planar wall–vapour interface (or wall–liquid in the case of drying). The character of this next-to-leading order correction therefore does depend on the range of the intermolecular forces, since these determine the wetting layer thickness. For systems with short-ranged forces, recall that $\ell_\pi \approx -\xi_b \ln\delta\mu$, where ξ_b is the correlation length of the bulk phase adsorbed at the wall, i.e. $\beta_s^{co} = 0$. Strictly speaking this is a mean-field result but, in three dimensions (which is the upper critical dimension for short-ranged forces), interfacial fluctuation effects do not alter this in any significant way, altering only the amplitude by a factor $1 + \omega/2$, where $\omega = k_B T/4\pi\gamma\xi_b^2$ is the wetting parameter [1]. For long-ranged intermolecular potentials, on the other hand, the exponent $\beta_s^{co} = 1/(p+1)$, with $p = 2, 3$ for non-retarded and retarded dispersion forces, respectively [1]. The critical amplitude of the correction term is similar to that describing the well-known Derjaguin correction to the Kelvin equation for capillary condensation in a slit geometry [46]. Only for the case of short-ranged forces does the correction term have a simple geometrical interpretation arising from the wetting layer along the walls far from the apex.

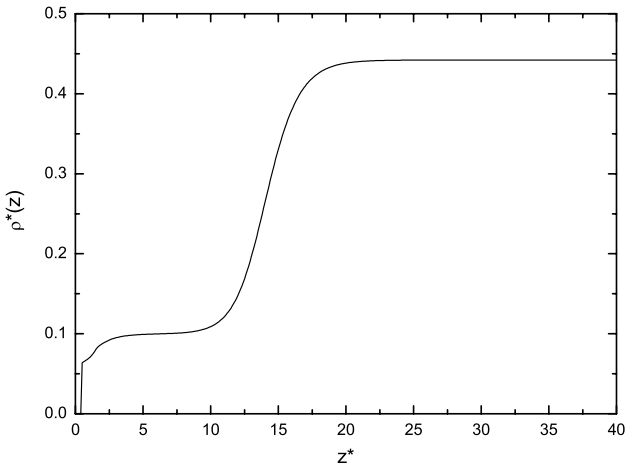

Figure 3. Density profile of a liquid near a planar hard wall for $T = 0.92\,T_c$ and $\rho_b^* - \rho_l^* = 10^{-6}$. Notice the presence of a thick drying layer of vapour whose density is close to that of the bulk gas. The density is lower at the wall, consistent with the pressure sum-rule.

In this section we test the effective Hamiltonian prediction (12) for the case of complete drying by vapour at a right angle hard wall wedge. We suppose the wedge is in contact with a bulk liquid at chemical potential $\mu > \mu_{sat}$. Then, as coexistence is approached from above a bubble of low density vapour forms at the corner, whose height from the apex should be described by equation (12). In our calculations we fix the temperature to $T = 0.92\,T_c$, for which bulk coexistence occurs at $\mu_{sat} = -3.965\,11\epsilon$. As a check of our 2D DFT numerical algorithm, we first studied the planar hard-wall–liquid interface. In this case, we fixed the particle density at $z = L$ to a bulk density ρ_b, which is slightly higher than the density of the liquid at saturation, $\rho_l = 0.431\,48\,\sigma^3$. In figure 3 we display a typical equilibrium density profile $\rho(z)$ showing a fairly thick drying layer of low density vapour. For comparison the bulk density of gas at this temperature is $\rho_g = 0.1\,\sigma^3$. The density near the wall falls and, at contact, $\rho_w \equiv \rho(\sigma)$ should be exactly given by the sum-rule $p = k_B T\rho_w$, where p is the bulk pressure. The measured value

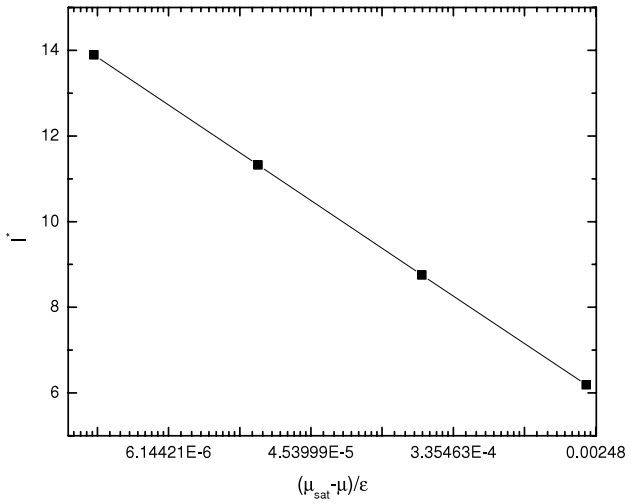

Figure 4. Plot of the film thickness $\ell_\pi^* = \ell_\pi/\sigma$ of the adsorbed layer of gas at a hard wall versus the over saturation, measured on a log scale, for $T = 0.92\,T_c$. The slope of the straight line determines the bulk gas correlation length.

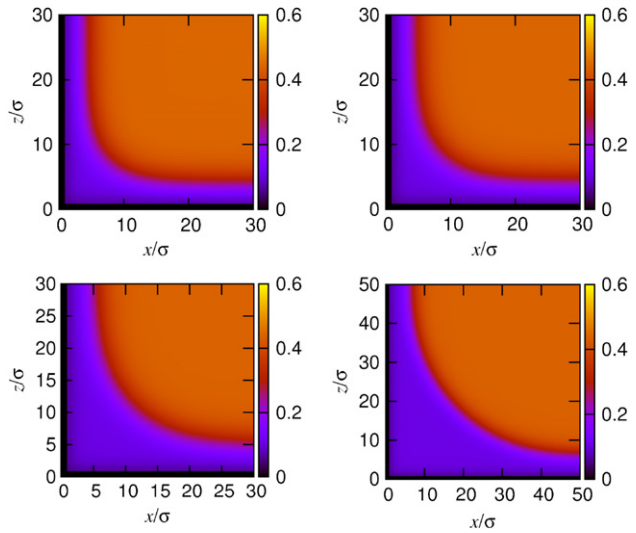

Figure 5. Fluid density profiles near a hard wedge in contact with a bulk liquid at temperature $T = 0.92\,T_c$. The bulk density differences ($\delta\rho \equiv \rho_b - \rho_l$) from top left to right bottom are: $\delta\rho\sigma^3 = 0.01$, 0.008, 0.005, and 0.003, respectively.

of the contact density with this grid size determines the bulk pressure with an error less than 0.01%.

From the equilibrium density profile we determine the adsorption $\Gamma = \int_\sigma^L (\rho(z) - \rho_b)\mathrm{d}z$, and from this the film thickness according to the standard definition $\ell_\pi = |\Gamma|/\Delta\rho$. In figure 4 we show the dependence of ℓ_π on the supersaturation. This is in excellent agreement with the expected logarithmic divergence for this cut-off LJ fluid, and allows us to identify the bulk correlation length of the gas phase $\xi_b^{\mathrm{gas}} = 1.11\,\sigma$. This agrees with the value obtained independently from the decay of the density for the wall–gas interface.

We now turn our attention to the hard wall wedge geometry, corresponding to the external potential (6), and numerically study the interface with a bulk liquid for different chemical potentials approaching bulk coexistence. In figure 5 we show four different 2D density profiles $\rho(x, z)$ for values of the chemical potential progressively closer to saturation. For the values of the chemical potential chosen, one can see qualitatively that far from the wedge apex the adsorption of gas is rather small, corresponding to thin drying films only a few σ thick. These are indicative of the planar wall–liquid interface. In contrast, even for the largest value of the chemical potential the geometry enhanced preferential adsorption of vapour at the apex, via the formation of a meniscus, is clearly apparent. Upon approaching saturation, the distance ℓ_w of the meniscus from the apex increases, and diverges as $\mu \to \mu_{\mathrm{sat}}$. This divergence is far stronger than the logarithmic increase of the drying film at a planar wall.

In figure 6 we show a numerically determined meniscus shape corresponding to the loci of the local mid-point interfacial density, where $\rho(x, z) = \frac{\rho_b+\rho_l}{2}$, for the case where $\rho_b = \rho_l + 0.003/\sigma^3$. The shape of the meniscus is very nearly circular, as can be seen from comparison with the green circle, which has the Laplace radius $R = \gamma/\delta\mu\Delta\rho = 36.3\,\sigma$ for this particular chemical potential. This gives us some

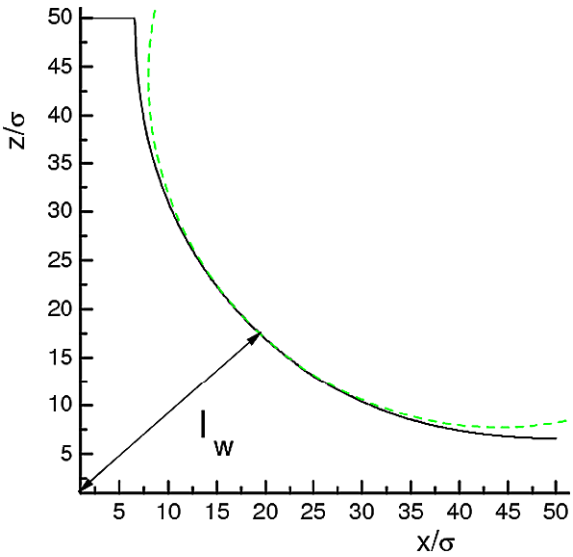

Figure 6. Contour of the meniscus between the vapour and liquid phases in a hard wedge at temperature $T = 0.92\,T_c$ and bulk density $\rho_b - \rho_l = 0.003/\sigma^3$. Also shown for comparison is a circular meniscus of Laplace radius $R = \frac{\gamma}{\delta\mu\Delta\rho}$.

confidence that even for the present small system sizes the predictions of macroscopic and effective Hamiltonian theory are still valid. Finally, and most importantly, the numerically determined divergence of the filling height, ℓ_w, is shown in figure 7 (symbols). The dashed curve is the macroscopic theoretical expression which corresponds to just the first term in (12). For $T = 0.92\,T_c$, this corresponds to the curve $\ell_w = 0.092\,63\,\sigma\varepsilon/\delta\mu$. The shape of this is very similar to the numerical results for the film thickness but lies systematically below it. The solid curve is the theoretical result now allowing for the next-to-leading order correction in (12)—which recall is logarithmic for the present cut-off LJ fluid. We emphasize,

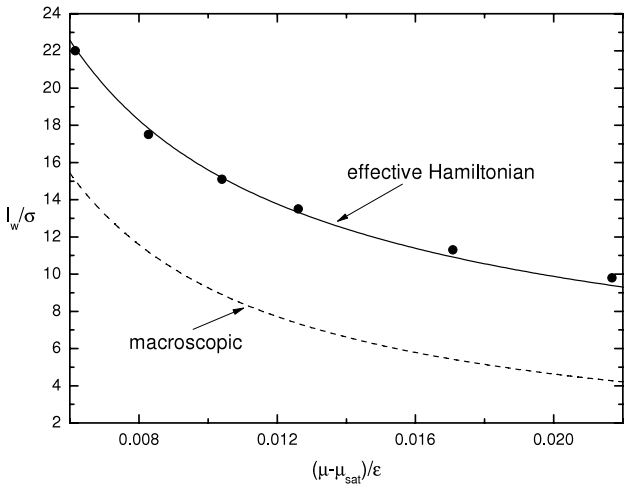

Figure 7. Numerical results (symbols) for the divergence of the meniscus filling height ℓ_w, shown in comparison with the macroscopic expression $\ell_w = \frac{\gamma(\sec\alpha - 1)}{\delta\mu\Delta\rho}$ (dashed curve) and the effective Hamiltonian prediction (12) (solid curve) which includes the logarithmic next-to-leading order correction.

since the agreement is so good, that this is not a fit and there are no adjustable parameters. Effective Hamiltonian theory therefore gives an excellent quantitative description of complete filling at a hard wall wedge. One simplifying feature of the hard wall in contact with a vapour wetting or drying layer, of course, is that there are no packing effects to worry about. Filling by liquid is potentially more complicated because of such effects. We turn to this in the next section in the context of the filling transition itself.

3.2. Filling with long-range wall–fluid forces

In this section we go beyond the pure hard wall wedge and turn on the long-range wall–fluid attraction. We consider three different interaction strengths; (i) $\varepsilon_w = 1.2\,\varepsilon$, (ii) $\varepsilon_w = \varepsilon$ and (iii) $\varepsilon_w = 0.8\,\varepsilon$. For each of these we first consider the corresponding planar wall–fluid interfaces and determine the temperature dependence of the contact angle $\theta(T)$ from the wall–gas and wall–liquid surface tensions using Young's equation $\cos\theta = (\gamma_{wg} - \gamma_{wl})/\gamma$. Each of these systems exhibits a wetting transition by liquid at a wall–vapour interface. As expected, these transitions are first-order, since the wall–fluid and fluid–fluid forces have different ranges. In figure 8 we show the numerically determined value of the wetting temperatures using both the 1D and 2D DFT calculations. The crossing of the wall–gas tension γ_{wg} and summed tensions $\gamma_{wl}+\gamma$ gives consistent values of $T_w^* = 1.18$ (or $T_w = 0.83\,T_c$), $T_w^* = 1.31$ (or $T_w = 0.93\,T_c$) and $T_w^* = 1.4$ (or $T_w = 0.99\,T_c$) for the cases (i)–(iii), respectively. For the strongest wall–fluid interaction, $\varepsilon_w = 1.2\,\varepsilon$, the wetting transition is strongly first-order, as can be seen from the crossing of the free energy branches. To further emphasize this we have determined numerically the interfacial binding potential $W(\ell)$ representing the excess free energy of a wetting film constrained to be of thickness ℓ. For $\varepsilon_w = \varepsilon$ this is shown at the upper panel of figure 9 for a temperature close

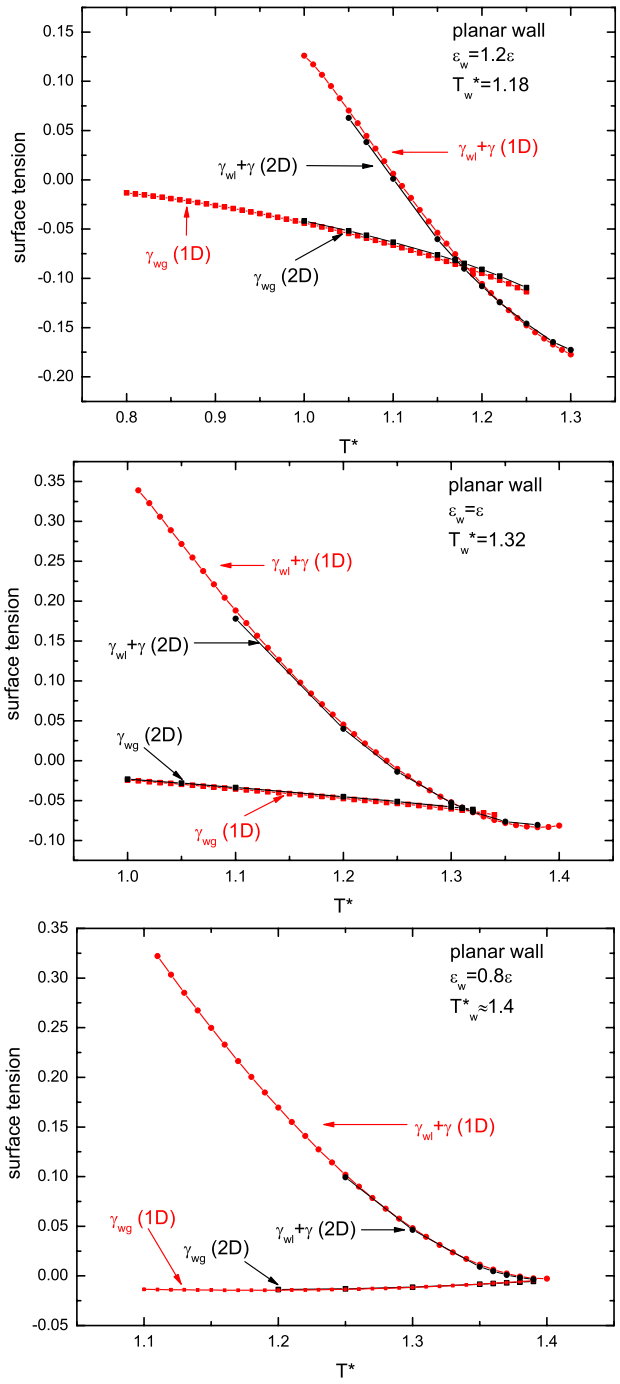

Figure 8. Determination of the wetting temperature T_w from the intersection of the wall–gas tension γ_{wg} and summed tensions $\gamma_{wl} + \gamma$. Results obtained from 1D calculations (in red) are compared with those of the 2D calculation (in black).

to T_w. As can be seen there is a clear activation barrier located near $\ell_B \approx 4\sigma$.

For the weakest wall–fluid potential $\varepsilon_w = 0.8\,\varepsilon$, where T_w is very close to the bulk critical temperature, the transition is weakly first-order, as can be seen from the near tangential meeting of the surface tensions. This is more apparent when one numerically determines the interfacial binding potential for $T \approx T_w$ for this interaction strength (see lower panel of figure 9) by minimizing the grand potential subject to

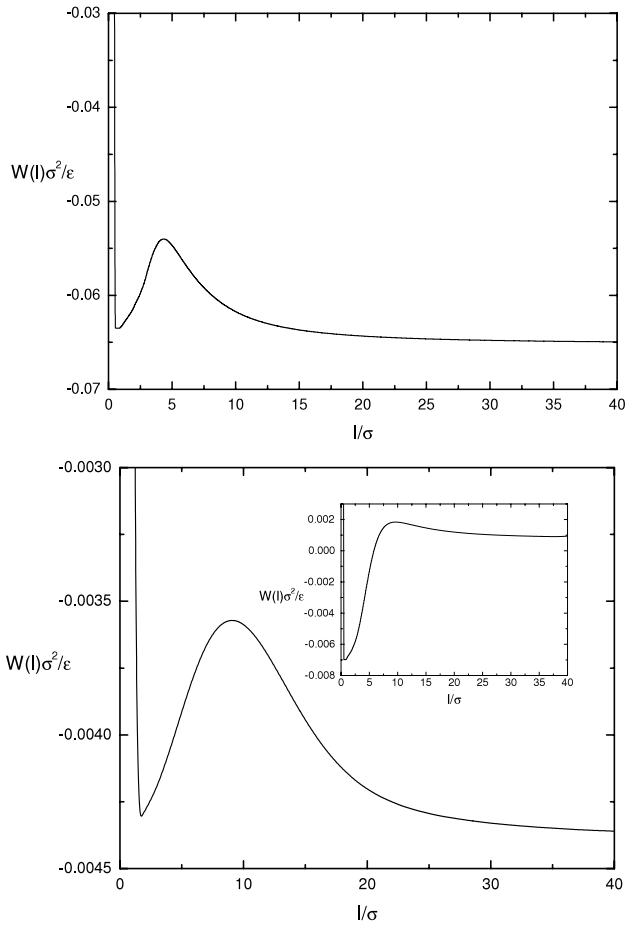

Figure 9. Interfacial binding potentials $W(\ell)$, in dimensionless units, as a function of the adsorbed film thickness. The upper panel corresponds to $\varepsilon_w = \varepsilon$ and for a temperature close to $T_w^* = 1.32$. Notice the presence of a prominent activation barrier at $\ell_B \approx 4\sigma$. In the lower panel we show the binding potential for $\varepsilon_w = 0.8\,\varepsilon$, also close to its wetting transition at $T_w^* = 1.4$. In this case, the activation barrier is an order of magnitude smaller and situated further from the wall at $\ell_B \approx 10\sigma$. In the inset we show the binding potential at a lower temperature which is close to the filling temperature $T_f^* \approx 1.38$ for this same system. Notice that an activation barrier is still present. In all cases the results correspond to a bulk coexistence.

a constraint of fixed film thickness [47]. This function still exhibits an activation barrier, but this is an order magnitude smaller than for the $\varepsilon_w = \varepsilon$ case and its location near $\ell_B \approx 10\sigma$ is far further from the wall. In the inset we show the binding potential at a lower temperature (at the filling transition), which we will return to later.

A plot of the contact angles as a function of temperature for each of the wall strengths is shown in figure 10, where the intersection with $\alpha = \pi/4$ gives, from the thermodynamic prediction (1), the theoretical value of the filling transition in a right angle wedge. These are $T_f^* = 1.075$ (or $T_f = 0.76\,T_c$), $T_f^* = 1.275$ (or $T_w = 0.90\,T_c$) and $T_f^* = 1.375$ (or $T_w = 0.97\,T_c$) for interaction strengths (i)–(iii) respectively.

We now turn our attention to the numerical analysis of the equilibrium density profiles and phase behaviour in the wedge geometry. Our first task is to numerically determine the location of any filling transition and compare

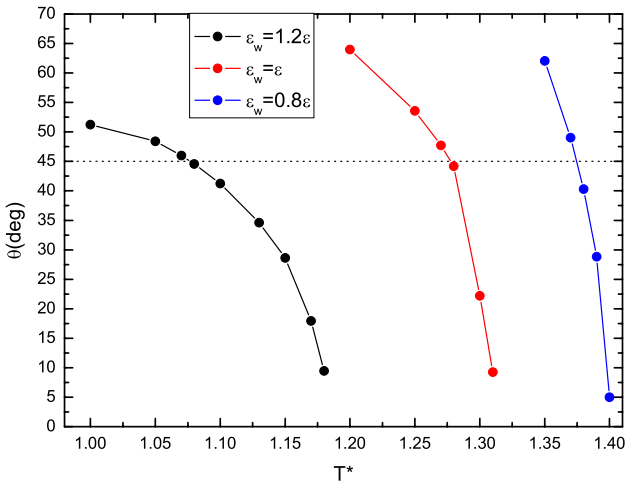

Figure 10. Variation of the contact angle with temperature for three different wall strengths. The intersection with the dashed line at $\theta = 45°$ is the thermodynamic prediction for the filling temperature for each system.

with the above theoretical predictions for the three different wall–fluid interaction strengths. To this end we sit at bulk coexistence $\mu = \mu_{sat}$ and minimize the grand potential $\Omega[\rho]$ to a global or local minimum Ω, starting from two different initial configurations: a high density liquid and a low density vapour. If the system exhibits a first-order filling transition then we can expect that in the vicinity of T_f these initial configurations will converge to different equilibrium profiles, corresponding to microscopic and macroscopic adsorptions of liquid, respectively. These will have identical grand potentials at the filling transition. Obviously finite-size constraints limit the size of the macroscopic liquid layer, the size of which scales with the box area L^2. If, on the other hand, the filling transition is continuous there will be a unique equilibrium phase. In this case a plot of the total adsorption versus T will have no hysteresis loop but should still show a dramatic continuous increase near T_f. Plots of the excess grand potential $\Omega^{ex} = \Omega + pV$ per unit length of the wedge obtained in this manner are shown in figures 11 and 12. For the two strongest interaction strengths there are two separate branches of the free-energy, indicating a first-order filling transition. The crossing of the free energies yields filling temperatures $T_f^* = 1.085$ and $T_f^* = 1.278$ for $\varepsilon_w = 1.2\,\varepsilon$ and $\varepsilon_w = \varepsilon$, respectively, which are close to the theoretical predictions obtained from $\theta(T_f) = \pi/4$. The slight discrepancy between the values is a consequence of the finite-size limitations of our numerical analysis. In figure 13 we show the coexisting density profiles, corresponding to microscopic (lower panel) and macroscopic (upper panel) states, at the filling temperature for wall interaction strength $\varepsilon_w = \varepsilon$. Notice that the macroscopic meniscus is nearly flat, as it should be since we are at bulk coexistence and the interface must meet the walls at a contact angle equal to $\pi/4$. Notice that for the microscopic configuration the thickness ℓ_w of the adsorbed layer is larger than the wetting layer thickness (far from the apex) but of the same order as the distance of the activation barrier ℓ_B for the corresponding

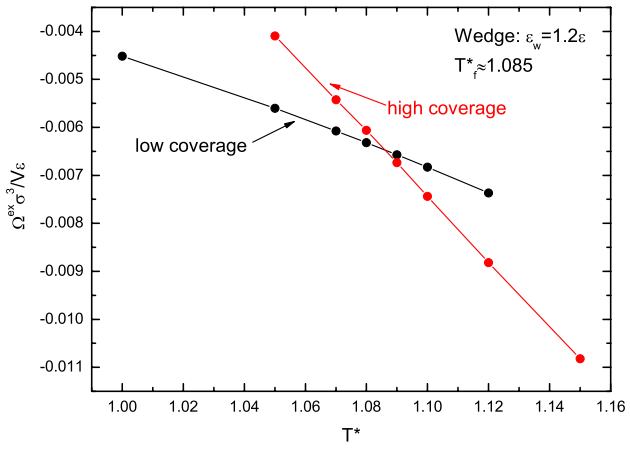

Figure 11. Location of a first-order filling transition from the crossing of two separate free energy branches corresponding to microscopic and macroscopic adsorptions in the wedge geometry for $\varepsilon_w/\varepsilon = 1.2$. Here V is the available volume, which is the length of the wedge multiplied by $(L-\sigma)^2$.

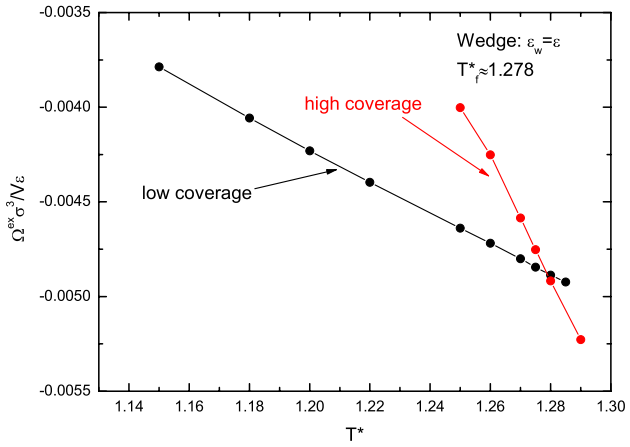

Figure 12. Location of a first-order filling transition from the crossing of two separate free energy branches corresponding to microscopic and macroscopic adsorptions in the wedge geometry for $\varepsilon_w = \varepsilon$.

binding potential for the wetting transition, see inset of figure 9. Both microscopic and macroscopic profiles show layering behaviour close to the apex. Also shown in figure 14 is a metastable configuration for $T < T_f$, representing a macroscopic adsorption of liquid with a concave meniscus. This curvature is necessary in order that the meniscus meets each wall at the correct contact angle.

Most interestingly, for the weakest wall strength $\varepsilon_w = 0.8\,\varepsilon$ we have found that there is only a single branch to the equilibrium grand potential, i.e. both high and low density initial coverages converge to a unique equilibrium phase. This means that either the filling transition is continuous (critical), or so weakly first-order that the present $L \times L$ finite-size grid is not large enough to see the jump in the adsorption. A plot of the adsorption $\Gamma = \int\int \mathrm{d}x\mathrm{d}z(\rho(x,z) - \rho_b)$ versus T is shown in figure 15. As is evident, there is indeed a dramatic but continuous increase in the adsorption near the anticipated $T_f^* \approx 1.38$, indicating that a continuous filling or possibly

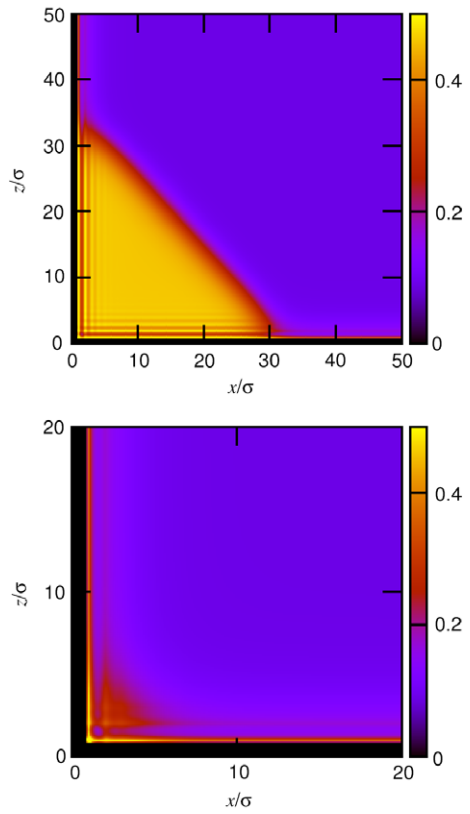

Figure 13. Coexisting density profiles for wedge–vapour interfaces at a first-order filling transition for wall strength $\varepsilon_w = \varepsilon$ (corresponding to $T_f^* = 1.28$). The upper panel shows the macroscopic configuration, in which the meniscus is far from the wall and meets each wall at the contact angle. The lower panel shows the coexisting microscopic configuration, in which the interface is tightly bound to the apex.

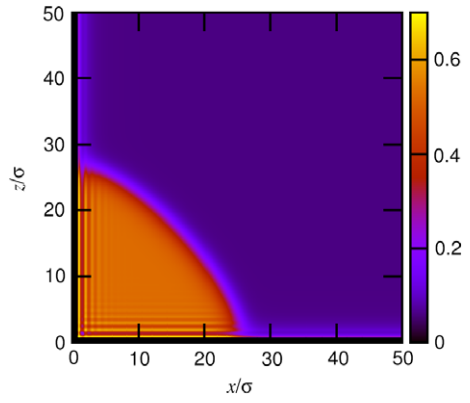

Figure 14. Example of a metastable configuration corresponding to a macroscopic meniscus with negative curvature at a temperature $T^* = 1.2$ which is below the filling temperature ($T_f^* = 1.28$).

finite-size rounded weakly first-order filling transition is taking place. Strong evidence that this a genuine critical filling transition comes from two sources. Firstly, consider the unique density profile at $T = T_f$ shown in figure 16. The thickness of the meniscus ℓ_w is much larger than the length-scale $\ell_B \approx 10\,\sigma$ associated with the wetting activation

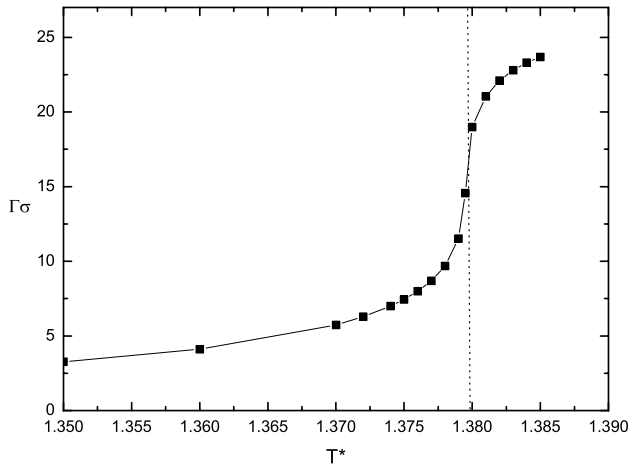

Figure 15. Plot of the adsorption (in reduces units) as a function of temperature for the wedge model with the weakest wall interaction, $\varepsilon_w = 0.8\,\varepsilon$. The adsorption increases sharply but continuously in the vicinity of the filling temperature, indicating that the transition is continuous.

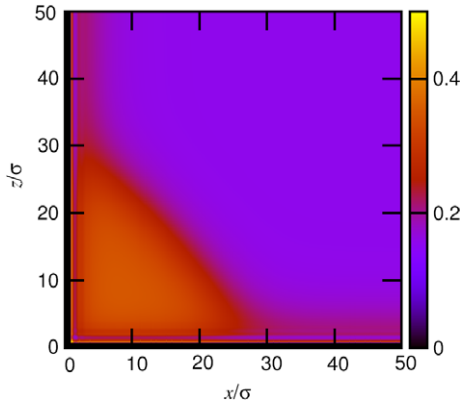

Figure 16. Density profile for the weakest wall interaction, $\varepsilon_w = 0.8\,\varepsilon$, near the filling temperature.

barrier. If finite-size rounding was an issue we would expect that $\ell_w < \ell_B$, or at least that these length-scales would be comparable. We also emphasize here that even though we are quite close to the bulk critical temperature (recall, $T_f \approx 0.975\,T_c$), the bulk (liquid) correlation length is still of the order of σ and is much smaller than the overall meniscus size. This is also clear in figure 16, where the width of the interface separating liquid from gas is much smaller than ℓ_w. This clearly indicates that the mean-field character of our DFT should not play any significant role regarding the location and the order of the transition. Secondly, we can compare with effective Hamiltonian theory for the meniscus thickness ℓ_w and adsorption at critical filling. This predicts that, in an infinite wedge, these diverge as [28]

$$\ell_w \sim (T_f - T)^{-\beta_w}, \qquad \Gamma \sim (T_f - T)^{-2\beta_w}, \tag{13}$$

where the adsorption is simply the square of the film thickness owing to the triangular shape of the meniscus. The mean-field value of the critical exponent $\beta_w = 1/p$ and, incidentally, is not altered by interfacial fluctuation effects

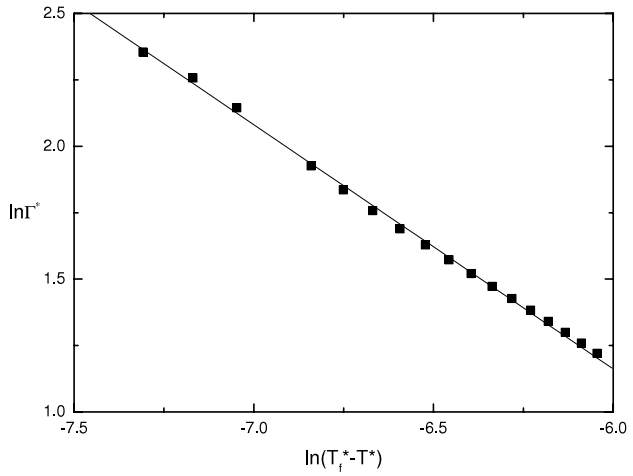

Figure 17. Log–log plot of the adsorption versus the scaling field $T_f - T$ for the weakest wall interaction strength, $\varepsilon_w = 0.8\,\varepsilon$. The slope of the straight line is -0.92.

in three dimensions provided $p < 4$, see [28]. In our model $p = 2$, so we should expect that if the filling transition is continuous the adsorption increases as $\Gamma \sim (T_f - T)^{-1}$ on approaching the filling temperature. In our final figure (figure 17) we show a log–log plot for the growth of the adsorption for $T < T_f$, in which we use the numerical estimate of the filling temperature $T_f^* = 1.38$. From this we estimate $\beta_w = 0.46 \pm 0.05$, which is in a reasonably good agreement with the effective Hamiltonian prediction.

4. Discussion

In this paper we have presented our results of numerical studies of complete, first-order and critical filling transitions in a rectangular wedge using a non-local density functional theory. To the best of our knowledge this is the first time that filling transitions have been studied using modern microscopic DFT and our work complements earlier effective Hamiltonian, square gradient and simulation studies. For the case of complete filling the results of the DFT confirm effective predictions for leading and next-to-leading order critical exponents and amplitudes to a remarkable accuracy. However, we believe our most important finding is that close to the bulk critical temperature the wedge filling transition is continuous even though the walls themselves exhibit first-order wetting. Crucially this occurs in the presence of realistic long-ranged wall–fluid interactions (and for a cut-off LJ fluid), which is the system that is most accessible experimentally. To end our paper we discuss this in more depth.

The change from first-order to critical filling occurs in the vicinity of the bulk critical temperature. In this region we can reasonably expect that universal properties arise due to the scaling behaviour associated with bulk and surface criticality. In fact, for systems with short-ranged forces there are predictions for the universal shift of T_w and T_f from T_c which depend only on the half opening angle $\psi = \pi/2 - \alpha$ as

follows [34]:

$$\frac{T_c - T_w}{T_c - T_f} = R_3(\psi)^{1/\Delta_1}, \tag{14}$$

where the universal amplitude $R_d(\psi)$ depends only on the dimension d and the tilt angle and Δ_1 is the surface gap exponent [48]. At mean-field level, and for a right angle wedge the prediction of Landau square-gradient theory is $R_3(\pi/4) = 0.518$ (and recall $\Delta_1 = 1/2$). If we naively assume that this scaling holds for our model, which recall has long-ranged wall–fluid interactions, this predicts that the filling temperature for the wall strength $\varepsilon_w = 0.8\,\varepsilon$ is $T_f^* = 1.364$. This is remarkably close to our numerical value $T_f^* = 1.375$ and is indicative that some scaling is present.

Finally, we mention that a possible change in the order of the filling transition had been predicted by effective Hamiltonian theory [28]. However, the mechanism originally proposed for this does not quite apply to the present DFT model. In the original effective Hamiltonian description, which applied only to rather shallow wedges, the mechanism arose because it was noted that the filling temperature T_f may be below the surface spinodal temperature T_{spin} at which the activation barrier in the wetting binding potential is first formed. However, this mechanism is only possible if the wall–fluid and fluid–fluid forces have the same range, since it requires that the Hamaker constant controlling the large distance algebraic decay of $W(\ell)$ changes sign at T_{spin}. In the present model, with cut-off LJ fluid–fluid forces and long-ranged wall–fluid forces, no such spinodal temperature exists and an activation is always present. This is shown explicitly in the inset of figure 9, which shows the binding potential at the filling temperature T_f. From this we can conclude that the change in order is a more general feature of filling transitions that occur close to the bulk critical temperature, where the 'short-range' properties occurring on the scale of the large bulk correlation length can compete with long-range dispersion forces. This is in keeping with the general expectation that long-ranged forces become less important near the bulk critical point. The observation in our model system that critical wedge filling is possible even if the walls exhibit first-order wetting, is encouraging that such continuous interfacial transitions can be seen experimentally. This would be particularly interesting, because fluctuation effects are far stronger for critical filling than for critical wetting. For example, for the present case of long-ranged forces (with $p = 2$), for which $\ell_w \approx (T_f - T)^{-1/2}$, the interfacial roughness (rms width) is predicted to diverge, due to capillary-wave-like fluctuations, with a universal power-law $\xi_\perp \approx (T_f - T)^{-1/4}$ which is independent of the range of the forces [28]. Of course such fluctuation induced interfacial roughness is not present in our mean-field DFT and in reality the density profiles $\rho(x, z)$ will be broader near the interface than calculated herein. However, this is a minor defect of the mean-field DFT analysis, which should be completely reliable as regards the location of the filling transition, its order and also the determination of the exponent β_w.

We believe our predictions are testable in the laboratory. For the case of complete wetting there have already been impressive experiments by Mistura and co-workers [49], who have verified the leading power-law and amplitude in equation (11). Repeating these experiments with more precisely manufactured wedges would allow one to look at the more subtle next-to-leading order behaviour, similar to that described here. Unfortunately, the materials used so far have precluded the study of fluids which exhibit partial wetting, which is of course necessary to see the filling transition. At the moment it appears more likely to us that this transition can be seen at the micron scale using colloid polymer mixtures, similar to studies of wetting and capillary condensation [50].

Our work can be extended in a number of ways. Obviously larger system sizes with finer grids would allow us to probe the critical regime for continuous filling with greater accuracy. Varying the tilt angle, interaction strengths and range of the forces would also be very informative and would allow us to see whether the filling transitions for the stronger potentials, where T_f is further from T_c, are turned continuous. Generalizing our analysis to asymmetric wedges with competing potentials at each wall would also be straightforward. Finally, at low temperatures it would be very interesting to see if one could induce corner crystalline structure near the wedge apex and defects due to the competition between the lattice directors and the geometrical confinement. We hope that this work stimulates further 2D and 3D DFT studies of adsorption at structured surfaces and experimental investigations of wedge filling.

Acknowledgment

AM acknowledges the support from the Czech Science Foundation, project 13-09914S. AOP gratefully acknowledges the financial support of the Universidad Carlos III Madrid and the bank of Santander for the award of a chair of excellence.

References

[1] Dietrich S 1988 *Phase Transitions and Critical Phenomena* vol 12, ed C Domb and J L Lebowitz (New York: Academic)
[2] Sullivan D E and Telo da Gama M M 1985 *Fluid Interfacial Phenomena* ed C A Croxton (New York: Wiley)
[3] Schick M 1990 *Liquids and Interfaces* ed J Chorvolin, J F Joanny and J Zinn-Justin (New York: Elsevier)
[4] Bonn D, Eggers J, Indekeu J, Meunier J and Rolley E 2009 *Rev. Mod. Phys.* **81** 739
[5] Saam W F 2009 *J. Low Temp. Phys.* **157** 77
[6] Evans R, Marini Bettolo Marconi U and Tarazona P 1986 *J. Chem. Phys.* **84** 2376
[7] Evans R 1990 *J. Phys.: Condens. Matter* **2** 8989
[8] Indekeu J O, Upton P J and Yeomans J M 1988 *Phys. Rev. Lett.* **61** 2221
[9] Stewart M C and Evans R 2005 *Phys. Rev.* E **71** 011602
[10] Parry A O, Rascón C and Morgan L 2006 *J. Chem. Phys.* **124** 151101
[11] Nold A, Malijevský A and Kalliadasis S 2011 *Phys. Rev.* E **84** 021603
[12] Rascón C and Parry A O 2000 *Nature* **407** 6807
[13] Bauer C and Dietrich S 2000 *Phys. Rev.* E **61** 1664
[14] Abraham D B, Parry A O and Wood A J 2002 *Europhys. Lett.* **60** 106

[15] Parry A O, Greenall M J and Romero-Enrique J M 2003 *Phys. Rev. Lett.* **90** 046101
[16] Rascón C and Parry A O 2005 *Phys. Rev. Lett.* **94** 096103
[17] Parry A O, Rascón C and Morgan L 2005 *J. Chem. Phys.* **123** 234105
[18] Tasinkevych M and Dietrich S 2006 *Phys. Rev. Lett.* **97** 106102
[19] Tasinkevych M and Dietrich S 2007 *Eur. Phys. J.* E **23** 117
[20] Parry A O and Rascón C 2010 *J. Chem. Phys.* **132** 204704
[21] Parry A O and Rascón C 2011 *Phys. Rev. Lett.* **107** 206104
[22] Shuttleworth R and Bailey G L J 1948 *Discuss. Faraday Soc.* **3** 16
[23] Concus P and Finn R 1969 *Proc. Natl Acad. Sci. USA* **63** 292
[24] Pomeau Y 1986 *J. Colloid Interface Sci.* **113** 5
[25] Hauge E H 1992 *Phys. Rev.* A **46** 4994
[26] Rejmer K, Dietrich S and Napirkówski M 1999 *Phys. Rev.* E **60** 4027
[27] Parry A O, Rascón C and Wood A J 1999 *Phys. Rev. Lett.* **83** 5535
[28] Parry A O, Rascón C and Wood A J 2000 *Phys. Rev. Lett.* **85** 345
[29] Parry A O, Rascón C and Wood A J 2001 *Fluid Phase Equilib.* **185** 139
[30] Parry A O, Wood A J and Rascón C 2001 *J. Phys.: Condens. Matter* **13** 4591
[31] Abraham D B and Maciołek A 2002 *Phys. Rev. Lett.* **89** 286101
[32] Abraham D B, Mustonen V and Wood A J 2003 *Europhys. Lett.* **63** 408
[33] Romero-Enrique J M and Parry A O 2005 *Europhys. Lett.* **72** 1004
[34] Parry A O, Wood A J, Carlon E and Drzewisnki A 2001 *Phys. Rev. Lett.* **87** 196103
[35] Romero-Enrique J M and Parry A O 2007 *New J. Phys.* **9** 167
[36] Bernardino N R, Parry A O and Romero-Enrique J M 2011 *J. Phys.: Condens. Matter* **24** 182202
[37] Parry A O and Rascón C 2011 *J. Phys.: Condens. Matter* **23** 015004
[38] Milchev A, Müller M, Binder K and Landau D P 2003 *Phys. Rev. Lett.* **90** 136101
Milchev A, Müller M, Binder K and Landau D P 2003 *Phys. Rev.* E **68** 031601
[39] Müller M and Binder K 2005 *J. Phys.: Condens. Matter* **17** S333–61
[40] Evans R 1979 *Adv. Phys.* **28** 143
[41] Roth R and Parry A O 2011 *Mol. Phys.* **109** 1159
[42] Malijevský A 2012 *J. Chem. Phys.* **137** 214704
[43] Rosenfeld Y 1989 *Phys. Rev. Lett.* **63** 980
[44] Roth R 2010 *J. Phys.: Condens. Matter* **22** 063108
[45] Malijevský A and Parry A O 2013 *Phys. Rev. Lett.* **110** 166101
[46] Derjaguin B V 1940 *Acta Physicochim. URSS* **12** 181
[47] Henderson J R 2005 *Phys. Rev.* E **72** 051602
[48] Nakanishi H and Fisher M E 1982 *Phys. Rev. Lett.* **49** 1565
[49] Bruschi L, Carlin A and Mistura G 2002 *Phys. Rev. Lett.* **89** 166101
[50] Aarts D G A L 2005 *J. Phys. Chem.* B **109** 7407

Paper VI

IOP Publishing Journal of Physics: Condensed Matter
J. Phys.: Condens. Matter **26** (2014) 315002 (7pp) doi:10.1088/0953-8984/26/31/315002

Complete wetting near an edge of a rectangular-shaped substrate

Alexandr Malijevský

Department of Physical Chemistry, Institute of Chemical Technology, Prague, 166 28 Praha 6, Czech Republic
Department of Aerosol Chemistry and Physics, ICPF, Academy of Sciences, 16502 Prague 6, Czech Republic

Email: malijevsky@icpf.cas.cz

Received 28 February 2014, revised 9 April 2014
Accepted for publication 12 May 2014
Published 11 June 2014

Abstract

We consider fluid adsorption near a rectangular edge of a solid substrate that interacts with the fluid atoms via long range (dispersion) forces. The curved geometry of the liquid–vapour interface dictates that the local height of the interface above the edge ℓ_E must remain finite at any subcritical temperature, even when a macroscopically thick film is formed far from the edge. Using an interfacial Hamiltonian theory and a more microscopic fundamental measure density functional theory (DFT), we study the complete wetting near a single edge and show that $\ell_E(0) - \ell_E(\delta\mu) \sim \delta\mu^{\beta_E^{co}}$, as the chemical potential departure from the bulk coexistence $\delta\mu = \mu_s(T) - \mu$ tends to zero. The exponent β_E^{co} depends on the range of the molecular forces and in particular $\beta_E^{co} = 2/3$ for three-dimensional systems with van der Waals forces. We further show that for a substrate model that is characterised by a finite linear dimension L, the height of the interface deviates from the one at the infinite substrate as $\delta\ell_E(L) \sim L^{-1}$ in the limit of large L. Both predictions are supported by numerical solutions of the DFT.

Keywords: adsorption, wetting, density functional theory, fundamental measure theory, surface phase transitions

(Some figures may appear in colour only in the online journal)

1. Introduction

It is well known that the adsorption properties of solid substrates strongly depend on the substrate geometry. In particular, the nature of pertinent surface phase transitions on non-planar substrates may qualitatively differ from those on planar walls. The surface geometry can have a profound influence on the location of the phase transitions, their order, and the values of the critical exponents, and it can even induce entirely new interfacial phase transitions and fluctuation effects [1–8]. Recent theoretical studies also have revealed new examples of surprising connections between adsorption in different geometries [9, 10]. These findings are not only interesting in their own rights but also have useful and far-reaching consequences for applications that require the design of modified surfaces, whose adsorption properties can be sensitively controlled at the nanoscale. Indeed, recent advances in nano-lithography have opened up an entirely new area of research with exciting implications for modern technologies [11–13] that address the properties of fluids that are geometrically constrained to a molecular scale. Examples of the products of this sort of innovation include self-cleaning materials [14], responsive polymer brushes [15] or 'lab-on-a-chip' devices [16].

A prerequisite to these applications is a detailed description of fluid adsorption on structures of the most fundamental non-planar geometries. This paper focuses on the adsorption of a simple fluid near a substrate edge. In the simplest case of a single edge, the substrate geometry can be characterised by an internal angle $\phi < \pi$, where two semi-infinite planes meet. This (convex) object should be distinguished from a (concave) linear wedge model, because the fluid behaviours on these two substrates are strikingly different. While the wedge geometry promotes fluid condensation and shifts the temperature where macroscopic coverage occurs below the wetting temperature T_w of a corresponding planar wall [5, 6], the presence of the substrate edge implies that the height of the liquid–vapour

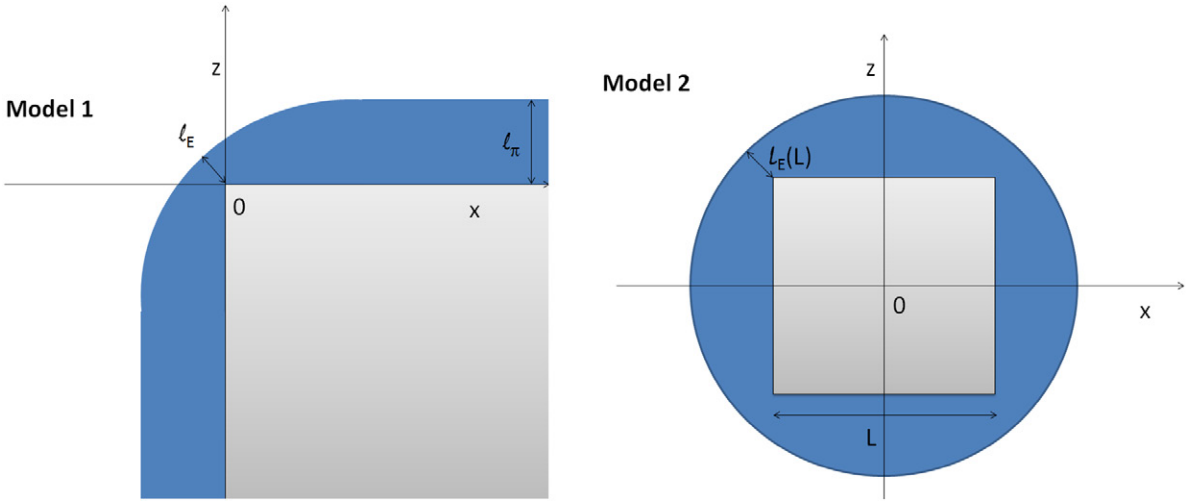

Figure 1. Left: a sketch of model 1 in the x–z projection. The liquid film thickness above the edge of the substrate is ℓ_E, while far away from the edge the film thickness approaches the value ℓ_π corresponding to an adsorbed layer above a planar wall. Right: a sketch of model 2 in the x–z projection. The liquid film thickness above each of the four edges of the substrate is $\ell_E(L)$, which now depends on the linear dimension of the wall L. In both cases, the wall is assumed to be infinitely long along the Cartesian y-coordinate.

interface above the edge ℓ_E remains finite at any subcritical temperature, even when the interface far from the edge ℓ_π unbinds from the wall. This suppression occurs because of the surface free energy cost, that must be paid for interface bending above the edge, similarly to adsorption on a spherical wall where the growth of an adsorbed film is restricted by the Laplace pressure arising from the curved liquid–vapour interface [17, 18].

A proper understanding of how the presence of the edge affects the wetting properties of the wall is important to obtain a comprehensive picture of adsorption on structured (or sculpted) surfaces. Recently, theoretical and experimental studies have shown that a planar wall etched with an array of rectangular grooves exhibits more adsorption regimes than the simple flat wall [10], [19–24]. A recent density functional (DFT) study [24] revealed that hydrophilic grooved surfaces experience the wetting transition at temperature $T > T_w$, which is in contrast with the predictions based on macroscopic approaches, such as the Wenzel model, predicting that surface corrugation promotes the surface's wetting properties [12]. Furthermore, the regimes that are characterised by the formation of a laterally inhomogeneous film with the interface pinned at the groove edges and followed by a discontinuous unbending [25] of the interface have been observed. In these cases, the presence of the groove edges plays a crucial role and the explanation of these phenomena is incomplete without our knowledge of what occurs in the immediate vicinity of an isolated edge.

A study by Parry *et al* [26] provides a description of the adsorption near an edge that focuses on the limit of $\phi \to \pi$ and shows a connection between complete wetting near a shallow edge and critical wetting on a planar wall. Here, motivated by the previously mentioned studies of rectangular grooves, we adopt a model with a long-range wall-fluid potential and fix the internal angle to $\phi = \pi/2$. We seek for the dependence of the local height of the adsorbed liquid film above the edge ℓ_E on the chemical potential offset from saturation $\delta\mu \equiv \mu_s(T) - \mu$ when the bulk coexistence is approached from below, $\delta\mu \to 0^+$. To this end, we consider two substrate models, as schematically pictured in figure 1. Using Model 1, the effective Hamiltonian theory reveals that

$$\ell_E(0) - \ell_E(\delta\mu) \sim \delta\mu^{\beta_E^{co}} + \mathcal{O}(\delta\mu), \tag{1}$$

as $\delta\mu \to 0^+$ with a non-universal critical exponent $\beta_E^{co} = p/(p+1)$, where the parameter p characterises a decay of the binding potential far from the edge $W(\ell) \sim \ell^{-p}$ (for $\delta\mu = 0$). In the most relevant case of (3D) non-retarded van der Waals forces $p = 2$, whence $\beta_E^{co} = 2/3$. In contrast, the next-to-leading term in equation (1) scales linearly with $\delta\mu$, regardless of the nature of the molecular interaction. We confirm this prediction by the numerical solution of a microscopic DFT. However, for small $\delta\mu$, the requirements on the system size become rather challenging. Therefore, as an alternative, we also consider Model 2 with a finite wall of a square cross-section with a linear dimension L and use scaling arguments to relate the height of the interface above the edge $\ell(L)$ with the wall size:

$$\ell_E - \ell_E(L) \sim L^{-1} + \mathcal{O}\left(L^{-\frac{3}{2}}\right), \tag{2}$$

where all powers now depend on the molecular model and can be expressed in terms of the critical exponents characterising wetting on a planar wall. This prediction is also confirmed by the DFT, whose implementation for Model 2 is rather straightforward.

We conclude this section by briefly recalling some properties of complete wetting on a planar wall for 3D systems with long-range forces (see, e.g., [27]) that are relevant for our purposes. We fix the temperature to a value between the wetting temperature T_w and the bulk critical temperature T_c and consider the limit $\delta\mu \to 0^+$. The mean thickness of the wetting layer $\ell_\pi(\delta\mu)$ is driven by the effective interaction (binding potential) between the wall surface and the liquid–vapour interface:

$$W(\ell) = \delta\mu\Delta\rho\ell + B\ell^{-p} + \cdots \tag{3}$$

where $B > 0$ is the Hamaker constant and $\Delta\rho = \rho_l - \rho_v$ is the difference between the liquid density and the vapour density at the bulk coexistence. The global minimum of $W(\ell)$ is at the finite value of ℓ_π for any $\delta\mu > 0$, but as $\delta\mu \to 0^+$, ℓ_π continuously diverges. The singularity of $W(\ell_\pi)$ at $\delta\mu = 0$ can be characterised by the set of critical exponents, in particular [28]:

$$\ell_\pi \sim \delta\mu^{-\beta_s^{\rm co}}, \quad \beta_s^{\rm co} = 1/(p+1), \tag{4}$$

$$\xi_\parallel \sim \delta\mu^{-\nu_\parallel^{\rm co}}, \quad \nu_\parallel^{\rm co} = (p+2)/(2p+2), \tag{5}$$

$$f_{\rm sing} \sim \delta\mu^{2-\alpha_s^{\rm co}}, \quad \alpha_s^{\rm co} = (p+2)/(p+1), \tag{6}$$

where $\xi_\parallel$ is the transverse correlation length, and $f_{\rm sing}$ denotes a singular part of the surface free energy. We recall that the upper critical dimension for complete wetting is $d_u < 3$ for any finite value of p, so that the expressions (4)–(6) are also valid beyond the mean-field approximation in our three-dimensional model [28].

The remainder of the paper is organised as follows. In section 2, we describe our DFT model. An effective Hamiltonian theory and the finite-size scaling arguments are presented in section 3, and their predictions are compared with the DFT in section 4. The results are summarised and discussed in section 5.

2. Density functional theory

In the classical density functional theory [29], the equilibrium density profile minimises the grand potential functional

$$\Omega[\rho] = \mathcal{F}[\rho] + \int {\rm d}\mathbf{r}\rho(\mathbf{r})[V(\mathbf{r}) - \mu], \tag{7}$$

where μ is the chemical potential, and $V(\mathbf{r})$ is the external potential. The intrinsic free energy functional $\mathcal{F}[\rho]$ can be separated into an exact ideal gas contribution and an excess part:

$$\mathcal{F}[\rho] = \beta^{-1}\int {\rm d}\mathbf{r}\rho(\mathbf{r})\left[\ln(\rho(\mathbf{r})\Lambda^3) - 1\right] + \mathcal{F}_{\rm ex}[\rho], \tag{8}$$

where Λ is the thermal de Broglie wavelength and $\beta = 1/k_{\rm B}T$ is the inverse temperature. As is common in the modern DFT approaches, the excess part is modelled as a sum of hard-sphere and attractive contributions where the latter is treated in a simple mean-field fashion:

$$\mathcal{F}_{\rm ex}[\rho] = \mathcal{F}_{\rm hs}[\rho] + \frac{1}{2}\int\int {\rm d}\mathbf{r}{\rm d}\mathbf{r}'\rho(\mathbf{r})\rho(\mathbf{r}')u_{\rm a}(|\mathbf{r}-\mathbf{r}'|), \tag{9}$$

where $u_{\rm a}(r)$ is the attractive part of the fluid-fluid interaction potential.

Minimisation of (7) leads to an Euler–Lagrange equation

$$V(\mathbf{r}) + \frac{\delta\mathcal{F}_{\rm hs}[\rho]}{\delta\rho(\mathbf{r})} + \int {\rm d}\mathbf{r}'\rho(\mathbf{r}')u_{\rm a}(|\mathbf{r}-\mathbf{r}'|) = \mu. \tag{10}$$

The fluid atoms are assumed to interact with one another via the truncated (i.e., short-ranged) and non-shifted Lennard-Jones-like potential

$$u_{\rm a}(r) = \begin{cases} 0; & r<\sigma, \\ -4\varepsilon\left(\dfrac{\sigma}{r}\right)^6; & \sigma<r<r_{\rm c}, \\ 0; & r>r_{\rm c}, \end{cases} \tag{11}$$

which is cut-off at $r_{\rm c} = 2.5\sigma$, where σ is the hard-sphere diameter.

The hard-sphere part of the excess free energy is approximated using the FMT functional [30],

$$\mathcal{F}_{\rm hs}[\rho] = \frac{1}{\beta}\int {\rm d}\mathbf{r}\,\Phi(\{n_\alpha\}), \tag{12}$$

which accurately takes into account the short-range correlations between fluid particles. From the number of various FMT versions (see, e.g., [31]), we have adopted the original Rosenfeld theory.

The wall atoms, which are assumed to be uniformly distributed with a density of $\rho_{\rm w}$, interact with the fluid particles via the Lennard–Jones-like potential

$$\phi(r) = -\frac{4\varepsilon_{\rm w}\sigma^6}{(r^2+\sigma^2)^3}, \tag{13}$$

where r is the distance between the fluid and the wall atoms.

In the following, two substrate models (walls) are considered. Within Model 1, the external potential $V(\mathbf{r})$ is induced by two semi-infinite planes that meet at an angle $\phi = \pi/2$ as sketched in figure 1 (left). The wall is assumed to be impenetrable for the fluid particles, so that

$$V_1(x,z) = \begin{cases} \infty; & x>0 \wedge z<0, \\ \widetilde{V}_1(x,z); & \text{otherwise}, \end{cases} \tag{14}$$

which defines the attractive part of the wall potential $\widetilde{V}_1(x,z)$. Assuming the translation invariance of the system along the edge, $\widetilde{V}_1$ is given by integrating over the entire depth of the wall:

$$\widetilde{V}_1(x,z) = \rho_{\rm w}\int_0^\infty {\rm d}x'\int_{-\infty}^\infty {\rm d}y'\int_{-\infty}^0 {\rm d}z' \phi\left(\sqrt{(x-x')^2+y'^2+(z-z')^2}\right), \tag{15}$$

which upon substitution from equation (13), results in

$$\widetilde{V}_1(x,z) = -\frac{1}{4}\pi\varepsilon_{\rm w}\sigma^3\rho_{\rm w}\left\{\pi + 2\arctan\left(\frac{x}{\sigma_w}\right) + \frac{2\sigma\left[\sigma^2(x-z) + xz\left(z - x - \frac{2\sigma^2+x^2+z^2}{\sqrt{\sigma^2+x^2+z^2}}\right)\right]}{(\sigma^2+x^2)(\sigma^2+z^2)} - 2\arctan\left(\frac{z}{\sigma}\right) - 2\arctan\left(\frac{xz}{\sigma\sqrt{\sigma^2+x^2+z^2}}\right)\right\}. \tag{16}$$

This expression can be compared with the potential of the planar wall based on the same molecular interaction:

$$V_\pi(z>0) = -\frac{1}{2}\pi\varepsilon_{\rm w}\rho_{\rm w}\sigma^3\frac{\pi(\sigma^2+z^2) - 2\sigma z - 2\arctan\left(\frac{z}{\sigma}\right)(\sigma^2+z^2)}{\sigma^2+z^2}, \tag{17}$$

which has an expected z^{-3} asymptotic behaviour:

$$V_\pi(z \gg \sigma) \approx -\frac{2}{3}\pi\varepsilon_w\rho_w\sigma^6 z^{-3} + \mathcal{O}(z^{-5}). \tag{18}$$

Within Model 2, the substrate remains infinite along the y axis, but the two other dimensions are a finite value L as sketched in figure 1 (right). In this case, the substrate potential is

$$V_2(x, z) = \begin{cases} \infty; & |x| < L/2 \wedge |z| < L/2, \\ \widetilde{V}_2(x, z); & \text{otherwise}, \end{cases} \tag{19}$$

with

$$\widetilde{V}_2(x, z) = \rho_w \int_{-L/2}^{L/2} \mathrm{d}x' \int_{-\infty}^{\infty} \mathrm{d}y' \int_{-L/2}^{L/2} \mathrm{d}z' \, \phi\left(\sqrt{(x-x')^2 + y'^2 + (z-z')^2}\right), \tag{20}$$

leading to

$$\widetilde{V}_2(x, z) = -\frac{\pi}{2}\varepsilon_w\sigma^6\rho_w \int_{-L/2-x}^{L/2-x} \mathrm{d}x' \left[\Psi\left(x', \frac{L}{2}-z\right) - \Psi\left(x', -\frac{L}{2}-z\right)\right], \tag{21}$$

where $\Psi(x, z) = \dfrac{z(3x^2+2z^2+3\sigma^2)}{(x^2+\sigma^2)^2 (x^2+z^2+\sigma^2)^{\frac{3}{2}}}$, which can be solved analytically.

Using the external potentials $V_i(x, z)$, $i = 1, 2$, the Euler–Lagrange equations (10) are numerically solved for the equilibrium profile $\rho(x, z)$ on a 2D Cartesian grid with a spacing of 0.05σ, and the corresponding integrals are performed using a Gaussian quadrature as described in [24]. To model the coupling of the system with the bulk reservoir, we impose the following boundary conditions: For Model 1, we set $\rho(L_c, z > 0) = \rho_\pi(z)$ and $\rho(x < 0, -L_c) = \rho_\pi(-x)$, where L_c is a cut-off of the wall, and $\rho_\pi(z)$ is the equilibrium density profile on a corresponding planar wall. For each bulk density (chemical potential), the grand potential minimisation is performed for different values of L_c to check possible finite-size effect on the density distribution near the edge. For Model 2, we simply fix the density along the boundary of the system to the value of the vapour bulk density ρ_b.

3. Interface Hamiltonian theory and finite size scaling

From a more phenomenological perspective, the adsorption near an edge can also be studied using the interfacial Hamiltonian model [6, 26]:

$$H[\ell] = \int \mathrm{d}\tilde{x} \left[\frac{\gamma}{2}\left(\frac{\mathrm{d}f(\tilde{x})}{\mathrm{d}\tilde{x}}\right)^2 + W(\ell(\tilde{x}))\right]. \tag{22}$$

The Hamiltonian is now expressed in a new Cartesian coordinate system $\{\tilde{x}, \tilde{y}, \tilde{z}\}$, which is related to the original system $\{x, y, z\}$ by a rotation about the y axis through a tilt angle $\alpha = (\pi - \phi)/2$ (see figure 2); thus, the height of the wall is $\tilde{z}_w = -\tan(\alpha)|\tilde{x}|$. Bearing in mind that for a rectangular wedge $\alpha = \pi/4$, the following analysis leaves the tilt angle unspecified. The function $f(\tilde{x}) = \ell(\tilde{x}) - \tan(\alpha)|\tilde{x}|$ denotes the local height of the liquid-gas interface relative to the horizontal, and $\ell(\tilde{x})$ is the local film thickness measured vertically. The first term in equation (22) penalises the increase of the liquid–vapour surface because of its non-planar shape, where γ is the corresponding surface tension, while $W(\ell)$ is the planar binding potential describing the interaction of the interface and the wall. Since the translation invariance of ℓ along the y axis is assumed, $H[l]$ denotes the Hamiltonian of the system per unit length. We notice that $W(\ell)$ can be obtained from the DFT as a coarse-grained excess (over bulk) grand potential (7) using a sharp-kink approximation to the density profile [27]. In a mean-field approximation, the Hamiltonian (22) is simply minimised to yield the Euler-Lagrange equation

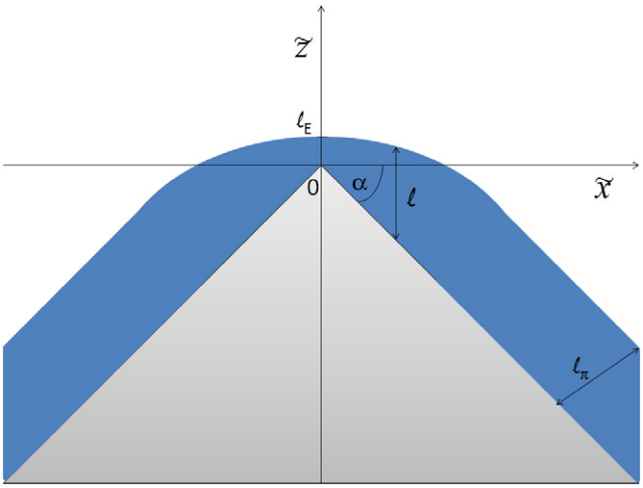

Figure 2. A sketch of the substrate model that was used by the interface Hamiltonian theory. The geometry of the substrate is identical to that of model 1, so that the tilt angle $\alpha = \pi/4$. However, the coordinate system is now different, as depicted.

$$\gamma\ddot{\ell}(\tilde{x}) = \frac{\partial W(\ell(\tilde{x}))}{\partial \ell}, \tag{23}$$

subject to the boundary conditions $\dot{\ell}(0^+) = \tan\alpha$ and $\lim_{\tilde{x}\to\infty} \ell(\tilde{x}) = \ell_\pi \sec\alpha$, where ℓ_π is the equilibrium film thickness on a planar wall, and $\dot{\ell} \equiv \dfrac{\mathrm{d}\ell(\tilde{x})}{\mathrm{d}\tilde{x}}$ (note that $\ddot{\ell} = \ddot{f}$). The Euler-Lagrange equation has a first integral, which provides an implicit equation for the height of the interface above the edge ℓ_E:

$$\frac{\gamma\tan^2\alpha}{2} = W(\ell_E) - W(\ell_\pi \sec\alpha), \tag{24}$$

which can be solved solely from knowledge of the wetting properties of the corresponding planar wall ($\alpha = 0$).

At the bulk coexistence, $\ell_\pi \to \infty$ for $T > T_w$, thus the last term in equation (24) vanishes. Then the height of the interface above the edge acquires a simple form (cf. [26]):

$$\ell_E^0 \equiv \ell_E(\delta\mu = 0) = \sqrt{\frac{2B}{\gamma\tan^2\alpha}}, \tag{25}$$

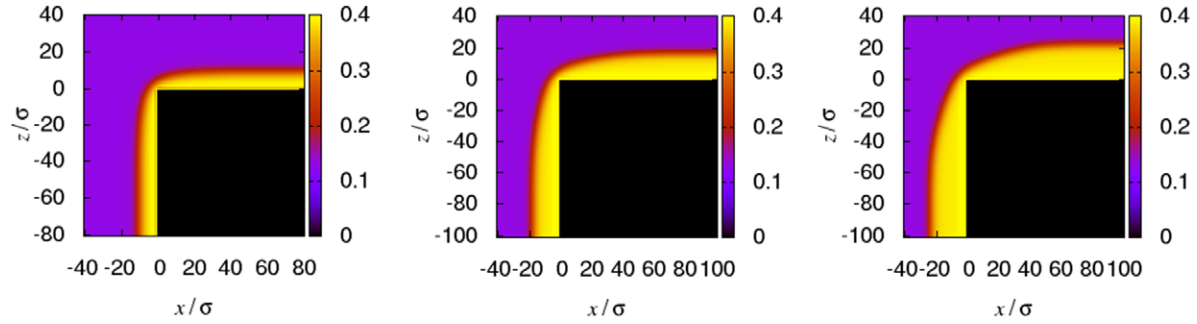

Figure 3. Density profiles $\rho(x, z)$ for a fluid at the interface between a semi-infinite rectangular substrate and a bulk vapour of temperature $k_BT/\varepsilon = 1.35$ and undersaturation $(\rho_v - \rho_b)\sigma^3$ (from left to right): (*a*) 10^{-3}, (*b*) 10^{-4} and (*c*) $2 \cdot 10^{-5}$.

where B is the Hamaker constant defined by equation (3). Because the fluid-fluid interaction is short-ranged, the Hamaker constant can be obtained from equation (18):

$$W(\ell) = -\Delta\rho \int_{\ell}^{\infty} \mathrm{d}\, z \overline{V}_{\pi}(z) = \frac{B}{\ell^2} + \mathcal{O}(\ell^{-4}), \qquad (26)$$

with $B = \frac{\pi}{3}\varepsilon_w \rho_w \sigma_w^6 \Delta\rho$.

We are now concerned with the limit $\delta\mu \to 0^+$. Substituting $\ell_E = \ell_E^0 + \delta\ell$ into equation (24) and introducing the abbreviation $A = \gamma \tan^2(\alpha)/2$, one obtains

$$A = \delta\mu\Delta\rho\ell_E^0 + \frac{B}{\left(\ell_E^0\right)^2} - \frac{2B}{\left(\ell_E^0\right)^3}\delta\ell - W(\ell_\pi \sec\alpha) + \text{H.O.T.} \qquad (27)$$

Using (6) and (25), it follows that

$$\delta\ell \sim -C_1\delta\mu^{2-\alpha_s^{co}} + C_2\delta\mu, \qquad (28)$$

as $\delta\mu \to 0$ and C_1, $C_2 > 0$. Finally, upon substituting α_s^{co} from equation (6), the exponent β_E^{co} defined in equation (1) becomes $\beta_E^{co} = p/(p+1)$. More specifically, for van der Waals forces ($p = 2$):

$$\delta\ell = -C_1\delta\mu^{\frac{2}{3}} + C_2\delta\mu + \mathcal{O}\left(\delta\mu^{\frac{4}{3}}\right). \qquad (29)$$

In terms of Model 2, the asymptotic result (28) must be modified due to the finiteness of the linear dimension of the wall L competing with the correlation length $\xi_\parallel$. Therefore, recalling the finite-size scaling arguments (see, e.g., [32]), the result of equation (28) valid for $L \to \infty$ becomes rescaled with a scaling function F:

$$\begin{aligned}\delta\ell_E(L) &\propto \delta\mu^{2-\alpha_s^{co}} F\left(\frac{L}{\xi_\parallel}\right) + \mathcal{O}\left(\delta\mu F\left(\frac{L}{\xi_\parallel}\right)\right) \\ &\propto \delta\mu^{2-\alpha_s^{co}} F(L\delta\mu^{\nu_\parallel^{co}}) + \mathcal{O}\left(\delta\mu F(L\delta\mu^{\nu_\parallel^{co}})\right)\end{aligned} \qquad (30)$$

which must remain finite as $\delta\mu \to 0$. Therefore,

$$\begin{aligned}\delta\ell_E(L) &\propto L^{\frac{\alpha_s^{co}-2}{\nu_\parallel^{co}}} + \mathcal{O}\left(L^{-\frac{1}{\nu_\parallel^{co}}}\right) \\ &\propto L^{-1} + \mathcal{O}(L^{-3/2})\end{aligned} \qquad (31)$$

where the values $\alpha_s^{co} = 4/3$ and $\nu_\parallel^{co} = 2/3$ were substituted in the final expression.

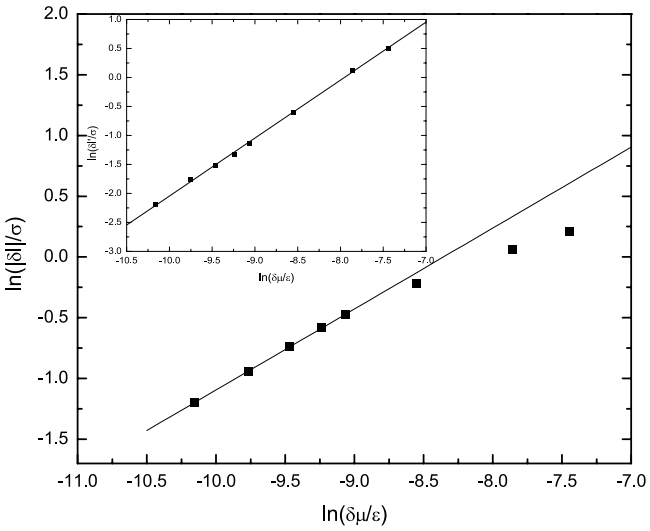

Figure 4. A log–log plot of the dependence of the film thickness above the edge relative to the saturation value, $\delta\ell = \ell_E - \ell_E^0$, on the chemical potential offset from the coexistence $\delta\mu$ for $k_BT/\varepsilon = 1.35$. The symbols represent the DFT results as obtained by model 1. The fitting line has a gradient of 3/2, suggesting $\delta\ell \sim \delta\mu^{2/3}$, which is consistent with equation (29). In the inset, a log–log plot of the dependence of $\delta\ell' = \delta\ell + C_1\delta\mu^{2/3}$ on $\delta\mu$ is shown. The fitting line has a gradient of 1, which supports the linear form of the second-order correction as predicted by the effective Hamiltonian theory, see equation (29).

4. Numerical results

We now examine the functional forms of (29) and (30) by a comparison with the numerical solution of the microscopic DFT, as described in section 2. We adopt σ and ε as the length and energy units, respectively, and we fix the strength of the wall potential to $\varepsilon_w = 0.4\varepsilon$, for which the wetting temperature is $k_BT_w/\varepsilon = 1.25$, which is sufficiently below the bulk critical temperature $k_BT_c/\varepsilon = 1.41$. We begin with the case of a semi-infinite wall as described by Model 1. For a given value of $\delta\mu$, we first determine the equilibrium density profile $\rho_\pi(z)$ for a corresponding system with a planar wall, which constitutes a boundary condition for the system with a single edge. For the sake of numerical consistency, the profile $\rho_\pi(z)$, albeit varying only in one dimension, is determined on the same two-dimensional grid as used for the edge. This also provides a good test of our numerics, since the difference between the planar density profile that is constructed from a 2D calculation proved not to appreciably differ from that obtained from a standard

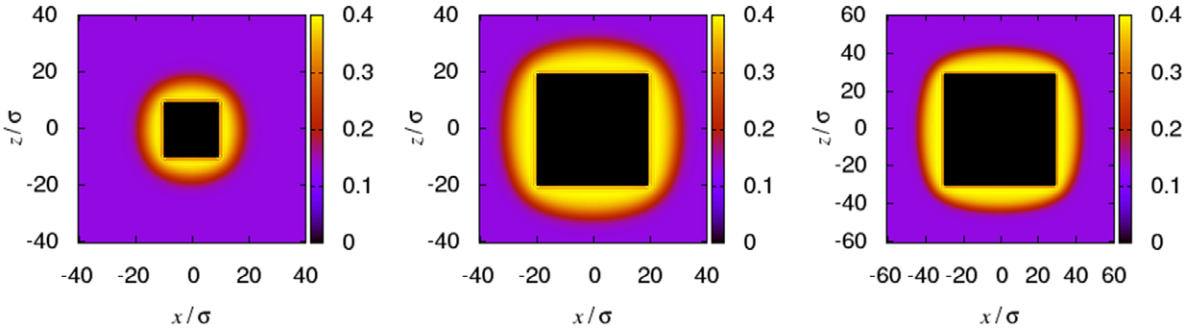

Figure 5. Examples of density profiles $\rho(x, z)$ of a fluid at the interface between a bulk saturated vapour at temperature $k_BT = 1.35\epsilon$ and a rectangular substrate of the size (from left to right): (*a*) $L = 20\sigma$, (*b*) $L = 40\sigma$ and (*c*) $L = 60\sigma$.

1D treatment. Moreover, the numerical accuracy of the full 2D DFT code, described in details in [24], was verified by comparison of the DFT results with the exact pressure sum-rule [33]. Then we set the boundary conditions such that $\rho(L_c, z > 0) = \rho_\pi(z)$ and $\rho(x < 0, -L_c) = \rho_\pi(-x)$, where the value of the wall cut-off L_c ranges from $L_c = 40\sigma$ to $L_c = 100\sigma$ to verify that the system size does not affect ℓ_E.

The representative samples of the equilibrium density profiles are shown in figure 3. The height of the fluid interface above the edge is defined as follows:

$$\ell_E = \frac{\sqrt{2}}{\Delta\rho}\int_{-\infty}^{0} \mathrm{d}\,x\big(\rho(x, -x) - \rho_b\big), \qquad (32)$$

where ρ_b is the density of the gas reservoir. Equation (32) allows us to compare the DFT results with the prediction based on the interface Hamiltonian theory as given by (29). The comparison that is displayed in figure 4 reveals a consistency between the two approaches and verifies the values of the exponents of the two first terms in equation (29).

Next, we consider Model 2 and examine the validity of the expansion (30). In the DFT, the density at the boundary of the system is fixed to the value of the bulk density of the saturated vapour, $\rho_b = \rho_v$, and the linear dimension of the box size is chosen from a range between 80σ and 120σ. Varying the wall size L, we find the equilibrium state of each system as shown in figure 5. In figure 6, we display a log-log plot of the height of the interface above the edge ℓ_E versus the wall size L. The values of ℓ_E are again determined using formula equation (31), where the upper limit is $-L_c/2$. The fitted line shows a good agreement between the DFT and the analytic expression (30), and for the region of $L > 20\sigma$, the first-order term in equation (30) appears to dominate. The consistency between the gradient of the fitted line and the predicted value −1 is within an error of 0.2%.

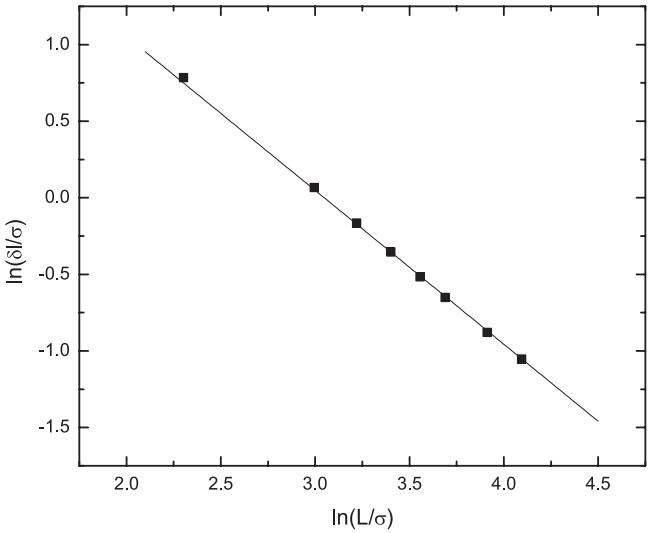

Figure 6. A log–log plot of the dependence of the meniscus height above the edge on the linear dimension of the wall of size L. The symbols represent the numerical DFT data corresponding to systems with saturated bulk vapour at $k_BT = 1.35\epsilon$. The gradient of the straight line fit is −1.002 compared to a predicted gradient of −1, see equation (31).

5. Conclusion

In this work, we used an interfacial Hamiltonian theory and a fundamental-measure DFT to study the fluid adsorption near a rectangular edge of a substrate interacting with the fluid via van der Waals forces. When the two-phase bulk coexistence is approached from below at a fixed temperature, i.e., the deviation of the chemical potential from the coexistence $\delta\mu = \mu_s - \mu \to 0^+$, macroscopically thick films are formed at the wall far away from the edge. Because these asymptotic interfaces must eventually merge to form a meniscus, the local height of the interface above the edge ℓ_E remains finite and indeed rather small even at the bulk coexistence. In this paper, we have shown that for an infinitely long substrate, $\ell_E(\delta\mu)$ approaches the coexistence value according to $\delta\ell = \ell_E(0) - \ell_E(\delta\mu) \sim \delta\mu^{\beta_E^{co}}$ as $\delta\mu \to 0^+$. The exponent depends on the range of the molecular interaction, such that $\beta_E^{co} = p/(p+1)$, where p defines the asymptotic decay of the binding potential $W(\ell) \sim \ell^{-p}$. The second-order correction to $\delta\ell$ is linear in $\delta\mu$ regardless of the molecular interaction. Both findings were verified by the DFT numerical calculations. We also showed that if the substrate is of finite size L, the previous result corresponds to the scaling of ℓ_E as $\ell_E - \ell_E(L) \propto L^{-1} + \mathcal{O}\left(L^{-\frac{3}{2}}\right)$, as also confirmed by the DFT. We conclude with two remarks about the generality of these findings. First, throughout this study, the substrate geometry was maintained fixed such that the substrate edge was rectangular. This geometry was selected because the model of a right-angle edge appears important considering its connection with other fundamental substrate models as discussed in the

introduction. Technically, the external potential for the rectangular geometry remains rather simple, which facilitates the numerics in the DFT, and the application of the finite-size arguments is straightforward. Nevertheless, we believe that the result given by equation (1) is valid for an arbitrary internal angle, since the value of ϕ was not assumed in the derivation of (1). Second, because the edge geometry does not induce any new divergence compared to a planar wall, the upper critical dimension d_u corresponding to complete wetting must be identical for the two substrates. Since $d_u < 3$ for a finite p for a planar wall [28], our mean-field results remain unaffected by the capillary-wave fluctuations.

Acknowledgments

I am grateful to A Parry for useful discussions. The financial support from the Czech Science Foundation, project 13-09914S, is acknowledged.

References

[1] Dietrich S 1999 *New Approaches to Problems in Liquid State Theory* ed C Caccamo *et al* (Dordrecht: Kluwer)
[2] Bonn D, Eggers J, Indekeu J, Meunier J and Rolley E 2009 *Rev. Mod. Phys.* **81** 739
[3] Saam W F 2009 *J. Low Temp. Phys.* **157** 77
[4] Hauge E H 1992 *Phys. Rev.* A **46** 4994
[5] Rejmer K, Dietrich S and Napiórkowski M 1999 *Phys. Rev.* E **60** 4027
[6] Parry A O, Rascón C and Wood A J 1999 *Phys. Rev. Lett.* **83** 5535
[7] Rascón C and Parry A O 2000 *Nature* **407** 986
[8] Silvestre N M, Eskandari Z, Patricio P, Romero J M and Telo Da Gama M M 2012 *Phys. Rev.* E **86** 011703
[9] Rascón C and Parry A O 2005 *Phys. Rev. Lett.* **94** 096103
[10] Tasinkevych M and Dietrich S 2006 *Phys. Rev. Lett.* **97** 106102
[11] Whitesides G M and Stroock A D 2001 *Phys. Today* **54** 42
[12] Quéré D 2008 *Annu. Rev. Mater. Res.* **38** 71
[13] Rauscher M and Dietrich S 2008 *Annu. Rev. Mater. Res.* **38** 143
[14] Fürstner R, Barthlott W, Neinhuis C and Walzel P 2005 *Langmuir* **21** 956
[15] Minko S 2006 *Polymer Rev.* **46** 397
[16] Service R F 1998 *Science* **282** 399
[17] Stewart M C and Evans R 2005 *Phys Rev.* E **71** 011602
[18] Nold A, Malijevský A and Kalliadasis S 2011 *Phys. Rev.* E **84** 021603
[19] Bruschi L, Carlin A and Mistura G 2002 *Phys. Rev. Lett.* **89** 166101
[20] Bruschi L, Fois G, Mistura G, Tormen M, Garbin V, di Fabrizio E, Gerardino A and Natali M 2006 *J. Chem. Phys.* **125** 144709
[21] Tasinkevych M and Dietrich S 2007 *Eur. Phys. J.* E **23** 117
[22] Hofmann T, Tasinkevych M, Checco A, Dobisz E, Dietrich S and Ocko B M 2010 *Phys. Rev. Lett.* **104** 106102
[23] Checco A, Ocko B M, Tasinkevych M and Dietrich S 2012 *Phys. Rev. Lett.* **109** 166101
[24] Malijevský A 2013 *J. Phys.: Condens. Matter* **25** 445006
[25] Rascon C, Parry A O and Sartori A 1999 *Phys. Rev.* E **59** 5697
[26] Parry A O, Greenall M J and Romero J M 2003 *Phys. Rev. Lett.* **90** 046101
[27] Dietrich S 1988 *Phase Transitions and Critical Phenomena* vol 12, ed C Domb and J L Lebowitz (New York: Academic)
[28] Lipowsky R 1984 *Phys. Rev. Lett.* **52** 1429
[29] Evans R 1979 *Adv. Phys.* **28** 143
[30] Rosenfeld Y 1989 *Phys. Rev. Lett.* **63** 980
[31] Roth R 2010 *J. Phys.: Condens. Matter* **22** 063102
[32] Fisher M E and Nakanishi H 1981 *J. Chem. Phys.* **75** 5857
[33] Malijevský A and Parry A O 2013 *J. Phys.: Condens. Matter* **25** 305005

Paper VII

Does adsorption in a single nanogroove exhibit hysteresis?

Alexandr Malijevský
Department of Physical Chemistry, Institute of Chemical Technology, Prague, 166 28 Prague 6, Czech Republic and E. Hála Laboratory of Thermodynamics, Institute of Chemical Process Fundamentals, Academy of Sciences, 16502 Prague 6, Czech Republic

(Received 21 September 2012; accepted 14 November 2012; published online 6 December 2012)

A simple fluid, in a microscopic capillary capped at one end, is studied by means of fundamental measure density functional. The model represents a single, infinitely long nanogroove with long-range wall-fluid attractive (dispersion) forces. It is shown that the presence or absence of hysteresis in adsorption isotherms is determined by wetting properties of the wall as follows: Above wetting temperature, T_w, appropriate to a single wall of the groove, the adsorption is a continuous process corresponding to a rise of a meniscus from the capped to the open end of the groove. For a sufficiently deep capillary, the meniscus rise is shown to be a steep, yet continuous process taking place near the capillary condensation of a corresponding slit. However, for temperatures lower than T_w the condensation exhibits a first-order transition accompanied by hysteresis of the adsorption isotherm. Finally, it is shown that hysteresis may occur even for $T > T_w$ as a consequence of prewetting on the side and bottom walls of the groove. © *2012 American Institute of Physics*. [http://dx.doi.org/10.1063/1.4769257]

The interfacial properties of fluids in confining geometries play a key role in several branches of physics and chemistry, and are vital for numerous engineering applications, see, e.g., Ref. 1. Two of the most fundamental interfacial phenomena involve a development of a liquid phase on a single wall and between two parallel unbounded walls at a pressure below the phase coexistence. The first, known as complete wetting, is characterized by a growth of an adsorbed liquid film $\ell \sim \Delta\mu^{-\beta_s^{co}}$. Here, ℓ is the film thickness and $\Delta\mu$ is a deviation of the chemical potential from its saturation value, $\mu_{\rm sat}(T)$, above a wetting temperature T_w (which corresponds to a zero contact angle). The exponent β_s^{co} is non-universal and depends on the character of molecular interaction; in particular, $\beta_s^{co} = 0$ for short-ranged forces, while $\beta_s^{co} = 1/3$ when dispersion forces are involved.[2] The second phenomenon, capillary condensation, differs from the previous one in two respects. First, it is a first-order transition, and, second, it reflects the finite size shift of the (3D) bulk phase boundary rather than surface phenomena at the wall. For a non-retarded van der Waals fluid-wall interaction and in the limit of a large distance L between the walls, the modified Kelvin equation[3,4] predicts the undersaturation at which the capillary condensation occurs at $T > T_w$

$$\Delta\mu(L) = \mu_{\rm sat} - \mu_{\rm cc}(L) \approx \frac{2\gamma}{(\rho_l - \rho_g)(L - 3\ell)}. \qquad (1)$$

Here, γ is the surface tension of a free liquid-gas interface, ρ_l and ρ_g are densities of the coexisting bulk phases, and ℓ is an adsorbed-film thickness. It should be noted that the details of the intermolecular forces in (1) are reflected only in the Derjaguin's correction (the factor of three multiplying the film thickness).

While adsorption phenomena in systems that can be described by a one-dimensional density distribution are rather well understood, interfacial phenomena on patterned surfaces, which are characterised by a variation in the density distribution at least in 2D, have recently become the focus of considerable interest, see, e.g., Ref. 5. The presence of a complex distribution of possible substrate topographies introduces a challenging task of relating geometrical and well-defined substrate models to the thermodynamics of fluid adsorption. Models suited to this task include linear wedges, cones, grooves, and pitted surfaces to name a few of the most popular.[6–13] The interest in this research has been largely motivated by new advances in nanofabrication techniques[14] which made possible a direct comparison between theoretical predictions and experiment.[15] Apart from the theoretical interest, the adsorption in nanopatterned surfaces has attracted considerable attention due to its application in micro- and nanofluidics.[16]

The purpose of the paper is to give a microscopic description of the adsorption of a simple fluid in a single, infinitely long groove of finite depth. In particular, we wish to know whether the adsorption isotherms in this model exhibit hysteresis or not. The main conclusion based on earlier studies[11–13,17,18] is that in the case of complete wetting the hysteresis vanishes due to the presence of the bottom wall. Here, we present a detailed microscopic study of this issue and discuss the effect of the wetting properties on the character of the groove-adsorption.

Consider a semi-infinite solid slab with a uniform one-body density ρ_w spanning a domain $\mathbb{S} = \mathbb{R} \otimes \mathbb{R} \otimes (-\infty, L_z)$, $L_z > 0$, in 3D Cartesians. Imagine that an infinitely long groove of width L_x and depth L_z, occupying a subspace $\mathbb{G} = (0, L_x) \otimes (-\infty, \infty) \otimes (0, L_z)$, is sculpted into the slab. We assume that the groove is subject to a potential

$$V(x,z) = \begin{cases} 0, & x < \sigma_w \text{ or } x > L_x - \sigma_w \text{ or } z < \sigma_w, \\ \tilde{V}(x,z), & \text{elsewhere}, \end{cases} \qquad (2)$$

where $\tilde{V}(x,z) = \rho_w \int_{\mathbb{W}} \phi_w(|\mathbf{r}-\mathbf{r}'|)\mathrm{d}\mathbf{r}'$, $\mathbb{W} = \mathbb{S} \setminus \mathbb{G}$, and

$$\phi_w(r) = -4\varepsilon_w \left(\frac{\sigma_w}{r}\right)^6. \tag{3}$$

Thus, we assume that the fluid particles interact with the substrate atoms via long-ranged (dispersion) forces characterized by the parameters ε_w and σ_w.

After integration, $\tilde{V}(x,z)$ can be expressed as follows:

$$\tilde{V}(x,z) = V_1(z) + V_2(x,z) + V_2(L_x - x, z), \tag{4}$$

with $V_1(z) = \frac{2\alpha_w}{z^3}$ and $V_2(x,z) = \alpha_w[\psi(x,z) + \psi(x, L_z - z)]$, where we have defined $\alpha_w = -\frac{1}{3}\pi\varepsilon_w\rho_w\sigma_w^6$ and

$$\psi(x,z) = \frac{2z^4 + x^2z^2 + 2x^4}{2x^3z^3\sqrt{x^2+z^2}} - \frac{1}{z^3}.$$

The fluid-fluid interaction is given by

$$\phi(r) = \begin{cases} \infty, & r < \sigma; \\ -4\varepsilon\left(\frac{\sigma}{r}\right)^6, & \sigma < r < r_c; \\ 0, & r > r_c. \end{cases} \tag{5}$$

In the following, parameters σ and ε will be used as length and energy units, respectively, and the cutoff is set to $r_c = 2.5\,\sigma$. The wall parameters are fixed to $\sigma_w = \sigma$ and $\varepsilon_w = 1.2\varepsilon$. The wetting temperature for such a model is $T_w = 0.83\,T_c$, where $k_BT_c/\varepsilon = 1.41$ is the critical temperature.

Within a classical density functional theory (DFT),[19] the equilibrium density profile is found by minimizing the grand potential functional

$$\Omega[\rho] = \mathcal{F}[\rho] + \int \mathrm{d}\mathbf{r}\rho(\mathbf{r})[V(\mathbf{r}) - \mu], \tag{6}$$

where μ is the chemical potential. $\mathcal{F}[\rho]$ is the intrinsic free energy functional of the one-body density, $\rho(\mathbf{r})$, whose excess (over ideal gas) part is treated as a perturbation about a hard-sphere reference fluid

$$\mathcal{F}_{\mathrm{ex}}[\rho] = \mathcal{F}_{\mathrm{hs}}[\rho] + \frac{1}{2}\int \mathrm{d}\mathbf{r}\rho(\mathbf{r}) \int \mathrm{d}\mathbf{r}\rho(\mathbf{r}')\phi(|\mathbf{r}-\mathbf{r}'|). \tag{7}$$

The hard sphere part of the excess free energy functional is approximated by means of the Rosenfeld fundamental measure theory (FMT)[20]

$$\mathcal{F}_{\mathrm{hs}}[\rho] = \frac{1}{\beta}\int \mathrm{d}\mathbf{r}\Phi(\{n_\alpha\}), \tag{8}$$

where Φ is a function of the weighted densities $\{n_\alpha(\mathbf{r})\}$, and $\beta = 1/k_BT$. Numerical calculations were carried out on a 2D grid with mesh $0.05\,\sigma$.

One should note that the functional (7) with $\mathcal{F}_{\mathrm{hs}}[\rho]$ obtained from the FMT is known to properly account for the short-ranged correlations that play a significant role in confined systems. In our nanogroove model, one expects strong packing effects at the vicinity of the walls (as in the case of common slit models) but additional and particularly strong inhomogeneities are also expected at the edges of the groove. Finally, our DFT is thermodynamically consistent and yields the correct divergence of wetting film thickness for systems that exhibit dispersion forces. All these properties are of key importance for a reliable description of the phase behaviour of the model.

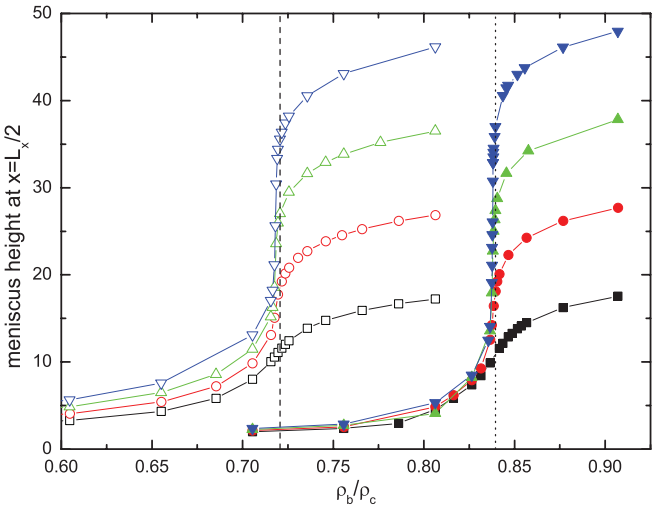

FIG. 1. Meniscus rise in a groove of width $L_x = 7\,\sigma$ (empty symbols) and $L_x = 12\,\sigma$ (full symbols) as a function of undersaturation (ρ_b is the bulk density, ρ_c is the critical density). The depths of the grooves are from the bottom $L_z/\sigma = 20$, 30, 40, and 50. The curves are the guides to the eye. The vertical lines denote densities corresponding to capillary condensation in an infinite slit of a width $L_x = 7\,\sigma$ (dashed) and $L_x = 12\,\sigma$ (dotted). For $T = 0.92\,T_c$.

In the following, we summarize the most-important features of adsorption in the model groove that can be inferred from our DFT calculations. We start by considering temperature $T = 0.92\,T_c$, which is above the wetting temperature, T_w, of a corresponding planar wall. In such a case, a meniscus separating a gas-like and a liquid-like phase is formed near the bottom end, and continuously rises upon increasing the chemical potential towards the two-phase coexistence region. Position of the meniscus can be defined as $\ell(x) \equiv \int \mathrm{d}z(\rho(x,z) - \rho_b)/\Delta\rho$, where $\Delta\rho = \rho_l - \rho_g$ is the difference between liquid and vapour densities at the bulk coexistence. In Fig. 1, the meniscus rise is shown for grooves of $L_x = 12\,\sigma$ and $L_x = 7\,\sigma$ and several depths. As is apparent, the groove filling is a continuous process, which should be contrasted to capillary condensation in infinite slits. Furthermore, as L_z is increased, the meniscus rise becomes steeper and steeper upon approaching the capillary condensation indicated by the vertical lines. Such results should be compared with a schematic plot (Fig. 1) in Ref. 13.

Next, consider $T = 0.81\,T_c$, which is slightly below T_w. Now, the scenario of the fluid adsorption dramatically changes. As displayed in Fig. 2, the system exhibits a hysteresis in adsorption per unit length $\Gamma = \int_{\mathbb{G}} \rho(x,z)\,\mathrm{d}x\,\mathrm{d}y$, indicating a first order transition resembling capillary condensation in infinite slits. In order to understand the different behaviour of the adsorption in the two cases, let us discuss the mechanism of the groove filling for $T > T_w$ and $T < T_w$.

For $T > T_w$, the groove filling can be described with the help of a simple slab model, as schematized in Fig. 3. Substituting a sharp-kink approximation for the density profile in (6), the excess (over the groove completely filled with a liquid) grand potential

$$\frac{\Omega^{\mathrm{ex}}(\ell_x,\ell_z)}{L} = (p_l^+ - p)(L_x - 2\ell_x)(L_z - \ell_z) + \gamma[2(L_z - \ell_z) + (L_x - 2\ell_x)] + \frac{\rho_g - \rho_l}{L}\int_{V_g} V(\mathbf{r})\mathrm{d}\mathbf{r}, \tag{9}$$

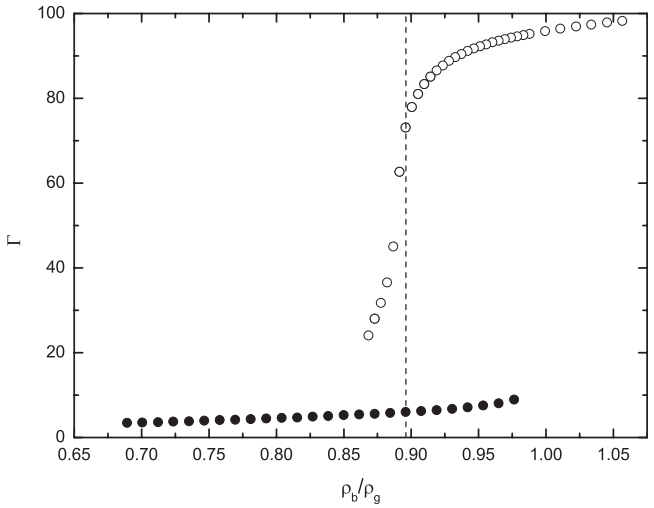

FIG. 2. Adsorption isotherm at temperature $T = 0.81\,T_c$ in a groove of width $L_x = 12\,\sigma$ and depth $L_z = 20\,\sigma$; ρ_b is the bulk density, ρ_g is the density of a saturated gas. Full symbols denote the adsorption path, empty symbols denote the desorption path. The vertical dashed line denotes a density where two distinct states coexist.

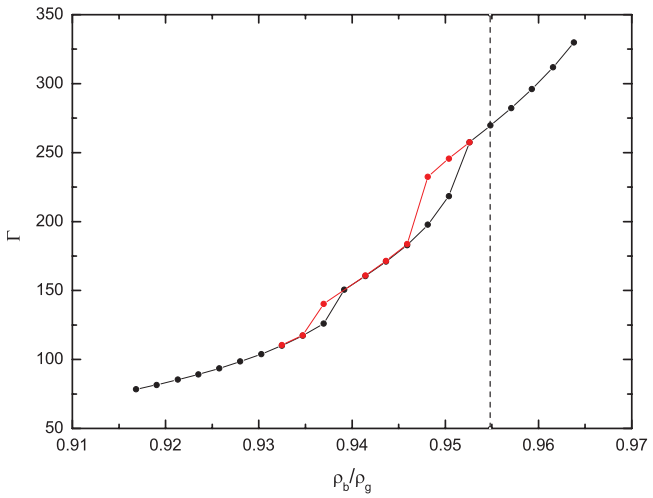

FIG. 4. Adsorption isotherm at temperature $T = 0.91\,T_c$ in a groove of width $L_x = 50\,\sigma$ and depth $L_z = 50\,\sigma$. Black symbols denote the adsorption path, red symbols denote the desorption path. The lines are the guides to the eye. The vertical dashed line denotes a density corresponding to the prewetting transition in an open slit of width $L = 50\,\sigma$.

where p_l^+ is the bulk pressure of the metastable liquid and p is that of the gas reservoir. When minimized with respect to ℓ_z (minimization with respect to ℓ_x reproduces Eq. (1)), one obtains in the limit of large L_z

$$\Delta p + \frac{A}{\ell^4} + \mathcal{O}\left(1/\ell_z^6\right) = 0, \tag{10}$$

where $\Delta p = p - p_l^+ - \frac{2\gamma}{L_x - 3\ell_x}$ and $A = \frac{9}{8}\frac{\alpha_w(\rho_l - \rho_g)L_x(L_x - 2\ell_x)}{L_x - 3\ell_x}$. Comparing (10) with (1) and assuming that $\Delta\mu(L_x)$ is small, the meniscus rise satisfies (cf. Ref. 13)

$$\ell_z \sim (\mu_{cc}(L_x) - \mu)^{-1/4}. \tag{11}$$

The same conclusion was obtained in Ref. 13. However, in Ref. 13 the authors ignored the influence of ℓ_x, while the connection with Eq. (1) has been made more explicit here. Thus, for $T > T_w$ one observes a continuous filling of a groove, similar to a complete wetting on a planar wall. However, the differences with the latter are: (i) the deep groove becomes filled in the limit $\mu \to \mu_{cc}(L_x)$ rather than for $\mu \to \mu_{\rm sat}$; and (ii) the critical exponent of the groove filling is 1/4, i.e., the process is somewhat slower than the complete wetting.

In contrast, for $T < T_w$ only a microscopically thin film is formed on a free wall. Therefore, the system behaves in a qualitatively same fashion as in an open slit and undergoes a first-order transition accompanied by pronounced hysteresis. We emphasize that Eq. (10) cannot be applied anymore in this regime, since inclusion of higher order terms due to repulsive interactions would be needed. These would give a global minimum of $\Omega^{\rm ex}$ at a finite distance of ℓ_z.

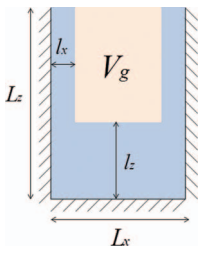

FIG. 3. Schematic illustration of the slab model.

Finally, let us consider temperature $T = 0.91\,T_c$. Such a temperature is again above T_w but this time (slightly) lower than T_{cs}, the prewetting critical temperature corresponding to a single wall. It is well known[21] that the prewetting transition between a thin and thick layers on a single wall may also occur in slits, but the phenomenon is preceded by capillary condensation unless the separation between the walls is large. It is interesting to examine how prewetting is reflected in our model groove in the absence of capillary condensation (above T_w). In Fig. 4, an adsorption isotherm for a model $L_x = L_z = 50\,\sigma$ is depicted. We observe that the otherwise-continuous increase in adsorption, due to meniscus rise, exhibits two small van der Walls loops, both slightly below the bulk density appropriate to prewetting. The first of the two loops corresponds to a discontinuous jump in the meniscus height, reflecting prewetting on the bottom wall, cf. Fig. 5 (top). Such a transition is shifted to a higher undersaturation compared to prewetting on a single wall, $\rho_b^{\rm pw}/\rho_{\rm sat}$, due to the influence of the side walls that decreases the potential inside the groove. The second loop corresponds to prewetting on the side walls, cf. Fig. 5 (bottom). Again, this transition is shifted below $\rho_b^{\rm pw}/\rho_{\rm sat}$ but the difference is smaller, since the effect of the bottom wall on the vertical liquid films is relatively weak (for large z the potential of the bottom wall decays as z^{-3}). However, the scenario may be different and the sequence of the two transitions be reversed if the side walls are stronger adsorbents than the bottom wall.

In summary, we have employed a mean-field FMT-DFT to describe adsorption in a single nanogroove with attractive walls that exhibit a first-order wetting transition. At high temperatures, the results support the picture of the onset of a liquid phase due to a heterogeneous nucleation on a bottom wall, followed by a continuous rise of the meniscus separating vapour-like and liquid-like phases, and no hysteresis in

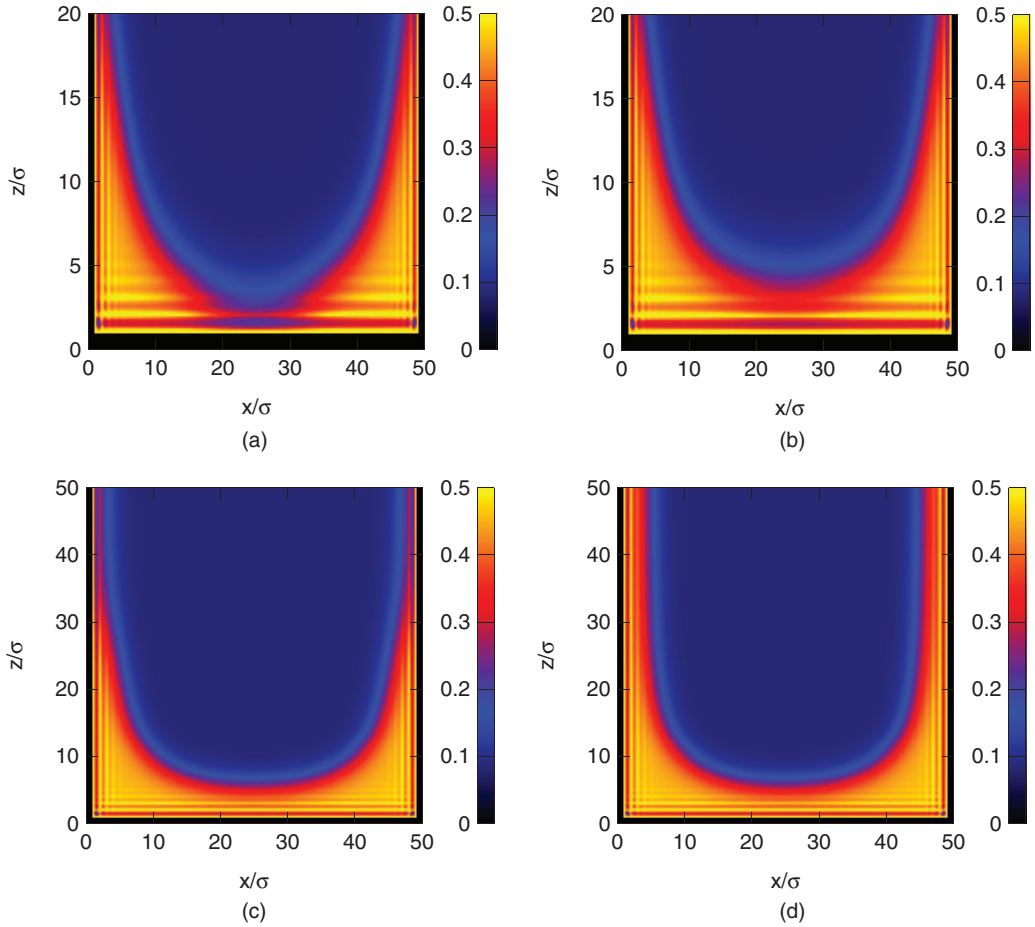

FIG. 5. Density distributions (x-z projection) in a groove with attractive walls at temperature $T = 0.91\,T_c$. $L_x = L_z = 50\,\sigma$. (Top) Coexisting states at a density $\rho_b/\rho_g = 0.93695$. (Bottom) Coexisting states at a density $\rho_b/\rho_g = 0.94813$.

adsorption appears in this case (see Fig. 1). However, as we have demonstrated, such a scenario is valid only for temperatures above the wetting temperature of a corresponding single wall. Below T_w, the adsorption exhibits a first-order transition (accompanied by hysteresis) as in an open slit. Thus, T_w, which represents a crossover between partial and complete wetting for a single wall, represents a boundary separating first-order and continuous transition regimes for a nanogroove. Some care is needed, though. For large widths, a wedge filling may take place at the corners of the groove at temperatures above a filling temperature, which may cause a shift of this boundary below T_w; for the model considered here, the filling temperature (of a rectangular wedge) is $T_f \approx 0.76\,T_c$. We have not observed such a phenomenon even for a groove width as large as $L_x = 50\,\sigma$, but one cannot rule out this possibility. Finally, it has been shown that in the temperature interval (T_w, T_{sc}), the groove-adsorption isotherm may exhibit two loops, reminiscent of prewetting. The first (if the bottom and side walls are adsorbents of the same strength) corresponds to a jump of the meniscus, which is followed by a discontinuous thickening of the liquid films on the side walls.

We believe that the observed phenomena will motivate further experimental measurements and give some contribution into the long-standing issue of a well-known but still actively debated phenomenon of hysteretic behaviour of fluid adsorption in mesoporous media.

[1]L. D. Gelb, K. E. Gubbins, R. Radhakrishnan, and M. Sliwinska-Bartowiak, Rep. Prog. Phys. **62**, 1573 (1999).
[2]S. Dietrich, in *Phase Transitions and Critical Phenomena*, edited by C. Domb and J. L. Lebowitz (Academic, New York, 1988), Vol. 12.
[3]B. V. Derjaguin, Zh. Fiz. Khim. **137**, 14 (1940).
[4]R. Evans and U. M. B. Marconi, Chem. Phys. Lett. **114**, 415 (1985).
[5]D. Bonn, J. Eggers, J. Indekeu, J. Meunier, and E. Rolley, Rev. Mod. Phys. **81**, 739 (2009).
[6]C. Rascón and A. O. Parry, Nature (London) **407**, 986 (2000).
[7]A. O. Parry, C. Rascón, and A. J. Wood, Phys. Rev. Lett. **85**, 345 (2000).
[8]M. Napiórkowski, W. Koch, and S. Dietrich, Phys. Rev. A **45**, 5760 (1992).
[9]C. Rascón and A. O. Parry, Phys. Rev. Lett. **94**, 096103 (2005).
[10]M. Tasinkevych and S. Dietrich, Phys. Rev. Lett. **97**, 106102 (2006).
[11]U. M. B. Marconi and F. Van Swol, Phys. Rev. A **39**, 4109 (1989).
[12]G. A. Darbellay and J. M. Yeomans, J. Phys. A **25**, 4275 (1992).
[13]C. Rascón, A. O. Parry, N. B. Wilding, and R. Evans, Phys. Rev. Lett. **98**, 226101 (2007).
[14]L. Bruschi and G. Mistura, J. Low Temp. Phys. **157**, 206 (2009).
[15]T. Hofmann, M. Tasinkevych, A. Checco, E. Dobisz, S. Dietrich, and B. M. Ocko, Phys. Rev. Lett. **104**, 106102 (2010).
[16]H. Bruss, *Theoretical Microfluidics* (Oxford University Press, Oxford, 2008).
[17]L. D. Gelb, Mol. Phys. **100**, 2049 (2002).
[18]R. Roth and A. O. Parry, Mol. Phys. **109**, 1159 (2011).
[19]R. Evans, Adv. Phys. **28**, 143 (1979).
[20]Y. Rosenfeld, Phys. Rev. Lett. **63**, 980 (1989).
[21]R. Evans and U. M. B. Marconi, Phys. Rev. A **32**, 3817 (1985).

Paper VIII

IOP Publishing Journal of Physics: Condensed Matter
J. Phys.: Condens. Matter **26** (2014) 355003 (12pp) doi:10.1088/0953-8984/26/35/355003

Condensation and evaporation transitions in deep capillary grooves

Alexandr Malijevský[1,2] **and Andrew O Parry**[3]

[1] Department of Physical Chemistry, ICT Prague, 166 28 Praha 6, Czech Republic
[2] Institute of Chemical Process Fundamentals, Academy of Sciences, 16502 Prague 6, Czech Republic
[3] Department of Mathematics, Imperial College London, London SW7 2B7, UK

E-mail: malijevsky@icpf.cas.cz

Received 9 May 2014, revised 13 June 2014
Accepted for publication 16 June 2014
Published 31 July 2014

Abstract

We study the order of capillary condensation and evaporation transitions of a simple fluid adsorbed in a deep capillary groove using a fundamental measure density functional theory (DFT). The walls of the capillary interact with the fluid particles via long-ranged, dispersion, forces while the fluid-fluid interaction is modelled as a truncated Lennard–Jones-like potential. We find that below the wetting temperature T_w condensation is first-order and evaporation is continuous with the metastability of the condensation being well described by the complementary Kelvin equation. In contrast above T_w both phase transitions are continuous and their critical singularities are determined. In addition we show that for the evaporation transition above T_w there is an elegant mapping, or covariance, with the complete wetting transition occurring at a planar wall. Our numerical DFT studies are complemented by analytical slab model calculations which explain how the asymmetry between condensation and evaporation arises out of the combination of long-ranged forces and substrate geometry.

Keywords: wetting, adsorption, capillary condensation, density functional theory, fundamental measure theory, Lennard–Jones

(Some figures may appear in colour only in the online journal)

1. Introduction

It is well known that confining a fluid can dramatically alter its properties and induce new examples of phase transitions and critical phenomena. Important examples of this include wetting, pre-wetting and layering at planar walls [1–4], capillary condensation, critical point shifts and interfacial delocalization in parallel plate geometries [5–8] and filling transitions in wedges [9–13]. A simple extension of these idealized geometries, which has received a great deal of recent attention, is a groove or capped capillary formed by scoring a narrow deep channel or array of channels into a solid surface (see figure 1). Capping a capillary strongly influences the nature of condensation and evaporation, compared to that occurring in an infinite open capillary-slit, because of the presence of a meniscus, which must unbind from the groove bottom (top) at condensation (evaporation) [14–24]. The purpose of the present paper is to investigate the nature of this meniscus unbinding in a model microscopic density functional theory (DFT) incorporating realistic long-ranged intermolecular forces. In doing so we wish to study a number of predictions for the possible asymmetry between the condensation and evaporation branches of the adsorption isotherm occurring both above and below the wetting temperature [22]. In particular, we report for the first time a precise connection, or covariance, between evaporation transitions in capillary grooves and complete wetting at planar walls.

Consider a simple fluid which, in the bulk, shows coexistence between liquid and gas phases, with densities ρ_l and ρ_g respectively, along a saturation chemical potential curve $\mu_{\rm sat}(T)$ which terminates at a bulk critical temperature T_c. Now suppose the fluid is confined between two parallel plates, of infinite area, separated by a distance L. Such confinement shifts the location of the coexistence, which now occurs between capillary gas and capillary liquid phases along a capillary condensation curve $\mu_{\rm cc}(L)$ and which ends at a capillary critical temperature [5, 7]. In the limit of macroscopically

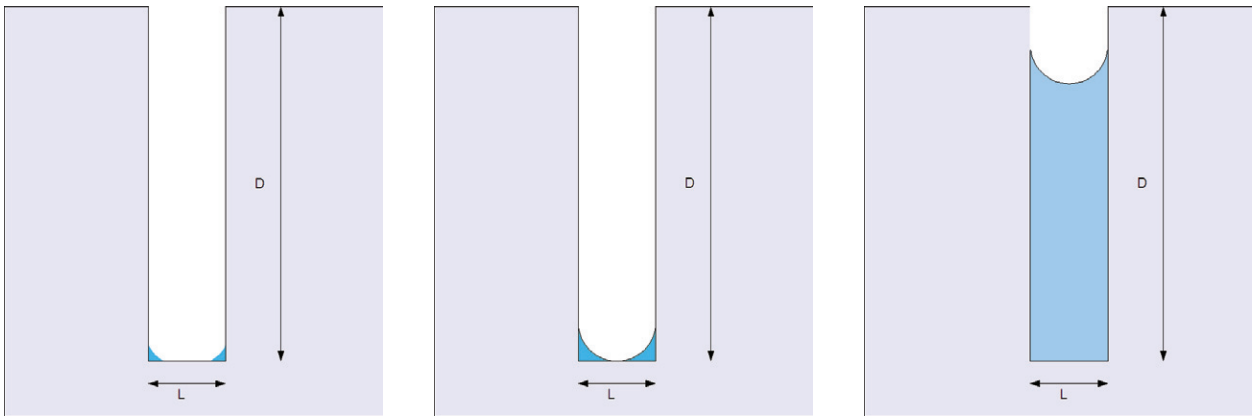

Figure 1. Sketch of a cross section of a capillary groove of width L and depth $D \gg L$ and three different configurations of the meniscus. On the far left a near empty capillary is shown corresponding to $\mu < \mu_{cc}$ with two small corner menisci near the capillary bottom. On the far right is a near filled capillary corresponding to $\mu < \mu_{cc}$ in which a single meniscus is close to the groove opening. The middle configuration shows an empty capillary corresponding to $\mu \approx \mu_{cc}$, but with much more prominent corner menisci which may correspond to a stable or a metastable configuration depending on the order of the condensation transition.

wide capillaries and small undersaturation, $\mu_{cc}(L)$ satisfies the Kelvin equation [25]:

$$\mu_{cc}(L) = \mu_{sat} - \frac{2\gamma \cos\theta}{L\Delta\rho} + \cdots, \tag{1}$$

where $\Delta\rho = \rho_l - \rho_g$, γ is the liquid-gas interfacial tension and θ is the contact angle. For temperatures below the wetting temperature T_w, corresponding to $\theta > 0$, the Kelvin equation is known to be accurate even for microscopically narrow slits which are only several molecular diameters wide [6]. However, for $T > T_w$, when $\theta = 0$ and thick wetting films form at the walls, it is necessary to also allow for Derjaguin's correction which reduces the effective slit width [5, 6, 26] (see appendix). In this case the Derjaguin corrected Kelvin equation is known to be accurate down to slit widths of a few hundred molecular diameters [6]. In most DFT studies of capillary condensation one supposes translational invariance along the walls so that the density profile depends only on one Cartesian coordinate. In this case capillary condensation is certainly a first-order transition, at which the density profile jumps, at μ_{cc}, from a low coverage to a high coverage state. Thus at mean-field level, below the capillary critical temperature $T_c(L)$, adsorption isotherms exhibit a van der Waals loop, characterised by metastable extensions and spinodals. The Kelvin equation is usually derived by equating the grand potentials of coexisting capillary liquid and capillary gas phases each of which have distinct bulk and surface free-energy contributions [6]. Alternatively, it can be understood geometrically as the value of the chemical potential where a circular meniscus of Laplace radius $R = \gamma/(\mu_{sat} - \mu_{cc})\Delta\rho$ meets the walls at the contact angle θ, thus establishing a stable separation of the coexisting capillary phases.

This simple picture of capillary condensation is enriched considerably when one end is capped to form a deep capillary groove, as shown schematically in figure 1. Hereafter we suppose that the side walls and cap are made from the same material so there is only one macroscopic contact angle θ. In such a macroscopically deep groove condensation must still occur at $\mu_{cc}(L)$ since the contribution to the free energy from the capped and open ends do not scale with the depth D. However it is now necessary to distinguish between condensation and evaporation since these two transitions are distinct. Condensation involves the unbinding of the meniscus from the bottom of the groove, which is filled mostly with capillary gas along the adsorption branch, as the chemical potential is increased to μ_{cc}. Evaporation on the other hand involves the unbinding of the meniscus from the top of the groove, which is filled mostly with capillary liquid along the desorption branch, as the chemical potential is decreased to μ_{cc}. Recent theoretical studies [15, 19–21] have predicted that for $T > T_w$ when the walls are completely wet by liquid the condensation involves the continuous unbinding of the meniscus. Thus, if ℓ_C denotes the equilibrium height of the meniscus above the groove bottom, we can characterise the divergence on approaching condensation by

$$\ell_C \sim (\mu_{cc} - \mu)^{-\beta_C}, \tag{2}$$

which is valid for deep grooves $D \gg \ell_C \gg L$. Similarly, for $T > T_w$ the evaporation transition is also predicted to be continuous [22] in which case the distance of the meniscus from the groove top diverges as

$$\ell_E \equiv (D - \ell_C) \sim (\mu - \mu_{cc})^{-\beta_E}, \tag{3}$$

which is again valid for $D \gg \ell_E \gg L$. Strictly speaking these power laws only apply to macroscopically deep grooves but as we shall see they also describe the behaviour of the meniscus in grooves of finite depth. The values of the exponents β_C and β_E (which are referred to as β_A and β_D in [15]) are, in general, distinct with both depending sensitively on the range of intermolecular forces. In particular, for dispersion-like forces, effective Hamiltonian considerations lead to the mean-field predictions $\beta_C = 1/4$ and $\beta_E = 1/3$ which are almost entirely insensitive to interfacial fluctuation effects (see later) [15]. Thus even when the condensation and evaporation are both continuous there is still an asymmetry between them with the condensation being a slightly sharper transition. Note that the value of the evaporation exponent β_E is the same as that one describing the growth of the complete wetting films at planar

walls in systems with dispersion forces. In fact, this is not coincidental and points to a much deeper connection between groove evaporation and planar complete wetting which we shall discuss at length in this paper.

The situation for walls which are partially wet by liquid is however quite different [21–23]. Below a temperature $T^*(L) \approx T_w$ it has been predicted that the condensation transition becomes first-order due to the preferential adsorption of fluid, or corner menisci, at the bottom of the groove (see the left panel in figure 1). In this case at μ_{cc} a low coverage configuration coexists with one in which the groove is completely filled with liquid (see the right panel in figure 1) similar to the standard interpretation of condensation. Note that the macroscopic size and shape of such corner menisci are determined uniquely by the simple geometrical requirement that they have a Laplace radius $R = \gamma/(\mu_{sat} - \mu)\Delta\rho$ and meet the side and bottom walls at the correct contact angle θ. Such low coverage configurations persist into a metastable regime $\mu > \mu_{cc}$ which terminates at a spinodal μ_{sp} where the menisci meet, determined by the complementary Kelvin equation [22]

$$\mu_{sp}(L) = \mu_{cc}(L) + \frac{2\gamma \sin\theta}{L\Delta\rho} + \cdots . \tag{4}$$

The phenomena that we focus on in this paper are the condensation and evaporation transitions and in particular their order above and below the wetting temperature T_w. To fully understand them we must also consider them in the context of other phase transitions both at mean-field level and beyond. As mentioned earlier, the groove is itself a generalization of other geometries which exhibit known and well-studied phase transitions. Suppose for example that the separated side walls exhibit (in the limit $L \to \infty$) a first-order wetting transition at temperature T_w and chemical potential $\mu = \mu_{sat}$. Associated with this is a pre-wetting line which extends above T_w and to $\mu < \mu_{sat}$ which is the locus of coexistence between two distinct phases with thin and thicker wetting layers. In a capillary of finite width L, the wetting transition is of course suppressed but a finite-size shifted capillary pre-wetting line will still, in general, exist. In this case one should distinguish between capillary-gas phases which have either thin or thick wetting films at the side walls. However for narrow capillaries, which will be exclusively considered in this paper, the capillary pre-wetting occurs in a metastable region since it is preceded by capillary condensation. Similarly, the bottom of a capped capillary comprises two right-angle corners each of which, if separated by an infinite distance, would, at bulk two phase coexistence, exhibit a filling transition at a temperature $T_f < T_w$ (when the contact angle $\theta = \pi/4$). In a capillary of finite width L the filling transition is again suppressed since the corner menisci can not become macroscopically large. But, if the filling transition is first-order one may suspect that a pre-filling line, corresponding to transitions from thin to thick corner menisci states, exists at either corner of a finite width capillary. However there are two reasons why such transitions are irrelevant for our discussion of condensation and evaporation. First, analogous to pre-wetting at the side walls, for narrow grooves, the pre-filling line exists in a metastable region of the phase diagram since it is preceded by capillary condensation. The second reason is that, strictly speaking, the pre-filling transition is an artefact of the mean-field approximation in model density functional theories. In reality, any pre-filling-like jump in the adsorption near the corners is rounded owing to the pseudo one-dimensional nature of the transition. Exactly the same reasoning applies to any pre-wetting like transition associated with the bottom wall which must also be rounded beyond mean-field. We will return to this last point at the end of our paper. In summary, pre-wetting and pre-filling associated with the bottom wall are irrelevant artefacts of mean-field treatments, while pre-wetting at the side walls is only of interest for rather wide capillaries.

In this paper we use a highly accurate fundamental measure DFT to examine different properties of condensation and evaporation in a narrow groove geometry for systems with long-ranged intermolecular forces. We aim to answer the following questions; Firstly regarding continuous capillary condensation above T_w, is the effective Hamiltonian prediction that the $\beta_C = 1/4$ observable in our studies of grooves of large but finite depth? Secondly does the transition become first order below the wetting temperature and if so how accurate is the complementary Kelvin equation? Similarly for evaporation we wish to test the prediction that above T_w the exponent $\beta_E = 1/3$ and to determine the order of the transition below T_w. In doing this we will show that due to the presence of long-ranged forces, for capillary evaporation there is a hidden connection or covariance with the very well understood phenomena of complete wetting at a planar wall i.e. the adsorptions characterising these different phase transitions in two distinct geometries are precisely related to each other.

The rest of our paper is organised as follows. In section 2 we describe our DFT, our choice of intermolecular forces and the substrate geometry in more detail. In section 3 we present our DFT results for condensation and evaporation below section 3.1 and above section 3.2 the wetting temperature and determine numerically the critical exponents β_C and β_E. We also show that above the wetting temperature, where corner menisci are not of crucial importance, the values of the critical exponents can be obtained analytically from a simple slab or shark-kink model the details of which are provided in an Appendix. Finally, we discuss in detail the covariance between groove evaporation and complete wetting on a planar wall and finish with a summary of our results and a discussion of the nature of the capillary wetting transition beyond mean-field.

2. Density functional theory

Within DFT [27], the equilibrium density profile is found by minimising the grand potential functional

$$\Omega[\rho] = \mathcal{F}[\rho] + \int d\mathbf{r}\rho(\mathbf{r})[V(\mathbf{r}) - \mu], \tag{5}$$

where μ is the chemical potential and $V(\mathbf{r})$ is the external potential. It is convenient to divide the intrinsic free energy

functional $\mathcal{F}[\rho]$ into an exact ideal gas contribution and an excess part:

$$\beta\mathcal{F}[\rho] = \int \mathrm{d}\mathbf{r}\rho(\mathbf{r})[\ln(\rho(\mathbf{r})\Lambda^3) - 1] + \beta\mathcal{F}_{\mathrm{ex}}[\rho], \quad (6)$$

where Λ is the thermal de Broglie wavelength, which we set to unity and $\beta = 1/k_BT$ is the inverse temperature. To continue we follow the traditional van der Waals or perturbative approach and model the excess term as a sum of hard-sphere and attractive contributions where the latter is treated in a simple mean-field fashion. Thus we write

$$\mathcal{F}_{\mathrm{ex}}[\rho] = \mathcal{F}_{\mathrm{hs}}[\rho] + \frac{1}{2}\iint \mathrm{d}\mathbf{r}\mathrm{d}\mathbf{r}'\rho(\mathbf{r})\rho(\mathbf{r}')u_{\mathrm{a}}(|\mathbf{r} - \mathbf{r}'|), \quad (7)$$

where $u_{\mathrm{a}}(r)$ is the attractive part of the fluid–fluid interaction potential.

Minimisation of (5) leads to an Euler–Lagrange equation:

$$V(\mathbf{r}) + \frac{\delta\mathcal{F}_{\mathrm{hs}}[\rho]}{\delta\rho(\mathbf{r})} + \int \mathrm{d}\mathbf{r}'\rho(\mathbf{r}')u_{\mathrm{a}}(|\mathbf{r} - \mathbf{r}'|) = \mu. \quad (8)$$

In our model, the fluid atoms are assumed to interact with each other via a truncated (but non-shifted) Lennard–Jones-like potential

$$u_{\mathrm{a}}(r) = \begin{cases} 0; & r<\sigma, \\ -4\varepsilon\left(\dfrac{\sigma}{r}\right)^6; & \sigma<r<r_c, \\ 0; & r>r_c. \end{cases} \quad (9)$$

which is cut-off at $r_c = 2.5\ \sigma$, where σ is the hard-sphere diameter. Hereafter, we will use the parameters σ and ε as the length and energy units.

The hard-sphere part of the excess free energy is approximated by the fundamental measure theory (FMT) functional [28],

$$\mathcal{F}_{\mathrm{hs}}[\rho] = \frac{1}{\beta}\int \mathrm{d}\mathbf{r}\Phi(\{n_\alpha\}). \quad (10)$$

There exist various recipes for constructing FMT functionals in terms of the weighted densities $n\alpha$, all of which are known to accurately model the short-rage correlations. Here we follow the modified version of the Rosenfeld original functional proposed in [29], which is known to satisfy exact statistical mechanical sum rules and thermodynamic conditions at planar walls and corners [12, 13].

To construct the external potential $V(\mathbf{r})$ we consider a semi-infinite solid slab of uniform density ρ_w, into which is cut an infinitely long narrow groove of width L and depth D as shown in figure 1. The wall atoms interact with the fluid particles via the attractive part of Lennard–Jones potential

$$\phi(r) = -4\varepsilon_w\left(\frac{\sigma}{r}\right)^6, \quad (11)$$

so that total external potential experienced by the fluid atoms inside the groove is

$$V(x, z; L, D) = \begin{cases} \infty, & x<\sigma \text{ or } x>L-\sigma \text{ or } z<\sigma, \\ \rho_w\int\phi(|\mathbf{r}-\mathbf{r}'|)\,\mathrm{d}r' & \text{elsewhere}, \end{cases} \quad (12)$$

where the integral is over the solid volume and we have incorporated a hard-wall repulsion set by the atomic diameter σ which prevents $V(x, z)$ from diverging. Thus the external potential is translationally invariant along the y-axis running parallel to the groove. The integrals can be done analytically and the potential can be written as a sum of contributions from the bottom wall and vertical walls on the LHS and RHS respectively:

$$V(x, z; L, D) = V^{(1)}(z) + V^{(2)}(x, z; D) + V^{(2)}(L - x, z; D), \quad (13)$$

The potential due to the bottom wall is particularly simple and decays as a pure power law,

$$V^{(1)}(z) = \frac{2\alpha_w}{z^3}, \quad (14)$$

where we have introduced the pre-factor

$$\alpha_w = -\frac{1}{3}\pi\varepsilon_w\rho_w\sigma^6. \quad (15)$$

The contribution due to each vertical wall is more complicated and is most conveniently written as [13]

$$V^{(2)}(x, z; D) = \alpha_w(\psi(x, z) + \psi(x, D-z)), \quad (16)$$

where

$$\psi(x, z) = \frac{2z^4 + x^2z^2 + 2x^4}{2x^3z^3\sqrt{x^2+z^2}} - \frac{1}{z^3}. \quad (17)$$

It is straightforward to show that in the limits $L \to \infty$ and $D \to \infty$ the potential $V(x, z)$ reduces to that corresponding to a rectangular corner [13].

Using the external potential $V(x, z)$ we numerically solve the Euler-Lagrange equation (8) for the equilibrium profile $\rho(x, z)$ on a two-dimensional Cartesian grid with a spacing $0.05\ \sigma$.

In our numerical studies we set the wall strength $\varepsilon_w = 1.2\ \varepsilon$. In this case it is known that, for a planar wall-gas interface at bulk coexistence $\mu = \mu_{\mathrm{sat}}$, there is a strongly first-order wetting transition at a temperature satisfying $k_{\mathrm{B}}T_w = 1.18\ \varepsilon$ which is far below the bulk critical temperature (occurring at $k_{\mathrm{B}}T_c = 1.41\ \varepsilon$) [13]. Similarly for a single right-angle corner there exists a strongly first-order filling transition occurring also at bulk coexistence but at a lower temperature satisfying $k_{\mathrm{B}}T_f = 1.08\ \varepsilon$. Before we considered the capped groove we first studied an infinite open slit for which the external potential $V(x) = 2\alpha_w(x^{-3} + (L-x)^{-3})$. For this system we determined the equilibrium grand potentials and thus computed the capillary coexistence curve μ_{cc} as a function of T for representative widths $L = 7\sigma$ and $L = 12\sigma$. We then cap this geometry leaving an open end in order to study the nature of the condensation and evaporation transitions. For this we chose a groove with depth $D = 50\sigma$ which is sufficiently deep to observe the meniscus unbinding and accurately determine critical exponents for these transitions. To model the boundary with the bulk reservoir at the top of the groove we use the simple boundary condition $\rho(x, D) = \rho_b\exp[-\beta V(x, D; L, D)]$ where ρ_b is the bulk vapour density. This precludes us studying wetting films on top of the sculpted surface but does not influence the condensation and evaporation occurring within a deep groove

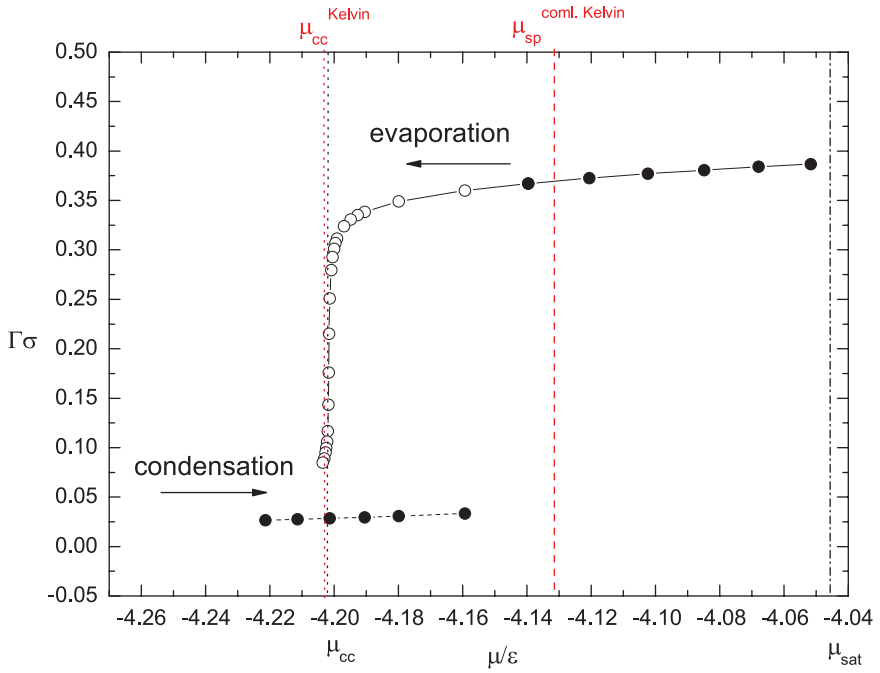

Figure 2. Adsorption isotherms (full symbols) found by increasing μ and desorption isotherms (empty symbols) found by decreasing μ in a capillary groove of width $L = 7\sigma$ and depth $D = 50\sigma$, at a temperature $T/T_w = 0.97$. The black vertical dotted line denotes the value of the chemical potential corresponding to the capillary condensation determined independently from a 1D DFT for an open slit of width $L = 7\sigma$; the red vertical dotted lines denotes the chemical potential corresponding to the capillary condensation determined from the Kelvin equation (1). The red dashed line denotes the position of the spinodal as predicted by the complementary Kelvin equation (4). The vertical dotted-dashed line denotes the saturated chemical potential.

for chemical potentials close to μ_{cc}. Having determined the density profile $\rho(x, z)$ we construct the total adsorption

$$\Gamma_C = \iint \mathrm{d}x\mathrm{d}z\big(\rho(x, z) - \rho_b\big), \tag{18}$$

which directly measures the height of the meniscus from the bottom and is thus an appropriate order parameter for condensation in a groove. For evaporation, it is more suitable to consider an excess over the density of the (metastable) bulk liquid density ρ_l^+:

$$\Gamma_E = \iint \mathrm{d}x\mathrm{d}z|\rho(x, z) - \rho_l^+|, \tag{19}$$

which is proportional to the height of the meniscus from the top. We have determined adsorption isotherms of Γ_C and Γ_E versus μ, for a variety of temperatures above and below T_w which directly reflect the order of the condensation and evaporation transitions. For condensation we start from a low coverage configuration corresponding to $\mu \ll \mu_{cc}$ and increase the chemical potential until either a spinodal is reached or the groove continuously fills. For evaporation we consider the reverse scenario and start from a high coverage at a chemical potential $\mu > \mu_{cc}$ (but still below the saturation value μ_{sat}) and approach μ_{cc} from above.

3. Results

3.1. Condensation and evaporation below the wetting temperature

In figure 2 we show a representative adsorption and desorption isotherms in a groove of width $L = 7$ and depth $D = 50$ at a temperature $T/T_w = 0.97$. Consider first the condensation branch which follows the adsorption as the chemical potential is increased from an initial low value. It can be seen that the coverage remains small as one approaches the chemical potential μ_{cc} at which, in an infinitely deep groove, there is coexistence with a high density configuration. The density profile at μ_{cc} is shown in figure 3 and illustrates some preferential adsorption near the corners. There is however no macroscopic meniscus. We note that the numerically determined value for μ_{cc} is extremely close to that predicted by the Kelvin equation, which is to be anticipated since $T < T_w$. For $\mu > \mu_{cc}$ the low density configuration is metastable with respect to a high coverage state and persists up to a spinodal value μ_{sp}. The numerically obtained value $\mu_{sp} = -4.15\varepsilon$ is also close, within 0.5%, to that predicted by the complementary Kelvin equation (4), although the agreement is not as good as for that between μ_{cc} and the Kelvin equation. The accuracy of the complementary Kelvin equation is remarkable in view of the fact that it was derived using entirely macroscopic arguments based on the merging of corner menisci even though these are not present at these microscopic scales.

Consider next moving along the desorption line starting from a high-density state we observe a continuous and dramatic decrease in Γ. Representative density profiles for different μ are shown in figure 4 and show a meniscus whose distance from the open end increases continuously as $\mu \to \mu_{cc}$. A log–log plot of Γ_E versus $\mu - \mu_{cc}$ is shown in figure 5 and is consistent with the result $\beta_E = 1/3$. We will return to this in the next section.

These numerical results show that within our model of a macroscopically deep groove, below the wetting temperature,

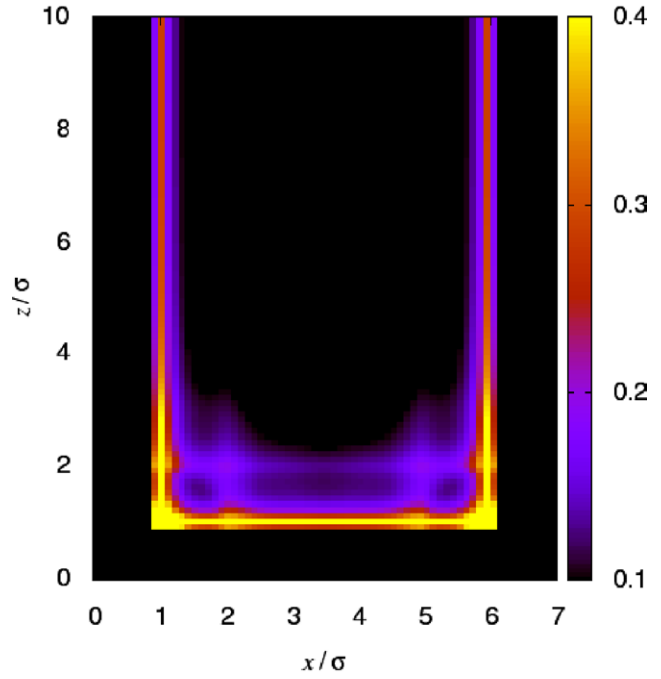

Figure 3. Density profile corresponding to a low-adsorption state in a groove of $L = 7\sigma$ and $D = 50\sigma$ (displayed only to $z = 10\sigma$) at $T/T_w = 0.97$ at capillary coexistence $\mu = \mu_{cc}$.

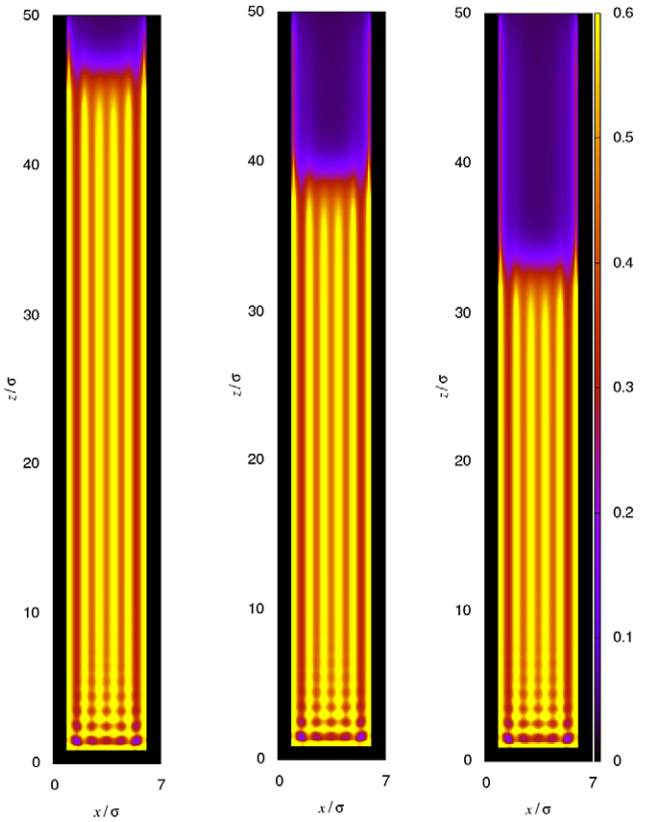

Figure 4. Density profiles corresponding to the evaporation branch for a capillary groove of width $L = 7\sigma$ and depth $D = 50\sigma$, at a temperature $T/T_w = 0.97$. From left to right the undersaturation $\delta\mu = \mu - \mu_{sat}$ is: 10^{-3}, 10^{-4}, and $5 \cdot 10^{-5}$ in units of ε.

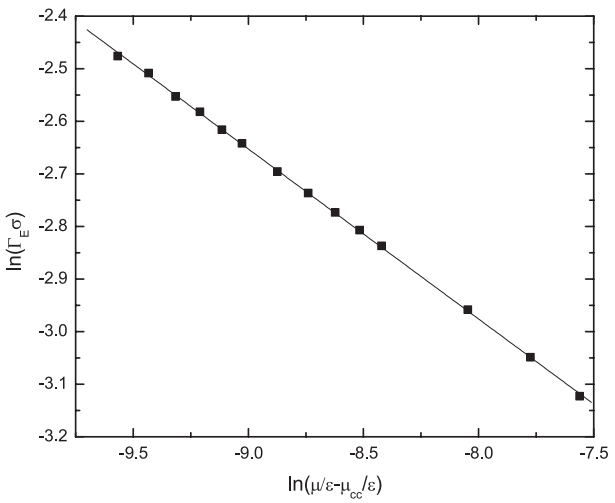

Figure 5. A log–log plot of the adsorption Γ_E for the evaporation branch, $\mu \to \mu_{cc}^{+}$ for a groove of width $L = 7\sigma$ and depth $D = 50\sigma$ at sub-wetting temperature $T/T_w = 0.97$. The straight line has a slope −1/3.

the condensation is first-order while the evaporation is continuous. Of course, in a groove of finite depth the evaporation transition is a subject to finite size effects which limit the distance of the meniscus from the open end. In this case, at mean-field level, the evaporation branch must also reach a spinodal μ_{sp}^{evap} which lies slightly below μ_{cc} (see figure 2). However, as D becomes larger, μ_{sp}^{evap} tend to μ_{cc}. It is in this sense that the evaporation transition is ultimately continuous in a macroscopically deep groove.

In contrast, the spinodal point μ_{sp}^{cond}, corresponding to the condensation branch, remains distinct from μ_{cc} as D is increased indicating that the transition is first-order. In fact for condensation one needs to consider the opposite limit and ask what happens to the transition as the groove depth is decreased. We have checked numerically that, for a variety of temperatures below T_w, the condensation transition remains first-order until the depth D becomes microscopically small, comparable to the width L.

Beyond mean-field level the condensation/evaporation transition is rounded for all finite D since the groove geometry is pseudo-one-dimensional. However standard finite-size scaling arguments imply that the width of the rounding $\Delta\mu_{round}/\mu_{cc} \approx \exp(-\gamma\beta LD)$ which is completely negligible once the groove depth and width are greater than the bulk correlation length.

3.2. Condensation and evaporation above the wetting temperature

3.2.1. Numerical DFT results. In figure 6 we show the adsorption and desorption isotherms obtained for $T/T_w = 1.1$ in a groove of width $L = 12\sigma$ and depth $D = 50\sigma$. In this case there is no hysteresis so that the condensation and evaporation branches are connected continuously. This finding is consistent with the prediction of the complementary Kelvin equation since the contact angle $\theta = 0$. In figure 7 we show

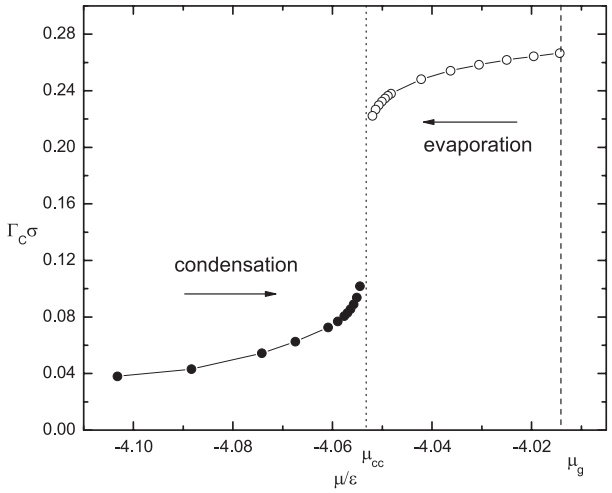

Figure 6. Adsorption isotherm in a capillary groove of width $L = 12\sigma$ and depth $D = 50\sigma$, at a temperature $T/T_w = 1.1$. The vertical dotted line denotes the location of the chemical potential μ_{cc} corresponding to the capillary condensation determined independently from the 1D DFT for an open slit of width $L = 12\sigma$; the vertical dashed line denotes saturated vapour density at the same temperature.

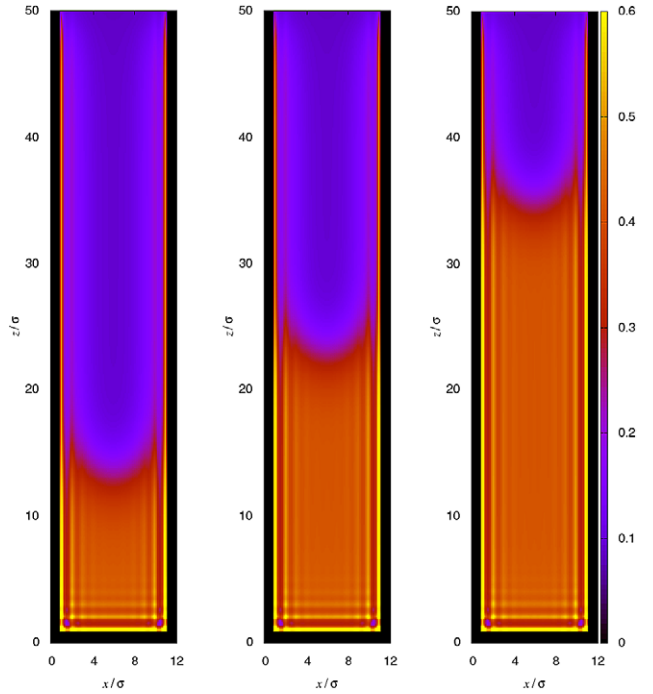

Figure 7. From left to right density profiles for chemical potentials slightly below ($\mu/\mu_{cc} = 0.98$, close to $\mu/\mu_{cc} \approx 1$) and slightly above ($\mu/\mu_{cc} = 1.02$) that of capillary condensation for a capillary groove of width $L = 12\sigma$ and depth $D = 50\sigma$, at a temperature $T/T_w = 1.1$.

density profiles obtained below, at, and slightly above μ_{cc}, which illustrate the continuous movement of the meniscus from the near cap to groove top as the chemical potential is increased. The absence of spinodals indicates that in the limit of macroscopic D both condensation and evaporation transitions occur via the continuous unbinding of the meniscus from the bottom and top, respectively. However, while both transitions are continuous there remains a quantitative difference between them characterised by the critical exponents β_C and β_E. This is shown in figure 8 where we present log–log plots of the adsorption and complementary adsorption as μ_{cc} is approached from below and above, respectively. For the evaporation branch, we find the same value $\beta_E = 1/3$ obtained for the case of $T < T_w$. For condensation on the other hand our results indicate that $\beta_C = 1/4$.

3.2.2. Slab model analysis. Our numerical DFT results illustrate the asymmetry between condensation and evaporation. Below the wetting temperature condensation is first-order while the evaporation is continuous. This qualitative difference can be understood due to the behaviour of the corner menisci and is accurately quantified, even for narrow slits, by the complementary Kelvin equation. Above the wetting temperature on the other hand the difference between condensation and evaporation is more subtle since both transitions are continuous. However an asymmetry still persists through the distinction between the adsorption critical exponents β_C and β_E. In this section we present details of a sharp-kink or slab model calculation, valid above the wetting temperature, which predicts, analytically, the values of the critical exponents. This is similar to the original effective Hamiltonian analysis of continuous condensation and evaporation presented in [15] but improves on by accounting for thick complete wetting films which will allow us to derive a formula for μ_{cc} consistent with the Derjaguin corrected Kelvin equation.

In sharp-kink approximation we assume that the full two dimensional density profile $\rho(x, z)$ simply arises from a) a flat meniscus constrained to be at height ℓ above the groove bottom, b) wetting films of thickness ℓ_π at each wall lying above the meniscus. Hence vapour at pressure p occupies a volume V_g while a metastable bulk liquid at pressure p_l^+ is adsorbed at the capillary walls and below the meniscus (see figure 9). Such a parameterization neglects the shape of the meniscus which is approximately circular. However, allowing for a fixed circular shape adds only a constant term to the free-energy and thus does not influence in any way the equilibrium values of the meniscus height and wetting film thickness. More importantly this parameterization does not allow for corner menisci and is therefore not appropriate for modelling condensation occurring below the wetting temperature.

For a macroscopically deep groove, the equilibrium value of the wetting film thickness at the side walls is independent of the meniscus height and is the same as that for an infinite open slit, given by

$$\ell_\pi = \left(\frac{2|\alpha_w|}{\mu_{sat} - \mu}\right)^{\frac{1}{3}} + \mathcal{O}\left(L^{-\frac{5}{3}}\right). \tag{20}$$

The first term here is the equilibrium film thickness of a complete wetting film at a single planar wall while the $\mathcal{O}\left(L^{-\frac{5}{3}}\right)$ correction arises from the interaction between the wetting

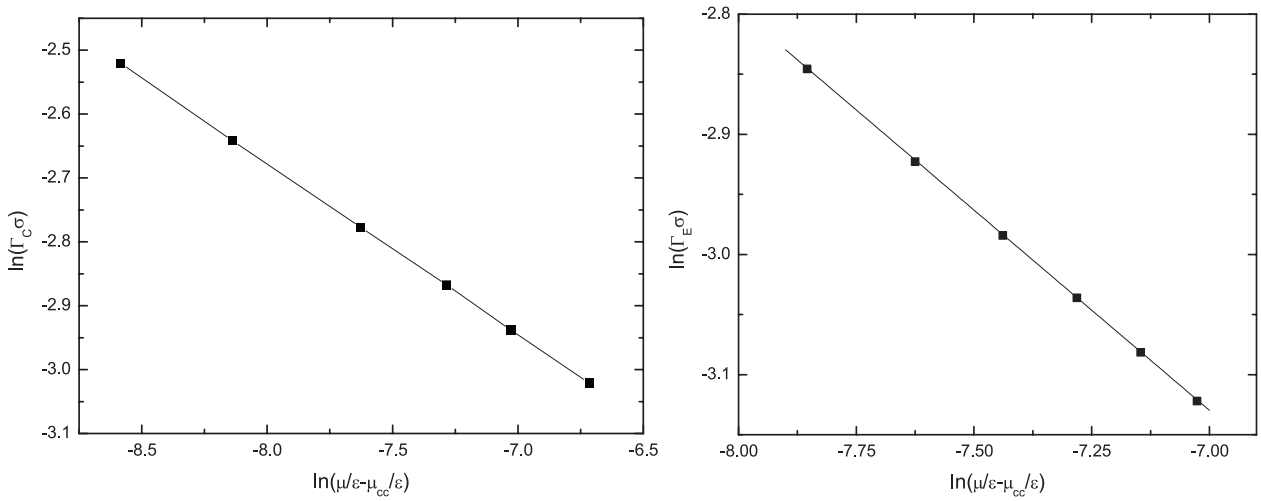

Figure 8. Left: a log–log plot of the adsorption, Γ_C, for the condensation transition occurring as $\mu \to \mu_{cc}^-$. The straight line fit has gradient −0.2507 (compare to the theoretical prediction $\beta_C = 1/4$). Right: a log–log plot of the complementary adsorption, Γ_E, for the evaporation transition occurring as $\mu \to \mu_{cc}^+$. The straight line fit has gradient −0.3332 (compare to the theoretical prediction $\beta_E = 1/3$). These results pertain to a capillary groove of width $L = 12\sigma$ and depth $D = 50\sigma$, at a temperature $T/T_w = 1.1$.

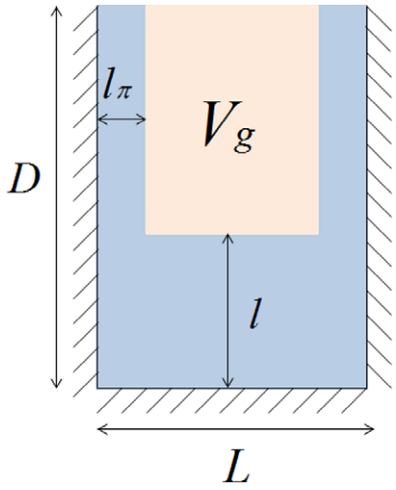

Figure 9. Slab model parameterization of the density profile showing a meniscus of height ℓ in a capped capillary groove of width L and height D appropriate above the wetting temperature. V_g denotes the volume filled by gas at pressure p. The side walls are coated with complete wetting films of thickness ℓ_π.

films on the opposite walls which can be safely ignored. Using this value for ℓ_π we now substitute the trial density profile into the functional $\Omega[\rho]$ and obtain a grand potential $\Omega(\ell)$ which is a function of the meniscus height. Per unit length $L_\parallel$ of the groove, the constrained, excess, contribution to the grand potential density $\omega(\ell) = \Omega(\ell)/L_\parallel$ is given by

$$\omega^{\rm ex}(\ell) = (p_l^+ - p)(L-2\ell_\pi)(D-\ell) + \gamma\left[2(D-\ell) + (L-2\ell_\pi)\right] - \frac{\Delta\rho}{L_\parallel}\int_{V_g} V(\mathbf{r})\,\mathrm{d}\mathbf{r}. \tag{21}$$

where we have defined the relevant excess contribution by subtracting off a constant term corresponding to the free-energy of a completely filled groove. Minimization of $\omega^{\rm ex}$ determines the equilibrium meniscus height ℓ_C and ℓ_E, details of which are presented in the appendix.

In the limit $D \to \infty$ the minimization also determines the value of the chemical potential at which condensation/evaporation occurs as

$$\mu_{\rm cc}(L) \approx \mu_{\rm sat} - \frac{2\gamma}{\Delta\rho(L-3\ell_\pi)}, \tag{22}$$

which is precisely the Derjaguin corrected Kelvin equation which allows for the shift in condensation due to thick complete wetting layers at the vertical walls.

For the condensation branch, occurring as μ approaches $\mu_{\rm cc}$ from below, we find that in the limit $D \to \infty$ of a macroscopically deep groove, the equilibrium height of the meniscus above the groove bottom is [21]

$$\ell_C = \left(\frac{9|\alpha_w|L}{8(\mu_{\rm cc}-\mu)}\right)^{\frac{1}{4}} + \cdots \tag{23}$$

where the ellipsis denote negligible non-diverging higher order terms. Similarly for the evaporation branch, occurring as μ approaches $\mu_{\rm cc}$ from above, we find that in the limit of a macroscopically deep groove, the equilibrium height of the meniscus from the groove opening is

$$\ell_E = \left(\frac{2|\alpha_w|}{\mu-\mu_{\rm cc}}\right)^{\frac{1}{3}} + \cdots. \tag{24}$$

where we have again ignored non-diverging terms.

At this point we make the following remarks:

(a) The values of the exponents $\beta_C = 1/4$ and $\beta_E = 1/3$ are exactly the same as those predicted in the effective Hamiltonian study of [15] which adopted a slightly simpler parameterization of the density profile. Thus as expected the only influence of the thick wetting films at side walls is change the location of the capillary condensation, $\mu_{\rm cc}$, in keeping with Derjaguin corrected Kelvin equation. The values of these exponents, obtained in a slab model for an infinitely deep groove, are in excellent

agreement with our numerical DFT results obtained for the condensation and evaporation in a groove of finite depth $D = 50\sigma$.

(b) As discussed earlier the present slab model calculation cannot be used to study condensation occurring below T_w since the parameterization of the profile does not allow for corner menisci. However it can used to study evaporation for $T < T_w$ since in the limit of an infinitely deep groove, for all $\mu > \mu_{cc}$, the meniscus is always far from the groove bottom. Thus as for the case $T > T_w$ there is only a single meniscus. Because the vertical walls are now partially wet there is no need to allow for thick wetting films and one can set the parameter $\ell_\pi = 0$ in the slab model analysis. In this case it is easy to show that the result for the divergence of the meniscus depth remains $\ell_E = (2|\alpha_w|/(\mu - \mu_{cc}))^{1/3}$. The only difference is that the location of capillary condensation, μ_{cc}, is given by the by standard macroscopic Kelvin equation (1). Thus for our present system, with long-ranged wall-fluid and short-ranged fluid-fluid interactions, the slab model predicts that evaporation remains continuous even below the wetting temperature T_w. This is completely consistent with our numerical DFT results. We shall return to this point later where we shall try to generalise the criteria for the order of the evaporation transition.

3.3. Covariance between groove evaporation and complete wetting

The slab model analysis points to a remarkably simple connection between groove evaporation, occurring for $T > T_w$, in systems with dispersion forces, and complete wetting at a planar wall. Recall that the complete wetting transition occurs above the wetting temperature and refers to the divergence of the equilibrium thickness, $\ell_\pi(\mu)$, of an adsorbed liquid film, at a planar wall-gas interface, as the chemical potential μ of the bulk gas, is increased to saturation μ_{sat}. In general one writes this divergence as $\ell_\pi(\mu) \approx |\mu - \mu_{sat}|^{-\beta_s^{co}}$ where the exponent β_s^{co} is determined by the range of the intermolecular forces and also possible interfacial fluctuation effects. For three dimensional systems, fluctuations are negligible, and for dispersion (van der Waals) forces the exponent takes the mean-field value $\beta_s^{co} = 1/3$ first explained by the Russian school of Derjaguin and Frumkin [26]. However, from the slab model results,

$$\ell_E(\mu) \approx \left(\frac{2|\alpha_w|}{|\mu - \mu_{cc}|} \right)^{\frac{1}{3}}, \quad \ell_\pi(\mu) \approx \left(\frac{2|\alpha_w|}{|\mu - \mu_{sat}|} \right)^{\frac{1}{3}}, \tag{25}$$

we see that the connection between groove evaporation and complete wetting goes much deeper. Thus, while ℓ_π diverges as $\mu \to \mu_{sat}$ from below and ℓ_E diverges as $\mu \to \mu_{cc}$ from above, the divergences are otherwise characterised by precisely the same power-law functions, apart from the shift in the location of the respective transition. That is

$$\ell_E(\mu - \mu_{cc}) = \ell_\pi(\mu_{sat} - \mu). \tag{26}$$

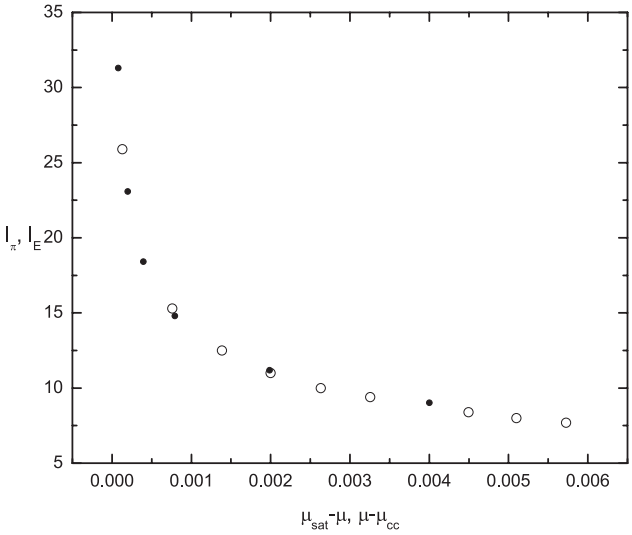

Figure 10. Test of the covariance law showing comparison of the growth of the wetting layer thickness ℓ_π for complete wetting on a planar wall (open symbols) with the meniscus position ℓ_E for evaporation in a capillary groove (filled symbols) of width $L = 12\sigma$ and depth $D = 50\sigma$ at temperature $T/T_w = 1.1$. The results are expressed in the molecular units of σ and ε.

This is a further example of a covariance relation relating adsorptions at phase transitions on different substrates, similar that observed in studies of wedge and cone filling [30–32].

We have tested this prediction using our microscopic DFT by comparing the divergences of $\ell_\pi = \Gamma/\Delta\rho$ and $\ell_E = \Gamma_E/\Delta\rho$ at a temperature $T/T_w = 1.1$ in a groove of depth $D = 50\sigma$ and width $L = 12\sigma$. The results are shown in figure 10 and show a near perfect collapse of the two curves $\ell_\pi(\mu)$ and $\ell_E(\mu)$. In drawing the shifted curve for ℓ_E we have treated the value of μ_{cc} as a fitting parameter which determined as $\mu_{cc}^{fit} = -4.0541\varepsilon$. This compares very well with the value $\mu_{cc} = -4.0529\varepsilon$ obtained from the independent 1D DFT analysis for an infinite open slit. The small difference between these values is attributable to the finite depth of our groove.

The origin of the covariance can be easily understood by simply recasting the slab model analysis in the language of an effective potential. The equilibrium film thickness ℓ_π of a complete wetting layer, is the minimum of a binding potential $W_\pi(\ell)$ defined as the excess grand potential per unit area of a wetting film at a planar wall which constrained to be of height ℓ. Within the slab model analysis this is determined in standard fashion as

$$W_\pi(\ell) = (\mu_{sat} - \mu)\Delta\rho\ell - \Delta\rho \int_\ell^\infty V^{(1)}(z)\mathrm{d}z, \tag{27}$$

where the first term is the thermodynamic cost of having a layer of liquid which is metastable in the bulk and the second arises from the integral over the long-ranged wall-fluid forces. This gives rise to an effective repulsion between the interfaces

$$W_\pi(\ell) = (\mu_{sat} - \mu)\Delta\rho\ell + \frac{A}{\ell^2} + \cdots, \tag{28}$$

where the Hamaker constant $A = -\alpha_w\Delta\rho$, which is positive. Minimization of this determines ℓ_π in agreement with

equation (20). Now we turn our attention to the evaporation occurring in an infinitely deep groove and understand the structure of the analogous binding potential $\omega^{\rm ex}(\ell)$ where we have suppressed the dependence on the wetting films at the side walls. The slab model result for this is

$$\frac{\omega^{\rm ex}(\ell)}{L} = (\mu - \mu_{\rm cc})\Delta\rho(D-\ell) + \frac{A}{(D-\ell)^2} + \mathcal{O}((D-\ell)^{-3}), \tag{29}$$

where we have divided by the slit width so that the dimensions are the same as for $W_\pi(\ell)$. Here the first term is now the thermodynamic cost of having a volume of capillary-gas which is metastable in the groove. This is the direct analogue of the first term in $W_\pi(\ell)$ and determines the shift in the location of the transition from $\mu_{\rm sat}$ to $\mu_{\rm cc}$. The second term is the all important repulsion of the meniscus from the capillary opening and can be understood as follows: consider an infinite open capillary slit exactly at $\mu = \mu_{\rm cc}$, and place a meniscus at some arbitrary position. Now imagine slicing off the side walls at height $D - \ell$ from the meniscus and replacing this by the vapour. The change to the excess grand potential from removing this volume of wall involves precisely the same integral over the dispersion interaction as in equation (27) apart from a slab of thickness L which contributes to the error term in equation (29). Minimization of $\omega^{\rm ex}(\ell)$ recovers the above expression for ℓ_E and hence the covariance law.

For completeness we remark that for the condensation transition the binding potential is given by

$$\frac{\omega^{\rm ex}(\ell)}{L} = (\mu_{\rm cc} - \mu)\Delta\rho\ell + \frac{9AL}{8\ell^3} + \cdots. \tag{30}$$

This has a very similar interpretation to the potential for evaporation with the first term representing the energy cost of having a volume of metastable capillary liquid for $\mu < \mu_{\rm cc}$. The reason why the meniscus repulsion from the groove bottom is higher order than for the evaporation can also be understood by dimensional analysis: imagine first that we are at coexistence in an open slit then cap the geometry by adding a slab of solid that fits between the side walls a distance ℓ below the meniscus. Since this is of finite width L the integration of the intermolecular forces over this volume produces a power law which is one order higher compared to that for wetting at a planar wall and evaporation.

4. Conclusion

In this paper we have used a mean-field DFT and slab model analysis to determine the order of condensation and evaporation transitions in a deep capillary groove with long-ranged wall-fluid forces. We have shown that the condensation transition becomes first order below the wetting temperature due to the presence of corner menisci and shown that the complementary Kelvin equation accurately describes the associated size of the metastable regime. For evaporation on the other hand our results indicate that the transition remains continuous at all temperatures and confirm the mean-field value of the critical exponent $\beta_E = 1/3$. Our analysis of evaporation also revealed a remarkably simple covariance relation with complete wetting at a planar wall.

Our study has been entirely at mean-field level and neglects the long wavelength, interfacial, fluctuations of the meniscus, the most dominant of which arise from those in the height of the meniscus along the groove. As discussed in [15] this means that the fluctuation theory of meniscus unbinding is analogous to that of two dimensional complete wetting but with a stiffness parameter, resisting the undulations of the meniscus, which is $\propto \gamma L$. Thus, for continuous condensation, the mean-field power-law divergence $\ell_C \approx ((\mu_{\rm cc} - \mu)/L)^{-1/4}$ will, as $\mu \to \mu_{\rm cc}$, eventually cross-over to $\ell_C \approx (L^2(\mu_{\rm cc} - \mu))^{-1/3}$ describing the true asymptotic critical behaviour (assuming the groove is macroscopically long). However, a simple matching of these power laws shows that the size of the asymptotic regime is negligibly small since it scales as L^{-11}. Thus to all intents and purposes the mean-field description of the continuous capillary condensation is exact. Similar remarks apply to continuous evaporation. The repulsive term $\propto (D-\ell)^{-2}$ appearing in the effective potential (29) is marginal which implies that that value of the exponent $\beta_E = 1/3$ is not altered by fluctuation effects. The only influence of these is that they slightly change the critical amplitude of the divergence of ℓ_E so that the mean-field result (24) is multiplied by a factor $1 + \mathcal{O}(\beta\gamma L^2)^{-1}$. This is only significant if the evaporation occurs in the immediate vicinity of the capillary critical point and is otherwise entirely negligible.

An important generalization of the present study is to include fully long-ranged fluid-fluid forces which decay as $\phi(r) \propto -\epsilon/r^6$. Indeed, within the slab model of evaporation it is trivial to allow for such forces, at leading order, since the integrals they introduce into the analysis are identical to those arising from the wall-fluid forces. The upshot of this is that the prediction for the meniscus height is altered to

$$\ell_E(\mu) \approx \left(\frac{2(\alpha_f - \alpha_w)}{\mu - \mu_{\rm cc}}\right)^{\frac{1}{3}} \tag{31}$$

where

$$\alpha_f = -\frac{1}{3}\pi\varepsilon\sigma^3. \tag{32}$$

Equivalently, the Hamaker constant appearing in the potentials (28) and (29) is replaced by $A \propto \Delta\rho(\alpha_f - \alpha_w)$. This result tells us that the covariance law (26) for evaporation occurring for $T > T_w$ and complete wetting remains unchanged. More interestingly however it suggests that the evaporation becomes first-order when the Hamaker constant changes sign. This occurs under two circumstances: (a) at the wetting temperature T_w associated with critical (second-order) wetting transition of the side walls (b) at the spinodal temperature T_s associated with first-order wetting transition of the side walls. This is defined as the temperature at which the activation barrier in the wetting binding potential $W_\pi(\ell)$ first appears. Interestingly, these conditions are precisely the same as the slab model predictions for the order of wedge

filling transitions and point to a possible deeper connection with that phase transition [10]. We emphasize that this prediction of a possible change in the order of the evaporation transition is entirely consistent with the present numerical DFT study since in our current model, the short-ranged nature of the fluid-fluid forces means there is no spinodal temperature associated with the first-order wetting transition. However some caution is needed with this prediction regarding the change in order of evaporation since below the wetting temperature one should also consider the higher order terms in the binding potentials for which we need to go beyond the sharp kink approximation. For example it is certainly not the case that the higher order terms in (28) and (29) are the same which is the reason why the covariance law (26) only applies above T_w. In addition for very narrow slits it is necessary to carefully model the opening of the groove into the bulk reservoir since the structure of this may lead to additional interfacial pinning. This requires more study using numerical DFT rather than simple slab model considerations.

Finally we mention that there is one phenomenon occurring in the groove geometry that we have not considered at all. This is the capillary-wetting transition defined as the divergence in the adsorption Γ_C as the temperature is increased towards $T \approx T_w$ along the capillary-coexistence line $\mu = \mu_{cc}$ [22]. The complementary Kelvin equation tells us that macroscopically the transition must occur at T_w since this is the temperature at which the contact angle vanishes implying the end of any metastability associated with corner menisci. The reason why we have avoided discussion of this transition is that here the mean-field character of the DFT is unreliable. According to the present DFT the capillary wetting transition is first-order and with it is associated a capillary pre-wetting line extending off capillary-coexistence and for $T > T^*(L)$. The first-order nature of this transition can be seen from the structure of the condensation binding potential (30). While the slab model parameterization does not allow for corner menisci for $T < T_w$ it does tell us that if a single meniscus were to be formed at a distance ℓ above the groove bottom then it must be repelled from it (since the Hamaker constant $A > 0$). However we know that below T_w the lowest free-energy configuration is due to bound corner menisci. Thus there is always a potential barrier between bound corner menisci and a single meniscus state located above the bottom. Thus the transition must be first-order. However this mean-field reasoning is incorrect because the capillary wetting transition must belong to the universality of two dimensional critical wetting with short-ranged forces since the $\mathcal{O}(\ell^{-3})$ interaction of the meniscus with the wall appearing in equation (30) is irrelevant. This implies not only that the transition is continuous and hence that there is no capillary pre-wetting line but that the location of $T^*(L)$ is renormalized by fluctuations and occurs below its mean-field prediction because the meniscus can tunnel out of the barrier which binds it to the corner(s). However modelling this using an effective interfacial Hamiltonian, while taking into account the influence of long-ranged forces, is difficult because it is necessary to model two corner menisci and single meniscus configurations. This will be the subject of future work.

Acknowledgments

We are grateful to C Rascón for useful discussions. AM acknowledges the financial support from the Czech Science Foundation, project 13-09914S. AOP acknowledges the financial support from the EPSRC UK for grant EP/J009636/1.

Appendix A. Slab model integrals

The essential ingredient in the slab model calculation of the constrained grand potential $\omega^{ex}(\ell)$ given by equation (21) is the integration of the external potential over the volume of the gas. Per unit length of the capillary, this is given by:

$$\begin{aligned}\frac{1}{L_\parallel}\int_{V_g} V(\mathbf{r})\mathrm{d}\mathbf{r} &= \int_\ell^D \mathrm{d}z \int_{\ell_\pi}^{L-\ell_\pi} \mathrm{d}x V(x,z)\\ &= \alpha_w \int_\ell^D \mathrm{d}z \int_{\ell_\pi}^{L-\ell_\pi} \mathrm{d}x \left[\frac{2}{z^3} + \psi(x,z) + \psi(x,D-z)\right.\\ &\quad \left. + \psi(L-x,z) + \psi(L-x,D-z)\right]\\ &= \alpha_w \int_\ell^D \mathrm{d}z \int_{\ell_\pi}^{L-\ell_\pi} \mathrm{d}x \left[\frac{2}{z^3} + 2(\psi(x,z) + \psi(x,D-z))\right]\\ &= 2\alpha_w \int_\ell^D \mathrm{d}z \left[\frac{L-2\ell_\pi}{z^3} + \Psi(L-\ell_\pi,z) - \Psi(\ell_\pi,z)\right.\\ &\quad \left. + \Psi(L-\ell_\pi,D-z) - \Psi(\ell_\pi,D-z)\right],\end{aligned}$$

where we have defined

$$\Psi(x,z) \equiv \int \psi(x,z)\mathrm{d}x = -\frac{x}{z^3} + \frac{(2x^2-z^2)\sqrt{x^2+z^2}}{2z^3x^2}. \quad \text{(A.1)}$$

Thus, when we minimise Ω^{ex} with respect to ℓ, we can make use of the relation

$$\begin{aligned}\frac{\partial}{\partial \ell}\left[\frac{1}{L_\parallel}\int_{V_g} V(\mathbf{r})\mathrm{d}\mathbf{r}\right] &= -2\alpha_w\left[\frac{L-2\ell_\pi}{\ell^3} + \Psi(L-\ell_\pi,\ell)\right.\\ &\quad - \Psi(\ell_\pi,\ell) + \Psi(L-\ell_\pi,D-\ell)\\ &\quad \left. - \Psi(\ell_\pi,D-\ell)\right], \quad \text{(A.2)}\end{aligned}$$

which can be expanded

$$\begin{aligned}\frac{\partial}{\partial \ell}\left[\frac{1}{L_\parallel}\int_{V_g} V(\mathbf{r})\mathrm{d}\mathbf{r}\right] &= -2\alpha_w\left[\frac{1}{\ell_\pi^2} - \frac{1}{(L-\ell_\pi)^2} + \frac{2\ell_\pi - L}{(D-\ell)^3}\right.\\ &\quad \left. + \frac{9}{16}\frac{L(L-2\ell_\pi)}{\ell^4} + \cdots\right]. \quad \text{(A.3)}\end{aligned}$$

Combining with (21) one obtains

$$\begin{aligned}&(p-p_l^+)(L-2\ell_\pi) - 2\gamma + 2\alpha_w \Delta\rho\left[\frac{1}{\ell_\pi^2} - \frac{1}{(L-\ell_\pi)^2}\right.\\ &\left. + \frac{2\ell_\pi - L}{(D-\ell)^3} + \frac{9}{16}\frac{L(L-2\ell_\pi)}{\ell^4} + \cdots\right] = 0 \quad \text{(A.4)}\end{aligned}$$

and substituting ℓ_π from equation (20) gives:

$$(p-p_l^+)(L-3\ell_\pi)-2\gamma + 2\alpha_w\Delta\rho\left[\frac{2\ell_\pi-L}{(D-\ell)^3}+\frac{9}{16}\frac{L(L-2\ell_\pi)}{\ell^4}+\cdots\right]=0. \quad \text{(A.5)}$$

which determines the equilibrium height of the meniscus in a finite depth groove. Finally, using $p-p_l^+\approx(\mu_{\rm sat}-\mu)\Delta\rho$ and equation (1) we find that for $\mu<\mu_{\rm cc}$, in the limit $D\to\infty$, the equilibrium position of the meniscus height above the groove bottom ℓ_C satisfies

$$\mu=\mu_{\rm cc}(L)+\frac{9}{8}\frac{\alpha_w(L(L-2\ell_\pi))}{(L-3\ell_\pi)}\frac{1}{\ell_C^4}+\cdots \approx \mu_{\rm cc}(L)+\frac{9}{8}\frac{\alpha_w L}{\ell_C^4} \quad \text{(A.6)}$$

Conversely, for $\mu>\mu_{\rm cc}(L)$, in the limit $D\to\infty$, with $D-\ell$ fixed, the equilibrium distance of the meniscus from the top of the groove ℓ_E satisfies

$$\mu=\mu_{\rm cc}(L)-\frac{2\alpha_w(L-2\ell_\pi)}{(L-3\ell_\pi)}\frac{1}{\ell_E^3}+\cdots \approx \mu_{\rm cc}(L)-\frac{2\alpha_w}{\ell_E^3}. \quad \text{(A.7)}$$

References

[1] Sullivan D E and Telo M M 1985 *Fluid Interfacial Phenomena* Croxton C A (New York: Wiley)
[2] Dietrich S 1988 *Phase Transitions and Critical Phenomena* vol 12 eds C Domb and J L Lebowitz (New York: Academic)
[3] Schick M 1990 *Liquids and Interfaces* Charvolin J *et al* (New York: Elsevier)
[4] Bonn D, Eggers J, Indekeu J, Meunier J and Rolley E 2009 *Rev. Mod. Phys.* **81** 739
[5] Evans R, Tarazona P and Marini Bettolo U 1986 *J. Chem. Phys.* **84** 2376
[6] Evans R 1990 *J. Phys.: Condens. Matter.* **2** 8989
[7] Fisher M E and Nakanishi H 1981 *J. Chem. Phys.* **75** 5857
[8] Parry A O and Evans R 1990 *Phys. Rev. Lett.* **64** 439
[9] Rejmer K, Dietrich S and Napirkówski M 1999 *Phys. Rev.* E **60** 4027
[10] Parry A O, Rascón C and Wood A J 2000 *Phys. Rev. Lett.* **85** 345
[11] Milchev A, Müller M, Binder K and Landau D P 2003 *Phys. Rev. Lett.* **90** 136101
[12] Malijevský A and Parry A O 2013 *Phys. Rev. Lett.* **110** 166101
[13] Malijevský A and Parry A O 2013 *J. Phys.: Condens. Matter.* **25** 305005
[14] Darbellay G A and Yeomans J M 1992 *J. Phys.* A **25** 4275
[15] Rascón C, Parry A O, Wilding N B and Evans R 2007 *Phys. Rev. Lett.* **98** 226101
[16] Tasinkevych M and Dietrich S 2007 *Eur. Phys. J.* **E23** 117
[17] Bruschi L and Mistura G 2009 *J. Low Temp. Phys.* **157** 206
[18] Hofmann T, Tasinkevych M, Checco A, Dobisz E, Dietrich S and Ocko B M 2010 *Phys. Rev. Lett.* **104** 106102
[19] Boelen H, Parry A O, Diaz-Herrera E and Schoen M 2008 *Eur. Phys. J.* E **25** 103
[20] Roth R and Parry A O 2011 *Mol. Phys.* **109** 1159
[21] Malijevský A 2012 *J. Chem. Phys.* **137** 214704
[22] Rascón C, Parry A O, Nürnberg R, Pozzato A, Tormen M, Bruschi L and Mistura G 2013 *J. Phys.: Condens. Matter* **25** 192101
[23] Yatsyshin P, Savva N and Kalliadasis S 2013 *Phys. Rev.* E **87** 020402
[24] Malijevský A 2013 *J. Phys.: Condens. Matter* **25** 445006
[25] Thomson W 1871 *Phil. Mag.* **42** 448
[26] Derjaguin B V 1940 *Acta Physicochim. URSS* **12** 181
[27] Evans R 1979 *Adv. Phys.* **28** 143
[28] Rosenfeld Y 1989 *Phys. Rev. Lett.* **63** 980
[29] Malijevský A 2006 *J. Chem. Phys.* **125** 194519
[30] Parry A O, Greenall M J and Wood A J 2002 *J. Phys.: Condens. Matter* **14** 1169
[31] Parry A O, Greenall M J and Romero-Enrique J M 2003 *Phys. Rev. Lett.* **90** 046101
[32] Rascón C and Parry A O 2005 *Phys. Rev. Lett.* **94** 096103

Paper IX

IOP PUBLISHING JOURNAL OF PHYSICS: CONDENSED MATTER
J. Phys.: Condens. Matter **25** (2013) 445006 (13pp) doi:10.1088/0953-8984/25/44/445006

Filling and wetting transitions at grooved substrates

Alexandr Malijevský

E Hála Laboratory of Thermodynamics, Institute of Chemical Process Fundamentals, Academy of Sciences, 16502 Prague 6, Czech Republic
Department of Physical Chemistry, Institute of Chemical Technology, Prague, 166 28 Praha 6, Czech Republic

E-mail: malijevsky@icpf.cas.cz

Received 24 June 2013, in final form 4 September 2013
Published 26 September 2013
Online at stacks.iop.org/JPhysCM/25/445006

Abstract
The wetting and filling properties of a fluid adsorbed on a solid grooved substrate are studied by means of a microscopic density functional theory. The grooved substrates are modelled using a solid slab, interacting with the fluid particles via long-range dispersion forces, to which a one-dimensional array of infinitely long rectangular grooves is sculpted. By investigating the effect of the groove periodicity and the width of the grooves and the ridges, a rich variety of different wetting morphologies is found. In particular, we show that for a saturated ambient gas, the adsorbent can occur in one of four wetting states characterized by (i) empty grooves, (ii) filled grooves, (iii) a formation of mesoscopic hemispherical caps (iv) a macroscopically wet surface. The character of the transition between particular regimes, that also extend off-coexistence, sensitively depends on the model geometry. The temperature at which the system becomes completely wet is considerably higher than that for a flat wall.

(Some figures may appear in colour only in the online journal)

1. Introduction

Wetting and related phenomena at planar surfaces have been thoroughly studied for the last several decades and are currently fairly well understood at least for simple fluids [1–3]. More recently, the subject of fluid adsorption on structured surfaces has received considerable attention from researchers and engineers (see, e.g., [4] and references therein). From an engineering viewpoint, the perspective on materials that possess large surface-to-volume ratios has been appreciated. Indeed, recent advances in lithography have allowed the decoration of solid surfaces on the micro- and nano-scales and facilitated the fabrication of such devices [5]. From a more fundamental viewpoint, it was recognized that structured substrates, when exposed to a gas that is close to coexistence with its liquid phase, can produce quite distinct adsorption characteristics compared to planar systems [6, 7]. For instance, macroscopic considerations that are based on Young's and Laplace's equations predict that the adsorption properties of a substrate with a linear-wedge shape can be sensitively controlled by its opening angle [8]. As a consequence, a large amount of the emerged liquid phase may adsorb near the apex even though only a microscopic film of the liquid is adsorbed far from the wedge apex. However, statistical mechanics has to be incorporated to learn more about the nature of interfacial phenomena on non-planar surfaces, particularly with respect to the phase transitions that they induce. Among other findings, such a more microscopic approach has resulted in the discovery of interesting hidden symmetries (or so-called covariances) that relate the adsorption properties of different substrate geometries [9, 10].

One class of structured surface that has recently attracted a strong interest motivated by recent experiments [11–13] comprises solid substrates patterned with regular arrays. A sketch of such a model substrate used in this work is provided in figure 1. This 'grooved substrate' is characterized by the presence of rectangular capillary grooves of depth D and width L_2, which are etched into a solid slab. The grooves form an infinite periodic one-dimensional array along the x-direction with a periodicity L and are assumed to be unbounded in the y-direction. It is further assumed that the substrate is formed with uniformly distributed atoms, which interact with the fluid particles with a long-range potential that decays as $1/r^6$ at large distances.

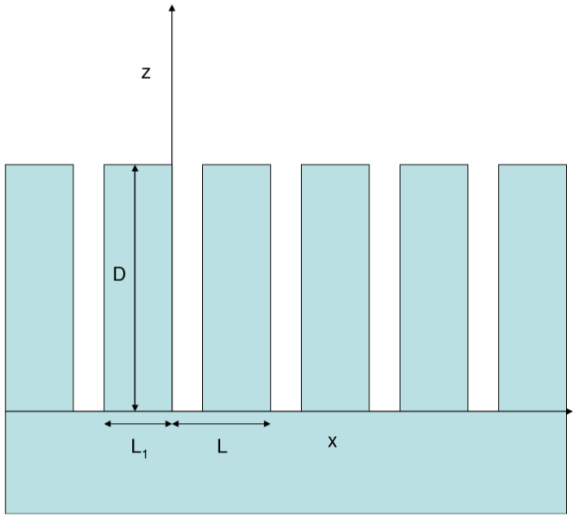

Figure 1. Illustration of the model. The grooves (each of width $L_2 = L - L_1$ and depth D) form an infinite one-dimensional array along the x-axis. The sketch corresponds to the projection $y = \text{const}$.

Related substrate models were considered rather recently by Dietrich *et al* [10, 14, 15] in a study of the complete wetting of geometrically structured substrates by interfacial Hamiltonian theory, derived from the so-called sharp-kink approximation of density functional theory (DFT) [1]. In this paper a more microscopic model is used, which takes into account the short-range correlations between fluid particles by adopting Rosenfeld's fundamental measure theory (FMT) [16]. In particular, this allows us to address the questions such as: what is the equilibrium structure of an adsorbed fluid for a particular substrate geometry? How does the structure respond to a change in temperature and bulk pressure (chemical potential)? What type of phase transitions does the system exhibit and how does this depend on the individual parameters that characterize the substrate geometry?

The remainder of the paper is organized as follows. In section 2, fundamental adsorption phenomena at substrates, to which the current model reduces in special cases, is briefly recalled. In section 3, we formulate the molecular model of the substrate and the fluid and outline the main features of the microscopic DFT used in this work. The numerical results including surface phase diagrams for several representative geometrical models are presented in section 4. The main points of the work are summarized and discussed in section 5 and a link with the earlier works based on an interface Hamiltonian is made. The paper concludes with appendices which provide the details of the derivations of some formulae presented earlier.

2. Behaviour of the model substrate in special cases

In this section, we make a link between the substrate model sketched in figure 1 and the more familiar model substrates to which the current model reduces after taking the special limits of the substrate geometric parameters. The main adsorption characteristics of the resulting systems are briefly recalled.

2.1. $L_1 \to \infty$ *or* $L_2 \to \infty$ *or* $D \to 0$

If any of these limits is realized (alternatively, one can also take $L_1 \to 0$ or $L_2 \to 0$), the grooved substrate reduces to a simple planar wall. At the liquid–vapour bulk coexistence, the planar wall (preferentially adsorbing liquid phase) exhibits wetting transition at the wetting temperature T_w. Typically, the transition is first-order but can also be continuous (critical) depending on the range and strength of the intermolecular interactions. It should be noted that the latter phenomenon is notably rare in nature; in fact it has not been observed for solid substrates and has only been detected for a few binary liquid mixtures.

Alternatively, the wetting layer may develop at a constant temperature $T > T_w$ upon approaching the saturation value of the chemical potential $\mu \to \mu_{sat}(T)^-$. In this complete wetting process the width of the liquid film ℓ_π develops according to

$$\ell_\pi \sim \delta\mu^{-\beta_s}, \tag{1}$$

as $\delta\mu = \mu_{sat}(T) - \mu \to 0$. The critical exponent $\beta_s = 1/3$ if the dominating force at large distances originates from dispersion interactions. If the wetting transition at T_w is first-order, the singularity of the first derivative of the free energy at T_w is prolonged off-coexistence in a prewetting line representing the loci of the thin–thick first-order transitions. This line terminates at its own critical temperature T_{sc} and approaches the coexistence line tangentially at T_w as $|\delta\mu| \sim (T - T_w)^{3/2}$.

2.2. $L \to \infty$ *or* $D \to \infty$

Either of these two limits defines a capped capillary (single groove). Because of the presence of the bottom wall, a meniscus separating capillary-gas and capillary-liquid is formed near the bottom for $\mu < \mu_{cc}(H)$, whereas for $\mu > \mu_{cc}(H)$ the pore must be filled with a liquid, so that the meniscus is to be found at the top. Here, $\mu_{cc}(H)$ is the chemical potential of a slit (parallel plate) pore of a width H, at which the capillary condensation occurs. Interestingly, in contrast with the capillary condensation in a slit pore, which is a first-order transition, the condensation in the capped capillary proves to be continuous for walls that are completely wet [10, 17–23]. The condensation is then given by an unbinding of the meniscus separating the capillary-gas and the capillary-liquid from the bottom end according to the power law [17]

$$\ell_{cc} \sim (\mu - \mu_{cc}(H))^{-\beta_{cc}}, \tag{2}$$

with $\beta_{cc} = \frac{1}{4}$ for long-range forces. In the most recent studies it was revealed [22, 23] that the order of the transition is controlled by the wetting regime of the bottom wall, such that below T_w the adsorption in a capped capillary exhibits first-order transition.

While these features are experienced by single grooves specified by either of the two limits, it should be noted that the phase transitions and criticality of the former one with D finite must be necessarily rounded beyond the mean-field approximation (1D Ising model universality class).

2.3. $D \to \infty$ and $L_2 \to \infty$

In this case, the grooved substrate reduces to the geometry of a linear wedge with an opening angle $\psi = \pi/2$. Such a model exhibits a wedge filling transition that differs from both wetting and capillary condensation: at the vapour–liquid coexistence, a wedge becomes completely filled with liquid at the filling temperature T_f that corresponds to the contact angle of the liquid drop on the wall [8, 24, 25]:

$$\theta(T = T_f) = (\pi - \psi)/2. \tag{3}$$

The filling transition is critical whenever the corresponding wetting transition is also critical; however, if the wetting transition is first-order, the filling transition can be either first-order or critical depending on the opening angle [26–28].

3. Theory

3.1. Potential of the grooved substrate

The model grooved substrate, as sketched in figure 1, enters into the theory as an external field $V(\mathbf{r})$ exerted on the fluid atoms. Owing to the periodicity along the x-axis and its translational invariance in the y-dimension, one can write

$$V(x, z) = V_1(z) + \sum_{n=-\infty}^{\infty} V_2(x + nL, z). \tag{4}$$

Here, $V_1(z)$ is the potential of a planar wall $\mathbb{W} = \{x \in \mathbb{R}, y \in \mathbb{R}, z \in (-\infty, 0)\}$, and $V_2(x, z)$ is the potential of a rectangular body $\mathbb{B} = \{x \in (-L_1, 0), y \in \mathbb{R}, z \in (0, D)\}$ with a property $V_2(x, z) = V_2(-x - L_1, z)$.

The substrate is treated as a continuous distribution of atoms with a one-body density ρ_w, each of which interacts with the fluid atoms via a Lennard-Jones tail

$$\phi_w(r) = -4\varepsilon_w \left(\frac{\sigma}{r}\right)^6, \tag{5}$$

where r is the distance between the substrate and the fluid particles. After integrating $\phi_w(\mathbf{r})$ over the entire domain of the wall (see appendix A) and introducing a hard-wall barrier to model a short-range repulsion between fluid and wall atoms, the potential of the substrate can be expressed as follows:

$$V_1(z) = \begin{cases} \tilde{V}_1(z); & z > \sigma, \\ \infty; & z < \sigma \end{cases} \tag{6}$$

and

$$V_2(x, z) = \begin{cases} \infty; & x \in (-L_1 - \sigma, \sigma) \cap z \in (0, D + \sigma), \\ \tilde{V}_2(x, z); & \text{otherwise}, \end{cases} \tag{7}$$

with

$$\tilde{V}_1(z) = \frac{2\alpha_w}{z^3}, \tag{8}$$

$$\tilde{V}_2(x, z) = \alpha_w \left[\psi_{z,D}(L_1 + x) - \psi_{z,D}(x)\right], \tag{9}$$

$$\alpha_w \equiv -\tfrac{1}{3}\pi\varepsilon_w\rho_w\sigma^6 \tag{10}$$

and

$$\psi_{z,D}(x) \equiv \frac{2x^4 + x^2(z - D)^2 + 2(z - D)^4}{2x^3(z - D)^3\sqrt{x^2 + (z - D)^2}} - \frac{2x^4 + x^2z^2 + 2z^4}{2x^3z^3\sqrt{x^2 + z^2}}. \tag{11}$$

3.2. Density functional theory

Within classical DFT [29], the equilibrium density profile is obtained by minimizing the grand potential functional

$$\Omega[\rho] = \mathcal{F}[\rho] + \int \mathrm{d}\mathbf{r}\, \rho(\mathbf{r})[V(\mathbf{r}) - \mu], \tag{12}$$

where μ is the chemical potential and $V(\mathbf{r})$ is the external potential. Here, $\mathcal{F}[\rho]$ is the intrinsic free energy functional of the fluid one-body density, $\rho(\mathbf{r})$, which can be split into ideal and excess parts. As is common in modern DFT, the excess free energy functional is further divided into a hard-sphere term and an attractive contribution

$$\mathcal{F}_{ex}[\rho] = \mathcal{F}_{hs}[\rho] + \tfrac{1}{2}\iint \mathrm{d}\mathbf{r}\,\mathrm{d}\mathbf{r}'\rho(\mathbf{r})\rho(\mathbf{r}')u_a(|\mathbf{r} - \mathbf{r}'|), \tag{13}$$

where $u_a(r)$ is the attractive portion of the fluid–fluid interaction potential. In our analysis, we consider this to be a truncated Lennard-Jones-like potential

$$u_a(r) = \begin{cases} 0; & r < \sigma, \\ -4\varepsilon\left(\frac{\sigma}{r}\right)^6; & \sigma < r < r_c, \\ 0; & r > r_c \end{cases} \tag{14}$$

which is cut-off at $r_c = 2.5\sigma$, where σ is the hard-sphere diameter. It should be noted that since the range of the wall–fluid and fluid–fluid interactions are different, the Hamaker constant of the system is always positive (at least within the sharp-kink approximation), which ensures that wetting transition at the corresponding planar wall is first-order [1]. Note that the same molecular model was used recently in [27, 28].

The hard-sphere part of the excess free energy is approximated by the FMT functional [16],

$$\mathcal{F}_{hs}[\rho] = \frac{1}{\beta}\int \mathrm{d}\mathbf{r}\, \Phi(\{n_\alpha\}), \tag{15}$$

where $\beta = 1/k_BT$ is the inverse temperature. The function Φ depends on six weighted densities $n_\alpha(\mathbf{r})$ which can be expressed as double integrals for the rectangular symmetry as is dictated by the external field (4) (see appendix B).

The minimization of (12) results in an Euler–Lagrange equation

$$\mu_{id}(\rho(\mathbf{r})) + \frac{\delta\mathcal{F}_{hs}[\rho]}{\delta\rho(\mathbf{r})} + \int \mathrm{d}\mathbf{r}'\rho(\mathbf{r}')u_a(|\mathbf{r} - \mathbf{r}'|) = \mu, \tag{16}$$

where μ_{id} is the ideal part of the chemical potential. The equilibrium density profile is obtained by solving equation (16) numerically on a two-dimensional Cartesian grid with a spacing of 0.1σ. The convolution term in (16) is recast into a two-dimensional integral (see appendix C).

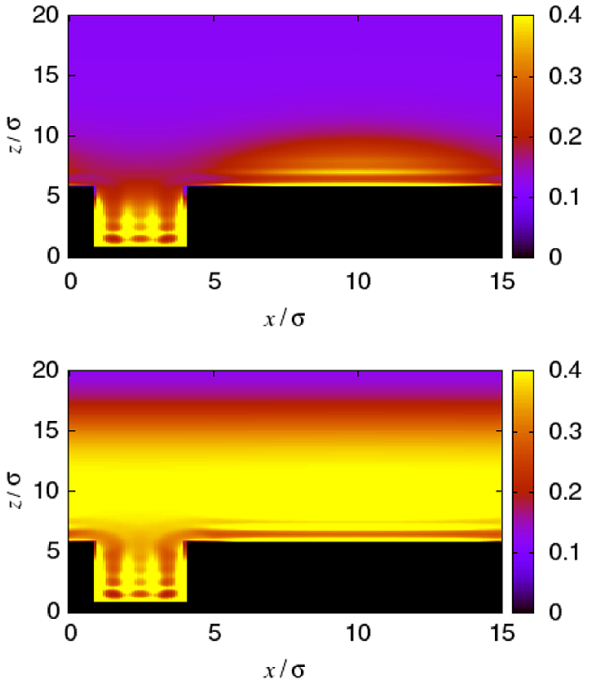

Figure 2. Coexisting density profiles for a model with $L^* = 15$, $L_1^* = 10$, and $D^* = 5$. The temperature of the systems is $T_{gw}^* = 1.33$ and the bulk phase is a saturated gas.

The thermodynamic properties of the corresponding bulk system are determined from equation (12), which is applied to $\rho(\mathbf{r}) = \text{const}$. From the resulting Helmholtz free energy the liquid–vapour phase boundary can be constructed. The binodal terminates at the bulk critical temperature $k_B T_c/\varepsilon = 1.41$.

4. Numerical results

Throughout this paper, we will adopt σ and ε as our length and energy units. Therefore, we will express our quantities in dimensionless units, such as $T^* = k_B T/\varepsilon$, $\rho^* = \rho\sigma^3$, $x^* = x/\sigma$, etc, unless stated otherwise. The interaction potential that characterizes the substrate strength is set to $\varepsilon_w = 1.2\varepsilon$, and we will restrict ourselves to the results for a substrate depth of $D = 5\sigma$.

4.1. Coexistence path

All results presented in this paragraph are for the liquid–gas coexistence with a boundary condition for the density profile $\rho(x, z_f) = \rho_v(T)$ for all x, where $\rho_v(T)$ is the particle density of a saturated vapour and z_f refers to a vertical size of the system. Our primary goal is to inspect the type of wetting regimes that a system with a particular geometry can acquire and compare with the wetting properties of the corresponding planar wall. When applied to a planar wall, the solution of the Euler–Lagrange equation (equation (16)) predicts a first-order wetting transition at a temperature $T_w^* = 1.17$ [27].

We start by considering a substrate model characterized by the parameters $L^* = 15$ and $L_1^* = 10$. In this case, the

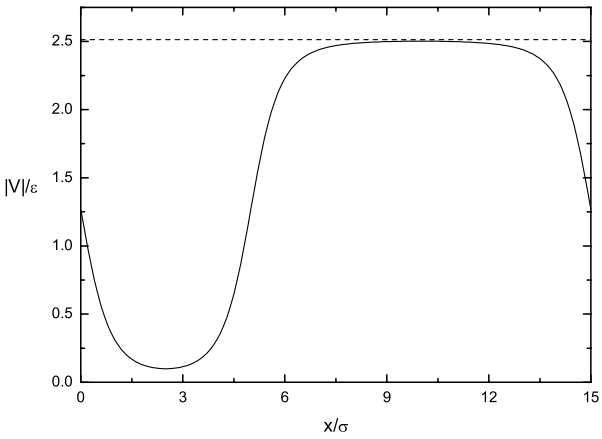

Figure 3. Absolute value of the potential of the grooved-surface model with $L^* = 15$, $L_1^* = 10$, and $D^* = 5$ at $z = D + \sigma$ (solid line) and the potential of the planar wall at $z = \sigma$ (dashed line).

minimization of the grand potential functional (12) leads to two different sets of results depending on the initial configuration. The temperature at which two different states yield the identical grand potential value defines the location of the first-order transition, and we will refer to this process as *groove-wetting*. This process is now compared with an ordinary wetting transition on a planar wall. First, as observed from the plots in figure 2 in which the coexisting low- and high-density profiles are displayed (for a single period), the symmetry breaking in the x-dimension induces a non-planar character of the liquid–vapour interface in the low-density state. This behaviour is in contrast with a liquid–vapour interface above a flat wall, in which case only the fluctuation effects disrupt its otherwise planar shape. The high-density state corresponds to a completely wet substrate, so that the non-uniformity of the substrate potential in the x-direction no longer influences the geometry of the unbounded liquid–gas interface. Second, the groove-wetting occurs at a temperature $T_{gw}^* = 1.33$, which is much closer to the bulk critical temperature (recall, $T_c^* = 1.41$) than the wetting temperature of a planar wall, $T_w^* = 1.17$. This result can be explained by comparing the strength of the potentials of the flat substrate and that of the grooved substrate. As shown in figure 3, the latter reaches the value of the planar wall about the middle of the ridges but the presence of the grooves significantly lowers the local absolute value of the potential at a given height above the substrate. Thus, the grooved substrate constitutes an effectively weaker adsorbent than the corresponding planar wall, which pushes the temperature at which the surface is completely wet upwards.

For thicker grooves, $L_1^* = 5$ (while maintaining $L^* = 15$), the adsorption scenario changes as the system can now realize three different regimes as displayed in figure 4. These regimes are separated by two first-order transitions—see figure 5, where the temperature dependence of the adsorption per unit length is shown. The latter is defined as

$$\Gamma = \iint \mathrm{d}x\,\mathrm{d}z\,(\rho(x, z) - \rho_b), \tag{17}$$

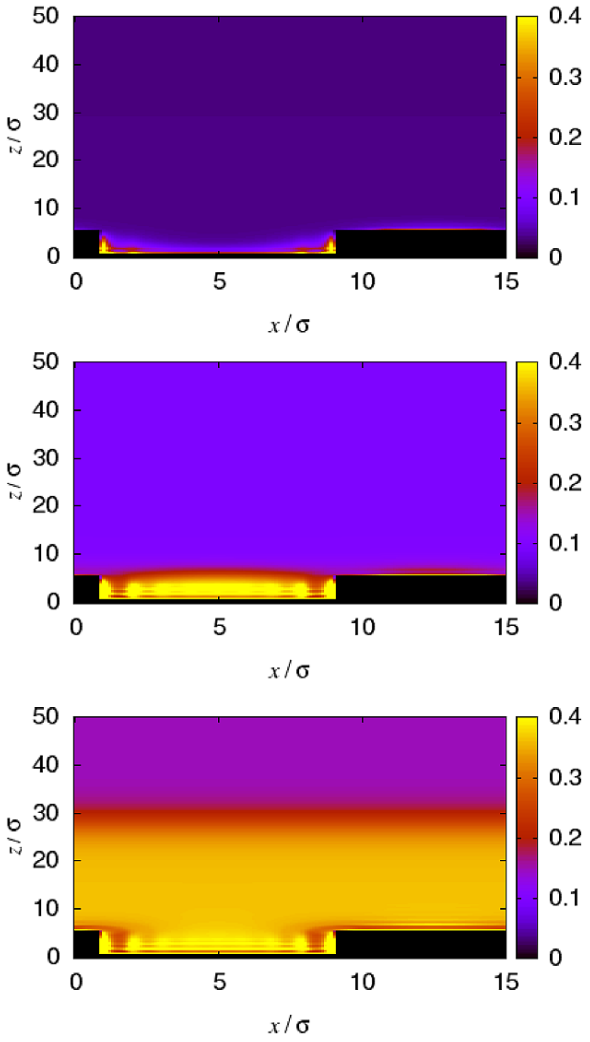

Figure 4. Density profiles of three distinct (separated by first-order transitions) phases for a model with $L^* = 15$, $L_1^* = 5$, and $D^* = 5$. The corresponding temperatures are (from above): $T^* = 1.1$, $T^* = 1.3$ and $T^* = 1.37$. In all cases the bulk phase is the saturated gas.

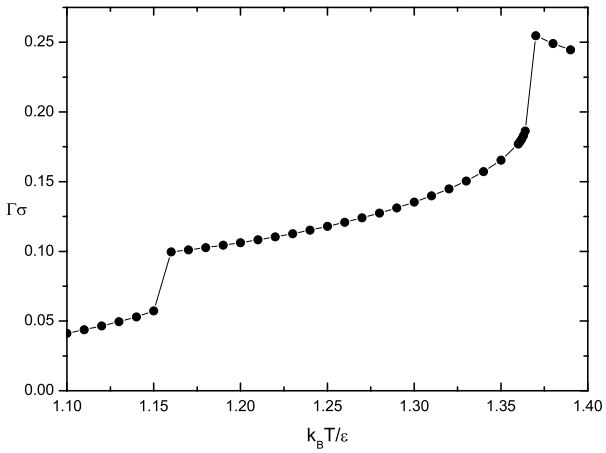

Figure 5. Temperature dependence of the adsorption on a bulk coexistence line for a model with $L^* = 15$, $L_1^* = 5$, and $D^* = 5$.

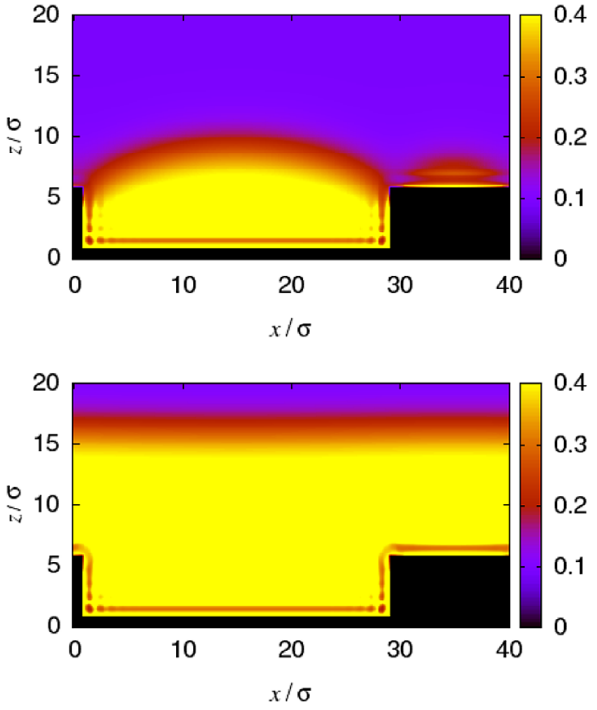

Figure 6. Coexisting density profiles for a model with $L^* = 40$, $L_1^* = 10$, and $D^* = 5$. The temperature of the systems is $T_{gw}^* = 1.19$ and the bulk phase is the saturated gas.

which in the current case refers to a bulk coexistence state $\rho_b = \rho_v(T)$, and the integral is taken over the volume of the system that is available for fluid particles within an interval $x \in (0, L)$. In contrast with the previous case, the width of the grooves is now sufficient to allow a *groove-filling* first-order phase transition before the system experiences groove-wetting. Beyond this, the system is already saturated, and the adsorption is effectively infinite.

We now increase the periodicity to $L^* = 40$ and examine the impact of the groove width on fluid adsorption. For $L_1^* = 10$, the situation is similar to the observations from the previous case: the system undergoes groove-filling ($T_{gf}^* = 1.16$) and groove-wetting transitions ($T_{gw}^* = 1.29$). Compared to the case where $L^* = 15$, the wall inhomogeneity is less dramatic and the complete wetting of the wall takes place closer to T_w. Now, below, but near T_{gw}, separate wetting layers with concave interfaces are formed at the grooves and the ridges, and groove-wetting occurs when the two layers merge, such that the resulting liquid–vapour interface becomes flat, see figure 6. When the groove width decreases (increasing L_1), both T_{gf} and T_{gw} progressively decrease and for a sufficiently large L_1 a new first-order transition is revealed as illustrated in figure 7 for $L_1^* = 30$. In addition to groove-filling ($T_{gf} = 1.09$) and groove-wetting ($T_{gw} = 1.23$), there is also an equilibrium between two density profiles that differ by the amount of the adsorbed liquid at the ridges as displayed figure 8. A sufficiently large value of L_1 enables the abrupt development of a thick layer at the ridges as a result of the partial unbinding of the liquid–vapour interface being pinned at the edges. We will refer to this process as *bounded-wetting*. The temperature of this transition T_{bw} also

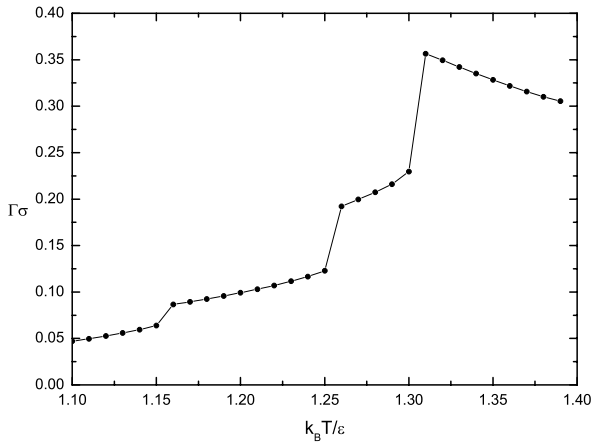

Figure 7. Temperature dependence of the adsorption on a bulk coexistence line for a model with $L^* = 40$, $L_1^* = 30$, and $D^* = 5$. For $T^* > 1.3$, the system is already saturated (because of its finite size).

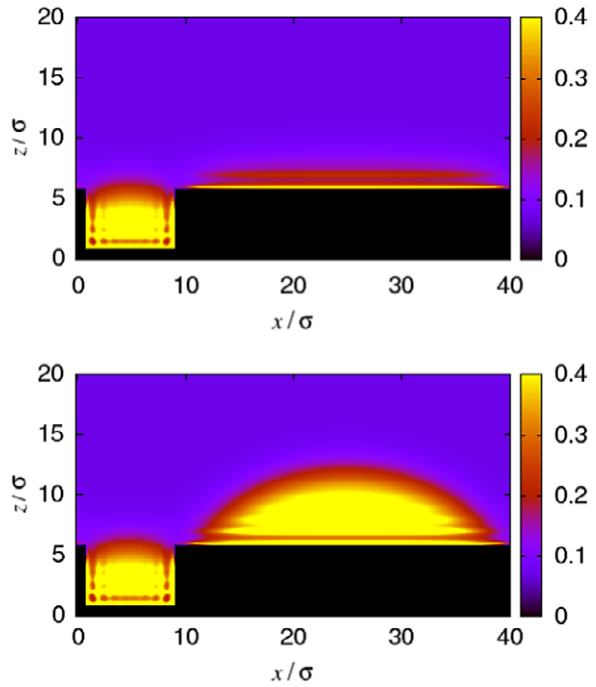

Figure 8. Coexisting density profiles for a model with $L^* = 40$, $L_1^* = 30$, and $D^* = 5$. The temperature of the systems is $T_{gw}^* = 1.24$ and the bulk phase is the saturated gas.

decreases with L_2, and the transition is metastable with respect to groove-wetting unless $T_{bw} < T_{gw}$. For the periodicity of $L^* = 40$, this relationship holds for $L_1^* \lesssim 33$.

4.2. Surface phase diagrams

Now we extend our considerations to off-coexistence states. In this case, the minimization of the grand potential (12) is subject to the boundary condition $\rho(z) = \rho_b$, where ρ_b is a bulk density of a gas with a chemical potential $\mu \leq \mu_{sat}$. At low values of μ, the adsorption (17) is microscopic, while

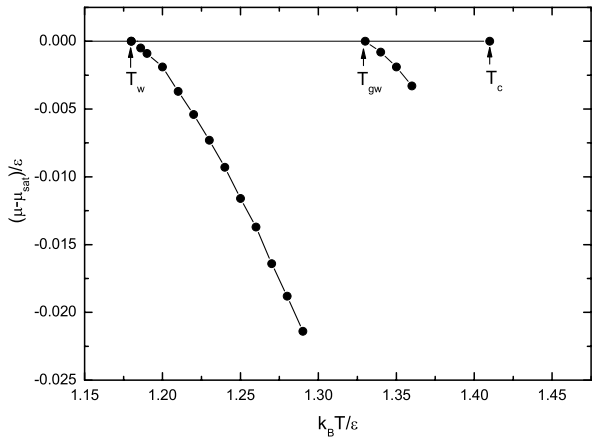

Figure 9. Phase diagram for a model with $L^* = 15$, $L_1^* = 10$, and $D^* = 5$. T_w showing the wetting temperature on a flat wall; T_{gw} is the groove-wetting temperature, and T_c is the bulk critical temperature. For a comparison, the prewetting line of a corresponding flat wall (joining the bulk coexistence at T_w) is also displayed.

its upper limit value (at μ_{sat}) is known from the previous considerations. We wish to learn the behaviour of Γ between these two limits.

We start with a periodicity of $L^* = 15$. For $L_1^* = 10$, the grooves are too narrow to undergo the filling transition; thus the only free-energy singularity on the coexistence path is at T_{gw}, which extends off-coexistence and terminates at its own critical point as displayed in figure 9. The loci of the first-order transitions characterized by a jump in Γ are similar to a prewetting line for a thin–thick transition on a planar wall. Thus, we will call the process *groove-prewetting*. However, in contrast with prewetting on a planar wall, in which case the two coexisting states differ only by a width of an adsorbed film, here the interface also changes its geometry, as shown in figure 10. At the higher-adsorption state (bottom panel in figure 10), the fluid inhomogeneity in the x-direction has no substantial influence and the system experiences ordinary complete wetting upon a further increase in μ.

A different scenario occurs for $L_1^* = 5$. In this case, the grooves are wide enough that groove-wetting is preceded by the groove-filling transition on the coexistence line. As shown in figure 11, the first-order groove-filling transition also continues off-coexistence and terminates at a temperature $T^* = 1.22$. Above this temperature, condensation in the grooves is a continuous process. We further note that below the temperatures $T^* \lesssim 1.1$, groove-filling becomes metastable with respect to a crystalline structure of the fluid atoms induced by the presence of the wall.

A larger periodicity gives rise to an even richer adsorption scenario. The surface phase diagram of a model that is specified by $L^* = 40$ and $L_1^* = 35$ is depicted in figure 12, where an off-coexistence extension of the bounded-wetting is present, in addition to groove-prewetting. This is illustrated in figure 13 for temperature $T^* = 1.27$: the adsorption isotherm, which is shown in the upper panel, clearly exhibits two first-order transitions that correspond to bounded-wetting and groove-prewetting. The loci of the equilibrium (stable) states

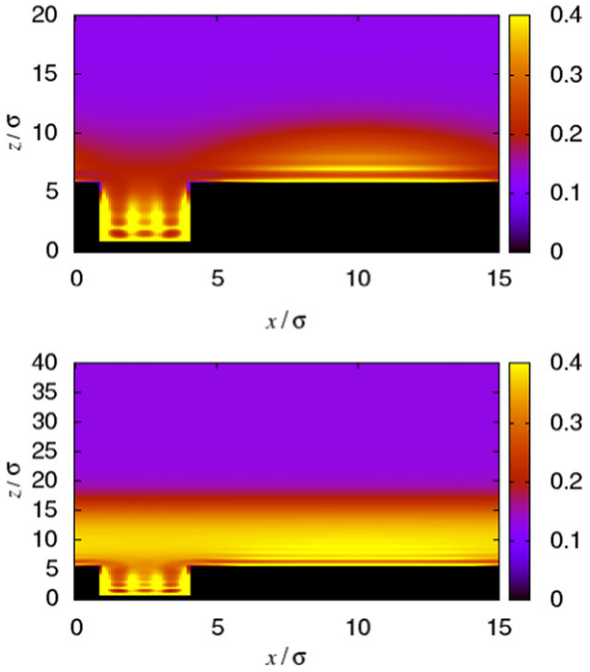

Figure 10. Density profiles of the coexisting states before (top panel) and after (bottom panel) groove-prewetting for a model with $L^* = 15$, $L_1^* = 10$ and $D^* = 5$. The temperature is $T^* = 1.34$.

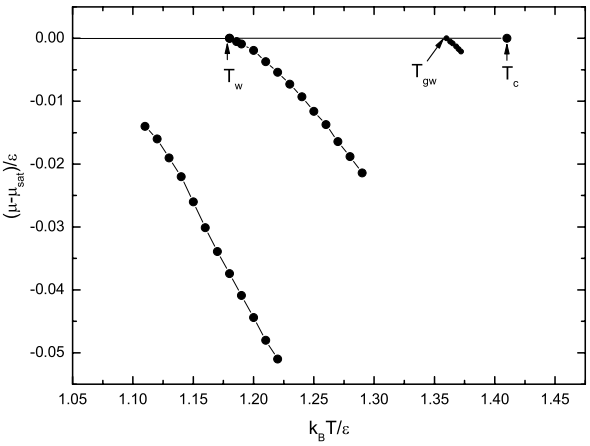

Figure 11. Phase diagram for a model with $L^* = 15$, $L_1^* = 5$, and $D^* = 5$. The nomenclature is the same as in figure 9. The low temperature curve corresponds to groove-filling, which terminates at its critical point at a temperature $k_B T/\varepsilon \approx 1.22$; the left end of the curve, which would normally connect the bulk coexistence (see figure 15), is truncated at the point where the first crystal nuclei induced by the wall occur. For comparison, the prewetting line of a corresponding flat wall (joining the bulk coexistence at T_w) is also displayed.

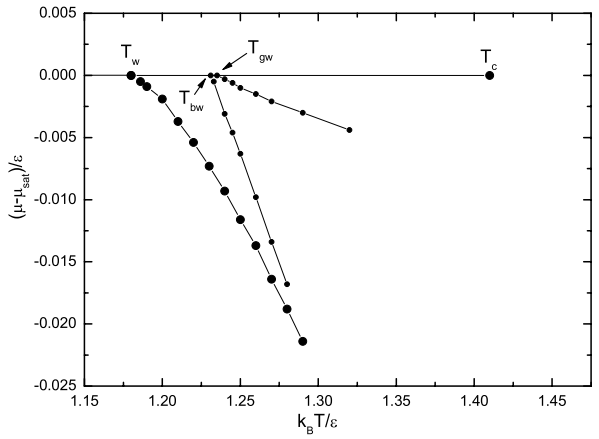

Figure 12. Phase diagram for a model with $L^* = 40$, $L_1^* = 35$, and $D^* = 5$. The nomenclature is the same as in figure 9. In addition, the bounded-wetting temperature T_{bw} is displayed. For comparison, the prewetting line of a corresponding flat wall (joining the bulk coexistence at T_w) is also displayed.

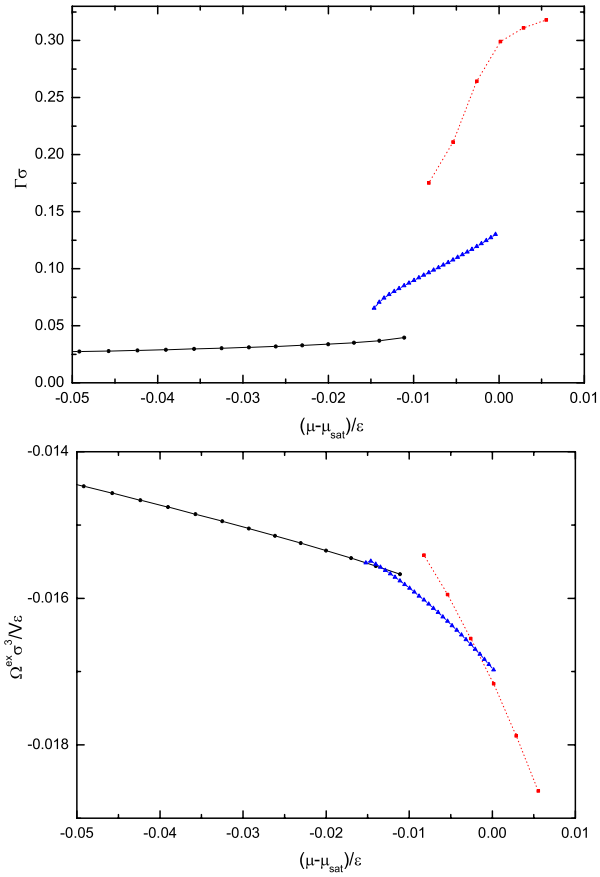

Figure 13. Adsorption isotherm (upper panel) and the excess grand potential dependence on chemical potential for a model with $L^* = 40$, $L_1^* = 35$, and $D^* = 5$ at a temperature $T^* = 1.27$.

are given by the concave envelope of $\Omega^{ex} = \Omega + pV$ displayed in the lower panel; the precise locations of the two-phase transitions can be determined as the cusps in $\Omega^{ex}(\mu)$.

The surface phase diagram of a substrate with somewhat broader grooves ($L^* = 40$ and $L_1^* = 30$) is further complemented by the groove-filling transitions, see figure 14. For this model, the bounded-wetting transition is unstable on the coexistence path ($T_{bw}^* = 1.24$, $T_{gw}^* = 1.23$). However, the curves that represent bounded-wetting and groove-prewetting intersect below the saturation line, which defines a triple point at which three configurations of finite adsorption coexist.

For even broader grooves, the width of the ridges no longer permits bounded-wetting. For the model of $L^* = 40$

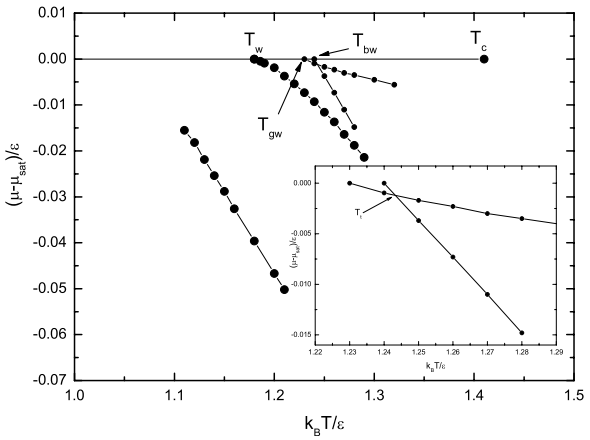

Figure 14. Phase diagram for a model with $L^* = 40$, $L_1^* = 30$, and $D^* = 5$. The nomenclature is the same as in figure 12. The symbols at low temperatures correspond to groove-filling. The low temperature curve corresponds to groove-filling, which terminates at its critical point at a temperature $k_BT/\varepsilon \approx 1.21$; the left end of the curve, which would normally connect the bulk coexistence (see figure 15), is truncated at the point where the first crystal nuclei induced by the wall occur. For comparison, the prewetting line of a corresponding flat wall (joining the bulk coexistence at T_w) is also displayed. In the inset, a triple point at which three different wetting morphologies coexist is shown.

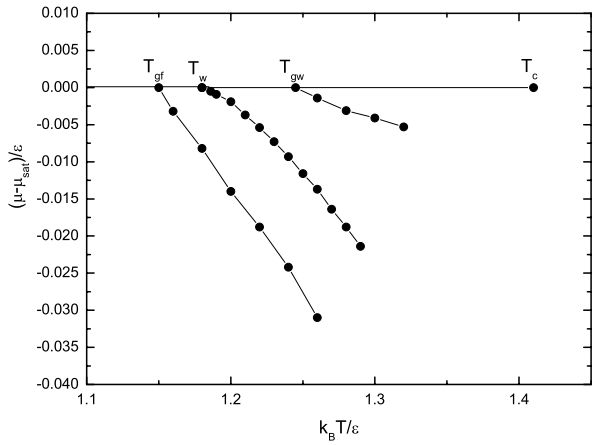

Figure 15. Phase diagram for a model with $L^* = 40$, $L_1^* = 20$, and $D^* = 5$. Here, T_{gf} denotes the filling temperature, T_w is the wetting temperature for a planar wall, T_{gw} is the groove-wetting temperature, and T_c is the bulk critical temperature. For comparison, the prewetting line of a corresponding flat wall (joining the bulk coexistence at T_w) is also displayed.

and $L_1^* = 20$ this results in a phase diagram in which only groove-filling and groove-prewetting persist, as illustrated in figure 15. This behaviour is somewhat similar to the observation for the model with $L^* = 15$ and $L_1^* = 5$ (see figure 11). However, groove-filling is now stable with respect to crystallization up to T_{gf}, and its critical point extends even beyond T_{gw}.

5. Discussion

In this work, phase transitions of simple fluids in contact with grooved substrates have been investigated using a mean-field non-local DFT. The adsorption properties of such substrates were shown to be remarkably complex as a consequence of an intricate interplay of various interfacial phenomena and sensitively dependent on the particular substrate geometry. The main conclusions that can be inferred from the presented results are summarized as follows.

- When exposed to a saturated vapour, the wetting state of a grooved substrate may pass through four different regimes.

  At lower temperatures, the system typically experiences the groove-filling transition, which is characterized by the condensation of the gas inside the grooves, provided the groove width is sufficiently large. For a given periodicity, the value of T_{gf} increases with the groove width. For narrow grooves, the groove-filling, although taking place well above the bulk triple point, is already metastable with respect to wall-induced freezing.

  The system becomes completely wet above a temperature T_{gw}, which is analogous to a wetting temperature T_w for a flat wall. This groove-wetting transition is always first-order for the considered molecular model since the range of the fluid–fluid and fluid–wall interactions is different; thus, their contributions to the Hamaker constant cannot be balanced.

  Finally, our DFT study predicts the presence of another transition, which we call bounded-wetting transition. This transition (if stable) precedes groove-wetting and can be thought of as a partial unbinding of a wetting film at the ridges, the remnant of an ordinary wetting transition on a planar wall, which would occur at T_w if the grooves were absent. Clearly, this transition is possible only if the ridges are sufficiently wide to accommodate mesoscopically thick films. Some analogy can be found with thin–thick wetting on planar walls for systems that exhibit long-range critical wetting [30–32]. Unlike the latter, which is a consequence of the competition of different interaction contributions, bounded-wetting is induced by lateral heterogeneity of the wall.

- For all models that are considered here, we have found that $T_{gw} > T_w$, and in most cases, the difference between the two temperatures was significant. This finding deserves some discussion considering that according to the macroscopic arguments, a corrugated surface of area A_s becomes completely wet, if

$$\gamma_{sv} = \frac{A}{A_s}\gamma_{lv} + \gamma_{sl}, \tag{18}$$

  where $A < A_s$ is the area of the liquid–vapour interface. Because this condition is easier to be met than the one for a planar wall, one would expect that the wetting of a grooved surface occurs at a lower temperature than wetting on a corresponding flat wall. Generally, macroscopic models such as the well-known Wenzel model [33] predict that the roughness of a solid surface enhances its wetting (or drying) properties; thus, corrugation makes hydrophilic substrates even more wettable. Other simple

phenomenological models, that consider the possibility of groove-filling, provide qualitatively similar predictions. We claim that this contradiction can be explained as follows.

(1) Classical models rely on an analysis of a macroscopic liquid drop deposited on a solid surface whose contact angle is controlled by the surface tensions involved. However, a proper description of the models involving tiny capillaries[1] necessitates a more microscopic treatment [34]. In particular, the concept of the binding potential, which is neglected in macroscopic models, is particularly crucial [35, 36]. For the present molecular model the binding potential at the local height $\ell(x)$ decays as $\ell^{-2}(x)$ with an amplitude depending on the strength and geometry of the wall. As illustrated in figure 4, the effective wall parameter is considerably weakened by the presence of the grooves, which tends to shift the temperature of complete wetting to higher values. Moreover, the molecular model presented here takes into account the strongly inhomogeneous character of the adsorbed fluid including packing effects that are particularly strong in the vicinity of the wall.

(2) Our model of the grooved substrate exhibits sharp edges at the ends of the ridges. Here, the surface tension prevents the local meniscus from unbinding from the substrate, even if far from the edge apex the height of the interface above the surface is macroscopic [37]. Furthermore, the macroscopic Young equation (even if the line tension contribution is taken into account) ceases to hold if the three-phase contact line is located at the edge, since the apparent contact angle exhibits ambiguity. The latter phenomenon, known as Gibbs' criterion, has often been invoked in conjecture with contact line pinning at the edge, see e.g. [38]. Note, however, that the concept of the contact line pinning was questioned in the recent more microscopic study dealing with nanoscopic sessile droplets [39] due to the presence of the accompanying wetting films.

- Each phase transition that occurs at the two-phase coexistence also extends to the undersaturation states and terminates at its own critical point as shown in figures 9, 11, 12, 14 and 15. In particular, the critical point corresponding to groove-filling occurs slightly above T_w and the difference is pronounced when the grooves (of a fixed depth) are wide (see figure 15). This should be contrasted with the groove-filling in a deep ($D \to \infty$) groove, where, as mentioned in section 2, this point corresponds to T_w and separates first-order and critical filling regimes. We note that the limited numerical accuracy does not allow us to determine the way in which the transition line connects the bulk coexistence, so that this remains an open question.

[1] Only shallow grooves were considered throughout of this work. No qualitative difference was found for the models with the deeper grooves (up to $D = 20\sigma$).

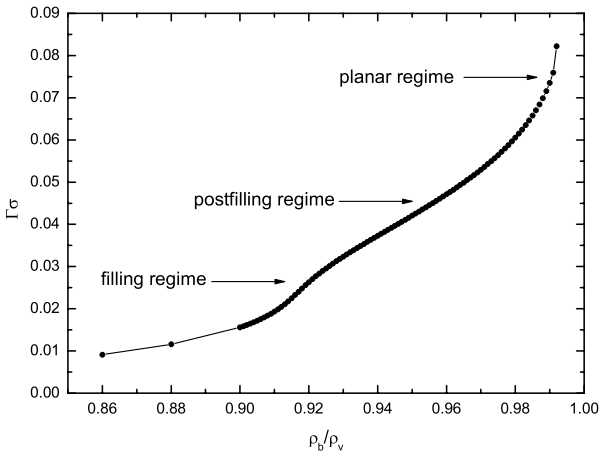

Figure 16. Adsorption isotherm for a model with $L^* = 40$, $L_1^* = 20$, and $D^* = 5$ at a temperature $T^* = 1.35$. Filling, postfilling and planar regimes can be distinguished. The undersaturation is expressed as a ratio between the bulk and saturated vapour densities.

- In [10], the authors report their results based on effective interfacial Hamiltonian theory for complete wetting of patterned substrates (including rectangular grooves) with long-ranged intermolecular potentials. They observed four distinct scaling regimes. This matches with the picture of adsorption for our model provided the isotherm corresponds to $T > T_{gw}$ and does not cross any of the first-order transition lines. As an example, we show in figure 16 the adsorption isotherm for one of the aforementioned substrate models at a sufficiently high temperature. Clearly, the filling regime corresponding to an abrupt rise of the meniscus inside the grooves is less pronounced than that for much deeper capillaries considered in [10]. The following postfilling regime is characterized by an almost linear dependence of the adsorption on undersaturation. Finally, the last regime corresponds to the power law behaviour, equation (1), as for the planar wall. The authors in [10] further split the latter into the effective planar scaling regime with a geometry-dependent Hamaker constant and the one for which the geometrical patterns are irrelevant.
- The last remark concerns the approximations and possible extensions of this work. As strictly of a mean-field character, the approximative DFT necessarily neglects some kinds of fluctuations such as those due to capillary waves and thus it is legitimate to ask whether the predicted phenomena could realistically be observed. Recall, first, that since the molecular model includes dispersion forces, the mean-field approximation is valid for wetting and filling transitions in three dimensions [1, 9, 40]. It is further important to emphasize that owing to an infinite extension of the groove array (together with a translation invariancy along the y-axis), the phase transitions considered here terminate at true critical points. However, as already mentioned in section 2, this would not be the case of a single groove (of finite depth), for which the groove-filling transition must be rounded due to its pseudo-1D character.

Throughout this work the concern was on the fluid phase of the adsorbent only. As we have seen, however, a strong wall-induced crystallization takes place well above the bulk triple point ($T_t^b \approx 0.5T_c$, see, e.g., [41]). Therefore, in some cases (see figures 11 and 14) the crystal nuclei form before the groove-filling lines connect the bulk coexistence. One could avoid such issue by considering a lower value of the parameter ε_w but then the other phase transitions would also be shifted and possibly vanish. The proper investigation of the equilibrium fluid solidification at the structured wall is definitely an interesting task but requires a more demanding (3D) treatment than used here.

There is a number of open questions as regards to the related models. For instance, one may ask to what extent the phase behaviour scenario will be modified by considering the atomic corrugation of the wall, as addressed, e.g., in [42–44]. In fact, the model itself could serve to mimic a periodically corrugated substrate if both D and L parameters are of the order of the molecular diameter σ. We note that for $D \approx 2\sigma$ the filling transition disappears. Also, it would be interesting to make a link with adsorption at chemically structured surfaces, especially in view of the 'morphological phase transitions' predicted in [45, 46].

Acknowledgment

The support from the Czech Science Foundation, project 13-09914S, is acknowledged.

Appendix A. Wall potential

In this appendix, the attractive contributions of the potentials $V_1(z)$ and $V_2(x, z)$ (equations (6) and (7)) as given by (8)–(11) are derived.

We assume that the wall is formed with uniformly distributed atoms with a density ρ_w, which interact with the fluid particles according to (5). A contribution of the semi-infinite planar wall, $V_1(z)$, is given by integrating $\phi_w(r)$ over the domain $\{x \in \mathbb{R}, y \in \mathbb{R}, z \in (-\infty, 0)\}$, which leads to a familiar z^{-3} expression:

$$\begin{aligned}\tilde{V}_1(z) &= \rho_w \int_{-\infty}^{\infty} dx' \int_{-\infty}^{\infty} dy' \int_{-\infty}^{0} dz' \\ &\quad \times \phi_w\left(\sqrt{x'^2 + y'^2 + (z - z')^2}\right) \\ &= -8\pi\varepsilon_w\rho_w\sigma^6 \int_0^{\infty} d\rho\, \rho \int_{-\infty}^{-z} dz' \frac{1}{(\rho^2 + z'^2)^3} \\ &= \frac{2\alpha_w}{z^3}, \qquad (\forall z > 0), \end{aligned} \tag{A.1}$$

with $\alpha_w = -\frac{1}{3}\pi\varepsilon_w\rho_w\sigma^6$.

The attractive potential exerted by a single rectangular body comprising a volume $\{x \in (-L_1, 0), y \in \mathbb{R}, z \in (0, D)\}$ is

$$\begin{aligned}\tilde{V}_2(x, z) &= \rho_w \int_{-L_1}^{0} dx' \int_{-\infty}^{\infty} dy' \int_0^D dz' \\ &\quad \times \phi_w\left(\sqrt{(x - x')^2 + y'^2 + (z - z')^2}\right) \\ &= -4\varepsilon_w\rho_w\sigma_w^6 \int_{-L_1}^{0} dx' \int_{-\infty}^{\infty} dy' \int_0^D dz' \\ &\quad \times \frac{1}{\left(\sqrt{(x - x')^2 + y'^2 + (z - z')^2}\right)} \\ &= -\tfrac{3}{2}\pi\varepsilon_w\rho_w\sigma_w^6 \int_{-L_1}^{0} dx' \int_0^D dz' \\ &\quad \times \frac{1}{\left[(x - x)'^2 + (z - z')^2\right]^{5/2}} \\ &= -\tfrac{3}{2}\pi\varepsilon_w\rho_w\sigma_w^6 \int_x^{L_1+x} dx' \\ &\quad \times \int_{z-D}^{z} dz' \frac{1}{\left(x'^2 + z'^2\right)^{5/2}} \\ &= -\tfrac{1}{2}\pi\varepsilon_w\rho_w\sigma_w^6 \\ &\quad \times \int_x^{L_1+x} dx' \frac{z'(3x'^2 + 2z'^2)}{x'^4\left(x'^2 + z'^2\right)^{3/2}}\Bigg|_{z'=z-D}^{z'=z} \\ &= \alpha_w\left[\psi_{z,D}(L_1 + x) - \psi_{z,D}(x)\right], \end{aligned} \tag{A.2}$$

where

$$\begin{aligned}\psi_{z,D}(x) \equiv &\frac{2x^4 + x^2(z - D)^2 + 2(z - D)^4}{2(z - D)^3x^3\sqrt{x^2 + (z - D)^2}} \\ &- \frac{2x^4 + x^2z^2 + 2z^4}{2x^3z^3\sqrt{x^2 + z^2}}. \end{aligned} \tag{A.3}$$

It can be checked that for $z > D$:

$$\lim_{x\to 0} \psi_{z,D}(x) = \lim_{x\to\infty}\left[\frac{2(z - D)^4}{2(z - D)^4x^3} - \frac{1}{x^3}\right] = 0$$

and

$$\lim_{x\to\infty} \psi_{z,D}(x) = \frac{1}{(z - D)^3} - \frac{1}{z^3}.$$

From these two limits it follows that (using (A.1))

$$\lim_{L_1\to\infty} \tilde{V}_2(0, z > D) = \frac{\tilde{V}_1(z - D)}{2} - \frac{\tilde{V}_1(z)}{2},$$

as one expects.

Furthermore, for $z < D$:

$$\lim_{x\to 0} \psi_{z,D}(x) = -\infty;$$

thus, $\tilde{V}_2(0, z < D)$ diverges as also expected.

Finally, in the limit of infinite D, (A.3) becomes

$$\lim_{D\to\infty} \psi_{z,D}(x) = -\frac{1}{x^3} - \frac{2x^4 + x^2z^2 + 2z^4}{2x^3z^3\sqrt{x^2 + z^2}}$$

and because

$$\lim_{x\to\infty}\lim_{D\to\infty} \psi_{z,D}(x) = -\frac{1}{z^3},$$

one obtains in the limit of both $D \to \infty$ and $L_1 \to \infty$

$$\lim_{L_1\to\infty}\lim_{D\to\infty}\left(\tilde{V}_1(z)+\tilde{V}_2(x,z)\right) = \alpha_{\rm w}\left[\frac{1}{z^3}+\frac{2x^4+x^2z^2+2z^4}{2x^3z^3\sqrt{x^2+z^2}}+\frac{1}{x^3}\right], \quad \text{(A.4)}$$

which is the potential of a rectangular wedge, cf [27].

Appendix B. Weighted densities

In this appendix, we derive the expressions of the Rosenfeld weighted densities for a hard-sphere $\mathcal{N}$-component mixture, exploiting the rectangular symmetry induced by the external potential (4).

The weighted densities are defined by a sum of convolutions

$$n_\alpha(\mathbf{r}) = \sum_{i=1}^{\mathcal{N}} \int \mathrm{d}\mathbf{r}'\,\rho_i(\mathbf{r}')w_\alpha^i(\mathbf{r}-\mathbf{r}'), \quad \text{(B.1)}$$

where, according to the original Rosenfeld fundamental measure theory [16], the weighted functions consist of four scalars

$$w_3^i(\mathbf{r}) = \Theta(R_i - r); \qquad w_2^i(\mathbf{r}) = \delta(\sigma/2 - r);$$
$$w_1^i(\mathbf{r}) = \frac{w_2(\mathbf{r})}{4\pi R_i}; \qquad w_0^i(\mathbf{r}) = \frac{w_2(\mathbf{r})}{2\pi R_i};$$

and two vectors

$$\mathbf{w}_2^i(\mathbf{r}) = \frac{\mathbf{r}}{r}\delta(R_i - r) \qquad \mathbf{w}_1^i(\mathbf{r}) = \frac{\mathbf{w}_2(\mathbf{r})}{4\pi R_i}.$$

Here, R_i refers to the radius of the ith species.

B.1. $n_3(x, z)$

The weighted density $n_3(x, z)$ is given by the following volume integral in the Cartesian coordinates:

$$n_3(x,z) = 2\sum_{i=1}^{\mathcal{N}}\int_{-R_i}^{R_i}\mathrm{d}z'\int_{-\sqrt{R_i^2-z'^2}}^{\sqrt{R_i^2-z'^2}}\mathrm{d}x' \times \sqrt{R_i^2-z'^2-x'^2}\,\rho(x+x', z+z'), \quad \text{(B.2)}$$

which can be solved numerically by any standard quadrature. However, it may be more convenient to transform the dummy variables $z' \to R_i z'$ and $x' \to x'\sqrt{R_i^2 - z'^2}$ to express $n_3(x, z)$ as the integral over the domain $(-1, 1) \times (-1, 1)$:

$$n_3(x,z) = 2\sum_{i=1}^{\mathcal{N}} R_i^3\int_{-1}^{1}\mathrm{d}z'(1-z'^2)\int_{-1}^{1}\mathrm{d}x'\sqrt{1-x'^2} \times \rho(x+R_i\sqrt{1-z'^2}x, z+R_iz'). \quad \text{(B.3)}$$

This form allows us to employ the Gaussian quadrature:

$$n_3(x,z) \approx 2\sum_{i=1}^{\mathcal{N}} R_i^3\sum_{k}^{n_{\rm L}} w_k^{\rm L}(1-(z_k^{\rm L})^2)\left[\sum_j^{n_{\rm c_2}} w_j^{\rm c_2} \times \rho(x+R_i\sqrt{1-(z_k^{\rm L})^2}x_j^{\rm c_2}, z+R_iz_k^{\rm L})\right], \quad \text{(B.4)}$$

where $x_k^{\rm L}, w_k^{\rm L}, k = \{1, n_{\rm L}\}$ are the nodes and the weights of the Legendre polynomials up to degree $n_{\rm L}$, and $x_k^{\rm c_2}, w_k^{\rm c_2}, k = \{1, n_{\rm c_2}\}$ are the nodes and the weights of the Chebyshev polynomials of the second kind up to degree $n_{\rm c_2}$.

B.2. $n_2(x, z), n_1(x, z), n_0(x, z)$

The 'surface' weighted function can be expressed as follows:

$$n_2(x,z) = 2\sum_{i=1}^{\mathcal{N}} R_i\int_{-R_i}^{R_i}\mathrm{d}z'\int_{-\sqrt{R_i^2-z'^2}}^{\sqrt{R_i^2-z'^2}}\mathrm{d}x' \times \frac{1}{\sqrt{R_i^2-z'^2-x'^2}}\rho(x+x', z+z'). \quad \text{(B.5)}$$

Now, because the integrand blows up at the boundaries of the inner integral, the use of the Gaussian quadrature is vital. Following the same transformation as above, (B.5) becomes

$$n_2(x,z) = 2\sum_{i=1}^{\mathcal{N}} R_i^2\int_{-1}^{1}\mathrm{d}z'\int_{-1}^{1}\mathrm{d}x' \times \frac{1}{\sqrt{1-x'^2}}\rho(x+R_i\sqrt{1-z'^2}x', z+R_iz') \approx 2\sum_{i=1}^{\mathcal{N}} R_i^2\sum_{k}^{n_{\rm L}} w_k^{\rm L}\left[\sum_j^{n_{\rm c_1}} w_j^{\rm c_1} \times \rho(x+R_i\sqrt{1-(z_k^{\rm L})^2}x_j^{\rm c_1}, z+R_iz_k^{\rm L})\right], \quad \text{(B.6)}$$

where $x_k^{\rm c_2}, w_k^{\rm c_2}, k = \{1, n_{\rm c_1}\}$ are the nodes and the weights of the Chebyshev polynomials of the first kind up to degree $n_{\rm c_1}$.

Similarly, for $n_1(x, z)$ and $n_0(x, z)$ one obtains

$$n_1(x,z) \approx \frac{1}{2\pi}\sum_{i=1}^{\mathcal{N}} R_i\sum_{k}^{n_{\rm L}} w_k^{\rm L}\left[\sum_j^{n_{\rm c_1}} w_j^{\rm c_1} \times \rho(x+R_i\sqrt{1-(z_k^{\rm L})^2}x_j^{\rm c_1}, z+R_iz_k^{\rm L})\right] \quad \text{(B.7)}$$

and

$$n_0(x,z) \approx \frac{1}{2\pi}\sum_{i=1}^{\mathcal{N}}\sum_{k}^{n_{\rm L}} w_k^{\rm L}\left[\sum_j^{n_{\rm c_1}} w_j^{\rm c_1} \times \rho(x+R_i\sqrt{1-(z_k^{\rm L})^2}x_j^{\rm c_1}, z+R_iz_k^{\rm L})\right]. \quad \text{(B.8)}$$

B.3. $\mathbf{n}_2(x, z), \mathbf{n}_1(x, z)$

The vectorial weighted densities can be dealt in the same manner. Thus, for the x-components of $\mathbf{n}_2(x, z)$ and $\mathbf{n}_1(x, z)$ we obtain

$$n_2^x(x,z) = 2\sum_{i=1}^{\mathcal{N}}\int_{-R_i}^{R_i}\mathrm{d}z'\int_{-\sqrt{R_i^2-z'^2}}^{\sqrt{R_i^2-z'^2}}\mathrm{d}x' \times \frac{x'}{\sqrt{R_i^2-z'^2-x'^2}}\rho(x+x', z+z')$$

$$\approx 2\sum_{i=1}^{\mathcal{N}} R_i^2 \sum_k^{n_{c_2}} w_k^{c_2} \left[\sum_j^{n_{c_1}} w_j^{c_1} x_j^{c_1} \times \rho(x + R_i\sqrt{1-(z_k^{c_2})^2}\, x_j^{c_1}, z + R_i z_k^{c_2}) \right], \tag{B.9}$$

and

$$n_1^x(x,z) \approx \frac{1}{2\pi}\sum_{i=1}^{\mathcal{N}} R_i \sum_k^{n_{c_2}} w_k^{c_2} \left[\sum_j^{n_{c_1}} w_j^{c_1} x_j^{c_1} \times \rho(x + R_i\sqrt{1-(z_k^{c_2})^2}\, x_j^{c_1}, z + R_i z_k^{c_2}) \right]. \tag{B.10}$$

Similarly, for the y-components it follows that

$$n_2^y(x,z) = 2\sum_{i=1}^{\mathcal{N}} \int_{-R_i}^{R_i} \mathrm{d}z' \int_{-\sqrt{R_i^2-z'^2}}^{\sqrt{R_i^2-z'^2}} \mathrm{d}x' \times \frac{1}{\sqrt{R_i^2 - z'^2 - x'^2}} \rho(x+x', z+z') \approx 2\sum_{i=1}^{\mathcal{N}} R_i^2 \sum_k^{n_L} w_k^L z_k^L \left[\sum_j^{n_{c_1}} w_j^{c_1} \times \rho(x + R_i\sqrt{1-(z_k^L)^2}\, x_j^{c_1}, z + R_i z_k^L) \right], \tag{B.11}$$

and

$$n_1^y(x,z) \approx \frac{1}{2\pi}\sum_{i=1}^{\mathcal{N}} R_i \sum_k^{n_L} w_k^L y_k^L \left[\sum_j^{n_{c_1}} w_j^{c_1} \times \rho(x + R_i\sqrt{1-(z_k^L)^2}\, x_j^{c_1}, z + R_i z_k^L) \right]. \tag{B.12}$$

Appendix C. $\int \mathbf{dr'}\rho(\mathbf{r'})u_a(|\mathbf{r}-\mathbf{r'}|)$

In this appendix, we develop the third term in equation (16):

$$I(\mathbf{r}) \equiv \int \mathrm{d}\mathbf{r}'\rho(\mathbf{r}')u_a(|\mathbf{r}-\mathbf{r}'|) = \int \mathrm{d}\mathbf{r}'\rho(\mathbf{r}+\mathbf{r}')u_a(r'), \tag{C.1}$$

with the attractive potential u_a given by (14). With $\rho(\mathbf{r}) = \rho(x,z)$, the function $I(\mathbf{r}) = I(x,z)$ reads

$$I(x,z) = \int u_a(r')\rho(x+x', z+z')\,\mathrm{d}\mathbf{r}' = \int u_a(r')\rho(x+x', z+z') \times \left[H(r_c - r') - H(\sigma - r')\right]\mathrm{d}\mathbf{r}', \tag{C.2}$$

where $H(x)$ is the Heaviside function, and we wish to express (C.2) as a double integral over the x and z coordinates.

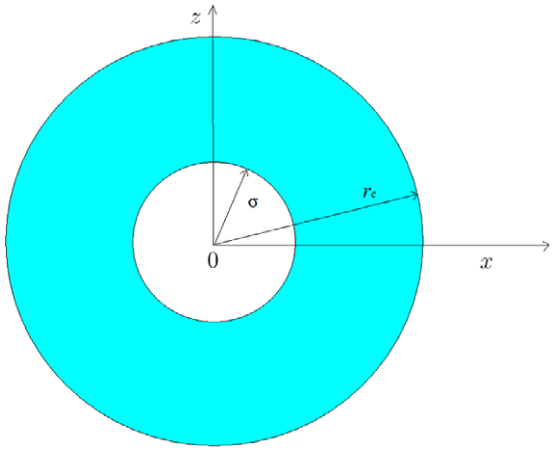

Figure C.1. Sketch of the integrated domain in the x–z projection for $y = 0$.

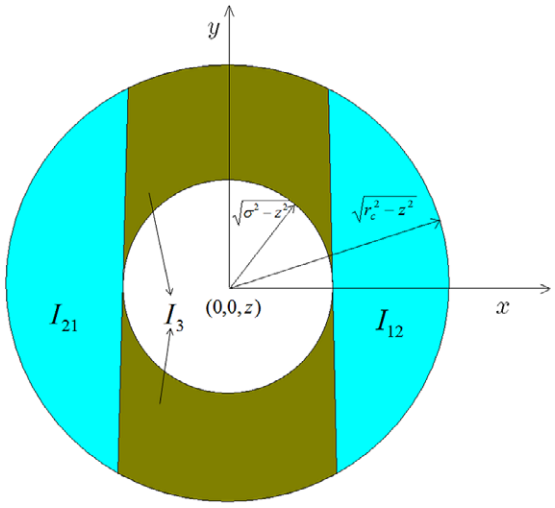

Figure C.2. Sketch of the integrated domain in the x–y projection for $z < \sigma$.

Apparently, one can treat $I(x,z)$ as the difference between two independent contributions over the spheres of radii σ and r_c. Unfortunately, although this approach would be possible for a potential such as the square-well, it cannot be applied for the present model, since $u_a(r)$ cannot be extended to zero. Instead, $I(x,z)$ is separated into five terms as follows (see figures C.1 and C.2):

$$I = I_{11} + I_{12} + I_{21} + I_{22} + I_3, \tag{C.3}$$

where

$$I_{11} = -8\varepsilon\sigma^6 \int_{\sigma}^{r_c} \mathrm{d}z' \int_{-\sqrt{r_c^2-z'^2}}^{\sqrt{r_c^2-z'^2}} \mathrm{d}x' \rho(x+x', z+z') \times \psi_{r_c}(x', z'),$$

$$I_{12} = -8\varepsilon\sigma^6 \int_{-r_c}^{-\sigma} \mathrm{d}z' \int_{-\sqrt{r_c^2-z'^2}}^{\sqrt{r_c^2-z'^2}} \mathrm{d}x' \rho(x+x', z+z') \times \psi_{r_c}(x', z'),$$

$$I_{21} = -8\varepsilon\sigma^6 \int_{-\sigma}^{\sigma} \mathrm{d}z \int_{-\sqrt{r_c^2-z^2}}^{-\sqrt{\sigma^2-z^2}} \mathrm{d}x\, \rho(x+x', z+z') \times \psi_{r_c}(x', z'),$$

$$I_{22} = -8\varepsilon\sigma^6 \int_{-\sigma}^{\sigma} \mathrm{d}z' \int_{\sqrt{\sigma^2-z'^2}}^{\sqrt{r_c^2-z'^2}} \mathrm{d}x'\, \rho(x+x', z+z') \times \psi_{r_c}(x', z'),$$

and

$$I_3 = -8\varepsilon\sigma^6 \int_{-\sigma}^{\sigma} \mathrm{d}z' \times \int_{-\sqrt{\sigma^2-z'^2}}^{\sqrt{\sigma^2-z'^2}} \mathrm{d}x' \rho(x+x', z+z') \tilde{\psi}_{\sigma,r_c}(x', z').$$

Here we use the following abbreviations:

$$\psi_{r_c}(x,z) \equiv \int_0^{\sqrt{r_c^2-z^2-x^2}} \frac{\mathrm{d}y}{(x^2+y^2+z^2)^3} = \frac{5r^2y_2+3y_2^3}{8r^4r_c^4} + \frac{3\arctan\left[\frac{y_2}{r}\right]}{8r^5},$$

and

$$\tilde{\psi}_{\sigma,r_c}(x,z) \equiv \int_{y_1(x,z;\sigma)}^{y_2(x,z;r_c)} \frac{\mathrm{d}z}{(x^2+z^2+z^2)^3} = \frac{1}{8r^5(r^2+y_1^2)^2(r^2+y_2^2)^2} \Bigg\{ r(y_1-y_2) \times [-5r^6 + 3y_1^3y_2^3 + r^4(-3y_1^2+7y_1y_2-3y_2^2) + r^2y_1y_2(5y_1^2-y_1y_2+5y_2^2)] + 3(r^2+y_1^2)^2(r^2+y_2^2)^2 \times \left[\arctan\left(\frac{r}{y_1}\right) - \arctan\left(\frac{r}{y_2}\right)\right]\Bigg\},$$

where $r(x,z) \equiv \sqrt{x^2+z^2}$, $y_1(x,z;\sigma) = \sqrt{\sigma^2-x^2-z^2}$, and $y_2(x,z;r_c) = \sqrt{r_c^2-x^2-z^2}$.

A singularity of $\tilde{\psi}_{\sigma,r_c}$ at $r \to 0$ is removable:

$$\lim_{r\to 0} \tilde{\psi}_{\sigma,r_c}(x,z) = -\frac{1}{5}\left(\frac{1}{r_c^5} - \frac{1}{\sigma^5}\right).$$

References

[1] Dietrich S 1988 *Phase Transitions and Critical Phenomena* vol 12, ed C Domb and J L Lebowitz (New York: Academic)
[2] Sullivan D E and Telo da Gama M M 1985 *Fluid Interfacial Phenomena* ed C A Croxton (New York: Wiley)
[3] Schick M 1990 *Liquids and Interfaces* ed J Chorvolin, J F Joanny and J Zinn-Justin (New York: Elsevier)
[4] Quéré D 2008 *Annu. Rev. Mater. Sci.* **38** 71
[5] Whitesides G M and Stroock A D 2001 *Phys. Today* **54** 42
[6] Dietrich S 1999 *New Approaches to Problems in Liquid State Theory* ed C Caccamo, J P Hansen and G Stell (Dordrecht: Kluwer)
[7] Rascón C and Parry A O 2000 *Nature* **407** 986
[8] Hauge E H 1992 *Phys. Rev.* A **46** 4994
[9] Rascón C and Parry A O 2005 *Phys. Rev. Lett.* **94** 096103
[10] Tasinkevych M and Dietrich S 2006 *Phys. Rev. Lett.* **97** 106102
Tasinkevych M and Dietrich S 2007 *Eur. Phys. J.* E **23** 117
[11] Bruschi L, Carlin A and Mistura G 2002 *Phys. Rev. Lett.* **89** 166101
[12] Bruschi L, Fois G, Mistura G, Tormen M, Garbin V, di Fabrizio E, Gerardino A and Natali M 2006 *J. Chem. Phys.* **125** 144709
[13] Javadi A, Habibi M, Taheri F S, Moulinet S and Bonn D 2013 *Sci. Rep.* **3** 1412
[14] Hofmann T, Tasinkevych M, Checco A, Dobisz E, Dietrich S and Ocko B M 2010 *Phys. Rev. Lett.* **104** 106102
[15] Checco A, Ocko B M, Tasinkevych M and Dietrich S 2012 *Phys. Rev. Lett.* **109** 166101
[16] Rosenfeld Y 1989 *Phys. Rev. Lett.* **63** 980
[17] Rascón C, Parry A O, Wilding N B and Evans R 2007 *Phys. Rev. Lett.* **98** 226101
[18] Marini Bettolo Marconi U and Van Swol F 1989 *Phys. Rev.* A **39** 4109
[19] Darbellay G A and Yeomans J M 1992 *J. Phys. A: Math. Gen.* **25** 4275
[20] Gelb L D 2002 *Mol. Phys.* **100** 2049
[21] Roth R and Parry A O 2011 *Mol. Phys.* **109** 1159
[22] Malijevský A 2012 *J. Chem. Phys.* **137** 214704
[23] Rascón C, Parry A O, Nürnberg R, Pozzato A, Tormen M, Bruschi L and Mistura G 2013 *J. Phys.: Condens. Matter* **25** 19201
[24] Rejmer K, Dietrich S and Napirkówski M 1999 *Phys. Rev.* E **60** 4027
[25] Parry A O, Rascón C and Wood A J 1999 *Phys. Rev. Lett.* **83** 5535
Parry A O, Rascón C and Wood A J 2000 *Phys. Rev. Lett.* **85** 345
[26] Milchev A, Müller M, Binder K and Landau D P 2003 *Phys. Rev. Lett.* **90** 136101
Milchev A, Müller M, Binder K and Landau D P 2003 *Phys. Rev.* E **68** 031601
[27] Malijevský A and Parry A O 2013 *Phys. Rev. Lett.* **110** 166101
[28] Malijevský A and Parry A O 2013 *J. Phys.: Condens. Matter* **25** 305005
[29] Evans R 1979 *Adv. Phys.* **28** 143
[30] Shahidzadeh N, Bonn D, Ragil K, Broseta D and Meunier J 1998 *Phys. Rev. Lett.* **80** 3992
[31] Indekeu J 2000 *Phys. Rev. Lett.* **85** 4188
[32] Gonzaález A and Telo da Gama M M 2000 *Phys. Rev.* E **62** 6571
[33] Wenzel R N 1936 *Indust. Eng. Chem.* **28** 988
[34] Rowlinson J S and Widom B 1982 *Molecular Theory of Capillarity* (Oxford: Clarendon)
[35] Evans R and Tarazona P 1984 *Phys. Rev. Lett.* **52** 557
[36] Rauscher M and Dietrich S 2010 *Soft Matter* **5** 2997
[37] Parry A O, Greenall M J and Romero-Enrique J M 2003 *Phys. Rev. Lett.* **90** 046101
[38] Semprebon C, Mistura G, Orlandini E, Bissacco G, Segato A and Yeomans J M 2009 *Langmuir* **25** 5619
[39] Dutka F, Napiórkowski M and Dietrich S 2012 *J. Chem. Phys.* **136** 064702
[40] Lipowsky R 1984 *Phys. Rev. Lett.* **52** 1429
[41] Tarazona P 1984 *Mol. Phys.* **52** 81
[42] Swain P S and Parry A O 1998 *Eur. Phys. J.* B **4** 459
[43] Rejmer K and Napiórkowski M 2000 *Phys. Rev.* E **62** 588
[44] Kubalski G P, Napiórkowski M and Rejmer K 2001 *J. Phys.: Condens. Matter* **13** 4727
[45] Bauer C, Dietrich S and Parry A O 1999 *Europhys. Lett.* **47** 474
[46] Bauer C and Dietrich S 1999 *Phys. Rev.* E **60** 6919

Paper X

Capillary Contact Angle in a Completely Wet Groove

A. O. Parry,[1] A. Malijevský,[2] and C. Rascón[3]
[1]Department of Mathematics, Imperial College London, London SW7 2BZ, United Kingdom
[2]Department of Physical Chemistry, Institute of Chemical Technology Prague, 16628 Praha 6, Czech Republic; ICPF, Academy of Sciences, 16502 Prague 6, Czech Republic
[3]GISC, Departamento de Matemáticas, Universidad Carlos III de Madrid, 28911 Leganés, Madrid, Spain
(Received 9 June 2014; published 30 September 2014)

We consider the phase equilibria of a fluid confined in a deep capillary groove of width L with identical side walls and a bottom made of a different material. All walls are completely wet by the liquid. Using density functional theory and interfacial models, we show that the meniscus separating liquid and gas phases at two phase capillary coexistence meets the bottom capped end of the groove at a capillary contact angle $\theta^{\rm cap}(L)$ which depends on the difference between the Hamaker constants. If the bottom wall has a weaker wall-fluid attraction than the side walls, then $\theta^{\rm cap} > 0$ even though all the isolated walls are themselves completely wet. This alters the capillary condensation transition which is now first order; this would be continuous in a capped capillary made wholly of either type of material. We show that the capillary contact angle $\theta^{\rm cap}(L)$ vanishes in two limits, corresponding to different capillary wetting transitions. These occur as the width (i) becomes macroscopically large, and (ii) is reduced to a microscopic value determined by the difference in Hamaker constants. This second wetting transition is characterized by large scale fluctuations and essential critical singularities arising from marginal interfacial interactions.

DOI: 10.1103/PhysRevLett.113.146101 PACS numbers: 68.08.Bc, 05.20.Jj, 64.60.F-, 68.03.Cd

The equilibrium contact angle θ of a macroscopic drop of liquid on a planar substrate (wall) is determined by the tensions of the wall-gas, wall-liquid and liquid-gas interfaces, by Young's equation [1–3]

$$\gamma_{wg} - \gamma_{wl} = \gamma_{lg}\cos\theta. \quad (1)$$

For complete wetting ($\theta = 0$), the tensions satisfy Antonow's rule $\gamma_{wg} = \gamma_{wl} + \gamma_{lg}$, which means that, as the pressure is increased towards saturation, $p \to p_{\rm sat}(T)$, at temperature T, a macroscopic layer of liquid must be adsorbed at the wall. However, for partial wetting ($\theta > 0$), the wetting layer thickness remains finite at $p_{\rm sat}$. It is well-known that fluid adsorption is strongly modified, and in general, enhanced by substrate geometry [4–14]. An example of this is the *capillary condensation* of liquid in a slit of width L at a shifted value of the pressure $p_{cc}(T;L)$ [15,16], the details of which depend on whether the slit is capped at one end, thus forming a rectangular groove [17–22]. Here, we point out that, in this groove geometry, one may identify a *capillary* contact angle $\theta^{\rm cap}(L)$, defined by analogy with the Young equation but at capillary coexistence p_{cc}, rather than at bulk coexistence $p_{\rm sat}$. This can be thought of as the angle at which the meniscus, separating capillary liquid and gas phases, meets the groove bottom as shown in Fig. 1. Intuitively, one may think that if all the walls are made of completely wet material ($\theta = 0$), then the capillary contact angle is also zero ($\theta^{\rm cap}(L) = 0$). This is indeed the case if all the walls are identical. However, if the bottom wall, which extends over the whole lower half-space, has a weaker long-ranged dispersion interaction with the fluid than the side walls, the capillary contact angle $\theta^{\rm cap}(L)$ is nonzero. Thus, while grooves made wholly of either material have $\theta^{\rm cap}(L) = 0$, somewhat counterintuitively, a groove made of a combination of both has $\theta^{\rm cap}(L) > 0$. In addition, we show that $\theta^{\rm cap}(L)$ vanishes in two limits: (a) as the slit becomes macroscopically wide, and (b) as L is reduced to a specific value determined by the mismatch in Hamaker constants of the side and bottom walls.

Consider the interface between a planar wall of infinite area, occupying the half-space $z < 0$, and a bulk vapor at a subcritical temperature $T < T_c$ and pressure $p < p_{\rm sat}(T)$ [or, equivalently, chemical potential $\mu < \mu_{\rm sat}(T)$]. If $\theta = 0$, then as $p \to p_{\rm sat}$, the equilibrium thickness ℓ_π of the

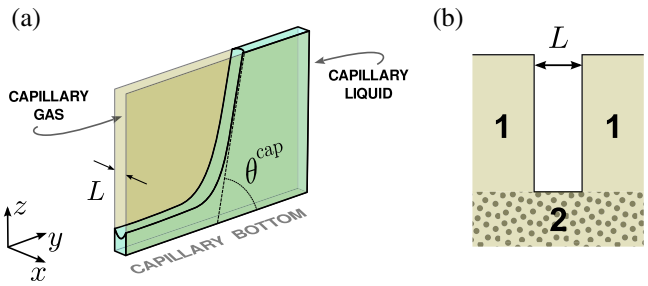

FIG. 1 (color online). (a) Schematic illustration of a mesoscopic droplet of capillary liquid in a heterogeneous groove at capillary coexistence. The meniscus is of near circular cross section, meeting the side walls tangentially, and forming an angle $\theta^{\rm cap}$ as it separates from the bottom. (b) Cross section of a heterogeneous groove made from two completely wet materials.

adsorbed liquid layer grows and would become macroscopic in the absence of gravity. The divergence of ℓ_π was first understood by Frumkin and Derjaguin using the concept of a disjoining pressure [23]. Equivalently, one determines a binding potential $W_\pi(\ell)$ defined as the excess grand potential per unit area of a wetting film constrained to be of thickness ℓ [2]. This quantity can be constructed from a microscopic density functional theory (DFT), where the Grand potential $\Omega[\rho] = F[\rho] - \int d\mathbf{r}\rho(\mathbf{r})(\mu - V(\mathbf{r}))$ is written as a functional of the one-body average density $\rho(\mathbf{r})$. Here, $F[\rho]$ is the intrinsic Helmholtz functional modeling fluid-fluid interactions and $V(\mathbf{r})$ is the external potential due to the wall(s) [24]. Thus, for a single wall, $V(\mathbf{r}) = \rho_w \int d\mathbf{r}' w(|\mathbf{r} - \mathbf{r}'|)$, where the integral is over the volume of the wall (of number density ρ_w) and $w(r)$ is the pair potential between fluid and wall atoms. The binding potential then follows from $\Omega[\rho]$ using a sharp-kink approximation for the density profile $\rho(\mathbf{r})$ in which one simply assumes that there is liquid of bulk density ρ_l below the interface and bulk gas of density ρ_g above it. For systems with dispersion forces whose wall-fluid and fluid-fluid potentials decay proportional to $-\varepsilon^w r^{-6}$ and $-\varepsilon r^{-6}$, respectively, the binding potential has the well-known form [2]

$$W_\pi(\ell) = \delta p \ell + \frac{A}{\ell^2} + \cdots, \tag{2}$$

where $\delta p = p_{\rm sat} - p$. The first term is the thermodynamic penalty of having a layer of a metastable liquid. The second emerges after the interaction potentials are integrated over the 3D volume of the wall and the thickness of the wetting layer, and its coefficient identifies the Hamaker constant $A \propto (\rho_l - \rho_g)(\rho_w \varepsilon^w - \rho_l \varepsilon)$, which is positive for complete wetting. Minimization of $W_\pi(\ell)$ determines the equilibrium film thickness $\ell_\pi \sim \delta p^{-1/3}$ [2].

Consider now a capillary groove of macroscopic length and depth but of microscopic width L which is capped at its bottom. The groove is made from three slabs (two identical side walls and a bottom) of two different materials which are both completely wet. The side walls, of material 1 with interaction strength ε_1^w, occupy the regions $z > 0$ and $|x| > L/2$. The slit is capped by having the third slab of material 2, with interaction strength ε_2^w, occupy the whole lower space, $z < 0$ [See Fig. 1(b)]. In practice, this can be achieved by depositing a layer of material 1 on material 2, and then etching a groove (or an array of them) whose width L is much smaller than the material dimensions. The open end ($z \to \infty$) at the top of the capillary groove is in contact with a bulk gas at pressure p and temperature T. In an uncapped slit, confinement between the side walls leads to the phenomenon of capillary condensation corresponding to the shift of the bulklike coexistence curve so that, at fixed L, capillary-liquid (CL) and capillary-gas (CG) phases coexist along a line $p_{cc}(T; L)$ which terminates at a capillary critical temperature $T_c(L)$. In the capped system, geometry necessitates the formation of a meniscus separating CL and CG phases at some distance ℓ_m from the bottom, which determines the adsorption $\Gamma \approx (\rho_l - \rho_g) L \ell_m$.

To find ℓ_m, we first consider a mean-field (MF) treatment and, using a sharp-kink approximation for the density profile, construct from $\Omega[\rho]$ a capillary binding potential $W_{\rm cap}(L)$ by constraining the meniscus to a uniform height along the groove and determine the excess grand potential per unit area of the groove bottom. If $\ell \gg L$, we find

$$W^{\rm cap}(\ell) = \Delta p \ell + \frac{A_2 - A_1}{\ell^2} + \frac{3A_1 L}{8\ell^3} \cdots, \tag{3}$$

where $\Delta p = p_{cc}(T; L) - p$ and A_1, A_2 are the (positive) Hamaker constants for the side and bottom walls, respectively. The first term is the thermodynamic penalty of having a thick layer of CL and is analogous to the term $\delta p \ell$ in $W_\pi(\ell)$ except that pressure is now measured relative to capillary condensation. Analysis at this order also determines the value of $p_{\rm sat}(T) - p_{cc}(T; L) = 2\gamma_{lg}/(L - 3\ell_\pi)$, which is the Kelvin-Derjaguin result for the shift of the coexistence line allowing for thick wetting films at the side walls [16]. The remaining terms in $W^{\rm cap}(\ell)$ arise from the dispersion forces and can be understood as follows: consider an infinite uncapped capillary slit exactly at $p = p_{cc}$ and place the meniscus at some arbitrary position. Now, cap the capillary by inserting an infinite slab of material type 1 of width L at some large distance ℓ below the meniscus. Since the width of this slab is finite, the contribution to $\Omega[\rho]$ from the dispersion forces can only decay as $\mathcal{O}(\ell^{-3})$ [see the final term of Eq. (3)]. When we make the capillary heterogenous, we must further imagine slicing off an infinite slab of material 1 at the same depth and replacing it with an infinite slab of material type 2. The contribution to $\Omega[\rho]$ from the dispersion forces for both these slabs now involves integration over a 3D semivolume, leading to the second term of Eq. (3). We now consider three scenarios:

(A) *A homogeneous capillary* ($A_1 = A_2$). In this case, the meniscus is repelled from the capped end by a term of $\mathcal{O}(\ell^{-3})$, which competes with the thermodynamic attraction proportional to $\Delta p \ell$. Minimization of $W^{\rm cap}(\ell)$ determines the MF meniscus height $\ell_m \sim \Delta p^{-1/4}$ [19]. The condensation occurring as $p \to p_{cc}^-$ is therefore a continuous capillary transition.

(B) *A heterogeneous capillary* ($A_1 < A_2$). Now, there is a stronger repulsion from the cap than in case A, and the meniscus height grows as $\ell_m \sim \Delta p^{-1/3}$, similar to complete wetting at a planar wall. The condensation transition remains continuous.

(C) *A heterogeneous capillary* ($A_1 > A_2$). Importantly, the difference between the Hamaker constants leads to an interfacial *attraction*, so that the meniscus remains bound at a distance $\ell_m \approx 9LA_1/16(A_1 - A_2)$ from the cap, even at

$p = p_{cc}$. This state coexists with one in which the groove is filled with CL.

The remarkable implication of this result is that, in a capillary with a less attractive bottom wall, the condensation transition is first order even though it would be continuous in a homogeneous capillary made entirely of either material. We emphasize that this phenomenon only occurs if the less attractive bottom wall occupies the *whole* lower half-space [See Fig. 1(b)]. If the slab of material type 2 capping the capillary occupies only the width of the slit, the effect is absent since the effective binding potential for this system is $W^{\rm cap}(\ell) = \Delta p \ell + 3A_2 L/8\ell^3 + \cdots$. The condensation remains continuous, as for case A, albeit with a different amplitude.

We have tested these predictions using a Rosenfeld-like DFT [25] with a mean-field treatment of the attractive fluid-fluid forces $F_{\rm att} = \frac{1}{2}\iint d\mathbf{r}_1 d\mathbf{r}_2 \rho(\mathbf{r}_1) u(r_{12}) \rho(\mathbf{r}_2)$. For the latter, we chose $u(r) = -4\varepsilon(\sigma/r)^6$, where σ is the hard-sphere diameter. This attractive pair potential is truncated at $r_c = 2.5\sigma$ and is set to zero inside the hard sphere [26].

The external potential $V(x, z)$ has a hard-wall contribution and a long-ranged tail, which can be determined analytically from integrating the potential $-4\varepsilon_i^w(\sigma/r)^6$ over the volumes of the side ($i = 1$) and bottom ($i = 2$) walls. Far from the bottom of the capillary ($\sim 50\sigma$), we fix the density to that of a CG phase in order to model the open end of the groove. Translational invariance is assumed along the capillary (the y axis). The temperature is set at $T = 0.96T_c$ ($k_B T_c = 1.41\varepsilon$), which is *above* the wetting temperatures of both the weaker ($\varepsilon^w = \varepsilon$, $T_w = 0.93T_c$) and stronger ($\varepsilon^w = 1.2\varepsilon$, $T_w = 0.83T_c$) attractive walls, ensuring complete wetting of all surfaces.

In Fig. 2, we show adsorption isotherms obtained from a full DFT calculation for three slits of width $L = 12\sigma$: $\varepsilon_1^w = \varepsilon_2^w = 1.2\varepsilon$ (case A), $\varepsilon_1^w = \varepsilon$ and $\varepsilon_2^w = 1.2\varepsilon$ (case B), and $\varepsilon_1^w = 1.2\varepsilon$ and $\varepsilon_2^w = \varepsilon$ (case C). As predicted, the condensation is continuous for the first two cases, and a log-log plot shows very good agreement with the predicted exponent values $1/4$ and $1/3$, respectively [(See Fig. 3(a)]. For the third case, with a less attractive bottom wall, the condensation transition is first order and, at capillary coexistence, a meniscus remains bound close to the cap [Fig. 3(b)].

Just as Young's equation allows us to define a contact angle θ from the three surface tensions associated with coexisting bulk phases and a single isolated wall at $p = p_{\rm sat}$, we may now define a *capillary* contact angle from the analogous free energies of the coexisting capillary phases at $p = p_{cc}$:

$$\gamma_{wg}^{\rm cap}(L) - \gamma_{wl}^{\rm cap}(L) = \gamma_{lg}^{\rm cap}(L)\cos\theta^{\rm cap}(L). \tag{4}$$

Here, $\gamma_{lg}^{\rm cap}(L)$ is the surface tension associated with the meniscus separating capillary liquid and capillary gas phases, defined as the excess grand potential per unit area of the capillary bottom. For wide slits, this tension is well approximated by $\gamma_{lg}^{\rm cap}(L) \approx \pi\gamma_{lg}/2$, owing to the near circular shape of the meniscus. Similarly, $\gamma_{wg}^{\rm cap}(L)$ and $\gamma_{wl}^{\rm cap}(L)$ are the surface tensions associated with the interface between the groove bottom and the CG phase (bound meniscus) and CL phase (unbound meniscus), respectively.

At MF level, we can identify $W^{\rm cap}(\ell_m) = \gamma_{lg}^{\rm cap}(L)((\cos\theta^{\rm cap}(L) - 1)$, which leads to

$$\theta^{\rm cap}(L) \approx \frac{32(A_1 - A_2)^{\frac{3}{2}}}{9\sqrt{3\pi\gamma_{lg}} A_1 L}; \quad L \to \infty, \tag{5}$$

valid for $A_1 > A_2$ and sufficiently large L. Otherwise, when $A_1 \le A_2$, the capillary contact angle vanishes.

The MF result [Eq. (5)] suggests that we can induce a capillary wetting transition by changing the sign of $A_1 - A_2$, similar to the standard mechanism for the critical wetting transition at a single planar wall [2,3]. However,

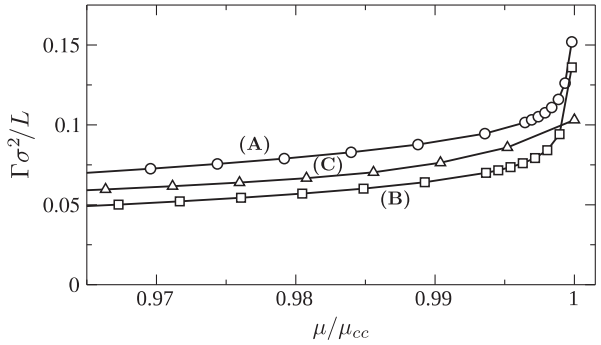

FIG. 2. Adsorption isotherms obtained by numerical minimization of the DFT for (a) a homogeneous capillary, (b) a capillary with a more attractive bottom wall, and (c) a capillary with a less attractive bottom wall, for $L = 12\sigma$ and $T = 0.96T_c$. Here, μ_{cc} is the chemical potential at capillary condensation determined independently for each infinite open slit.

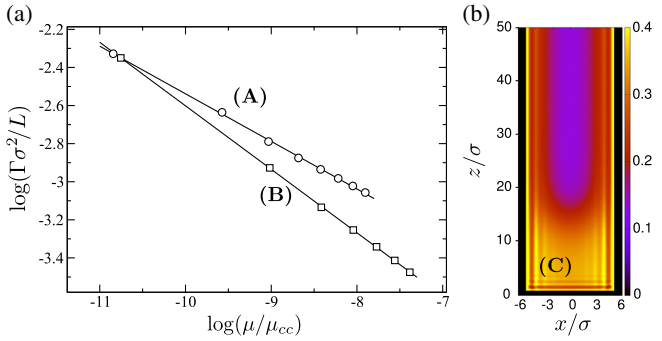

FIG. 3 (color online). (a) Log-log plot of adsorption isotherms for the two examples of continuous capillary condensation and comparison with the predicted slopes $-1/4$ and $-1/3$ [cases (A) and (B), respectively]. (b) For case (C), a two dimensional density profile $\rho(x, z)$ showing a bound state meniscus configuration that coexists with a completely filled capillary at $\mu = \mu_{cc}$.

rather than tuning the Hamaker constants, we focus instead on how $\theta^{\rm cap}(L)$ depends on L, while maintaining capillary coexistence $p = p_{cc}(L)$. To do this, we must go beyond MF and consider fluctuation effects arising from the wandering of the meniscus height along the groove (y axis). These are well described by the 1D interfacial Hamiltonian

$$H^{\rm cap}[\ell] = L \int dy \left\{ \frac{\gamma_{lg}^{\rm cap}(L)}{2} \left(\frac{d\ell}{dy} \right)^2 + W^{\rm cap}(\ell) \right\}, \quad (6)$$

where $\ell(y)$ denotes the local height of the meniscus at position y, and one may approximate $\gamma_{lg}^{\rm cap}(L) \approx \pi\gamma_{lg}/2$. The partition function can be evaluated exactly using standard transfer-matrix techniques, the spectrum of which follows from solution of a Schrödinger-like equation from which one can readily determine $\ell_m = \langle \ell \rangle$, the roughness $\xi_\perp = \sqrt{\langle \ell^2 \rangle - \ell_m^2}$, and the length scale ξ_y describing height correlations along the direction of the groove. Analysis shows that $\theta^{\rm cap}$ may vanish in two different ways. The first occurs when the slit becomes macroscopically wide, in which case interfacial (meniscus) fluctuations are suppressed. Thus, $\theta^{\rm cap}(L)$ vanishes according to [Eq. (5)] with the accompanying scaling behavior $\ell_m \sim L$, $\xi_\perp \sim \sqrt{L}$ and $\xi_y \sim L^2$ describing the growth of the meniscus.

The second type of capillary transition involving the meniscus occurs as the slit width decreases. According to the MF result [Eq. (5)], the capillary contact angle $\theta^{\rm cap}(L)$ continues to increase as the width becomes microscopic. However, the reduction in the stiffness coefficient $L\gamma_{lg}^{\rm cap}(L)$ enhances fluctuation effects, and the meniscus eventually tunnels out of the potential well in $W^{\rm cap}$. Thus, at a sufficiently small slit separation $L = L_w$, the capillary contact angle $\theta^{\rm cap}$ also vanishes, corresponding to another capillary wetting transition. This transition belongs to the intermediate fluctuation regime of two dimensional critical wetting, because the ℓ^{-2} interaction is marginal, making it highly sensitive to the short-ranged structure of the binding potential [27]. In our case, the final term in $W^{\rm cap}(\ell)$ [see Eq. (3)] is strongly repulsive, which means that the transition is characterized by essential singularities [28,29]. When the difference in the Hamaker constants is small, this identifies the value of the slit width L_w at which $\theta^{\rm cap}(L)$ vanishes as

$$L_w = \frac{k_B T}{2\sqrt{\pi\gamma_{lg}(A_1 - A_2)}}, \quad A_1 > A_2. \quad (7)$$

Note that the divergence of L_w as $A_2 \to A_1$ is consistent with the fact that this transition is absent in a homogeneous capillary. When $A_1 = A_2$, the capillary contact angle is always zero. As L is decreased towards L_w in a heterogeneous capillary, the capillary contact angle vanishes as

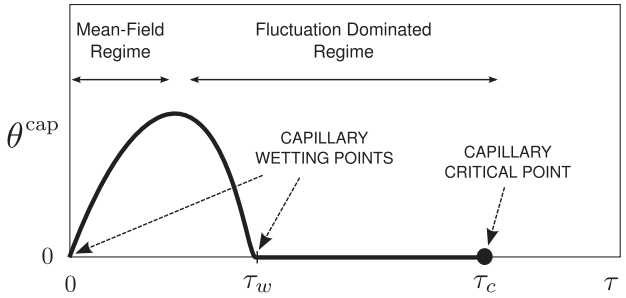

FIG. 4. Schematic behavior of the capillary contact angle $\theta^{\rm cap}$ as a function of the dimensionless variable $\tau \equiv \sqrt{k_B T/4\pi\gamma_{lg}L^2}$. The locations of the capillary wetting transitions and capillary critical point are shown.

$$\theta^{\rm cap}(L) \sim e^{-2\pi L_w/\sqrt{L^2 - L_w^2}}; \quad L \to L_w, \quad (8)$$

with the accompanying scaling $\ell_m \sim \xi_\perp \sim \xi_y^{1/2} \propto 1/\theta^{\rm cap}$, characteristic of fluctuation-dominated behavior. For narrower grooves ($L < L_w$), complete wetting of the cap is restored ($\theta^{\rm cap} = 0$) and eventually, coexistence ends at a conventional capillary critical point [15]. These features are illustrated schematically in Fig. 4, where we plot $\theta^{\rm cap}$ vs $\tau \equiv \sqrt{k_B T/4\pi\gamma_{lg}L^2}$. This dimensionless parameter may be interpreted in two ways. At fixed $T < T_c$, increasing τ corresponds to decreasing L to the critical slit width $L_c(T)$, at which capillary coexistence between CL and CG phases ends. Alternatively, at fixed L, increasing τ corresponds to increasing T towards the capillary critical temperature $T_c(L)$. The value of τ at the capillary critical point depends on the slit width but, in the limit $L \to \infty$, tends to a universal value τ_c. Using the known values of the critical amplitude ratios associated with the wetting parameter [30] and critical point shift $T_c(L) - T_c$ [26,31], this can be reliably estimated as $\tau_c \approx 0.1$. The vanishing of $\theta^{\rm cap}$, as described by Eqs. (5) and (8), corresponds to the two different capillary wetting transitions, which occur at $\tau = 0$ and $\tau = \tau_w \equiv \sqrt{(A_1 - A_2)/(k_B T)}$, respectively. The maximum value of $\theta^{\rm cap}$ occurs between these two transitions and is of order $A_1/k_B T$ if the difference between the Hamaker constants is large.

In summary, we have shown that, in a capillary groove, the competition between the wall-fluid dispersion forces at the bottom and side walls can lead to a nonzero capillary contact angle, though the isolated walls exhibit complete wetting. This finite $\theta^{\rm cap}$ will be present for all temperatures away from the near vicinity of the capillary critical point if the mismatch between the Hamaker constants is of order $k_B T$. Thus, even though the wetting transitions at $\tau = 0$ and $\tau = \tau_w$ may be difficult to observe experimentally, the qualitative change to the order of capillary condensation should be readily observable in grooves of micron size, very similar to the experiments of Mistura *et al.* reported in [21].

A. O. P. wishes to thank the support of the EPSRC UK for Grant No. EP/J009636/1. A. M. thanks the Czech Science Foundation for Grant No. 13-09914S. C. R. acknowledges support from Grants No. FIS2010-22047-C05 and No. MODELICO.

[1] J. S. Rowlinson and B. Widom, *Molecular Theory of Capillarity* (Clarendon Press, Oxford, New York, 1982).
[2] S. Dietrich, in *Phase Transitions and Critical Phenomena*, edited by C. Domb and J. Lebowitz (Academic Press, London, 1988), Vol. 12.
[3] D. Bonn, J. Eggers, J. O. Indekeu, J. Meunier, and E. Rolley, Rev. Mod. Phys. **81**, 739 (2009).
[4] D. Quéré, Annu. Rev. Mater. Res. **38**, 71 (2008).
[5] R. Finn, *Equilibrium Capillary Surfaces* (Springer-Verlag, New York, 1986).
[6] K. Rejmer, S. Dietrich, and M. Napiórkowski, Phys. Rev. E **60**, 4027 (1999).
[7] A. O. Parry, C. Rascón, and A. J. Wood, Phys. Rev. Lett. **85**, 345 (2000).
[8] D. B. Abraham and A. Maciolek, Phys. Rev. Lett. **89**, 286101 (2002).
[9] A. Milchev, M. Müller, K. Binder, and D. P. Landau, Phys. Rev. Lett. **90**, 136101 (2003).
[10] C. Rascón and A. O. Parry, J. Chem. Phys. **112**, 5175 (2000).
[11] C. Rascón and A. O. Parry, Nature (London) **407**, 986 (2000).
[12] M. Tasinkevych and S. Dietrich, Phys. Rev. Lett. **97**, 106102 (2006).
[13] L. Bruschi, A. Carlin, and G. Mistura, Phys. Rev. Lett. **89**, 166101 (2002).
[14] O. Gang, K. J. Alvine, M. Fukuto, P. S. Pershan, C. T. Black, and B. M. Ocko, Phys. Rev. Lett. **95**, 217801 (2005).
[15] R. Evans, U. M. B. Marconi, and P. Tarazona, J. Chem. Phys. **84**, 2376 (1986).
[16] R. Evans, J. Phys. Condens. Matter **2**, 8989 (1990).
[17] U. M. B. Marconi and F. Van Swol, Phys. Rev. A **39**, 4109 (1989).
[18] G. A. Darbellay and J. M. Yeomans, J. Phys. A Math. Gen. **25**, 4275 (1992).
[19] A. O. Parry, C. Rascón, N. B. Wilding, and R. Evans, Phys. Rev. Lett. **98**, 226101 (2007).
[20] A. Malijevský, J. Chem. Phys. **137**, 214704 (2012).
[21] C. Rascón, A. O. Parry, R. Nürenberg, A. Pozatto, M. Tormen, L. Bruschi, and G. Mistura, J. Phys. Condens. Matter **25**, 192101 (2013).
[22] P. Yatsyshin, N. Savva, and S. Kalliadasis, Phys. Rev. E **87**, 020402(R) (2013).
[23] J. R. Henderson, Eur. Phys. J. Spec. Top. **197**, 115 (2011).
[24] R. Evans, Adv. Phys. **28**, 143 (1979).
[25] Y. Rosenfeld, Phys. Rev. Lett. **63**, 980 (1989).
[26] See Supplemental Material at http://link.aps.org/supplemental/10.1103/PhysRevLett.113.146101 for details of the external potential used in the DFT calculation, and further discussion of fluctuation-regimes for 2D critical wetting.
[27] R. Lipowsky and T. M. Nieuwenhuizen, J. Phys. A **21**, L89 (1988).
[28] S. T. Chui and K. B. Ma, Phys. Rev. B **28**, 2555 (1983).
[29] D. M. Kroll and R. Lipowsky, Phys. Rev. B **28**, 5273 (1983).
[30] R. Evans, D. C. Hoyle, and A. O. Parry, Phys. Rev. A **45**, 3823 (1992).
[31] H. Nakanishi and M. E. Fisher, J. Chem. Phys. **78**, 3279 (1983).